Computational Modelling of Electrical Properties of Thyroid and Parathyroid Tissue

Malwina Matella

Supervisor 1: Dr Dawn Walker
Supervisor 2: Prof. Keith Hunter

A thesis submitted in partial fulfilment of the requirements for the degree of Doctor of Philosophy

in the

University of Sheffield
Faculty of Engineering
Department of Computer Science

December 11, 2023

Declaration

I, the author, confirm that the Thesis is my own work. I am aware of the University's Guidance on the Use of Unfair Means (www.sheffield.ac.uk/ssid/unfair-means). This work has not been previously been presented for an award at this, or any other, university.

Publications

Peer-reviewed journal paper:
M. Matella, K. Hunter, S. Balasubramanian, and D. C. Walker, "*Multiscale Model Development for Electrical Properties of Thyroid and Parathyroid Tissues*," IEEE Open J. Eng. Med. Biol., pp. 1–9, 2023.

Peer-reviewed conference paper:
M. Matella, D. C. Walker, and K. Hunter, *"Computational Modelling of Probe Configurations for Electrical Impedance Spectroscopy-based Differentiation of Thyroid and Parathyroid Tissues,"* in 2023 IEEE International Symposium on Medical Measurements and Applications (MeMeA), 2023, pp. 1–6.

Abstract

Parathyroid gland identification is an important consideration in order to decrease the incidence of post-surgical complications associated with thyroid surgeries. Electrical Impedance Spectroscopy (EIS) based tissue differentiation recently emerged as a promising non-invasive technique that could enhance the tissues separation, and parathyroid preservation in a surgery setting.

The aim of the work presented in this thesis is to implement a computational modelling approach in order to elucidate the differences between healthy thyroid and parathyroid tissue impedance spectra which could permit their differentiation during surgery. Multiscale finite element thyroid and parathyroid models have been constructed with the main objective to investigate the impact of morphology and composition on the bulk electrical behaviour of both tissues. The multiscale pipeline represents the hierarchical tissue structure from cellular to tissue scale including a novel mesoscale for the thyroid follicular arrangements.

A comprehensive inter- and intracompartmental sensitivity study provided an insight into the impact of the variations in geometrical and electrical properties of tissue structures on electrical impedance spectra of both tissue types suggesting a successful separability between the computed thyroid and parathyroid impedance spectra indices. Moreover, the modelled results obtained through the variation of geometrical parameters demonstrating the natural variability in tissue morphology provided a good agreement with the *in vivo* measured data acquired and published by Hillary et al.

In addition, the verification of selected homogeneity assumptions and the exploration of measurement accuracy and different probe configurations provided further recommendations for future work concerning computational modelling, experimental data collection and EIS device design improvements. In particular, the outcomes of this computational study revealed the importance of additional experimental work concerning the electrical properties measurements of biological tissue materials, and the significance of tissue preparation and measurement accuracy in obtaining thyroid and parathyroid measurements with a tetrapolar EIS probe.

Acknowledgements

I would like to express my gratitude to my supervisors Dr Dawn Walker and Prof. Keith Hunter for their support during the past four years. I am immensely grateful for the guidance and feedback I have received in order to learn and grow as a researcher and a person. Thank you also for the incredible support in prioritising my mental health during the first years of my project which overlapped with the global pandemic.

I would also like to thank Prof. Brian Brown for the guidance and expertise in computational modelling and Electrical Impedance Spectroscopy research and Prof. Saba Balasubramanian for the expertise in the thyroid and parathyroid surgeries and the incredible input concerning the surgeon's perspective on my research, without whom the successful completion of this project would be much more challenging. I would also like to acknowledge Zilico Ltd. for partially funding the project and for their technical guidance in designing my research. I would also like to thank Dr James Heath who happily shared his experience in Electrical Impedance Spectroscopy and did not mind answering my silly questions regarding ANSYS Mechanical APDL in the beginning of my project.

I also wanted to express my immeasurable gratitude to my parents who through their constant love and support helped me manage my work, my (often irrational) emotions and my mental health on a daily basis. Completing this project would not be possible without you. I also wanted to thank my brother that was always there to cheer me up with his good humour and all my friends for always listening to my complaints and positively distracting me with concerts, travels and (innocent) gossip.

Finally, I would like to thank all the bands, music and books that kept me sane throughout the four years of my project and made me realise that humanities and arts are equally as important as science and engineering. Especially wanted to mention Circa Waves, Blossoms and The Strokes that helped me go through the first months of the pandemic, and The Beatles and Arctic Monkeys whose music inspired me for years and was the spark that encouraged me to pursue my postgraduate studies in the United Kingdom. I also wanted to thank Neil Gaiman for restoring my love for stories, reading and humanity. *'Why? Love.'*

Contents

List of Figures

List of Tables

Chapter 1

Introduction and background

1.1 Introduction

The motivation for the study presented in this thesis arises from the complications associated with the accidental damage or removal of healthy parathyroid glands during surgery. It is often challenging to distinguish parathyroid glands from the surrounding tissues due to their small size and location on the posterior surface of thyroid gland [1]. It would be beneficial for the procedure outcomes to identify a non-invasive screening method that enables tissue evaluation in real time which could be incorporated into thyroid and parathyroid surgery. Electrical Impedance Spectroscopy (EIS) is a prospective tissue identification technique that utilises the dielectric properties of biological tissues that vary between tissue types due to the differences in their micro- and macrostructure, composition, and possible pathological state. EIS and its effectiveness in detecting the parathyroid glands and tissues surrounding them have already been investigated experimentally through *in vivo* rabbit [2] and human [3] tissue measurements. In this study, the utility of EIS for thyroid and parathyroid tissue applications will be further investigated using computational methods in order to elucidate the differences in the electrical properties of both tissue types. Notably, the examination of the relationship between the electrical properties and the structure and composition of the thyroid and parathyroid tissues will be of particular interest.

This chapter will provide the introductory information on the anatomy and histology of thyroid and parathyroid glands, thyroidectomy and the complications associated with this procedure which are the main motivation for this study. This will be followed by the overview of EIS and other parathyroid identification methods, the theory on electrical properties of biological tissues and the introduction of computational modelling methods. This chapter will be concluded by summarising the aims and objectives for this project with further thesis outline.

1.2 Thyroid and parathyroid glands – anatomy and morphology

1.2.1 Thyroid tissue

The thyroid gland (Fig. 1.1) is an endocrine gland located in the central part of the neck and it consists of two lateral symmetrical lobes connected by the medial structure called the isthmus. A typical size of the thyroid gland is of a few centimetres in all three dimensions – each lobe being about 5 x 2.5 x 2.5 cm in size [4]. The main structures present in thyroid tissues are two types of cells: follicular and parafollicular (C-cells), and spherical follicles filled with colloid (Fig. 1.2).

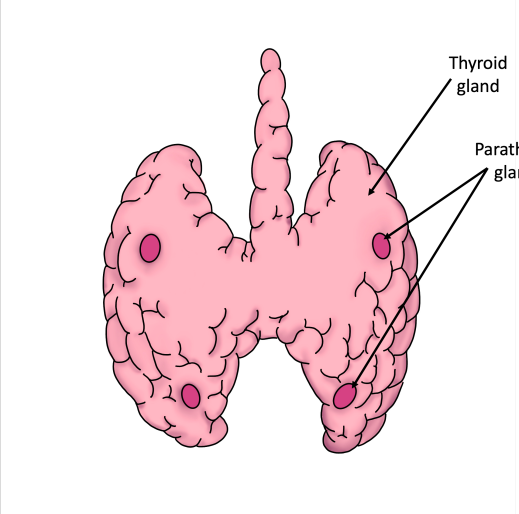

Figure 1.1: *Thyroid and parathyroid glands, posterior view*

Follicular cells, also known as thyrocytes, are responsible for thyroxine and triiodothyronine secretion which is the main function of the gland. They are the most abundant cells, and they build a single layer of cuboidal epithelium that encapsulates each follicle. Parafollicular cells, known as C cells, in contrast, produce calcitonin and are scattered across the whole gland separately or in groups of a few cells. These only account for about 0.1% of the thyroid mass [5]. Spherical structures, filled with protein-rich colloid, called follicles, are the most characteristic features of thyroid tissue that distinguishes it from the other endocrine glands, such as parathyroids where the follicles are entirely absent in the structure of those glands. The main function of thyroid follicles is to store thyroglobulin.

The entire thyroid gland is divided into several lobules encapsulated in collagenous connective tissue. Each one of them contains approximately 20-40 follicles which measure about 30-500 µm in diameter [5]. Size of the follicles is specific to every individual and it has been

reported that it varies with age, gender, can be altered by different pathologies and also depends on the location in the gland [6].

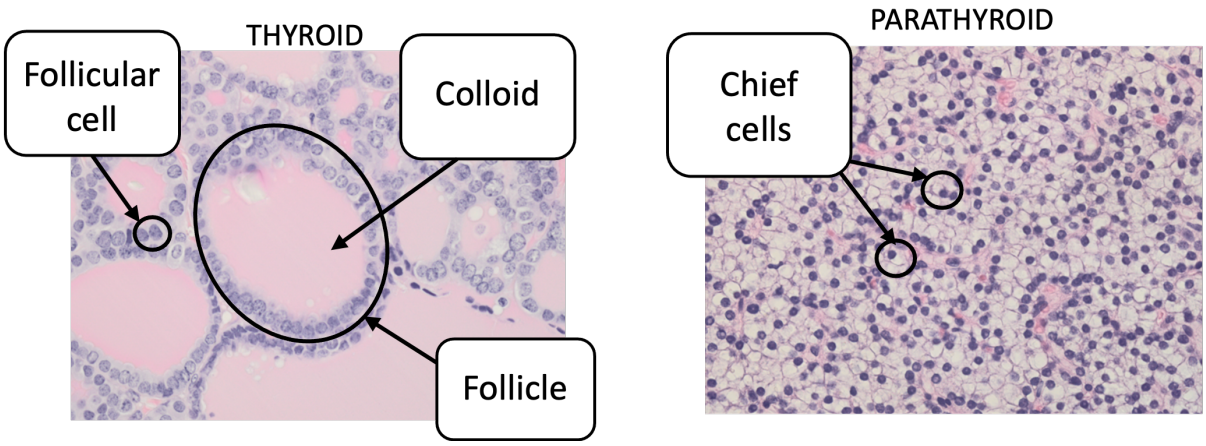

Figure 1.2: *Histology images of thyroid and parathyroid tissue with marked characteristic substructures highlighting differences in their morphology, stained with eosin and haematoxylin (K. Hunter – personal communication)*

1.2.2 Parathyroid tissue

The parathyroid glands are spherical structures of 3-7 mm in diameter [7] which are located on the posterior surface of the thyroid gland (Fig. 1.1). The typical number of the parathyroid glands is four, however, their number can vary. The main function of these glands is to maintain physiological calcium levels in the organism. In contrast to thyroid tissue, parathyroid glands have much denser structure consisting of closely packed groups of cells (Fig. 1.2). The main cell types that make up the tissue volume are chief, oxyphil and adipose cells.

Chief cells are the most abundant cells in parathyroid tissue with the main function of secreting parathormone (PTH), they are usually of spherical shape and 8-10 µm in size [8]. The second type of cells – oxyphil cells – are characterised with slightly bigger size and larger intracellular space content, however, their role in the parathyroid gland is unclear. All types of cells are randomly distributed across the tissue and are typically scattered in clusters.

1.3 Thyroidectomy

1.3.1 Surgery and complications

The term thyroidectomy refers to various surgical procedures comprising partial and total removal of the thyroid gland. Indications for the surgery can arise from both benign and malignant pathologies, and the type and severity of the disease determine to what extent the

gland has to be resected. The surgery carries the risks of unintentional damage or excision of one or more of the parathyroid glands, which are directly located on the posterior surface of thyroid. Such a situation might lead to adverse short- or long-term complications such as post-surgical hypoparathyroidism (PoSH) and hypocalcaemia [9].

Hypoparathyroidism is a state of lowered level of PTH that is followed by hypocalcaemia, a subsequent state of lower levels of calcium in the blood. The connection between different types of thyroid surgeries and aforementioned complications has been studied since the 1920s as documented in the review by Walter [10] and have continued also in more recent decades. Despite the modernisation in technology and treatment approach, PoSH and hypocalcaemia continue to be the most frequent thyroidectomy-related complications.

The incidence rates of both conditions vary wildly in the literature, making it difficult to estimate their significance. The discrepancy between the documented incidence rates arises mainly due to insufficient unification of the definitions used to describe PoSH and hypocalcaemia alongside with their determinants, such as severity and duration [9]. Moreover, both terms are often used interchangeably and there are non-uniform treatment approaches that have an impact on resultant PTH and calcium levels that might misrepresent the severity of the post-surgical conditions. The UK Registry of Endocrine and Thyroid Surgeons governed and collected data from about 90,000 endocrine procedures since 2004 and, to date, this is the most unified document concerning the outcomes of thyroid surgery and following the procedure complications [9]. According to that registry, 23.6% and 6.5% of the first-time thyroidectomy patients develop short- and long-term hypocalcaemia after the procedure respectively. Furthermore, the prevalence of PoSH can be estimated to be around 23 per 100,000 [11] .

Parathyroid glands can be impaired accidentally during thyroidectomy or, due to their small size and location on the posterior wall of the thyroid (Fig. 1.1), could be mistaken for other biological structures, such as benign thyroid nodules, clumps of adipose tissue or lymph nodes [12]. In order to reduce the risks of PoSH and hypocalcaemia among thyroidectomy patients, it is recommended that several improvements should be incorporated to the surgical procedure, such as the requirement to develop a surgical technique with a focus on the neck dissection region. To date, the ability to locate parathyroid glands has mostly depended on the surgeon's experience. To highlight the importance of the surgeon's skills in parathyroid detection, the quote by Doppman [13] is often cited as an example that '[. . .] the only localizing study (indicated in a patient with untreated hyperparathyroidism) is to localize an experienced parathyroid surgeon'. However, exploring additional methods of parathyroid identification has the potential to guide the surgeon to further decrease the risks of PoSH and hypocalcaemia.

1.3.2 Parathyroid detection methods

Currently, there are a few methods of differentiating the healthy or diseased parathyroid glands from the adjacent tissues. It is a common practice to perform ultrasonography imaging prior to the surgery, which is an accessible and non-invasive method to locate the patient's parathyroid glands. However, as reported in the literature, whilst ultrasonography is a good tool to detect abnormal and enlarged glands, it is, however, usually insufficient to help in locating healthy parathyroid glands [14]. Ultrasonography often accompanies other methods such as fine needle aspiration (FNA) which is a biopsy technique to detect pathologic changes in thyroid and parathyroid, and is substantially less invasive in comparison to conventional surgical biopsy techniques [15]. Nonetheless, carrying out a biopsy is time consuming as its results do not appear right away after the sample is acquired. Moreover, FNA seems to be a more suitable method for pathology diagnostics rather than for healthy parathyroid detection.

A promising technique to enhance the differentiation of parathyroids from adjacent tissues that emerged recently exploits the natural autofluorescence of these glands [16; 17]. This method utilises the parathyroid tissue's intrinsic fluorescent properties which exhibits in a natural tissue illumination after the exposition to radiation of a near-infrared wavelength without the need of additional agent injection. Parathyroid glands hold such properties possibly due to the substantial concentration of calcium-sensing receptors [18]. The advantage of this method is low cost and safety (no toxicity which is often associated with radioactive contrast injection), along with a reported satisfactory high rate of parathyroid glands identification. However, the accidental false positive illuminations from adjacent tissues (such as clumps of brown fat, thyroid nodules or metastatic lymph nodes [19]) might decrease the effectiveness of successful preservation of parathyroid glands.

In contrast to autofluorescence, there are a few methods of parathyroid identification benefiting from the injection of the exogenous fluorescent agent, such as indocyanine green (ICG) angiography. ICG binds to the plasma protein and illuminates when exposed to near-infrared radiation. This method is advantageous in detecting parathyroid glands, which have increased blood intake in comparison to the surrounding tissues, and therefore the elevated concentration of ICG. Using a radioactive agent, such as Tc-99m sestamibi, administered orally or through an injection before surgery is another way to detect parathyroid tissue. Similarly, through the rich blood uptake of the parathyroid glands, the reagent is delivered to parathyroids which makes them visible in the images taken with a scintigraphy machine. This method is usually introduced to detect abnormal parathyroid glands, e.g., in hyperparathyroidism. In a study with a substantial number of cases (290), the abnormal parathyroid glands detection with a sestamibi scintigraphy was documented with 74% sensitivity [20].

1.4 Electrical Impedance Spectroscopy

Electrical impedance spectroscopy (EIS) is another technique that could potentially enhance parathyroid tissue discrimination from the surrounding tissue in the surgery setting. EIS is based upon the biological tissues properties attributed to conducting and retaining the electrical current due to the presence of free and bound charges. This allows the measurement of these properties in a form of electrical impedance, where complex impedance can be defined as the frequency-dependent opposition expressed by the tissues to the flow of alternating current. During the measurement, the substantial fall in the real part of impedance resulting from the cell membrane polarisation (known as β dispersion) is measured by the EIS device after applying an alternating current. The measurement is repeated at various frequency points from the range of 100Hz-10MHz where the absorption of the electromagnetic radiation is mostly determined by the cellular structure [21]. There are many forms of the measured complex impedance data presentation, however, for biological tissues applications, the results are often plotted in a form of a real impedance spectrum (Fig. 1.3). The shape of the dispersion and the magnitude of impedance is characteristic for each tissue type based on the structure and composition, which makes it a potentially suitable method for tissue differentiation.

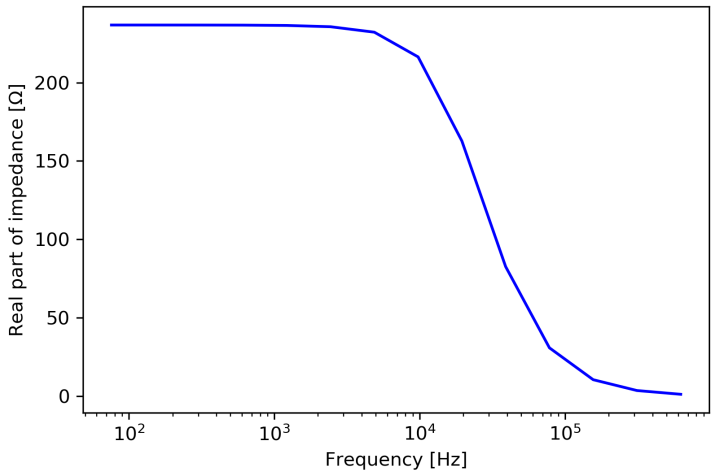

Figure 1.3: *An example of electrical impedance spectrum showing β dispersion, significant fall in real part of the impedance around the kHz region*

The EIS instrumentation developed and documented in the literature come in many different configurations of number and arrangement of electrodes, usually encompassing two to eight electrodes (bipolar: [22], tetrapolar: [23], six: [24] and eight: [25]). A tetrapolar tip is the most widely used configuration which benefits from lower electrode surface impedance compared to bipolar probes. The electrode polarisation occurs due to the molecular charge

organisation on the tissue-electrode contact surface caused by the presence of water molecules and hydrated ions [26]. This phenomenon dominates in the lower frequencies and depends highly on the electrode material and the measured tissue (the more conductive the tissue, the more prominent the electrode polarisation). It is a common practice to use gold or other noble metals for the electrodes of the device in order to mitigate the polarisation effects and to avoid measurements at frequencies lower than 100 Hz.

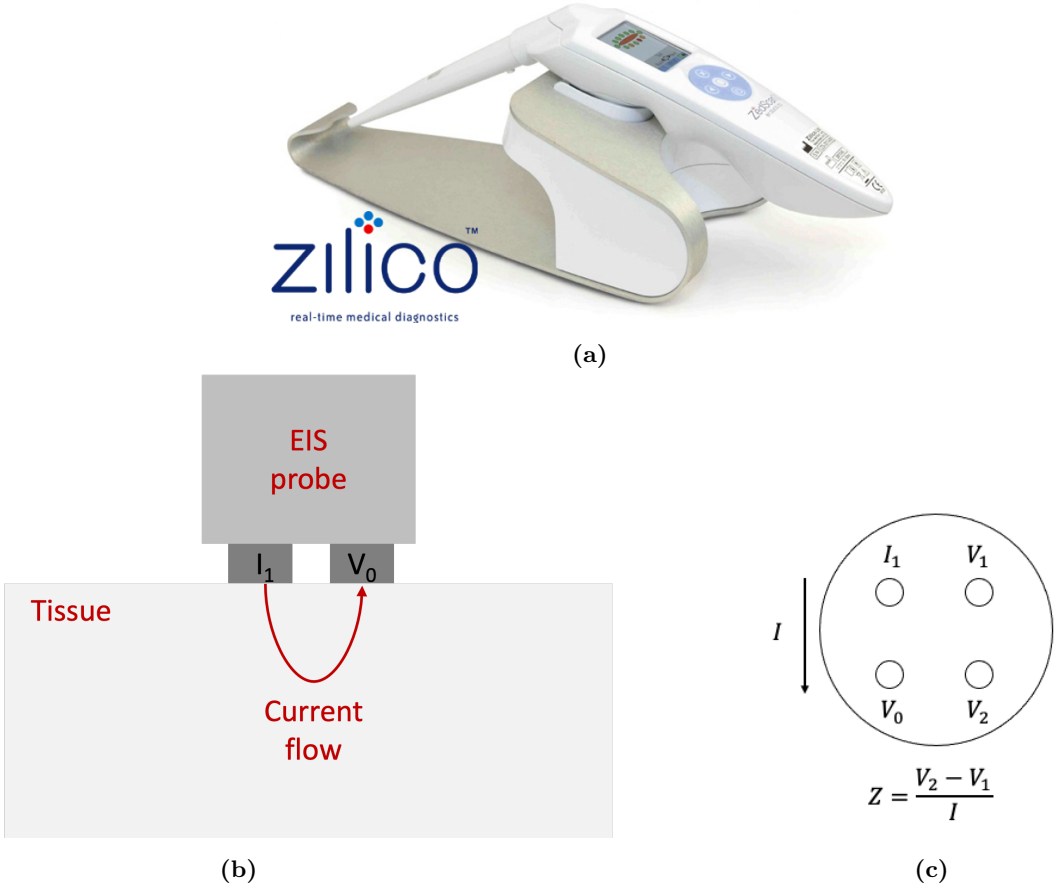

Figure 1.4: *Electrical Impedance Spectroscopy device: (a) ZedScan™ [23], (b) the schematic showing the current injected from EIS probe and flowing through the tissue, (c) tip of the tetrapolar probe showing the principle of the impedance Z measurement, a known current I flows between the active electrodes (I_1 and V_0) while the passive electrodes (V_1 and V_2) capture the potential difference at each frequency*

Fig. 1.4a shows one of the commercial tetrapolar EIS probes, ZedScan™, produced by Zilico Limited, originally developed and applied for the use in Cervical Intraepithelial Neoplasia (CIN) diagnosis. Fig. 1.4b visualises the current path induced by the EIS probe, and

Fig. 1.4c shows a diagram with a tip of a ZedScan™ tetrapolar measuring probe configuration highlighting the principle of its measurement. Impedance at each frequency is calculated according to the Ohm's law, as a ratio of the potential difference captured by a pair of passive electrodes V_1 and V_2, and the small current applied to a driving electrode I_1, penetrating the underlying structures, and flowing to the ground electrode V_0.

1.5 Electrical properties of tissues

1.5.1 Historical context

The utility of the EIS technology in the field of biological tissues is mainly attributed to the passive electrical properties of the tissue structures. These properties were the subject of researchers' interest for over a century and which were focused on understanding the interaction between electromagnetic fields and biological structures. Historically, the first studies were initiated in the early XXth century with the work of Höber [27] who was the first to observe the decreased impedance with increasing frequency in a suspension of erythrocytes. This led to the conclusion, that cells most likely consist of cytoplasm of low resistivity encapsulated in poorly conductive membrane. Those outcomes were further verified by Fricke and Morse [28], who obtained the capacitance of cell membrane from the suspension of erythrocytes through theoretical and experimental analysis and proposed a simple equivalent circuit demonstrating the behaviour of a singular cell consisting of conducting interior and exterior separated by capacitive cell membrane. Cole and Cole presented an empirical model to represent the dispersion and absorption properties of dielectrics [29] while Schwan continued the work in the frequency-dependent electrical properties of tissues and cell suspensions [30].

Typically, with increasing frequency of the external field applied to the tissues, there are three main regions of decreasing real part of measured impedance that are known as α, β and γ dispersions [31]. α dispersion occurs in the low frequencies (below 10kHz) and is a result of the counterion polarisation along the cell membrane. That type of relaxation is characteristic for muscle tissue and does not occur for some of the cell types, such as erythrocytes. γ dispersion (above 1GHz) is associated with the polarisation of water molecules. Around the kHz-MHz region, β dispersion occurs, which is related to the polarisation of cell membranes and big polar molecules, such as proteins (first observed in the work of Höber [27] and formulated by Schwan [30]).

1.5.2 Electrical properties of tissue structures

In basic terms, after being exposed to an external electrical field, the charge conduction by the biological structures is possible due to the ions concentrated in different structures. Moreover, tissues can conduct and retain electrical charge, the latter being attributed mainly to the properties of biolipid membranes, such as the cell membranes, or polar molecules. The

dielectric properties of tissues are often expressed in a form of electrical conductivity σ and dielectric permittivity ε. Electrical conductivity can be defined as the ease of the movement of the free charge within the material under the influence of an external electric field. There are two types of conductivity that can be distinguished, the steady state conductivity which occurs mainly due to the presence of hydrated ions in the biological tissues, and the frequency-dependent conductivity which is associated with the dielectric polarisation and the bound charges. Dielectric permittivity is often expressed as relative permittivity (also known as dielectric constant) ε_r (Eq. 1.1):

$$\varepsilon_r = \frac{\varepsilon}{\varepsilon_0}, \tag{1.1}$$

which relates a specific material permittivity ε with the permittivity of free space ε_0= 8.854 x 10^{-12} Fm^{-1}. Permittivity can be described as the ability of the bound charges to be disturbed or polarised under the influence of the external electric field. Such bound charges are often associated with the electrical bilayers, e.g. occurring at cell membranes or polar molecules with a permanent dipole moment. Dipole moment m (Eq. 1.2) can be given by a relationship of the distance s between the permanent unit charges q of the opposite sign:

$$m = qs, \tag{1.2}$$

The permanent charges in complex molecules are associated with the presence of ionisable acidic and basic amino acid sidechains in the protein structure [32]. Examples of structures with permanent electric dipole moment are water molecules, amino acids, polypeptides, proteins, DNA. Permittivity is a complex value, where the real part is responsible for the capacitive properties of tissues and the imaginary part is the dielectric loss and is an effect of the dissipative loss associated with the friction opposing the movement of polarisable molecules in the external medium.

Cell membranes are double layers of long-chain lipid molecules with a thickness of a few nanometres. The effective capacitance per unit area C_m [Fm^{-2}] of cell membrane is given by Eq. 1.3:

$$C_m = \frac{\varepsilon_0 \varepsilon_m}{d} \tag{1.3}$$

where ε_m is the permittivity of cell membrane and d – its thickness. The permittivity of cell membrane can be obtained directly through transmembrane measurements or derived from the model fitting methods from measurements on cell suspensions, which will be explained in more detail in the following Chapter. Cell membrane properties have a dominating role in the β dispersion, in the low frequencies the cell interior is insulated and the current flows through the extracellular space (ECS). However, with the increasing frequency, the membrane resistance is progressively short-circuiting by the reactance, the current starts

penetrating the cytoplasm, and the cell membrane capacitive reactance falls with increasing frequency. This results in an increasing conductivity and decreasing permittivity and impedance throughout the β dispersion.

Biological tissues have the ability to also interact with the magnetic fields, however, this kind of interaction is highly specific to nuclear magnetic moments or the unpaired electrons associated with paramagnetic ions or free radicals [32]. These, however, have a small impact on the bulk electrical properties compared to the impedance associated with the resistive and capacitive nature of the tissues. Moreover, the majority of EIS devices are insusceptible to the tissues magnetic properties, hence, the tissue-magnetic field interactions are not of a further interest of this thesis.

1.5.3 Impedance calculation for simple geometries

With the simplest example of electrical properties of a homogeneous, isotropic material of cuboid shape (Fig. 1.5), it is possible to derive the effective impedance of such material by calculating in the first instance its resistance (R) and capacitance (C) (Eq. 1.4 and 1.5):

$$R = \frac{d}{\sigma A} \tag{1.4}$$

$$C = \frac{\varepsilon_0 \varepsilon_r A}{d} \tag{1.5}$$

where d – material thickness, and A – cross-sectional area that define the dimensions of the model, ε_0 permittivity of free space, while σ and ε_r are the conductivity and permittivity that describe the electric behaviour of a specific material.

Subsequently, given R and C, the resultant complex impedance (Z^*) for a dielectric material representing behaviour of a simple circuit comprising a resistor and capacitor in series can be calculated from the relationship (Eq. 1.6):

$$Z^* = R + X_c \tag{1.6}$$

where R is the resistance resulting from the resistive nature of material and X_c – reactance related to the capacitive nature of dielectric and is represented by (Eq. 1.7):

$$X_c = \frac{1}{i\omega C} \tag{1.7}$$

Moreover, it is possible to calculate impedance of simple models consisting of a few layers of different materials connected in series or in parallel (Z_s and Z_p), it can be derived from Eq. 1.8 and Eq. 1.9:

$$Z_s = Z_1 + Z_2 + ... + Z_n \tag{1.8}$$

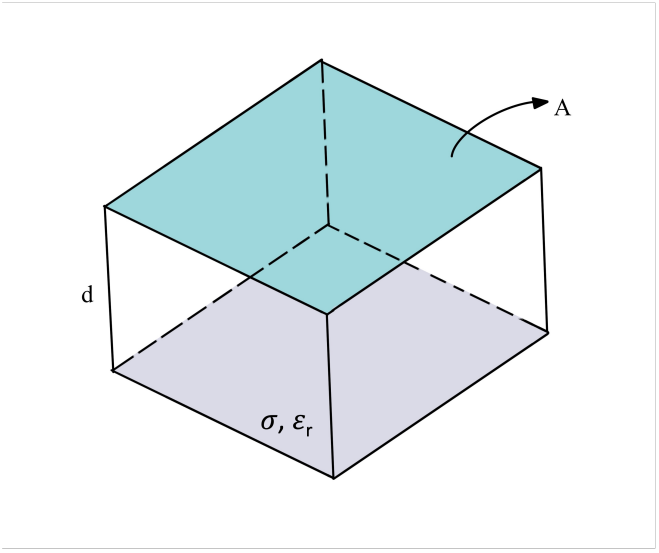

Figure 1.5: *Homogeneous, isotropic material of cuboid shape, with conductivity σ and relative permittivity ε_r, cross-sectional area A and thickness d*

$$Z_p = \frac{1}{\frac{1}{Z_1} + \frac{1}{Z_2} + ... + \frac{1}{Z_n}} \tag{1.9}$$

where Z_i defines the impedance of a single component or layer of the circuit. Nonetheless, most biological tissues are characterised with behaviours represented by more complex electrical circuits than a simple resistor-capacitor in series presented above. The alternative defining models describing the impedance tissue and biological structures are summarised in Chapter 2.

1.6 Computational modelling

The fundamental idea behind computational modelling is to use the available tools of mathematics, physics, and computer science in order to describe and predict the theoretical behaviour of complex systems and is a widely used tool in engineering and science. Even in the field of the frequency-dependent electrical properties of the biological tissues, there are well documented and developed approaches using fundamental physical principles, starting from simple analytical calculations and moving to more sophisticated numerical methods.

The principle of analytical modelling is deriving a direct and exact solution from a single or a system of mathematical equations describing the underlying physical phenomena of the investigated environment. Nonetheless, the accuracy of the solution is determined by the level of complexity considered in the model and the extent of assumptions that simplify the calculation. The analytical modelling methods can be used to predict the electrical prop-

erties of simplified tissue geometries (e.g. to investigate the layered skin structure [33]) or can be implemented for the analysis and interpretation of complex experimentally acquired impedance data (e.g. equivalent circuit model fitting methods used to parameterise the measured data [34]).

For systems representing more complex morphologies which cannot be easily investigated with the analytical methods, numerical modelling methods are implemented, where instead of a direct solution, an approximation of the real result is obtained. The main concept behind numerical modelling is the discretisation process, which reduces continuous partial differential equations that describe a given behaviour or phenomenon to their discrete alternatives which are easier to solve. The finite difference and finite volume methods are the simpler numerical methods in comparison with the finite element approach, which will be described in more detail in section 2.3 Chapter 2. The finite difference method is the most straightforward approach where the numerical solution is only computed at the discrete and regularly spaced grid points and the continuous differential equations are approximated with finite differences which are typically derived using Taylor series expansion [35]. However, in the finite volume method, often used in computational fluid dynamics problems, the differential equations solutions are approximated over finite-size volumes, known as 'cells', instead of just points as in the finite difference approach [35]. In this method the governing equations are integrated across the model cells in order to generate the finite volume equations.

The finite element (FE) method is a well-established numerical modelling tool which has been utilised in numerous fields, comprising engineering, mathematics, and physics. The main idea behind the FE method is dividing the domain, which is often a simplified geometrical representation of the object or system of interest, into smaller elements of defined shape and size to create a finite element mesh, upon which the governing equations are solved during a simulation under previously defined and known initial or boundary conditions [36]. In this method, the results are calculated at specific points, known as nodes, and are subsequently interpolated into the spaces between them using the initially chosen shape or interpolation functions. The more nodes and elements generated for an FE mesh, the higher order of shape functions and the more realistic initial conditions for the simulation, the more reliable the obtained results for the defined problem. However, with higher complexity comes increased computational expenses, hence, finding a compromise between accuracy, computational time and required resources is crucial for many applications. This is of great importance, e.g. in bioengineering, where the time aspect is critical in cases where FE aims to improve the decision-making process during medical procedures. Nonetheless, FE is a convenient tool for predictive and diagnostic tasks which allow to assess the current state of the studied biological system and to test the possible outcomes of treatment to support the clinicians. The FE modelling approach was successfully implemented to investigate the electrical properties of biological tissues such as skin [37], cervical epithelium [38], urinary bladder [39; 40] or

oesophagus [24].

In the following Chapter 2, various analytical and numerical modelling methods with examples of research aimed to investigate the electrical properties of tissues will be introduced and discussed.

1.7 Aims of the project and research objectives

The differences in the thyroid and parathyroid electrical properties acquired for healthy and pathological tissues with EIS devices have already been investigated empirically and documented in the literature [3; 34]. In particular, the commercial ZedScan™ device has been utilised for tissue differentiation during thyroid and parathyroid surgery [3] investigating the distinguishing features between healthy and pathological parathyroid glands impedance spectra from those obtained from the surrounding tissue. As reported by Hillary et al. [3], there are similarities in the *in vivo* median impedance spectra measured for healthy thyroid and parathyroid tissues, which did not provide sufficient evidence on how to distinguish both tissues by solely comparing their impedance spectra. Moreover, EIS, despite its advantages, such as real time and non-invasive assessment of tissues, is a technique that can only provide information on the bulk electrical properties without the ability to reveal the connection between the measured spectra and specific tissue characteristics responsible for observed behaviour. However, this connection can be investigated by applying computational modelling to complement and accompany the EIS experimental data.

As previous research in cervical epithelium [38] or oral tissues [41] has shown, the geometrical features and organisation of the structures within the tissue, along with the tissues' material composition and electrical characteristics, all influence the impedance spectra and, consequently, the impedance magnitude and the shape of the dispersion. Therefore, it is possible to anticipate that impedance curves with different characteristics will result from structural and composition variations at the cellular or supracellular level between tissue types. As highlighted in Fig. 1.2, the differences between thyroid and parathyroid tissue are substantial. Thyroid structure consists of an arrangement of cell-lined spherical follicles filled with a protein rich colloid, structures that are entirely absent in parathyroid glands, which are composed of closely packed clusters of chief cells. Computational modelling can be of great benefit to aid the implementation of the mechanistic approach into predicting theoretical electrical tissues' behaviour. This can also assist us in comprehending how each tissue component, relating to tissue morphology or tissue composition, can influence the respective characteristic of a "measured" EIS spectrum. **It is therefore plausible to hypothesise that computational modelling can elucidate the differences between the measured thyroid and parathyroid spectra that are driven by differences in their structure and composition.**

The aim of this study is to develop and apply computational modelling methods to investigate the potential of Electrical Impedance Spectroscopy to differentiate thyroid and parathyroid tissues during surgery. The constructed modelling framework is intended to elucidate how the tissue specific features (such as the morphological, structural characteristics and material composition), the surgery related conditions (the accuracy of the measurement) or the instrumentation (the arrangement of the electrodes on the EIS probe) can impact the measured electrical impedance spectra of both tissues. Additionally, modelling will aid to quantify how the aforementioned factors could influence the thyroid and parathyroid separability based on EIS measurements. This further permits the formulation of the main **Research Objectives (RO)** that will be explored in this thesis:

- **RO1**: to recreate the thyroid and parathyroid tissues' characteristic structure and composition and to simulate their electrical impedance;
- **RO2**: to compare the obtained results against the *in vivo* measurements provided by Hillary et al. [3];
- **RO3**: to assess the separability between thyroid and parathyroid tissue computed and *in vivo* measured EIS spectra from Hillary et al. [3];
- **RO4**: to investigate the influence of morphological and electrical properties of thyroid and parathyroid tissue structure on different characteristics of the impedance spectra through two complementary and comprehensive sensitivity study approaches;
- **RO5**: to explore the heterogeneous tissue morphology and its impact on the theoretical impedance spectra on different scales;
- **RO6**: to investigate the importance of accuracy of the measurement with the ZedScan$^{\text{TM}}$ probe and to propose suggestions for EIS tetrapolar hardware improvements for parathyroid glands identification.

Chapter 2 will present the literature review comprising different computational modelling methods used to investigate the electrical properties of biological tissues. Additionally, different techniques of acquiring electrical material properties of cellular and supracellular structures will be introduced along with review of studies concerning EIS applications in the thyroid and parathyroid surgeries. In Chapter 3 the multiscale model development for thyroid and parathyroid will be discussed by highlighting the impact of their unique micro- and macroscale structure on the created computational models for both tissue types. Moreover, model sensitivity to the natural tissues' geometrical characteristics variability and the uncertainties in the material properties of thyroid and parathyroid structures across various levels of complexity will be investigated using local and global methods and presented alongside the reference simulated impedance spectra in Chapter 4. The computational model results

verification and comparison with *in vivo* measured data will be covered in Chapter 5. This would also include a concluding discussion on the feasibility of the EIS measurement to distinguish between thyroid and parathyroid tissue. Chapter 6 summarises the exploration of different approaches to model tissue heterogeneity and irregular structure at various levels of complexity. Chapter 7 comprises complementary studies examining the effects of the EIS measurement precision with the proposed changes to the EIS probe design to increase the parathyroid tissue measurement accuracy and tissues separability. The final discussion of the results will be addressed in Chapter 8, along with a discussion of the methodology's limitations and recommendations for further research on the electrical properties of thyroid and parathyroid tissue using computational methods.

Chapter 2

Literature review

The purpose of this literature review was to evaluate the current state of knowledge in the analytical and numerical modelling methods in the field of electrical properties of biological tissues. Furthermore, the techniques of electrical properties measurements for tissues and their substructures will be introduced along with the overview of the applications of electrical impedance spectroscopy with the emphasis on the thyroid and parathyroid tissue applications.

2.1 Electrical Impedance Spectroscopy and Electrical Impedance Tomography applications

2.1.1 Applications of Electrical Impedance Spectroscopy

Electrical impedance spectroscopy is a technique with many applications across different fields of science and engineering. It is predominantly and extensively used in material science, eg. to investigate electronic ceramics and composite materials [42; 43]. EIS methods are also implemented in food quality assessment [44] or in biology with the examples of tree condition analysis [45], plant roots [46] or leaves research [47].

Over the years EIS has also been introduced as a diagnostic technique to monitor, compare, and detect various types of tissues in their healthy or pathological states. The significance of EIS has been broadly studied and exploited in the analysis of impedance spectra between different organs in various species for cancer and other pathologies detection, also for tissue differentiation. EIS has been studied as a tool to distinguish between different animal tissue types [48] or to monitor the state of tissues, such as myocardium during the occlusion of left anterior descending artery [49] or lungs, during bronchoscopy as an alternative to histological biopsy [50]. Nonetheless, the broadest application of EIS in medicine is for cancer diagnosis, where we can highlight works relating to benign and malignant skin pathologies [51], cervical [52], oral tissues [53], breast tissue [54] and prostate [55] cancers. Thyroid and parathyroid tissues have been a subject of several EIS studies in cancerous or benign pathologies diagnosis

[22; 34; 56; 57]. In particular, the identification of thyroid and parathyroid tissues in both their healthy and diseased states has also been the interest of a study in rabbit [2] and two studies on human [3; 34] neck tissues which will be evaluated in more detail later in this chapter along with other selected thyroid and parathyroid clinical studies.

2.1.2 Electrical Impedance Tomography

In contrast to EIS, which acquires the impedance at a particular point of interest and due to the small size and low number of electrodes provides the assessment of tissues' electrical properties from a relatively small region, Electrical Impedance Tomography (EIT) instrumentation is characterised by multiple electrodes. In EIT measurement, comparable to EIS, small electric current is applied to the tissue across the chosen frequency range and the resulting voltage is measured by an array of electrodes which is then converted into a visual impedance map. One of the first EIT systems was developed for pulmonary function monitoring applications [58], in particular for ventilation imaging and blood clot detection. Other common applications are breast tissue imaging for tumour detection [59] or brain tissue imaging to localise lesions in focal epilepsy [60].

Despite the feasibility of EIT for non-invasive tissue imaging in many applications providing more insight into the electrical assessment of the tissues compared to EIS devices, the impedance map (2D or 3D) is obtained using image reconstruction methods which can be time-consuming and are prone to reconstruction errors. Other drawbacks of this approach are the poor spatial resolution, the sensitivity to the ribcage movements in the lungs measurements, as much as the high impedance of the skull in the brain tissue assessment. Moreover, the high skin-probe contact impedance is a significant source of the measurement error since most of the measurements are performed superficially and are not applied to the tissues directly as in many measurements with EIS devices.

2.1.3 EIS and EIT studies relating to thyroid and parathyroid tissues

Out of the studies of the EIS applications for tissue differentiation during thyroidectomy, there are two studies, in particular, that explored the applicability of the commercial ZedScan™ EIS device with the emphasis on the parathyroid glands' discrimination from the adjacent tissues [3; 2]. Antakia et al. [2] performed impedance measurements on 9 rabbit specimens where thyroid, parathyroid, adipose and muscle tissues were examined at 14 frequencies from the range of 76-625,000 Hz. The median impedance spectra for thyroid, parathyroid and muscle tissue showed substantial differences across all frequencies. The results show that the thyroid tissue exhibits higher impedance below the 80 kHz relative to the parathyroid tissue. At higher frequencies the situation is reversed, and the parathyroid tissue showed greater impedance. This was explained by the assumption that thyroid cell-lined follicles are more resistive in the low-frequency range compared to parathyroid tissue with a compact cellular

structure. Furthermore, the *in situ* and *ex vivo* measurement conditions were compared, which exhibited clear variability in the obtained results, occurring due to differences in temperature and time between the *in situ* and *ex vivo* measurements. Additionally, the *ex vivo* results exhibited higher impedance for both tissue types across the whole frequency range compared to the *in situ* measurements.

Subsequently, Hillary et al. [3] performed a follow-up study where the electrical impedance measurements were performed on human neck tissues in fifty-six patients undergoing neck surgeries due to thyroid and parathyroid pathologies. In this case, the scope of the study was to use EIS to discriminate not only different tissue types, but also to detect parathyroid pathologies. Similarly to the previous study, there are differences in median impedance spectra between thyroid and parathyroid tissue especially in the shape and the dispersion region, however, the differences were more subtle compared to the study outcomes from rabbit tissues' measurement. Nonetheless, the results showed a similar trend in higher impedance values for thyroid compared to parathyroid. It is also worth noting that higher dispersion frequency and impedance after the dispersion was recorded for the parathyroid tissue, which is another characteristic that distinguishes the tissue types. Finally, similar differences between the *in vivo* and *ex vivo* measurements was documented in the preceding study [2], explaining the impedance results vary with the changes in the temperature during both sets of measurements. A concluding remark of this study was that, while there are EIS spectra characteristics that have potential to improve the separation between parathyroid from thyroid, the differences in those parameters, however, are too subtle to clearly distinguish between both glands and between healthy and diseased parathyroid tissue.

In addition, both studies acknowledged several limitations of the commercial ZedScan$^{\text{TM}}$ EIS device during thyroidectomy procedures, which was initially designed and manufactured for the cervical epithelium measurements accompanying colposcopy. One major restriction is the size and shape of the measuring probe. In comparison to the tissue specimen such as parathyroid glands (3-7 mm), the tip of the probe (5.5 mm in diameter) is often too large for precise coverage of the whole gland which can have direct impact on obtained results and the tissues adjacent to parathyroid can 'contaminate' the results. Moreover, the Cervical Intraepithelial Neoplasia being the primary application of the device, the device has a long-necked design which is ergonomically cumbersome and uncomfortable in the neck surgeries, where tissues are well exposed and located superficially after the neck incision.

More recently, a similar study by Wang et al. [34] has been performed on a larger group of patients (n=512) and focused on various neck tissues discrimination (thyroid, parathyroid, fat and lymph nodes) using a different tetrapolar EIS device. In addition, they performed a Cole-Cole model (which will be discussed in the following sections) fitting to the *in vivo* measured impedance curves and compared the obtained fitted Cole indices (Z_0, Z_∞, f_c and

a). As reported in the study, parathyroid tissue shows higher mean f_c values and lower mean Z_0/Z_∞ relative to thyroid. However, the ranges of Z_0/Z_∞ ratio shows a significant overlap between these tissue types.

EIS measurements have also been introduced to enhance detection of pathological tissues, as demonstrated in another study by Yun et al. [22], a bipolar EIS probe was utilised for *ex vivo* measurements to compare and differentiate cancerous and noncancerous thyroid tissues. The reported results showed similarities for lower frequencies with the largest difference of real part of impedance around the 250 kHz, where, for all the specimen, the cancerous tissue was characterised with higher impedance compared to healthy tissue. This observation was explained that the differences in results could be attributed to the conductive properties of the colloid material filling each follicle. In the cancerous tissue, there is a significant level of degradation of follicle structures being replaced by higher density of follicular cells, which can be contributing to the increase in impedance in the frequency range around 100 kHz.

Moreover, Cheng and Fu [61] used a coaxial probe to distinguish between normal and cancerous thyroid tissue in 48 patients in the gigahertz frequency range (between 0.5-8 GHz), frequencies considerably higher than the range explored in the previous studies. The study reported higher effective relative permittivity and higher effective conductivity for the cancerous tissue compared to healthy thyroid across the investigated frequency range.

EIS has also been used by Stojadinovic et al. [56] with an EIS probe setup which is placed on the skin superficially to the thyroid gland to measure the conductivity and capacitance of the underlying thyroid tissue. The voltage was applied to the tissue and the behaviour was captured by a 8x8 matrix of sensors making it closer to the EIT device, however, without the following image reconstruction. The aim of the study was to differentiate health and cancerous thyroid tissue under the assumption that cancerous tissue has higher conductivity or capacitance compared to healthy tissue as implied by the outcomes of the breast tissue study [62]. However, this assumption might not be correct for the thyroid tissue, as previous studies mentioned in this section suggest the increased impedance/decreased conductivity for the cancerous lesions in comparison with the healthy tissue. Another similar EIT device with 64 electrodes has been used for the applications to detect the cancerous thyroid nodules [63] suggesting that the thyroid tumours exhibit higher impedivities in comparison to the healthy tissue. Another superficial EIS device has been introduced by Zheng et al. [57], where not only capacitive but also inductive properties of tissues and changes in the resonance frequency in the case of the healthy and cancerous thyroid tissue were investigated. According to the study, such a device could indicate if a patient shows evidence of cancerous tissue, however, one of its limitations is that it is unable to identify a malignant nodule. Moreover, both studies ([56] and [57]) developed EIS inspired devices that during the measurement are not in the direct contact with the tissues of which properties they attempt to capture, and are placed

superficially on the skin above the thyroid tissue. Stojadinovic et al. [56], however, explained the calibration process and how the recorded data is processed to reduce the contamination from the skin, muscle and other surrounding tissue, a similar explanation is not provided by Zheng et al. [57].

2.2 Analytical modelling

There are a number of directions of analytical modelling in the field of electrical properties of tissues. First are the prognostic models trying to predict the electrical impedance of biological structures if the properties of its substructures are known. The examples of predictive models could be impedance studies of simplified layered structure (such as homogenised layers in skin [33]), or the prediction of properties of cell suspensions based on Maxwell's homogenisation theory [64]. Another group comprises descriptive models that utilise the knowledge obtained through previous empirical studies in order to explain the behaviour of a given system. The equivalent circuits are an example of the descriptive models, which are often used in the model fitting techniques. These are performed for the purpose of parameterisation of the measured impedance spectra and to further understand each tissue features' contribution to the measured bulk electrical behaviour.

2.2.1 Maxwell's mixture theory

One of the relevant analytical modelling methods is based on the work of Maxwell Garnett that proposed a homogenisation theory in 1904 [64] that has been adapted to the field of electrical properties of tissues. In its principle, the Maxwell's mixture theory estimates the effective permittivity of a heterogeneous material ε^*_{mix} (usually particles suspended in a medium) based on the permittivities of specific compartments, and the volume ratio of particles and the external medium. The formula in its most basic form is represented by Eq. 2.1:

$$\varepsilon^*_{mix} = \varepsilon^*_m \frac{1 + 2\varphi f^*_{cm}}{1 - \varphi f^*_{cm}} \tag{2.1}$$

where: $f^*_{cm} = (\varepsilon^*_p - \varepsilon^*_m)/(\varepsilon^*_p + 2\varepsilon^*_m)$ and the indexes mix, m, and p represent the complex permittivities ε^* of the mixture, medium and particle respectively, φ is the volumetric fraction of the particles in the suspension.

The Maxwell-Wagner equation (Eq. 2.2) is derived from the Eq. 2.1, which is adjusted to calculate the effective permittivity of the cell suspension ε^*_{eff}:

$$\varepsilon^*_{eff} = \varepsilon^*_m \left(1 + 3v_c \frac{\varepsilon^*_{cell} - \varepsilon^*_m}{\varepsilon^*_{cell} + 2\varepsilon^*_m}\right) \tag{2.2}$$

where ε^*_{cell} and ε^*_m represent the complex permittivity of cell and medium, v_c is the volumetric fraction calculated from Eq. 2.3:

$$v_c = \frac{nR^3_{cell}}{R^3_m} \tag{2.3}$$

under the assumption of n number of spherical cells of radius R_{cell} suspended in a spherical medium of radius R_m. The effective permittivity of a cell ε^*_{cell} can be obtained from the simplest single-shell model which assumes a single membrane is separating the cell interior (cytoplasm) from the medium. The compartments of a single-shell model are visualised in Fig. 2.1. In this example, however, the presence of a nucleus surrounded by a nuclear membrane is discarded. In the Eq. 2.4 the volumetric fraction v_c is replaced by $(R_1 - R_2)^3$ where the R_1 and R_2 are the radii of the whole cell and the cytoplasm respectively:

$$\varepsilon^*_{cell} = \varepsilon^*_{mem} \frac{(2\varepsilon^*_{me} + \varepsilon^*_{cyt})R^3_2 + 2(\varepsilon^*_{cyt} - \varepsilon^*_{mem})R^3_1}{(2\varepsilon^*_{me} + \varepsilon^*_{cyt})R^3_2 - (\varepsilon^*_{cyt} - \varepsilon^*_{mem})R^3_1} \tag{2.4}$$

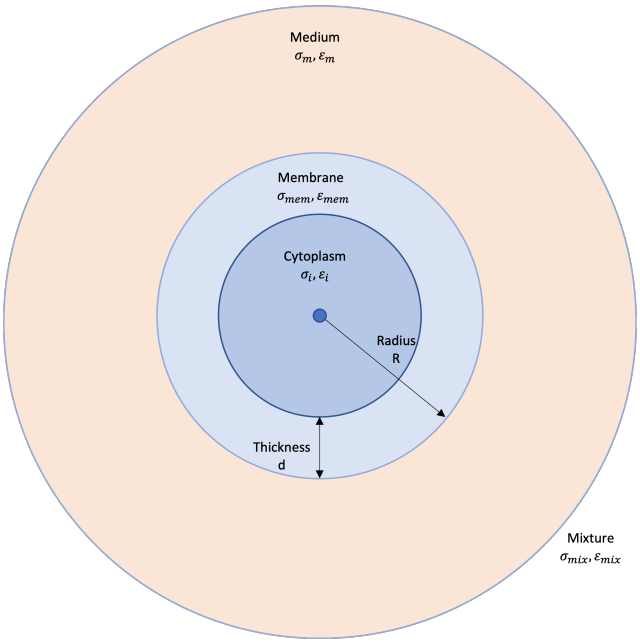

Figure 2.1: *Single shell cell model visualisation*

Despite the simplicity of deriving the dielectric permittivity of cells based on the properties of their components or assessing the properties of the cell substructures based on the bulk electrical properties obtained from the cell suspension measurements, this method has several limitations that arise from (i) the assumption of the particles being uniform, and spherical in shape, where cells often come in irregular shapes and sizes and (ii) is applicable mainly for a small volumetric fraction of cells, assuming there is abundant extracellular material in the tissue. Both of those assumptions are not suitable for many tissue structures, hence, over

time the equation was adapted depending on the application. A comprehensive summary of different variations of Maxwell's mixture theory and applications can be found in Markel [65] and Nasir and Ahmad [66]. Nonetheless, this approach would be of limited value for more complex tissue structures, in particular, it would not be feasible to use this analytical approach to account for the properties of the cell-lined follicular structure of the thyroid tissue.

2.2.2 Equivalent circuit models

Electrical equivalent circuit models are a method that can be used in conjunction with the EIS measurement to parameterise the impedance spectrum in terms of representing the electrical behaviour of different structures by combining its resistive and capacitive components in series or parallel in order to recreate the measured electrical spectrum of the whole tissue system [67]. There are a few examples of the electric equivalent circuits describing the electrical properties of cells and tissues which vary in complexity and the structures considered in the model.

For example, the electric behaviour of a single cell or cell suspension is often described by a simple resistor-capacitor (RC) electric circuit (Fig. 2.2) including components that define the resistances of ECS (resistor R) and intracellular content (resistor S), and capacitance of cell membrane (capacitor C). This equivalent electric circuit for cell has been first proposed by Fricke and Morse [28], and further summarised in a form of the Debye model (Eq. 2.5) initially concerning the impedance of suspension of dipoles:

$$Z(f) = Z_\infty + \frac{Z_0 - Z_\infty}{1 + \left(i\frac{f}{f_c}\right)} \tag{2.5}$$

In the case of simple cell and cell suspension models, Z^* is the complex impedance, f – frequency, Z_0 – low frequency impedance describing the properties of ECS (Eq. 2.6), Z_∞ – high frequency impedance describing the properties of intracellular space (cytoplasm) when the current flows throughout the whole structure past the β dispersion (Eq. 2.7), f_c – specific frequency defining the middle of the β dispersion (Eq. 2.8).

$$Z_0 = R \tag{2.6}$$

$$Z_\infty = \frac{RS}{(R+S)} \tag{2.7}$$

$$f_c = \frac{1}{2\pi C(R+S)} \tag{2.8}$$

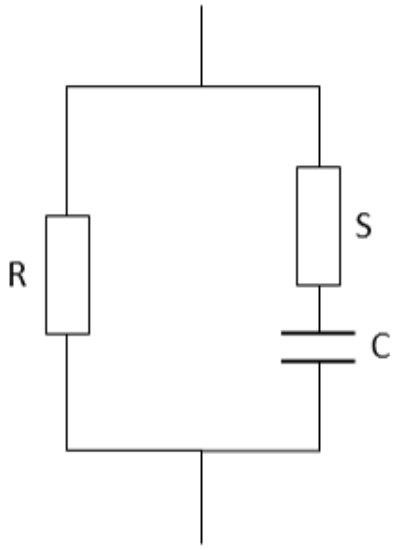

Figure 2.2: *Equivalent electric circuit of a single cell with resistive and capacitive elements: resistor R characterising extracellular space, resistor S – intracellular space and capacitor C – cell membrane*

An empirical Cole-Cole relaxation model [29] is an improved version of the Debye model which accounts more realistically for the width of the β dispersion in experimentally measured tissues, and is shown in Eq. 2.9:

$$Z(f) = Z_\infty + \frac{Z_0 - Z_\infty}{1 + \left(i\frac{f}{f_c}\right)^{1-\alpha}} \tag{2.9}$$

where α – is a parameter that characterises the width of the dispersion and takes the values from the range [0, 1]. The larger the parameter, the wider the dispersion, with the α values close to 0 indicating the behaviour represented by a Debye relaxation model.

The α parameter initially had no molecular and physical origin and was treated as an empirical parameter introduced to the model solely in order to better match with the impedance measurements of biological materials. However later it was hypothesised, that this parameter can indicate numerous Debye-type relaxations with a distribution of relaxation times. This could be further explained by the tissue's heterogeneity knowing the relationship between the relaxation time and sizes of cells or other tissue structures [32; 68]. Another justification points to the assumption that in biological tissues the charge conduction and dipole orientation processes are interdependent [68]. The first one is the most widespread and widely acceptable hypothesis, nonetheless, as the experimental work by Markx et al. [69] and Zhang et al. [47] suggest, there are most likely multiple factors influencing the α parameter and it is

not sufficient to attribute the cells sizes and time constant distribution in the tissues as the only influential factors.

2.2.3 Analytical modelling studies relating to EIS applications

An example of analytical modelling in EIS relating to skin tissues is the work presented by Birgersson et al. [33]. The proposed analytical model permits the investigation of stratum corneum properties from the EIS skin measurements with a circular tetrapolar probe. The simplified analytical calculations were verified against results obtained with a standard numerical analysis. This study determined the frequency range for which the analytical model is able to derive valid results to estimate the thickness and electrical properties of stratum corneum without the need of computationally expensive numerical solution for differential and constitutive equations. One important simplification introduced in this study was the fact that the cellular structure of tissues was not recreated and each of the skin layers were treated as homogenised compartments.

The Cole-Cole model and other equivalent circuit models are of often used for the parameterisation of the complex experimental or computed data for the comparison purposes with uniform fitted parameters. For example, the combined Cole-Cole and Maxwell mixture model fitting was implemented to derive the parameters characterising the liver and lungs of different levels of water content and presented by Etoz and Brace [70]. In study by Bora and Dasgupta [71], various alternative circuit models were fitted to the *in vivo* experimental skin impedance to propose the model that provides the best fit for the skin properties from ten different sides on human body. The Cole-Cole model fitting technique can also be implemented to compare the Cole parameters in order to quantitatively differentiate various tissues which electrical properties are acquired *in vivo* during thyroid surgery [34] or complementing colposcopy [72].

2.3 Numerical modelling: Finite Element Method

2.3.1 The principle of Finite Element Method

A detailed description of an FE pipeline for geometries of different levels of complexities and the applications in electromagnetism are described in the textbook by Polycarpou [36]. Following the textbook, a typical FE simulation methodology under the Galerkin scheme consists of following steps: domain discretisation, shape functions selection, deriving linear equations for each element, global matrix system formulation, boundary conditions imposition, solving the linear system of equations, and postprocessing.

Domain discretisation is the process of dividing the domain into a substantial number of small and finite elements. The visualisation of the model discretisation is presented in Fig. 2.3. Subsequently, the selection of suitable shape functions, also known as interpolation

functions, follows. These functions specify how the results calculated at the nodes can be interpolated to the rest of the element. The requirement for the shape function is to be continuous within an element and at least once differentiable. The number of shape functions relates to the number of nodes of the element or its degrees of freedom.

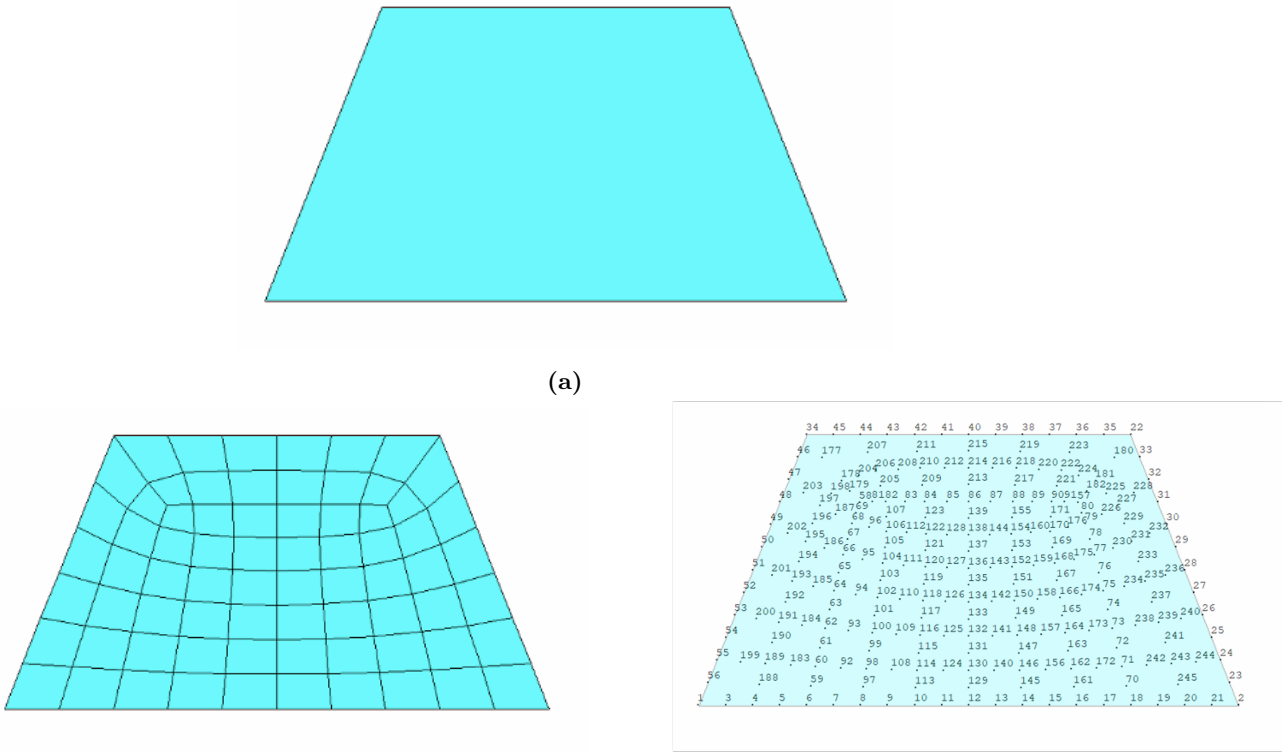

(a) **(b)** **(c)**

Figure 2.3: *Two-dimensional domain discretisation with a 2D 8-node element generated in Ansys Mechanical APDL, (a) the domain before discretisation, (b) discretised domain, (c) discretised domain with visualised nodes*

Subsequently, the finite element equations are derived by constructing the weighted residuals which are derived by moving all terms from governing differential equation on one side, multiplying by a weight function $w(x)$ and integrating over the element. By minimising the weighted residual and constraining it to equal zero, the approximate solution for the electric scalar potential V is calculated. For each choice of weighted function, an equation is formed to predict the electric scalar potential at given node, and the number of the weighted functions is required to be equal to the number of nodes.

Additionally, in the Galerkin FE method, for convenience, it is suggested that the weighted functions should be identical to the previously selected shape functions. The finite element equation for a single finite element can be obtained by substituting the approximate solution

in the weak form of the differential equation and taking identical weighted functions as the shape functions. The system of equations with unknown scalar potential values can be written in a matrix form where a matrix system corresponds to only one element. Subsequently from the element matrices, the global matrix system is constructed knowing how the elements are assembled with their connecting nodes.

Elements assembly is performed to generate the global matrix system and then the Dirichlet (Eq. 2.10) and Neumann (Eq. 2.11) boundary conditions are imposed to solve the electric scalar potential distribution:

$$V = V_0 \tag{2.10}$$

$$\sigma \nabla V \cdot n = 0 \tag{2.11}$$

The Dirichlet boundary condition restricts the electric scalar potential V known values of V_0, and the Neumann boundary condition confines the current flow within the model by stating that the normal component of the electric field is zero.

Constructing the global system matrix is performed in a way that the equations regarding the same node are added together and the matrix size reduces from *2Ne* to *Ne+1*, where *Ne* is the number of nodes. The boundary conditions application further eliminates the number of the equations to solve by constraining the value of electric scalar potential at certain nodes. Subsequently the global system matrix is solved and the electric scalar potential is derived at each node of the FE mesh, and the in-between values are obtained through the shape functions initially constructed for each element.

2.3.2 FE modelling studies relating to EIS applications

There have been several documented studies developing computational numerical models to investigate the electrical behaviour of the biological structures – starting from single cell studies and moving on to more complex tissue or organ models. Miller et. al [73] in the late 1980s were the first to implement the FE approach to investigate the bioimpedance of a single erythrocyte suspended in the medium to predict the transmembrane potential in comparison the results from spherical cell geometry which was verified against the analytical calculation. More recently, a novel parameterisation method to investigate the impact of the cell shapes on their electrical properties was proposed by Huclova et al. [74]. This study provided evidence that the cell shape is an influential factor in predicting the electrical properties in the frequencies below 1 MHz showing up to 35% and 15% deviations in effective conductivity and permittivity respectively from a reference spherical geometry.

Multiscale FE models relating to the measurements with the commercial tetrapolar ZedScan™ probe have been developed for several tissues to investigate the differences in the impedance of healthy and pathological tissues [38; 39; 41]. In the multiscale modelling method implemented in these studies, the macroscopic model is assigned with properties obtained from lower level, cellular simulations in order to decrease the computational expense that would result from including cellular details directly in the macroscopic geometry. The first published study on cervical epithelium by Walker [38] focused on computing the electrical impedance of the healthy epithelium and the changes resulting from the development of Cervical Intraepithelial Neoplasia. Additionally, a sensitivity analysis looking into the epithelial cell's geometrical and electrical properties impact on the EIS theoretical spectra has been performed. Similar multiscale methodology was expanded to the bladder tissue applications presented by Walker et al. [39] to investigate the changes in this organ's impedance due to oedema and inflammation, and more recently to oral tissues by Heath et al. [41], to determine the changes in tissues electrical properties in the case of oral potential malignant disorder.

There are several studies focusing on skin impedance models, such as a 3D multiscale FE model simulating the electrical properties of skin pathologies and predicting the current flow depth in an impedance measurement by the Electrical Impedance Tomography system as presented by Hartinger et al. [37]. They present an interesting approach of reducing the computational expenses associated with meshing small cellular substructures. Instead of meshing these structures with 3D elements which requires high level of refinement, cellular and nuclear membranes, and extracellular space were treated as surfaces (structures of negligible thickness) separating other compartments and meshed with 2D elements. Subsequently, the approximated electrical properties have been obtained from a bricked configuration of cells for each layer of epithelium, and assigned to a microscale level, similarly to the approach presented in the aforementioned cervical epithelium study [38]. Another example is a study by Huclova et al. [75] which is the continuation of the previous work on dielectric properties of cells [74], here, focusing on investigating skin properties using multiscale modelling approach with combined analytical and numerical methods. The main objective was to determine the optimal complexity of the multiscale model which would permit simulation of properties of skin obtained through *in vivo* experimental measurements. The results suggest a detailed numerical method (that considers realistic shapes of the cells and the anisotropy of each skin layer) provided the best fit with the experimental data. Additionally, the results revealed the limitations of each chosen analytical method in assessing the dielectric properties of skin.

Nonetheless, it has been demonstrated that the FE methods are not only useful to predict the electrical properties of biological tissues but can also be used as a tool to support the EIS probe manufacturing to determine the type, size and number of electrodes most adequate for a given application as demonstrated for oesophagus in the study by Jones et al. [76] and cervical epithelium by Gandhi et al. [77]. Additionally, the benefits of numerical methods

in assessing the importance of measurement accuracy are also shown by Schooling et al. [78] in a study investigating the precision of the Electrical Impedance Myography eight-electrode device placement on the impedance measurement of the tongue in the amyotrophic lateral sclerosis diagnosis. In this study, the heterogeneous muscle fibrous structure was considered in the FE model by generating a simplified layered geometry with varied material properties assigned to the layers. The results presented in this study revealed the dependence of the measured impedance magnitude and phase on the eight-electrode probe contact and placement on the lateral tongue.

There is only one study presented by Lv et al. [79] that documents a Finite Element model development to investigate the electrical and heat transfer properties of the thyroid tissue, with the emphasis on the impact of colloid's conductivity by taking the follicular structure into account in their framework. However, in this study the cellular structures have not been included in the model, instead of that the spaces separating each follicle (which usually is occupied by layers of cell and connective tissue) were assigned with electrical properties found in the literature and obtained from the whole thyroid gland measurement. To date, there are no computational studies investigating the electrical properties of parathyroid glands published in the literature.

2.4 Measurements of properties of fundamental tissue structures

In order to obtain reliable results through computational modelling, it is crucial to provide adequate material properties from the experimental measurements. An experimental study comprising dielectric properties of various biological tissues that was published and performed in the 1990s by Gabriel [26] is to date the most comprehensive compilation of the electrical properties data used in various computational modelling studies. The data was collected with various electrical impedance spectroscopy instrumentation and covered a broad frequency range from 10 Hz to 3 GHz.

The EIS technique provides an insight into the electrical impedance of whole tissue structures at a given tissue-probe contact point, however, it is impossible to use the obtained measurements to deliver the electrical properties of smaller substructures building the tissue. An EIS based instrumentation utilised specifically to investigate the properties of membranes and epithelia is known as Ussing chamber with examples of application for ventral epithelium [80] or glandular mucosa [76]. Analytical methods such as the equivalent circuit and model fitting techniques can convert the bulk impedance or effective permittivity measurements into estimated electrical properties of the substructures building the tissues. Nonetheless, it is additionally crucial to consider single cell spectroscopy methods as measurement techniques

for obtaining the electrical characteristics of single cells or cell suspension and its substructures.

Dielectrophoresis (DEP) is a phenomenon of the relative movement of the particles by a trapping force being a result of differences in polarisability of particles (cells) and surrounding medium when exposed to a non-uniform electric field. DEP is mostly used for many applications in medicine to investigate the healthy and pathological state of various cells. The induced translation force $\vec{F}$ by the non-uniform field $\vec{E}$ can be derived from the field gradient and the real part of the polarisation vector $\vec{P}$ (Eq. 2.12):

$$\vec{F} = (\vec{P}\nabla)\vec{E} \tag{2.12}$$

DEP can also be utilised to derive the electrical properties of cell compartments, such as cell membrane of murine myeloma cell line as documented in [81] or measurements of the dielectric properties of human blood cells with the emphasis on the protein rich cytoplasm [82].

Electroporation is another phenomenon used in single particle measurement, with the principle of a non-uniform rotating external field $\vec{E}$ exerting a torque $\vec{N}$ on a polarised particle (cell) which is proportional to the imaginary part of the polarisation vector $\vec{P}$ and can be derived as the cross product (Eq. 2.13):

$$\vec{N} = \vec{P} \times \vec{E} \tag{2.13}$$

Flow cytometry is a method through which the electrical properties of a single cell are obtained through a large number of cells passing at high speed and this approach is mostly widespread in the blood cells analysis with the first cytometer developed in 1950s [83]. The principle of measurement is to capture the properties of the cell flowing through two isolated channels in a form of the disruption to the electric field between two electrodes caused by the passing cell. This method is used to detect cells of different sizes and dielectric properties, since the impedance measured by a cytometer depends on those factors. Newer cytometers exploit other methods of cell detection such as optical systems where the absorption, reflection, scattering, or fluorescence emission is recorded following the cell's flow disturbance through the beam of laser light, or the piezoelectric properties of cells.

Advantages of the single cell spectroscopy methods are their simplicity that do not require sophisticated instrumentation and permits the analysis of the electric characteristics of a single cell, which is not possible with the EIS devices. Nonetheless, these methods provide the information on the electrical properties of a single cell or cell suspension, that is why, in order to derive the electrical conductivity and permittivity values of the cell substructures, adequate assumptions (of a fixed or uniform size of cells and cell membrane thickness) and

model fitting methods are required. Consequently, the assumptions made and the chosen theoretical model – which, even for a single cell, can take many different forms and have varying degrees of complexity — both play a significant role in the accuracy and dependability of the material properties that are derived from model fitting to experimentally obtained data. The importance of the model selection, methodology and measurement technique selection manifests in the differences in the obtained dielectric properties of tissues substructures documented in the literature which are often across multiple ranges of magnitude. The dielectric properties of the biological structures will be further discussed and presented in Chapter 3 in the context of the computational models development of thyroid and parathyroid tissue.

2.5 Summary

This Chapter comprised the current state of the EIS technology application in medicine, and in particular, the applications for thyroid and parathyroid surgery tissue differentiation have been examined and reviewed. Moreover, different computational modelling methods were introduced in order to highlight their applicability in the field of biological tissues electrical properties investigation, along with alternative measurement methods of electrical properties of tissue structures.

To summarise the review of EIS-based experimental studies, the electrical impedance of the health and pathologic neck soft tissues with the use of EIS and EIT devices was a subject of prominent number of studies, however, there are clear discrepancies between the reported results. These can be explained by differences in the studies' methodology, such as differences in studied species, measurement environment (*in vitro*, *in vivo*, *in situ*, temperature, humidity), type of measurement probe or device, which, without results normalisation or the conversion of impedance results into electrical conductivity or permittivity values, makes it difficult or even impossible to compare the presented raw impedance values measured by different devices of various geometrical characteristics. Despite the discrepancies, it is suggested that the low frequency impedance values should be higher for thyroid compared to parathyroid tissue. There is no similar consistency between the studies in the healthy and cancerous thyroid tissue impedance. Table 1 summarises the electrical conductivity and relative permittivity values presented in the literature for thyroid tissue obtained from the studies referenced in this review which can be used to verify the outcomes of the computational model developed in this thesis.

The analytical modelling methods highlighted in this Chapter permit the calculation of an exact solution for electrical properties of the tissues using mathematical equations and physical phenomena describing the behaviour. It is noteworthy that the calculation process is not demanding since the solution can be obtained relatively fast with low computational resources by solving single or a set of mathematical equations. However, the analytical cal-

Parameter [unit]	Frequency range	Value	Reference
Conductivity [Sm^{-1}]	<100 Hz	0.5	[26] modelled
Relative permittivity [-]	>1 MHz	>1e3	[26] measured
Conductivity [Sm^{-1}]	>1 MHz	>0.7	[26] measured
Conductivity [Sm^{-1}] healthy, *ex vivo*	251 kHz	0.405 ± 0.082	[22] measured
Conductivity [Sm^{-1}] cancerous, *ex vivo*	251 kHz	0.289 ± 0.056	[22] measured
Conductivity [Sm^{-1}] healthy	0.5-8 GHz	0.8395±0.2013 - 1.8730±0.0979	[61] measured
Conductivity [Sm^{-1}] cancerous	0.5-8 GHz	1.8960±0.5024 - 9.7461±0.9349	[61] measured

Table 2.1: *Comparison of the bulk electrical conductivity and permittivity values of thyroid tissue obtained through different methodology and presented in the literature*

culation is often associated with a significant level of assumptions, such as homogeneity and structures idealisation by omitting the complexity arising from the electrical properties of individual cells, their compartments and other molecules present in the biological material. Finally, none of the highlighted methods seems feasible to provide the estimation of the electrical impedance obtained through an EIS measurement with a tetrapolar probe which is the primary goal of this project, nor account for the effects arising from the unique follicular structure of the thyroid tissue. That is why numerical methods, despite their challenges associated with high computational time and resource requirements, seem to be more appropriate for the purpose of this computational study. The complexity of the thyroid and parathyroid micro- and macrostructures can be generated through a numerical modelling framework, and due to the availability of commercial numerical modelling software, this computational modelling approach will be feasible in order to investigate the addressed in this thesis research questions.

Chapter 3

Multiscale finite element model development

This chapter focuses on RO1 which is to recreate the characteristic structure and to simulate the reference electrical impedance of thyroid and parathyroid tissues. To fulfil this goal, it is necessary to derive the potential distribution in simulated tissue types when they're exposed to AC at multiple frequencies relating to the EIS measurement. It is, therefore, crucial to determine:

- The governing equations for the electric scalar potential distribution and how to solve them using numerical methods;
- The methods on how to recreate the complex structure of the biological tissues;
- Electrical properties of the tissues and their substructures investigated in this study;
- And model boundary conditions relating to the EIS measurement;

which will be addressed and detailed in the sections of this chapter.

3.1 Finite element modelling

3.1.1 FE software

In the literature review presented in Chapter 2, the limitations of the analytical methods applications, in particular, of the Maxwell's mixture theory, in predicting the electrical behaviour of complex biological structures were discussed. The numerical methods, mainly, the Finite Element Modelling approach is implemented in this study, in order to simulate the electrical behaviour of thyroid and parathyroid tissue after exposing them to alternating current. The numerical methods give the opportunity to investigate models of complex shapes without the strict shape and structure assumptions associated with the analytical approach,

e.g. they permit the exploration of the detailed cellular and follicular structures of parathyroid and thyroid tissues.

For all the FE simulation and geometries generation presented in this study, a commercial software Ansys Mechanical APDL with its quasi-static time-harmonic simulation [84] has been utilised. This type of analysis allows the simulation of the effects of an alternating electrical field without the need of running computationally demanding transient simulations. The assumptions for this analysis are that:

- The electromagnetic field is viewed as quasistatic,
- The time-harmonic electrical and magnetic fields remain uncoupled,
- Eddy currents are considered negligible,
- Electric field is derived from electric scalar potential.

According to the Ansys documentation [84], for this electric analysis with the quasistatic approximation, the following governing and charge density continuity equations which are derived from the Ampere's equation (Eq. 3.1 and 3.2) are solved:

$$\{E\} = -\nabla V \tag{3.1}$$

$$\nabla \cdot \left(\{J\} + \left\{ \frac{\partial \{D\}}{\partial t} \right\} \right) = 0 \tag{3.2}$$

where $\{E\}$ is electric field intensity vector, V – electric scalar potential, $\{J\}$ – current density vector, and $\{D\}$ – electric flux density vector. Eq. 3.1 informs us that the electric field intensity vector equals the negative gradient (∇) of the electric scalar potential, while the Ampere equation provides that the divergence ($\nabla\cdot$) of a sum of the current density vector (conduction electric current density) and the rate of change of electric flux density with time (displacement electric current density) equals zero.

Constitutive equations Eq. 3.3 and 3.4 for the electric fields describe the relationship between current density vector and the electric flux density vector with the electric field intensity vector:

$$\{J\} = [\sigma]\{E\} \tag{3.3}$$

$$\{D\} = [\varepsilon]\{E\} \tag{3.4}$$

where: *[σ]* – electrical conductivity matrix (Eq. 3.5) and *[ε]* – permittivity matrix (Eq. 3.6).

$$[\sigma] = \begin{bmatrix} \sigma_{xx} & 0 & 0 \\ 0 & \sigma_{yy} & 0 \\ 0 & 0 & \sigma_{zz} \end{bmatrix} \tag{3.5}$$

$$[\varepsilon] = \begin{bmatrix} \varepsilon_{xx} & 0 & 0 \\ 0 & \varepsilon_{yy} & 0 \\ 0 & 0 & \varepsilon_{zz} \end{bmatrix} \tag{3.6}$$

and where: σ_{xx}, ε_{xx}, etc., is the conductivity and permittivity in one of three directions x, y and z. These components, however, all take the same value under the assumption of homogeneous and isotropic materials.

The differential equation for the electrical scalar potential after substituting constitutive equations (Eq. 3.3 and 3.4) into Eq. 3.2, considering the governing equation (Eq. 3.1), takes the form of Eq. 3.7:

$$\nabla \cdot ([\sigma]\nabla V) - \nabla \cdot \left([\varepsilon]\nabla \frac{\partial V}{\partial t} \right) = 0 \tag{3.7}$$

The element type dedicated for the current based simulation in Ansys Mechanical ADPL is SOLID231 – a 3D 20-node current-based electric element with one degree of freedom – electric scalar potential. The SOLID231 element with its nodes is visualised in Fig. 3.1, however, it can take a shape of hexahedron or tetrahedron depending on the chosen meshing method. For a quasistatic time-harmonic electric analysis, knowing that the time derivative component $\frac{\partial}{\partial t}$ is replaced by $j\omega$ and hence, Eq. 3.7 can be rewritten in a form of Eq. 3.8:

$$-\nabla \cdot ([\varepsilon]\nabla V) + \frac{i}{\omega}\nabla \cdot (\ [\sigma]\nabla V) = 0 \tag{3.8}$$

where i is the imaginary number and ω is the angular frequency (ω=2πf). The electric scalar potential distribution is then predicted solely based on the conductive and dielectric properties of a given biological material and the frequency of the external electric field.

Overall, the governing equations are solved upon all nodes and subsequently, depending on the type and shape of the element, and the selected shape functions, interpolated to the rest of the element. The information on the electric scalar potential approximation over the element based on the calculated values at the nodes further explained in the Ansys documentation (Theory Reference for the Mechanical APDL and Mechanical Applications [84]), in the section concerning electric analysis with the quasistatic approximation. Additional information concerning the SOLD231 element and its shape functions and interpolation points depending on the shape of the solid element selected (hexahedron, tetrahedron, pyramid or wedge) can be found in Ansys documentation [84] in the SOLID231 - 3-D 20-Node Electric Solid section.

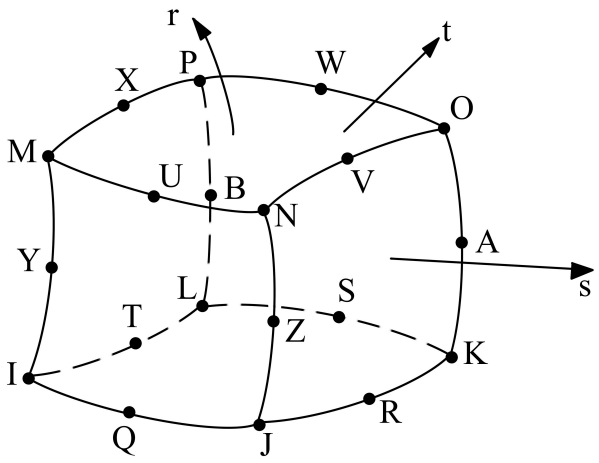

Figure 3.1: *SOLID231 element [84] I-Z, A-B mark the 20 nodes of the element which are marked at the element's corners and in the middle of each edge, r,s,t mark the local coordinate system of the element in which the translations u,v,w can occur*

3.2 Multiscale model development

As explained in Chapter 1, the unique frequency-dependent properties of tissues in the β dispersion region result from the capacitive properties of cell membranes, which makes them a crucial component to include in the computational model of biological tissues. However, due to their small size (approximately 8 nm), it is not computationally feasible to include them in a tissue model recreating the impedance measurement with a tetrapolar EIS probe, which requires a simulation volume in the order of a few centimetres. The initial estimation indicated that a tissue level model including such detailed cellular structures would result in a mesh comprising over 10^{12} nodes for a thyroid tissue geometry with the thickness of only 1 mm, which is computationally intractable.

To overcome this limitation, a multiscale modelling approach can be implemented, where the tissue's structure is considered as a set of connected hierarchical substructures, representing different levels of tissue complexity. In the case of thyroid and parathyroid tissues hierarchical structure, the cellular (microscale) and tissue (macroscale) levels can be distinguished. The multiscale modelling approach investigating the cellular and tissue structures separately has been implemented in the computational studies concerning the electrical properties of cervical epithelium [38], oral tissues [41] and skin [37; 75]. Nonetheless, the characteristic

structure of the thyroid tissue requires introduction of an additional scale (mesoscale) that would represent this tissue's basic structural unit – a follicle – which is not present in the case of parathyroid tissue. Therefore, in this study a novel follicle mesoscale model will be proposed and introduced to investigate the thyroid tissue electrical properties with the multiscale modelling approach. Fig. 3.2 shows the histology images of thyroid and parathyroid tussles with a marked hierarchy of substructures considered for each tissue's multiscale model.

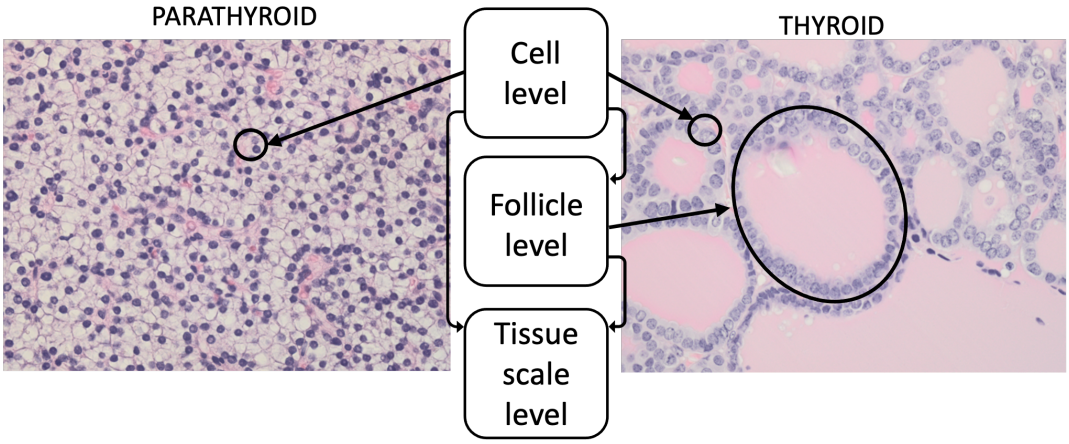

Figure 3.2: *Parathyroid and thyroid histology images with labelled levels of complexity corresponding to the levels of the multiscale computational model*

The simulation results at each level, starting with the lowest model hierarchy (microscale) are passed to the higher-level models in the form of element material properties. For lower scale models (cell and follicle), the effective transfer impedance is simulated. Subsequently, the computed transfer impedance results are processed to calculate effective conductivity (σ) and relative permittivity (ε_r) from Eq. 3.9 and 3.10, to assign as material properties in the appropriate higher-level model compartments:

$$\sigma(f) = \frac{d}{A \cdot Z'(f)} \tag{3.9}$$

$$\varepsilon_r(f) = \frac{Y''(f)}{2\pi f \cdot \varepsilon_0} \frac{d}{A} \tag{3.10}$$

where:

$$Y''(f) = \frac{-Z''(f)}{(Z'(f))^2 + (Z''(f))^2} \tag{3.11}$$

and knowing that:

$$C(f) = \varepsilon_0 \varepsilon_r \frac{A}{d} \tag{3.12}$$

and:

$$C^{'}(f) = \frac{Y^{''}(f)}{\omega} \tag{3.13}$$

where: d and A – thickness and cross-sectional area of the model, ε_0 – permittivity of free space (8.854 x 10^{-12} Fm^{-1}), $Z^{'}$ and $Z^{''}$ – real and imaginary part of effective impedance obtained from lower-level simulation, $Y^{''}$ – imaginary part of admittance, C - complex capacitance, $C^{'}$ - real part of complex capacitance, ω - angular frequency ($\omega = 2\pi f$).

The simulation frequency points were determined mostly considering the β dispersion region (kHz-MHz). Moreover, the computed theoretical results are aimed to be compared against the *in vivo* experimental data of thyroid and parathyroid tissue measured with the commercial tetrapolar Zedscan™ device presented by Hilary et al. [3]. In this *in vivo* experimental study, the impedance measurement is performed at 14 frequency points from the range of 76 Hz – 625 kHz. The exact 14 frequencies will be considered for the simulated impedance calculation in this computational study, in order to facilitate the qualitative and quantitative comparison of the data.

For simplification purposes, the homogenisation approach has also been implemented to this study, with the assumption that material properties from just one substructural unit on the micro- or mesoscale represents the material properties on the bigger scale. For example, it is assumed that a few cells or follicles with the same shape, size or composition are representative of the properties of the whole tissue. This assumption considerably reduces the computational time and resources required for solving the simulation. However, such an approach is insufficient to explore the impact of the biological tissues' inherent heterogeneity on both meso- and macroscales, which will be explored in more detail in Chapter 6.

A modelling pipeline implemented for each step in multiscale modelling, micro-, meso- and macroscale model simulations, is visualised in Fig. 3.3. The development of each substructural model will be presented separately based on the level of complexity in the following sections.

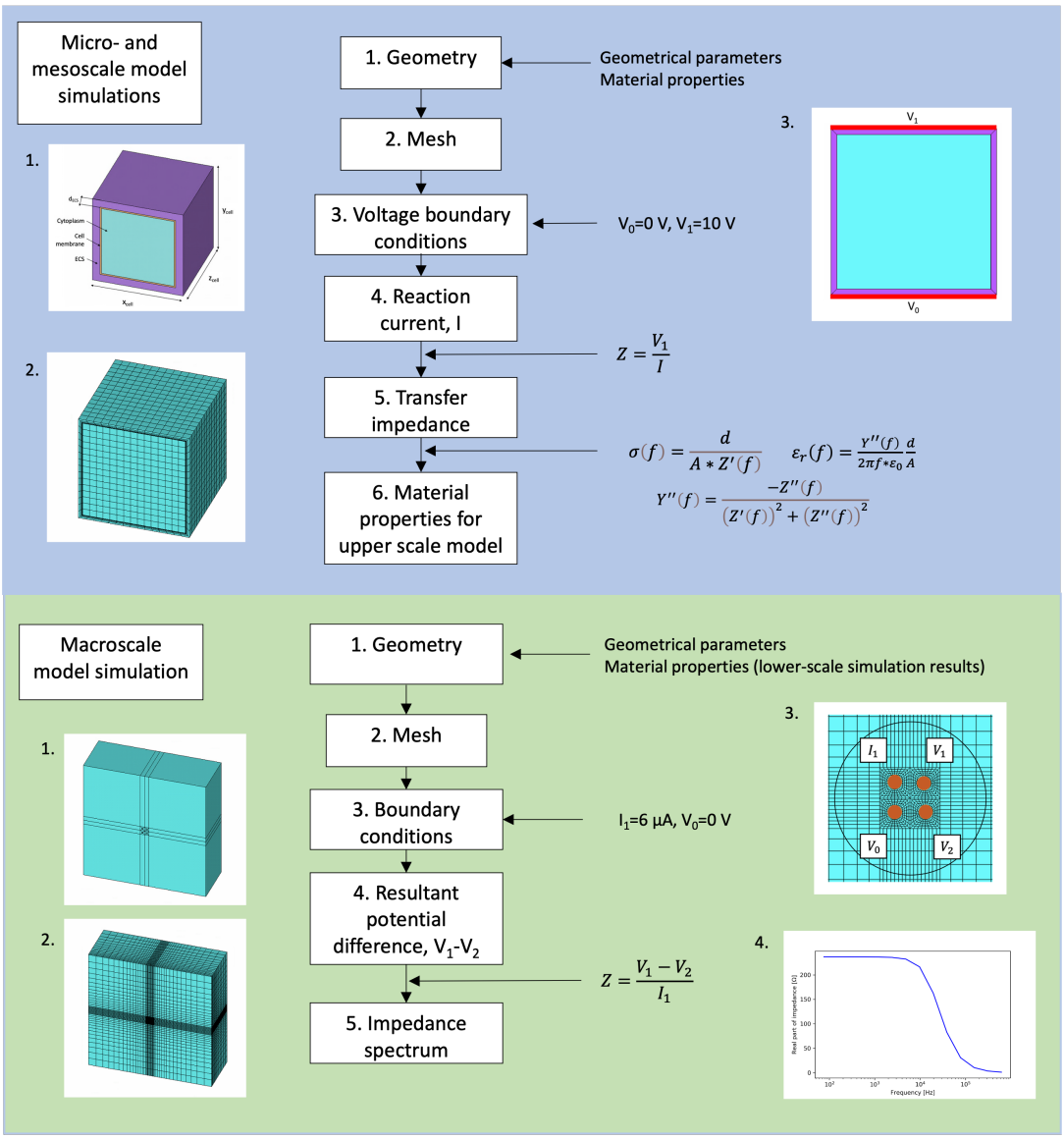

Figure 3.3: *Flow chart visualising the main stages of the preparation and simulation of the finite element multiscale models*

3.2.1 Microscale model development

3.2.1.1 Cell structure

Mammalian cells, regardless of their location and function in the organism, all exhibit equal heterogenous inner structure. A typical cell consists of a few compartments: innermost nucleus separated from the cytoplasm by a nuclear membrane, various organelles, cytoplasm filling in the cell and separating the organelles, the cell membrane separating the intra- and extracellular cell content, and the extracellular space (ECS).

To attempt to reproduce all of these cellular substructures would not be computationally practical, hence, for simplification purposes the choice of the structures included into the microscale level model was made based on the significance of these cell components in the bulk electrical properties of a singular cell. In particular, the nucleus has not been incorporated in the microscale model as prior research in the cervical epithelium [38] revealed, that these structures inclusion, mainly the nucleus and its membrane, had a negligible effect on the cell electrical properties. This can be linked to the nucleus membrane's greater conductive properties (0.7 mSm^{-1}) compared to the cell membrane (approximately 10^{-4} mSm^{-1}). Additionally, the same computational study investigated the cervical intraepithelial neoplasia where the nuclear-cytoplasmic ratio is one of the indices of the pathology progress which is not the case of this study where only the healthy tissues are considered. The importance of the cell membrane dielectric properties on the β dispersion has been highlighted in Chapter 1, which makes it a key structure to include in the model. Additionally, the extracellular space is often included even in the simplest cell models, such as in the cell equivalent circuit proposed by Fricke and Morse [28] and the impact of the ECS on the bulk tissue impedance in the frequencies below β dispersion was explored previously in computational and experimental research [38; 72].

To summarise, the microscale model for both thyroid and parathyroid tissue will consist of three compartments: cytoplasm, cell membrane and ECS layer. The three-compartmental cell geometry with the generated mesh is presented in Fig. 3.4.

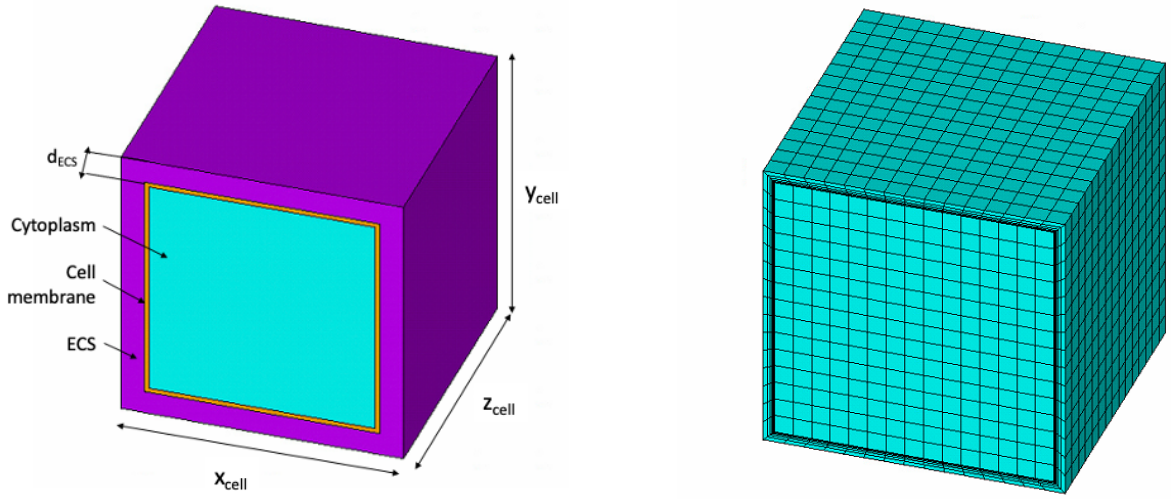

Figure 3.4: *Microscale model (a) geometry including marked cell compartments and its geometrical features: x_{cell}, y_{cell} and z_{cell} – size of the cell in three directions, d_{ECS} – ECS thickness; (b) the meshed geometry*

3.2.1.2 Microscale model properties

To simulate the electrical properties of a cell, the geometrical characteristics of each compartment are required along with their electrical conductivity and permittivity. Table 3.1 shows the mean values of the electrical properties of the selected cell compartments which have been documented in the literature. These are obtained from the studies on various cell types and species, there is no specific data on the human thyroid (thyrocytes) and parathyroid (chief cells).

Material	Conductivity [Sm^{-1}]	Relative permittivity [-]	Reference
Cytoplasm	0.55	150	[82; 85; 86; 87]
ECS	1.1	72	[82; 85; 88; 89]
Cell membrane	10^{-7}	8.7	[38; 90]

Table 3.1: *Mean material properties for the compartments of the microscale model presented in the literature*

To further simplify the computational model generation, the most abundant cell type was selected to represent each thyroid (thyrocyte) and parathyroid (chief cell) gland's microstructure, neglecting the presence of parafollicular, oxyphil cells and adipocytes in the respective tissue. Although thyrocyte and chief cells have slightly different shapes and sizes (the first being more cuboidal in shape while the later resembles more spherical shapes), one microscale model has been constructed for both tissue types where each size of the compartment is adjusted to serve the purpose of different cell types. To determine the size of each cell type, an additional literature search on their sizes has been performed. In particular, there are a few sources providing the quantitative data on the sizes of thyroid, parathyroid cells and their values are summarised in Table 3.2.

Structure (species)	Dimension	Reference
Thyrocyte (rat)	Height: 9.5-11 µm Area: 700-800 μm^2 Volume: 1,200-1,500 μm^3	[91]
Thyrocyte (rat)	Height: 8.26 ± 0.452 µm	[92]
Chief cell (human)	8-10 µm	[8]
Chief cell (human)	6-8 µm	[93]

Table 3.2: *Geometrical parameters of thyroid and parathyroid tissue structures as documented in the literature*

Additional manual histology images measurements (images provided by Prof. K. Hunter – personal communication) have been performed to provide further data of the morphology of cells of both tissue types. For this purpose, the image analysis software, such as ImageJ and ImageScope, has been used. Table 3.3 shows the results of the histology samples manual measurement. The sample size for the measurement was determined based on the mean value convergence – change of <0.5% compared to the mean value from a smaller sample size. The data convergence is visualised in the Appendix A. The measurements have been performed in up to four different locations in one histology image to investigate intrasubject variability of the structures.

Structure	Sample size	Specimen (Images)	Locations	Mean ± sd [µm]
Thyrocyte	200	5 (5)	3-4	8.53 ± 1.84
Chief cell	270	7 (7)	4	7.59 ± 1.45

Table 3.3: *The summary of selected geometrical parameters measured for thyroid (thyrocyte and follicle) and parathyroid tissue (chief cell), equal number of images and specimens means one image was taken per specimen*

The cell membrane's thickness is of a constant value for each cell type and is of order of a few nanometres (8 nm according to [94]). However, such a small thickness remains a challenge in the FE modelling of a cell since the surrounding compartments' size is a few orders of magnitude higher. Bearing this in mind, it is important to construct appropriate FE mesh where all the cell compartments are correctly connected, and the error associated with the numerical modelling and the mesh construction is small enough to not interfere with the results.

Due to the lack of high-resolution transmission electron microscopy (TEM) images for human thyroid and parathyroid tissue, the ECS thickness parameter had to be estimated for both studied cell types. This parameter has been mostly determined based on the values used in computational cervical epithelium cells simulations [38]. Additionally it was possible to perform manual measurements on ECS of the chief cells from camel parathyroid gland TEM images published by Al-Zghoul [95]. The measured ECS thickness ranged between 0.2-0.9 µm, which is similar to the values used for modelling the cells of cervical epithelium (0.05-0.8 µm) [38]. The effect of the ECS thickness on the electrical behaviour of cells and the tissue scale impedance values will be investigated in the following Chapter 4. Nonetheless, for the default thyrocyte and chief cell microscale models the values 0.3 µm and 0.5 µm have been selected respectively. This choice was based on exploratory simulations that suggested parathyroid cells with a thicker ECS compartment have a better agreement between computed and *in vivo* measured impedance spectra. Such an assumption can also be justified by the function these both cells play in the respective glands, e.g. thyrocytes' main function is to build a thin epithelial layer surrounding and containing the colloid in spherical structures,

which raises the assumption of more compact cell alignment compared to the parathyroid gland's structure which is less organised and allows more ECS between respective cells.

3.2.1.3 Meshing technique

Different meshing techniques have been verified in the APDL Mechanical, specifically the free and mapped meshing techniques with different element shapes (tetrahedral and hexahedral elements). Free meshing is an automated method which can generate elements in an unorganised pattern, however, is suitable for elements of different shapes to fit the geometry. Mapped meshing is a less automated method through which a highly organised mesh pattern of solely 2D quadrilateral or triangular or 3D hexahedron elements is created, which gives more freedom in determining the meshing process of each model volume. In particular, it permits the user to specify the number of element required along each edge of the model. Fig. 3.5 visualises the differences between a mapped hexahedral mesh and free tetrahedral mesh of an early-stage microscale model.

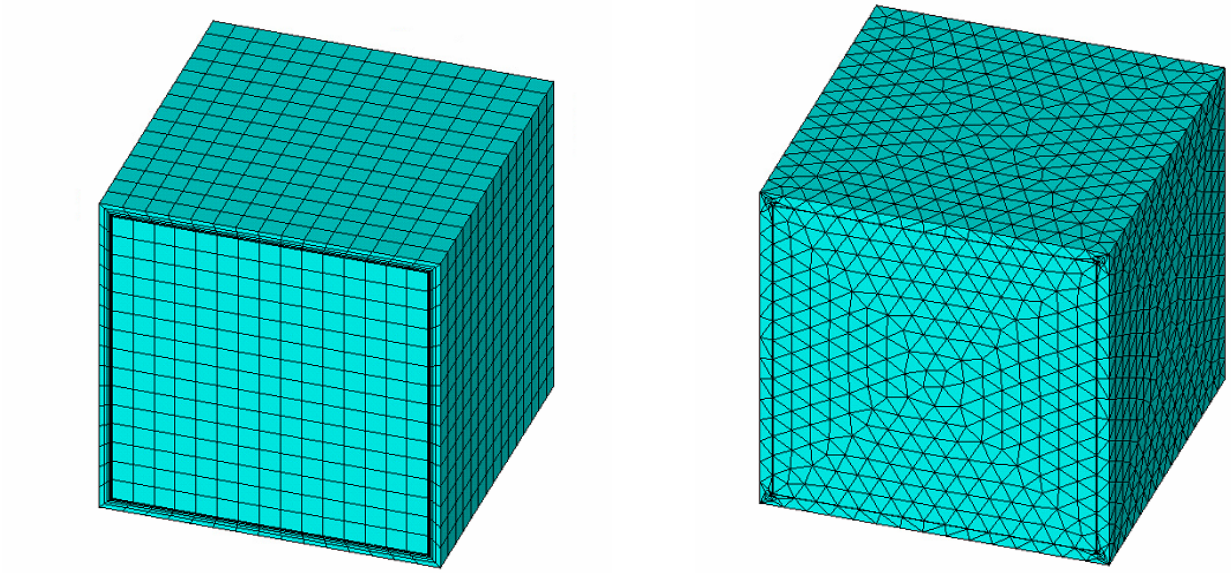

(a) **(b)**

Figure 3.5: *Visual differences between a) mapped mesh and b) free mesh performed on the 3D model prepared for mapped meshing, the thickness of the cell membrane is exaggerated in those models*

The mapped approach with the SOLID231 elements in the hexahedral shape was determined to be the preferred method of meshing for geometries across all levels of the multiscale modelling. Despite being a more time-consuming procedure, the main benefit of this type of mesh generation is that it comes with more control to create a well-structured mesh by manually defining the size and number of elements partitioning each edge, surface, or volume.

This approach allows a greater re-use of the a priori defined meshing procedure, e.g. in a sensitivity analysis where models with compartments of varied sizes are investigated.

For any geometry to match the requirements for a mapped mesh, it is necessary that it should be specially prepared beforehand or subdivided into smaller entities. For this approach to be successful, each volume must be brick-shaped, with six areas defining it, and the surfaces must be formed by three to four edges. In order to achieve this, each volume needs to be divided appropriately, or its lines and surfaces to be merged through a concatenation command.

3.2.1.4 Boundary conditions

To simulate the transfer impedance on the microscale level, the Dirichlet boundary conditions (Chapter 2 Eq. 2.10) were applied to opposite surfaces of the cuboid microscale model (as seen in Fig. 3.6) which constricts the potential of nodes on both surfaces to known values (for the micro- and mesoscale model $V_1 = 10$ V and $V_0 = 0$ V). The remaining surfaces are automatically assigned in Ansys APDL with the Neumann boundary conditions (Chapter 2 Eq. 2.11) which constrains the current flow within the domain.

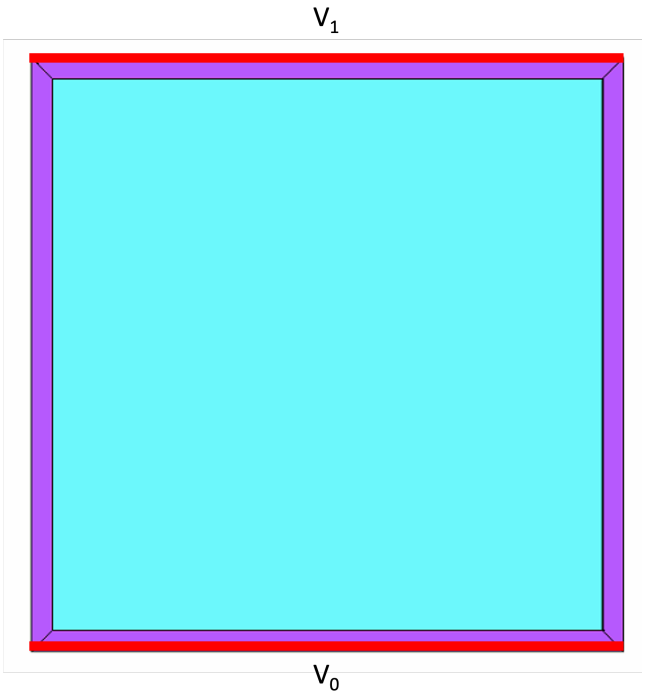

Figure 3.6: *Voltage Dirichlet boundary conditions applied to the microscale model for the transfer impedance simulation where $V_1 = 10$ V and $V_0 = 0$ V*

3.2.1.5 Solution

The reaction current on the surfaces with defined potential values is obtained through the simulation to derive the complex impedance results, which are subsequently converted into the effective conductivity and relative permittivity following Eq. 3.9-3.11. These are transferred to the mesoscale level in the case of thyroid tissue or macroscale level for parathyroid.

3.2.2 Mesoscale model development

3.2.2.1 Follicle structure

A follicle is a structural unit typical for the thyroid tissue and, as highlighted and visualised in Fig. 3.2, is characterised with a spherical shape. Each follicle comprises three main compartments: (i) colloid which fills the follicles and stores the thyroglobulin, (ii) single epithelial layer of thyrocytes which encapsulates the colloid and (iii) a thin layer of loose connective tissue which separates follicles from each other. Therefore, these three compartments have been chosen as the components of the thyroid mesoscale level model. Since the follicular structure is absent in the parathyroid tissue, the mesoscale model will only be implemented to investigate the electrical properties of the thyroid follicles. Fig. 3.7 visualises the mesoscale model geometry with its marked compartments and the constructed mesoscale mesh.

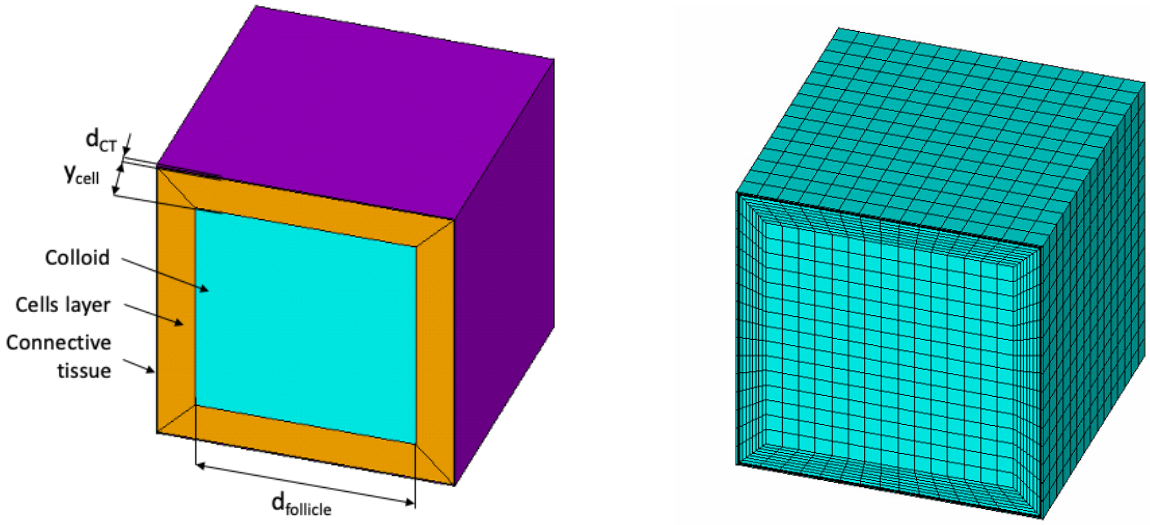

Figure 3.7: *Mesoscale model (a) geometry including marked follicle compartments and its geometrical features: $d_{follicle}$ – size of the follicle, y_{cell} – cell thickness obtained from the microscale model, d_{CT} – connective tissue thickness; (b) the meshed geometry*

3.2.2.2 Mesoscale model properties

The geometrical characteristics of the follicle, specifically the size of the colloid compartment was based on the values reported in the literature and the manual measurements of the available thyroid histology images (images provided by Prof. K. Hunter – personal communication) which are summarised in Table 3.4. The principle of the manual measurement of follicles is similar to the approach presented for cell measurements in Section 3.2.1.2 and futher details are comprised in Appendix A. To determine the follicle sizes, each individual follicle size was calculated as a mean from the shortest (d_{min}) and longest (d_{max}) diameter of the structure as visualised in Figure 3.8.

Data from the literature			
Parameter		Reference	
Diameter: 40-600 µm Most prevalent: 80-160 µm		[96]	
Data from the histological measurements			
Sample size	Specimen (Images)	Locations	Mean ± sd [µm]
186	6 (14)	1-4	113.77 ± 63.13

Table 3.4: *The geometrical characteristics of colloid compartment as documented in literature and determined by manual histology measurements, higher number of images than specimens means a few images were taken from the same specimen*

The cell layer thickness is determined by the size of the cell in the y direction (y_{cell}) which was used in the microscale level simulation for a given multiscale modelling simulation run. Due to the insufficient resolution of the thyroid histology images and the lack of the data published in the literature concerning the thickness of the connective tissue layer, the size of this compartment had to be estimated. Based on the exploratory simulations, the connective tissue default thickness was decided to be 1 µm (the range of 1-5 µm will be considered in the following sensitivity analysis presented in Chapter 4).

The electrical properties for the mesoscale model have been either acquired from the hierarchically lower microscale model (thyrocyte microscale simulation discussed in Section 3.2.1) and through the literature search (colloid and connective tissue). Since the electrical properties of the latter materials were not as thoroughly experimentally studied compared to those of the cell compartments, obtaining material properties for colloid and follicular connective tissue was not a straightforward process. Hence, an additional literature search on the materials composition and adequate substitutes has been performed which is summarised in the following sections.

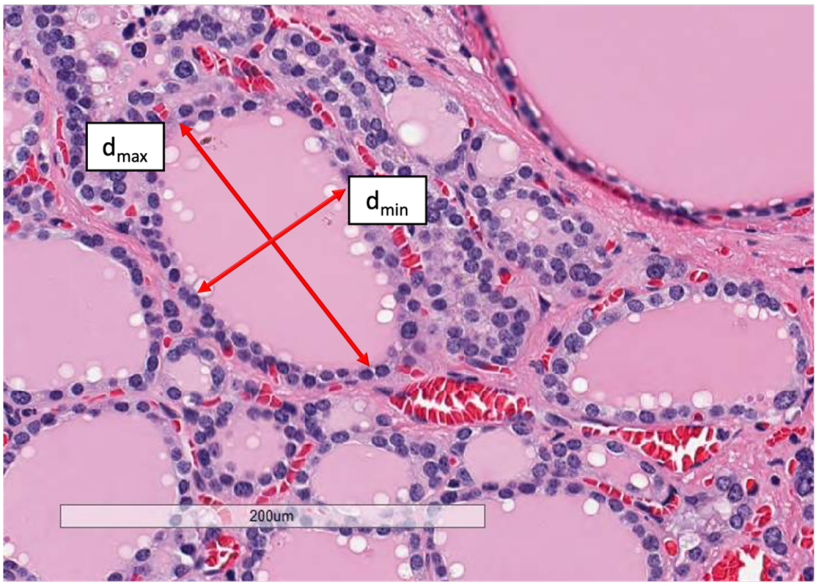

Figure 3.8: *Histology image of thyroid tissue showing the shortest (d_{min}) and longest (d_{max}) diameter manual measurement (K. Hunter – personal communication)*

3.2.2.3 Electrical properties of colloid

Colloid is a protein-rich homogeneous material filling up the thyroid follicles and its composition can vary from one specimen to another and within a single gland [6]. The major protein in the colloid is thyroglobulin which is a glycoprotein synthesised inside follicular cells. Thyroxine and triiodothyronine are peptide thyroid hormones that are synthesised during the process of iodinating the tyrosine residues on thyroglobulin and stored in thyroglobulin molecules that are accumulated in colloid. According to the literature [97; 98; 99], the relative thyroglobulin level compared to the entire protein amount is approximately 40-90%, in addition to the larger iodoproteins and albumin or pre-albumin fractions that can also be identified in the follicle colloid.

There are several studies investigating the electrical properties of colloid and thyroid tissue published throughout a few decades with first cases reported in the 1960s. Gorbman and Ueda [100] studied the electrical properties of thyroid follicles throughout the maturation period of tadpoles and in adult frogs. Moreover, the impact on the injection of thyroid-stimulating hormone (TSH) has been examined on mature specimens. Similarly, Krüskemper and Reichertz [101] were first to demonstrate that TSH hormone level, being an index of the thyroid gland activity, induces changes in thyroid gland electric behaviour. Williams [102] have reported that TSH treatment decreases the transmembrane potential that initiated the rise in capacitance of the follicle.

Despite the interest in the electrical properties of colloid and its dependence on the TSH levels in the aforementioned studies, neither of them provided data on the electrical conductivity or relative permittivity of this material that would be useful for this computational modelling study. Nonetheless, the presented examples show a connection between the thyroid electrical properties with the physiological activity of the gland, which is the direct response to the level of thyroid-stimulating hormone in the blood plasma. TSH stimulates the thyroid gland hormone production which means that the colloid composition varies with time and depends on the gland's activity.

The lack of measured data concerning the electrical properties of colloid remains a challenge, thus, it was crucial to examine the possible substitutes that would mimic this material in the mesoscale model. As previously mentioned, the most abundant protein in colloid is the thyroglobulin which is a certain type of glycoprotein. Therefore, significant amounts of glycoproteins was the first criterion for the search for appropriate colloid material substitutes. The materials that were taken into account were biological in nature and did not necessarily have to be specific to human tissues.

The material with significant glycoprotein concentration that was most broadly studied in terms of its electrical behaviour is vaginal mucus. Most of the reported studies concern vaginal electric resistance or conductance measurements. The presented data, however, remains of limited benefit since without any information concerning the geometrical characteristics of the material studied (area or thickness) or of the measurement probe, it is difficult to convert the conductance [S] values into conductivity [Sm^{-1}]. Other materials that have been considered are egg white and cytoplasm. Moreover, the main aim of the reported studies was to find a correlation between conductivity and temperature (egg white), fertility or the conceiving success (vaginal mucus). Finally, a set of gel-like materials (agar, agarose and gelatine) properties has also been included after being reported as appropriate substitutes for biological tissue phantoms, especially the brain tissue gel phantoms.

All materials considered as colloid substitutes and their electrical properties are summarised in Table 3.5. This literature review provided the possible range of conductivity (0.1-1.8 Sm^{-1}) and relative permittivity (75-150) to assign to the colloid compartment in the mesoscale model. The impact of the uncertainties in these parameters on the thyroid tissue simulated impedance will be further investigated in Chapter 4.

3.2.2.4 Electrical properties of connective tissue

Different types of connective tissue are present in many forms in the human organs, and in the case of thyroid tissue, it's a thin collagenous layer separating each follicle and follicles that are organised in lobules. This is a type of loose connective tissue with unstructured

Material	Species	Conductivity [Sm^{-1}]	Conductance [S]	Relative permittivity [-]	Reference
Vaginal mucus	Murrah buffaloes	Mean: 1.40 Range: 0.92-1.59			[103]
	Weaned sows		0.02-0.04		[104]
Egg white	Chicken	0.8-1.8			[105]
		0.4-1			[106]
		0.5			
		0.4 (at 300 MHz)		75 (at 100-300 MHz)	[107; 108]
		0.71 (at 40 MHz)			
		0.94		50-87	[109]
Gel materials	N/A	Mean: 0.25 Range: 0.1-0.4			[110]
Cytoplasm (mean values)	Various	0.55		150	Table 3.1
Range		0.1-1.8	0.02-0.04	75-150	

Table 3.5: *Summary of the electrical properties of biological materials consisting of significant amounts of glycoproteins and thyroid colloid potential substitutes*

collagen, elastin and reticular fibres embedded in the extracellular matrix. Similarly to the colloid material, there is no specific experimental data on the electrical properties of this tissue, therefore, the electrical properties of other types of connective tissue (based on the collagen content in the tissue) will been summarised in following, with the emphasis on the properties of tendon and dura mater.

However, it is important to bear in mind the differences in the structure and the arrangement of the collagen fibres in both substitutes compared to the loose connective tissue. Tendon is characterised by the dense, highly organised and hierarchical structure of the collagen fibres which comes from the requirement for their primary function to sustain high tensile forces and to transfer them from muscles to the skeletal system. Dura mater, by contrast, is made of dense irregular connective tissue which is the outermost layer of meninges that mechanically protect the brain and spinal cord. Structurally, the dura mater consists of fibroblasts and extracellular collagen fibres of slightly less regular arrangement in comparison to the tendon structure.

Table 3.6 summarises the literature review on the tendon and dura mater electrical properties. It is worth highlighting that the presented relative permittivity values are in the range across multiple orders of magnitude and the significant spread of this parameter will be investigated in the following Chapter 4.

Material	Conductivity [Sm^{-1}]	Relative permittivity [-]	Reference
Tendon	0.3	5 x 10^7	[26]
	0.25	10^5	[111]
Dura mater	0.05-0.67		[112]
	0.03		[113]
	0.6		[114]
	0.5	15 x 10^4	[115]
		27 x 10^4	[26]

Table 3.6: *Summary of the electrical properties of the thyroid connective tissue substitutes*

3.2.2.5 Boundary conditions

The methodology of assigning the voltage boundary conditions presented for the microscale model has been adapted for the mesoscale model due to the similarities in the cuboidal shape of both geometries and the feasibility to deliver the electrical properties from simulating the transferer impedance which is necessary for passing onto the higher-level model.

3.2.3 Macroscale model development

3.2.3.1 Model characteristics and boundary conditions

The macroscale models for thyroid and parathyroid tissues are hierarchically the final sub-models in the multiscale modelling pipeline, where the generated geometries enable the simulation of impedance relating to EIS measurement with the tetrapolar ZedScan^{TM} device for both glands respectively. The thyroid macroscale model is a single compartmental geometry (Fig. 3.9a, while the parathyroid model consists of two compartments (Fig. 3.9b). Due to the small size of the parathyroids (around 3-7 mm), it was necessary to include the tissue adjacent to this gland in its macroscale geometry which is in order of a few centimetres. For the default parathyroid model, thyroid was chosen as the surrounding tissue which recreates the location of parathyroid glands on its posterior surface. The frequency dependent properties assigned to the thyroid and parathyroid compartments are obtained from the lower-level model simulations (mesoscale results for thyroid, and microscale results for parathyroid).

The constructed tissue scale models replicate the electrode configuration of the tetrapolar EIS ZedScan^{TM} probe, with the 0.6 mm diameter electrodes arranged with the centres located on a circle of 2 mm diameter as shown in Fig. 3.10. The electrodes are not physically incorporated into the model due to the high impedance of the electrodes themselves and high surface impedance. The macroscale impedance is obtained according to Ohm's law by dividing the injected current of 6 µA assigned to the driving electrode (I_1) and flowing through

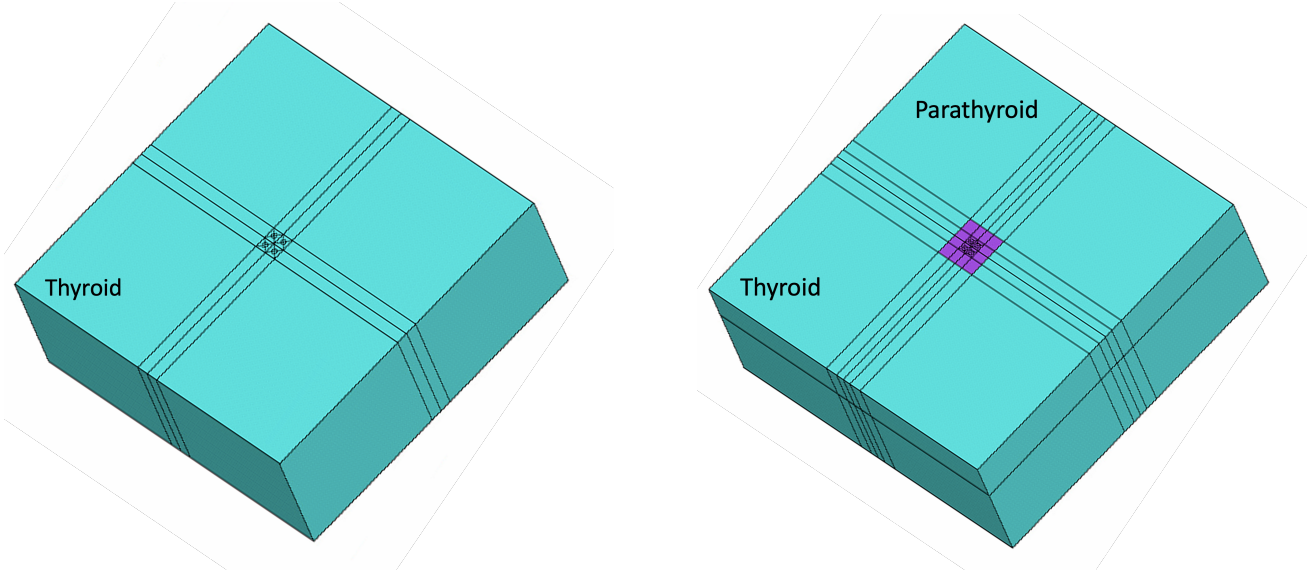

Figure 3.9: *Default macroscale model for (a) thyroid and (b) parathyroid tissue*

the underlying tissues to the ground electrode (V_0), by the potential difference recorded by the passive electrodes (V_1 and V_2). The electrode placement on the glands in the macroscale model geometry with their arrangement and FE mesh are visualised in Fig 3.10. The outer dimensions of the macroscale models were kept the same for both tissue types at 40x40x15 mm which was determined in the model shape study highlighted in Section 3.3.4.

3.2.3.2 Model configurations – fascia compartment

Fascia is a superficial loose connective tissue that has the main function of securing the organs and it's a thin layer that covers both thyroid and parathyroid glands (Fig. 3.11). During surgery prior to the EIS measurements, the surgeon removes the excessive fascia layer (S. Balasubramanian, endocrine surgeon - personal communication), however, it is impossible to guarantee the extent of the tissue removal. Hence, the remaining fascia can 'contaminate' the recorded impedance for both glands, that is why it is practical to investigate its electrical properties in this computational study at the macroscale level (Fig. 3.12). For simplification, both the connective tissue associated with thyroid follicles and fascia were treated as a similar material with the exact electrical properties that were summarised in Table 3.6. The effects of the uncertainty in this material's electrical properties and its thickness will be investigated in the following Chapter 4.

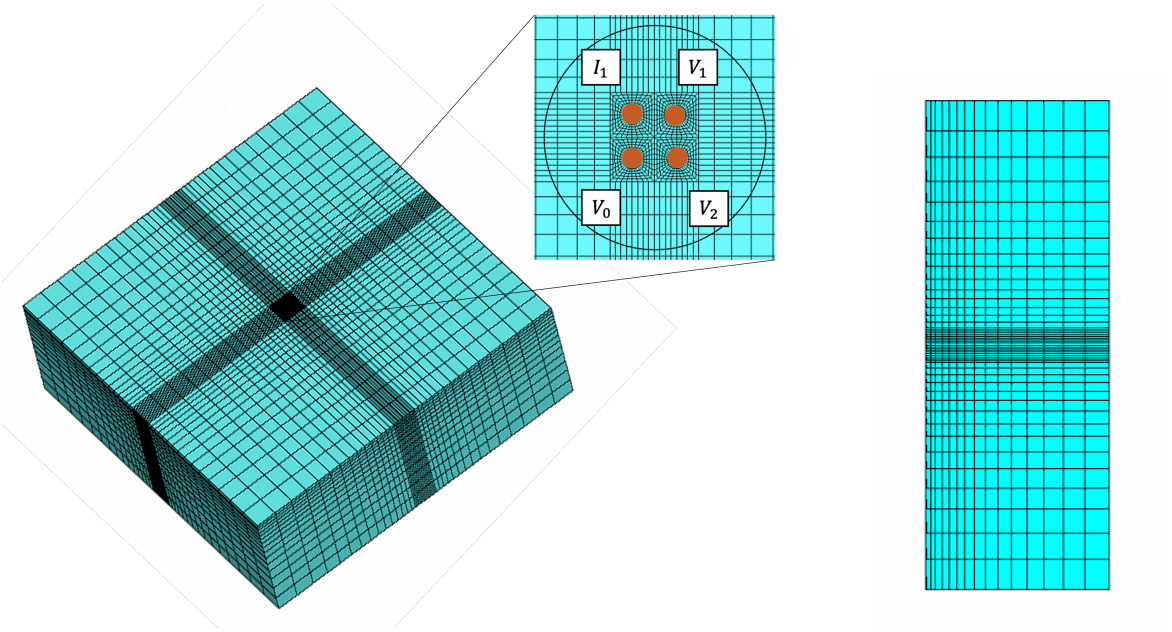

(a) **(b)**

Figure 3.10: *Typical mesh for the macroscale model, refined around the electrodes by the surface (a) isometric view, (b) side-on view*

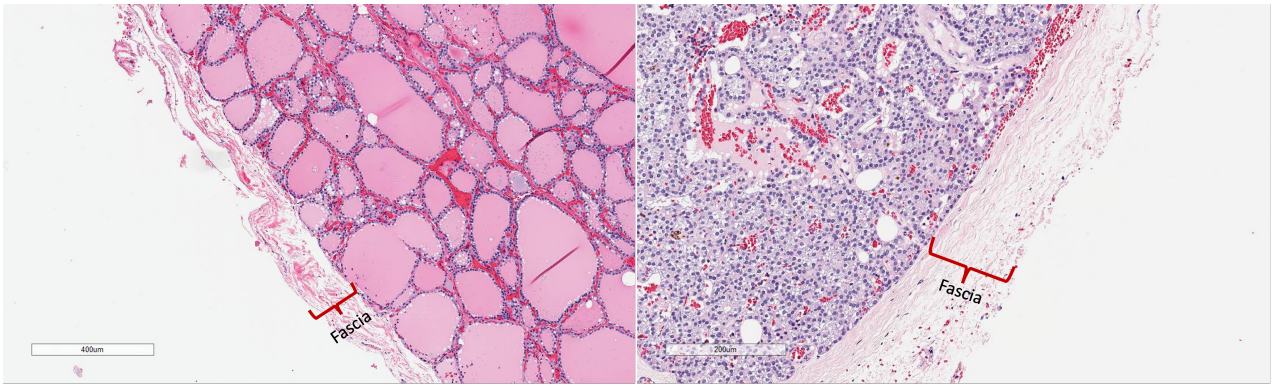

(a) **(b)**

Figure 3.11: *Histology images visualising the superficial fascia layer on (a) thyroid and (b) parathyroid, samples stained with eosin and haematoxylin, Prof. K. Hunter - personal communication*

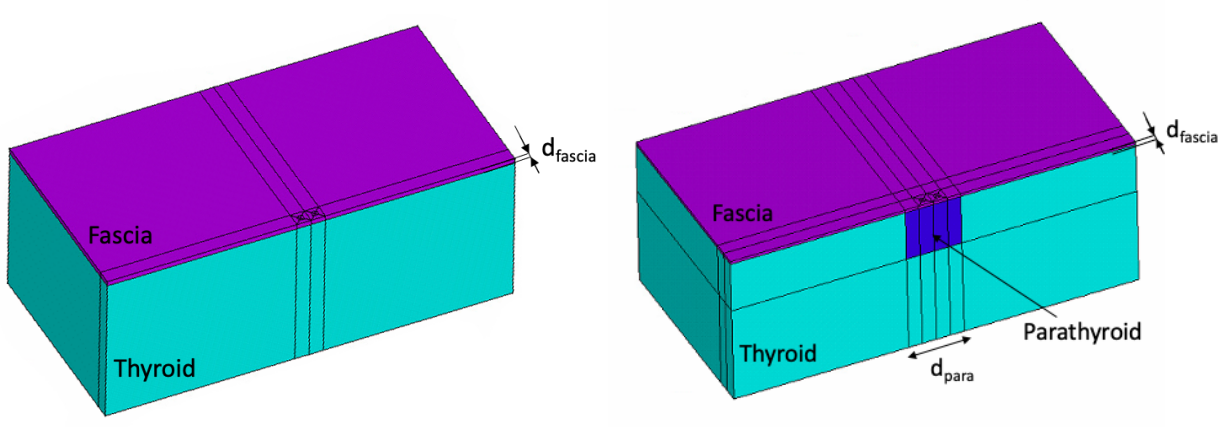

(a) **(b)**

Figure 3.12: *Cross-sectional view through (a) thyroid and (b) parathyroid (d_{para}) macroscale models with the superficial fascia layer (d_{fascia})*

3.3 Computational model verification

3.3.1 Solver verification

The first exploratory simulations were aimed to show the comparison between analytic and computed solutions for simple models and to ensure the reliability of the computed results. Single and multiple layered models have been constructed and the transfer impedivity (ρ^*) simulated for each model consisting of layers arranged in series and in parallel. Fig. 3.13 shows the boundary conditions for the layered model configuration.

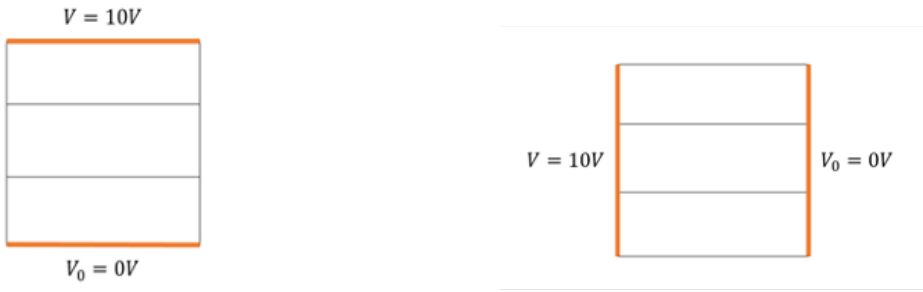

(a) **(b)**

Figure 3.13: *Boundary condition for the numerical impedivity simulation in two configurations of layered model (a) in series, (b) in parallel*

To compute the transfer impedivity, a known value of voltage is assigned to the opposite parallel surfaces of a cuboid model as visualised in Fig. 3.13. Subsequently, the reaction

current values are obtained through the simulation and the complex impedivity ρ^* was calculated utilising the Ohm's low and the relationship between computed complex impedance Z^* and impedivity (Eq. 3.14):

$$\rho^* = Z^* \frac{A}{d} \tag{3.14}$$

where A is the area of the surface where the boundary conditions are applied to, d is the thickness of the model. The layered model compartments composed of homogeneous materials, and were assigned with the electrical properties of the cell structures summarised in Table 3.1, where: Mat 1 – cytoplasm, Mat 2 – cell membrane, Mat 3 – ECS. These electrical properties were selected in order to verify the applicability of the chosen software to simulate the electrical behaviour of biological materials. The analytical solution has been calculated according to the selected number of material layers and boundary conditions type, using the Eq. 1.4-1.9 from Chapter 1. Fig. 3.14 shows the qualitative comparison between the computed and analytical impedivity results for a few simple layered geometries.

As seen in Fig. 3.14, there is a good agreement in the results in all studied cases, which indicates that the solver is providing computational results that correspond well to these obtained analytically. Results at each frequency were compared quantitatively, and errors under 0.5% were observed which is considered as negligible. This means that the chosen FE solver with the quasistatic time-harmonic electric simulation is suitable to predict the frequency-dependant behaviour of biological structures, which material properties were assigned to the simplified models for verification purposes. Moreover, this provides the confidence that the selected commercial solver is capable to model the electrical characteristics of tissues in the β dispersion region.

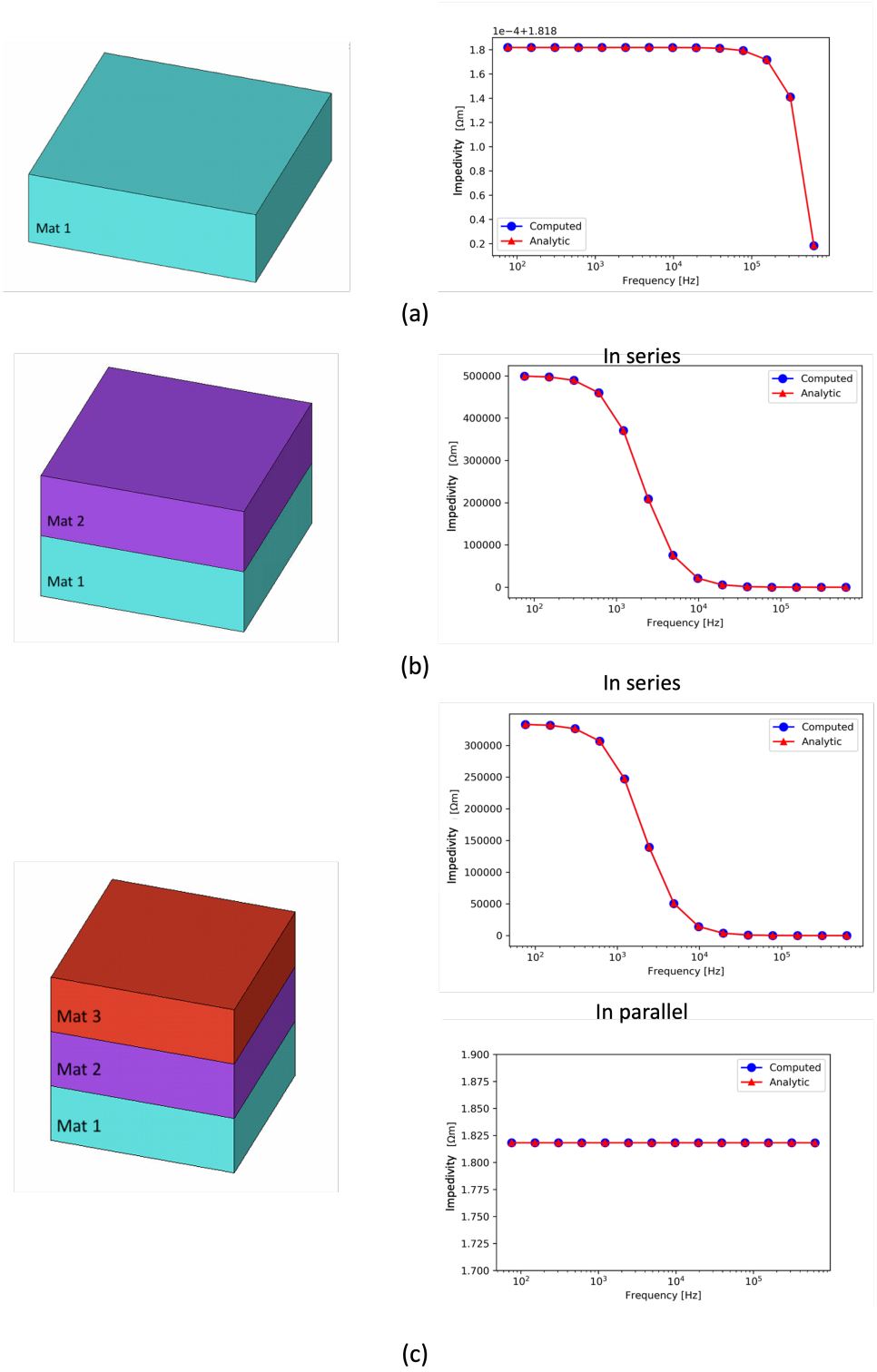

Figure 3.14: *A summary of the verification study of the computed and analytic impedivity results comparison. Mat1, Mat2, Mat3 refer to materials from Table 3.1 and represent cytoplasm, cell membrane, and ECS respectively comparing models with: (a) one, (b) two and (c) three layers*

3.3.2 Microscale results verification

Due to the lack of available experimental cell impedance data to validate the microscale model, the transfer impedance simulation results had to be verified differently. To achieve this, the simulation results were compared against the simple analytical calculation through the Eq. 1.1-1.7 from Chapter 1. To further simplify the verification process, uniform material properties of purely resistive material were assigned to all the compartments of the cell, with conductivity σ of 1 Sm^{-1} and without any dielectric properties (the relative permittivity ε_r set to 0). With this approach the model could have been treated as a simple cuboid geometry in the analytic calculation.

The results of a verification study with pure resistor properties assigned to the model should be characterised with: (i) the impedivity values remaining constant with the increasing frequency and (ii) for a well refined mesh, the error between the analytic and computed results should be smaller than the chosen error criterium (0.5% for models developed for this study). Both requirements were satisfied by the refined microscale model comprising 10,575 elements as visualised in Fig. 3.15. The mesh refinement of the microscale compartments is summarised in Appendix B Fig. B1.

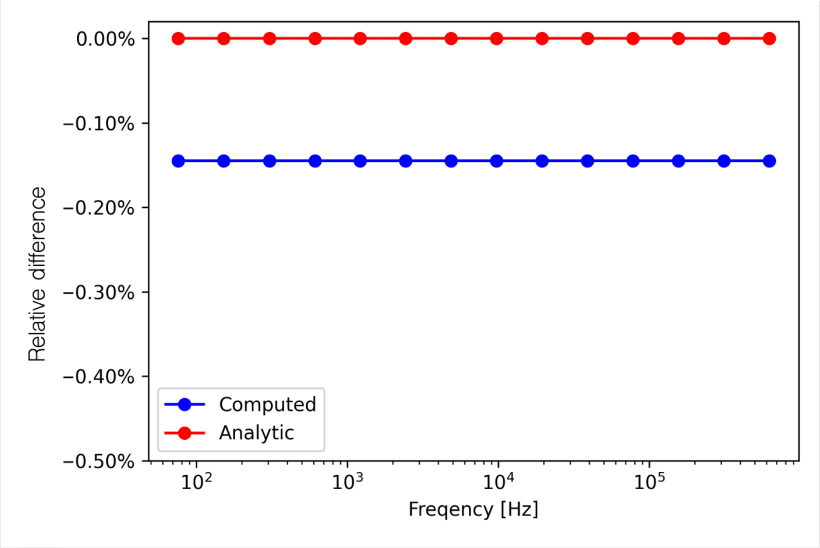

Figure 3.15: *Microscale level model mesh verification against the analytic calculation, where the relative difference between the computed and analytic impedivity showing the numerical error below 0.5%*

The reasons for the deviation between the analytical and numerical results arises from the interpolation of the results which are calculated at discrete points (nodes) in the domain. The numerical error can be minimised by increasing the number of nodes (increasing the mesh density) or by choosing higher-order shape functions which are used in the results

interpolation. It is also worth pointing out that this difference will never achieve zero which is associated with the precision of the machine used for the computational calculation and the resulting rounding error [36].

3.3.3 Mesoscale results verification

The thyroid mesoscale model underwent a similar verification process introduced for the microscale model due to the inaccessibility of experimental impedance data for a single or a group of follicles. At this stage of multiscale modelling, transfer impedivity data obtained through a simulation with uniform resistive material properties was verified against the analytical calculation. Fig. 3.16 shows that the results from the final refined mesoscale model with the mesh comprising 15,075 elements, are within the error threshold of 0.5% difference from the analytical solution which ensures the reliability of the constructed mesh. The mesh refinement of the mesoscale compartments is summarised in Appendix B Fig. B2.

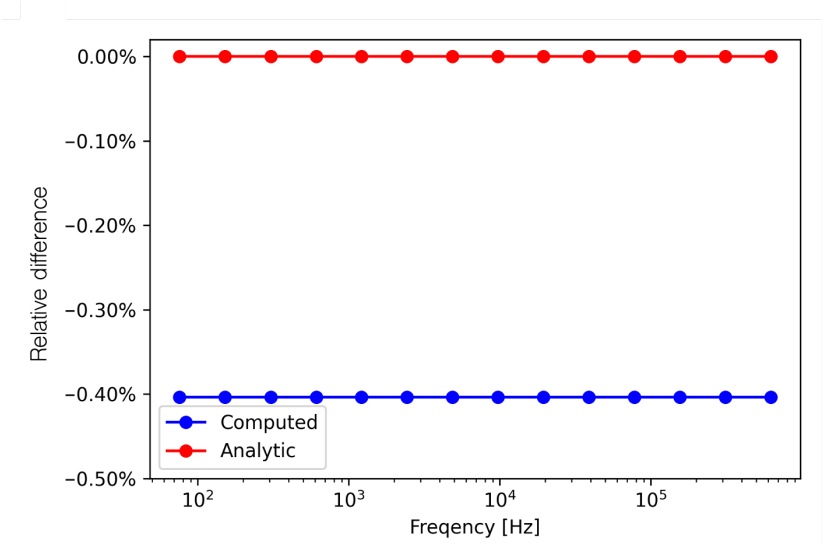

Figure 3.16: *Mesoscale level model mesh verification against the analytic calculation, where the relative difference between the computed and analytic impedivity showing the numerical error below 0.5%*

3.3.4 Macroscale model verification

The size of the macroscale model has been determined through a process of expanding its length in each direction until the effects of the model boundaries had no effect on the simulated impedance results, e.g. the increase in the size and the element number did not differ the impedance by over 0.5% compared to the previous setting (summarised in Appendix B, Fig. B4).

In the refinement process, the mesh density was maintained at its greatest level around the tetrapolar electrodes, as the element size and the density gradually decreased further from the model centre. The most impactful geometrical parameter on the computed impedance results uncertainty was the model depth, and as illustrated in Fig. 3.17, the impedance results converge around the model depth of 15 mm based on the thyroid model results. The refinement of other regions of the model (the number of elements along the long edges in x, y, and z direction, around the electrodes, as well as the element growth factor, were less impactful and mostly showed variations in the results in the order of 0.1% (Appendix B, Fig. B4). The default macroscale level consists of 91,504 and 137,700 elements for thyroid and parathyroid tissues respectively.

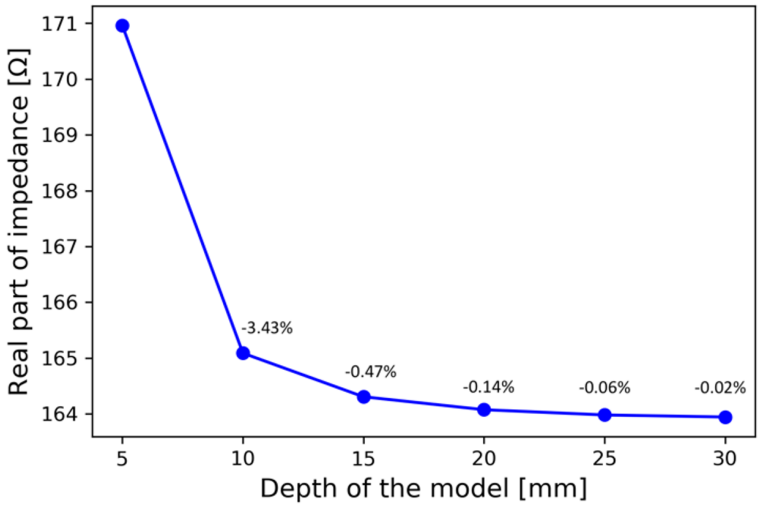

Figure 3.17: *The convergence of the real part of impedance depending on the depth of the macroscale model geometry*

3.4 Reference thyroid and parathyroid impedance spectra

3.4.1 Reference model parameters

For reference purposes, the multiscale modelling pipeline presented ealier in this Chapter was utilised to simulate and compare an initial set of computed macroscale impedance curves with both thyroid and parathyroid models assigned with the default geometrical and material properties. These parameters are summarised in Table 3.7. The model input characteristics for this set of simulations was decided based on the selected mean values documented in the literature or estimated. For example, as introduced earlier, the ECS thickness was estimated based on the values documented for cervical epithelium and electron emission microscopy

Parameter [unit]	Thyroid	Parathyroid
Microscale		
$cell_x$ [µm]	8.5	8.5
$cell_y$ [µm]	8.5	8.5
$cell_z$ [µm]	8.5	8.5
d_{ECS} [µm]	0.3	0.5
Mesoscale		
$d_{follicle}$ [µm]	100	n/a
d_{ct} [µm]	1	n/a
$\sigma_{colloid}$ [Sm^{-1}]	0.55	n/a
$\varepsilon r_{colloid}$ [-]	150	n/a
σ_{ct} [Sm^{-1}]	0.35	n/a
εr_{ct} [-]	1e5	n/a
Macroscale		
d_{para} [mm]	n/a	5

Table 3.7: *The default model parameters utilised for the reference thyroid and parathyoid simulations, where: $cell_x$, $cell_y$, $cell_z$ - cell dimensions, d_{ECS} - ECS thickness, $d_{follicle}$ - follicle size, d_{ct} - follicular connective tissue thickness, $\sigma_{colloid}$ - conductivity of colloid, $\varepsilon r_{colloid}$ - relative permittivity of colloid, σ_{ct} - conductivity of follicular connective tissue, εr_{ct} - relative permittivity of follicular connective tissue, d_{para} - size of the parathyroid gland*

images of dromedary camel parathyroid gland found in the literature [95]. Neither of the reference macroscale models contained a layer of superficial fascia layer.

3.4.2 Reference results

The frequency-dependent reference impedance spectra obtained for thyroid and parathyroid tissues with the nominal values of geometrical and electrical parameters presented in Table 3.7 are displayed in Fig. 3.18. These results suggest that it is expected to observe higher impedance across all frequencies for the parathyroid compared to thyroid when both models are at their default configuration of properties. According to the results, the parathyroid's impedance values are approximately 95% and 37% higher than the thyroid's impedance at 76 Hz and 625 kHz respectively. Moreover, these reference results are in qualitative agreement with the *in vivo* results acquired and published by Hillary et al. [3], which will be addressed and discussed in more detail in Chapter 5. The results presented in Fig. 3.18 are reference curves used for comparison with the results presented in the following result chapters.

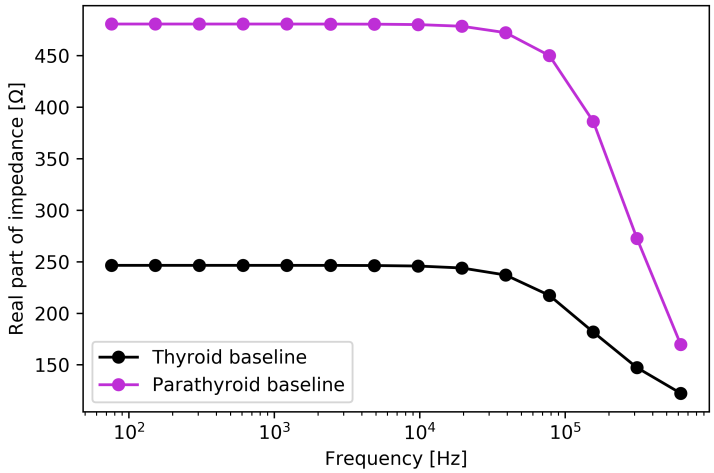

Figure 3.18: *Comparison between the reference thyroid and parathyroid computed spectra with both models assigned to the default values of the input parameters*

3.5 Computational resources

The multiscale model simulations were performed using Ansys Mechanical APDL 2019 R2 using the University of Sheffield High Performance Computing cluster ShARC (Sheffield Advanced Research Computer) in Shared Memory Parallel environment. The computational time to obtain the reference 14-frequency macroscale thyroid and parathyroid spectra was 0:40h and 1:15h respectively with 3 cores and over 11 GB memory requested for the simulation. The computation time of the remaining simulations presented in this thesis depended on the ShARC node selected for the simulation, the number of nodes requested for the analysis (approximately 3-8 throughout the study) and the complexity of the mesh. Each macroscale simulation required approximately between 0:30-1:30h of computational time.

3.6 Summary

This Chapter fulfilled the RO1 to provide the methodology for multiscale finite element modelling that recreates the specific hierarchical structure of thyroid and parathyroid in order to obtain the macroscale electrical impedance spectra for these tissue types. At each level of multiscale modelling, the model setups and simulation process were described by introducing and discussing each compartment's geometrical and electrical properties, along with boundary conditions, which were used to generate the results presented in this thesis. Moreover, the solver and mesh verification studies were carried out to minimise the numerical error associated with inadequate FE mesh construction, and to ensure the reliability of the results computed by following the presented methodology. Additionally, the reference results

obtained with the default model parameters, given in Fig. 3.18, show the initial set of the results, which further confirms the feasibility of the used methodology to compute the electrical impedance spectra of thyroid and parathyroid tissue. The reference results also highlighted the initial differences between these tissues, which suggest higher parathyroid impedance in comparison to thyroid results across studied frequency range.

Chapter 4

Model sensitivity analysis

This chapter introduces the concept of different model uncertainty and sensitivity analysis approaches and explores the RO4 in order to investigate the effect of natural variability of geometrical parameters and the material properties uncertainties on the computed impedance of thyroid and parathyroid tissues through a multiscale model sensitivity analysis using local and global approaches.

The local sensitivity study presented in this chapter formed the basis of the peer reviewed paper published in IEEE Open Journal of Engineering in Medicine and Biology, and titled: 'Multiscale Model Development of Electrical Properties of Thyroid and Parathyroid Tissues' [116].

4.1 Intoduction

4.1.1 Uncertainty and sensitivity analysis – aims

Uncertainty and sensitivity analyses methods are frequently employed in computational modelling studies in a variety of engineering fields in order to evaluate and understand the results provided by a previously developed model and to determine its limitations [117]. While uncertainty analysis is focused on quantifying the uncertainties in the model outcomes, sensitivity analysis attempts to identify the model inputs accountable for these uncertainties in the results.

In the multiscale FE thyroid and parathyroid models, whose development was shown in Chapter 3, three main sources of uncertainty can be recognised and these are associated with (i) the finite element numerical error, (ii) geometrical parameters natural variability and (iii) electrical properties uncertainties. The first source of uncertainty was addressed in the model development phase and was aimed to be minimised through appropriate geometry and mesh preparation (the mesh refinement and mesh density studies). At each level of the multiscale

modelling, the independence of the results from the constructed mesh was demonstrated by measuring the relative difference between the numerical and analytical impedance values and confirming that difference to be negligible (below 0.5%). Since the remaining sources of uncertainty have not yet been investigated, the sensitivity analyses presented in this chapter were designed primarily with the objective to investigate the effects of model input parameters relating to the geometrical parameters of the tissue structures and their electrical properties.

Firstly, as it has been observed in previous computational and clinical studies ([38; 72]), it is crucial to consider the dependence of impedance on the sizes and the organisation of the substructures in the tissue (e.g., cells or follicles in the case of thyroid tissue). Biological structures are often characterised by inter- and intrasubject variability, meaning that the differences can occur between specimens from different patients and vary depending on the location within the same tissue. Regarding thyroid and parathyroid tissues, the variation in the cell and follicle sizes (both documented in the literature and measured) have been summarised in Chapter 3. The sensitivity analysis will be performed to elucidate each geometrical parameter's impact on the resultant computed impedance and will allow a construction of a dataset visualising and quantifying the spread of the tissue impedance results exclusively associated with the natural variability of their structures. Moreover, the study presented in this Chapter will be solely focused on the tissues' geometrical characteristics, however, the organisation of the structures within the tissue and the validity of the homogenisation assumption will be explored separately in Chapter 6.

Secondly, the bulk impedance of biological materials naturally depends on the tissues capability to retain and conduct the electrical current which can be represented by electrical conductivity and relative permittivity parameter values. The range of electrical properties of the thyroid and parathyroid tissue substructures have been previously collected and discussed in the Chapter 3. Among the challenges recognised for the properties of the tissue types investigated in this thesis is the lack of documented electrical properties of thyroid and parathyroid specific materials, such as, follicular colloid, follicular loose connective tissue, or fascia layer encapsulating both glands. As discussed previously, the values estimated for these tissue structures are derived from substitutes considered to have similar properties based on comparable composition. Moreover, the electrical properties of some compartments documented in the literature lack in consistency – specifically, they are measured from different species (human, animal and other biological structures), in different conditions (temperature, humidity, DC or different AC frequencies, *in vivo* vs *in vitro*) or by using different instrumentations, previously highlighted in Chapter 2 Section 2.3.3. Furthermore, in a few instances, the range of documented material properties encompasses values across a few orders of magnitude. Such an example is the relative permittivity of tendon and dura mater acting as the substitute for fascia and follicular connective tissue, where these discrepancies are most likely associated to the differences in the structure of these tissues. Thus, sensitivity analysis will

be an effective tool to investigate directly how these inconsistencies in material properties will impact the computationally derived impedance, and the proposed models' accuracy.

A summary of the most common approaches for uncertainty and sensitivity analysis will be provided before discussing the methodology that was followed in this study.

4.1.2 Model uncertainty analysis methods

The aim of an uncertainty analysis, as mentioned before, is to determine the uncertainty of the results and to quantify the degree of confidence in the input parameters characterising the model. If the investigated model is deterministic (for a given set of input characteristics, the exact solution is derived from the model without additional effect of randomness), the uncertainty study is carried out through the repeated model evaluations by varying the chosen input parameter configurations, selected from their studied range. That variation and uncertainty in the input parameters influences the spread of the model results. The model uncertainty is presented as the distribution of the model output parameters, along with their statistical indices such as mean, median or variance.

A benchmark technique for the uncertainty analysis is the Monte Carlo (MC) simulation [118] characterised with multiple simulation runs performed using random or pseudo-random sampling of the parameter range based on previously identified probability distribution functions for each parameter. Standard MC methods require a high number of model evaluations as means to ensure the whole parameter space will be sufficiently represented in the study. That is why, with the random sampling approach, a typical MC simulation consists of a few thousands of model evaluations and this number usually varies depending on the number of input parameters associated with the model.

The Latin Hypercube Sampling (LHS) algorithm, which was firstly proposed by McKay, Conover and Beckman [119], is another sampling method belonging to the MC class, which is advantageous in terms of equal parameter space coverage with much fewer model evaluations required for the analysis. In the LHS approach, each parameter's distribution is divided into equiprobable intervals which the samples are independently chosen from. Additionally, the sampling is performed without the replacement, which means that a sample from each interval is selected only once. An example of an uncertainty study where the advantages of LHS and its comparison to the standard MC methods are investigated and further discussed is presented by Khan et al. [120].

4.1.3 Model sensitivity analysis methods

Sensitivity study usually accompanies and follows an uncertainty analysis and seeks to provide additional information on the contribution and influence that each individual parameter (and

its uncertainty) has on the range of model outcomes. Depending on the parameter space coverage considered in each study and the quantity of model evaluations required, we can distinguish between local and global methods.

4.1.3.1 Local sensitivity analysis methods

The local methods explore only a small section of the parameters' range where the parameters are varied around their reference or nominal values. A most common approach of a local sensitivity analysis is a one-at-a-time (OAT) method [117]. The principle behind this approach is to examine each input parameter separately, varying only one of them at a time. The remaining model parameters are set to their nominal values, and the model sensitivity is assessed based on selected input parameters' isolated effects on the model outputs. The examples of a local sensitivity analysis in a similar research context can be the investigation of the variations of the input parameters of a model investigating the tight junctions in the epithelial monolayer which is presented by Tervonen et al. [121] or the OAT model sensitivity study evaluating the impact of the electrical and geometrical properties of epithelial cells on the electrical impedance of cervical epithelium investigated by Walker [38].

The advantage of local methods is they usually do not require numerous model simulation runs, which is predominantly useful in initial parameter space screening. Moreover, the efficiency and low computational cost are beneficial in performing a local model sensitivity assessment which would preliminarily differentiate the influential parameters from these that are insignificant for the model results before moving onto more sophisticated global methods assessing the model sensitivity. However, it is crucial to be aware of the limitations of the local approaches and to verify the outcomes of the analysis, particularly for nonlinear models with a large number of input parameters. As discussed by Saltelli et al. [117], an investigation encompassing just a few points from the input parameter space cannot sufficiently and reliably assess the nonlinear input-output relationship. Moreover, the selective parameters range screening leaves the vast majority of the parameter space unexplored, which is additionally rising and gaining in significance with an increased number of input parameters included in the study. In these instances, it is crucial to implement global methods with adequate parameter sampling techniques in order to verify the local methods results and to broaden the understanding of the model's sensitivity.

4.1.3.2 Global sensitivity analysis methods

Global methods are a more sophisticated assessment of the model sensitivity, where the global impact of the variations of the input parameters is investigated at the same time and allows to capture the effect of the interactions between the input parameters. Global sensitivity methods usually utilise the same sampling approaches which were previously introduced for the uncertainty analysis – MC and LHS – where the LHS approach being the preferred op-

tion, due to the requirement of a smaller sample size and model evaluations.

Additionally, two categories of global model sensitivity assessment methodologies can be recognised: the correlation-based, and the variance decomposition methods [122]. The correlation-based methods determine the strength of the association between given input-output pair. For linear models, correlation measures, such as the Pearson correlation coefficient, partial correlation coefficients, and standardised regression coefficients can be recognised. For the nonlinear and monotonic models, however, more appropriate are approaches utilising Spearman rank correlation coefficient, partial rank correlation coefficient, and standardised rank correlation coefficient. The relevant sensitivity indices for correlation-based approaches take values from the range ± 1, with the values closer to +1 and -1 implying a strong linear association between an input-output pair, while values closer to 0 suggest a lack of such relationship. A comparison between the correlation-based methods is further explained in detail and visualised by assessing the sensitivity of the predator-prey Lotka-Volterra model by Marino et al. [122].

For nonlinear and non-monotonic models, the methods based on the variance decomposition are more appropriate compared to the introduced correlation approaches [122]. The golden standard in the variance decomposition sensitivity assessment is the Sobol method [123] with its sensitivity indices. In this method, the derived indices determine the contribution of each studied input parameter, and the possible interactions between them, to the model outputs variance. This is, however, a computationally demanding approach, and generally requires the number of model evaluations of order of a few thousands, depending on the chosen sampling method and number of parameters included in the study. There are reported global sensitivity studies where the Sobol indices are derived by following both the MC [124] and LHS [125] sampling methods.

The detailed methodology of calculating the Sobol indices is described by Zhang et al. [126] with the examples on the system pharmacology models. In summary, the first order Sobol indices indicate the fractional contribution of each parameter to the output variance, while the second order indices reveal the fractional contribution of the parameters' interactions. Finally, the total order indices take into account all lower order effects. The sum of all the lower order indices should take the value of 1 indicating that the whole variance of the output parameters is impacted solely by the input parameters and by the interactions between them.

Another variance-decomposition based sensitivity method worth mentioning is the Fourier amplitude sensitivity test (FAST) [127] and its extended method (eFAST) [128]. In this approach, similarly to the Sobol method, the sensitivity is assessed by varying all input parameters simultaneously and by evaluating their effects on the output variance. In the parameter sampling process, each parameter's space is assigned to a specific sinusoidal function

with a characteristic frequency, which is determined based on each parameter's range and distribution. Then, every parameter is varied according to different frequencies and the information about these parameters' samples is encoded at those frequencies. The subsequent Fourier analysis provides the information on the strength of each frequency in the model output and the parameters associated with these frequencies have the most significant effect on the model results.

4.1.4 Sensitivity analysis for multiscale models

Sensitivity analysis is more challenging when the complexity of the models expands, e.g. in the biological system models that range between different spatial and temporal scales. Since the models developed for thyroid and parathyroid tissue in this computational study are of a multiscale nature, it was crucial to review the existing methodology to approach this challenge during the sensitivity analysis. Renardy et al. [129] proposed three groups of sensitivity analysis approaches for multiscale models, and this categorisation was followed in the following summary.

The first group includes all-in-one sensitivity studies, which treats the model as a black box while investigating all of the model's parameters that belong to different scales, which is the simplest and most intuitive sensitivity analysis approach for multiscale models. Such an approach has been implemented, e.g, in a study by Possenti et al. [130] which investigates the microvascular flow including vasculature- and interstitium-related compartments. This approach requires a full multiscale model evaluation for each parameter's sample set, or evaluation of a particular part of the model, determined by the modelled hierarchy. The all-in-one approach, advantageous for its simplicity, works well with models of low complexity or with a small number of input parameters investigated. This is due to the fact that a bigger sample size and model evaluations demand a significant increase in computational resources, making this method ineffective.

The inter- and intracompartmental approach, on the contrary, aims to explore the model sensitivity separating the effects of the parameter variations within each level of a multiscale model (intercompartmental analysis) before moving into investigating the lower scale parameters' impact on the results in the higher-level scales (intracompartmental analysis). In this approach the multiscale model is no longer treated as a black box, but rather, the submodels from the various scales are considered to be independent systems interacting with one another according to the multiscale model architecture. Such an analysis provides a more thorough understanding of the investigated multiscale model compartments and their role in the entire hierarchy. An example of this approach could be the sensitivity performed on the cervical epithelium model [38], where the parameters associated with each scale (cellular and tissue scale) have been investigated separately within each scale before propagating the effects of

lower scale to the highest, tissue scale level.

In multiscale models that exhibit evident hierarchical structure with numerous compartments it is a common approach to perform the sensitivity analysis in a top-down manner. The sensitivity analysis is firstly carried out within each compartment, and their results are subsequently transferred, as now input parameters range, in the respective compartments in the higher levels. The main analysis begins with the highest level in the hierarchy and is moved down only to the significant compartments whose results had a crucial impact on the top level results. Limiting the number of compartments for evaluation and focusing solely on the submodels with the significant impact on the results in the compartment highest in the hierarchy considerably reduces the computational resources required for the analysis. The hierarchical approach for sensitivity analysis is further discussed in detail with examples on various mathematical models by Liu et al. [131].

Finally, the use of surrogate modelling (such as emulators and machine learning techniques) appears promising in cases where it is challenging to carry out a sufficient number of model evaluations for a thorough sensitivity analysis, especially by computationally demanding models like biological systems multiscale models. Surrogate models aim to mitigate computational demand by making a prediction of the model response based on previously computed results, providing additional model evaluation results with lower computational expenses. In the literature, there are examples documenting the utility of the emulators in the sensitivity analyses, such as the implementation of Gaussian process emulators to decrease the computational demands of a sensitivity analysis with the variance-decomposition method for the cardiac cell model [132] and the use of various machine learning algorithms as a surrogate model for agent based models [133].

4.2 Methodology

In this chapter, the multiscale model sensitivity will be investigated using local and global methods, in which results will be compared based on (i) the information on the model sensitivity they provide and (ii) the computational time they require. Moreover, local sensitivity analysis will be explored in the first instance as a parameter screening method, and its results will identify the parameters with their range, for inclusion in the subsequent global sensitivity analysis. The thyroid and parathyroid multiscale model impedance results are, as discussed previously, influenced by the input parameters variations which arise from the natural variability of the geometrical parameters and the uncertainties in the electrical material properties of the tissue structure. Considering the hierarchical nature of biological tissues and hence the models constructed, these two groups of input parameters are either introduced to a given compartment or transferred from the lower levels in the hierarchy.

The process of transferring the effect of input parameter variations in the hierarchy of the multiscale model for both tissue types is illustrated by a flow chart in Fig. 4.1. Geometrical input parameters and the material properties at each level originate either from the literature, histological measurements, estimation or are determined by the frequency-dependent conductivities and permittivities derived from the impedance results obtained from the lower scale submodels simulations. The thickness of the thyrocyte (y_{cell}), which defines the cell layer thickness compartment in the mesoscale of the thyroid tissue model, is, however, the only exception where the geometrical parameter is also passed from lower level and affects the dimensions of the higher-level compartment. The presented hierarchy and the input parameters are considered and addressed in the design of the local and global sensitivity studies presented in the following sections.

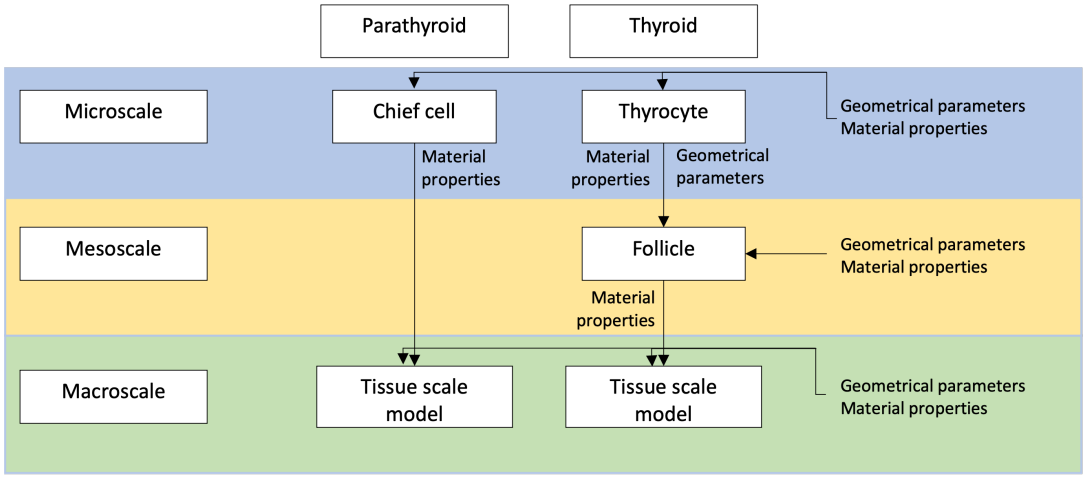

Figure 4.1: *The schematic showing the sources of the input parameters for different levels of the multiscale model for thyroid and parathyroid tissues*

4.2.1 Local sensitivity analysis

A local intercompartmental sensitivity analysis was performed in a one-at-a-time (OAT) manner to determine the isolated effects of the parameters on the macroscale scale simulation results. In the intercompartmental analysis, the studied input parameters belong to structures across different scales and their effects are propagated and evaluated at the highest scale, in this case by comparing the macroscale computed EIS spectra. For each parameter, its default value (usually the mean of values reported in the literature), minimum and maximum values have been chosen for analysis. In a few instances, more than three points have been selected to better cover the whole parameter range. For each input parameter evaluation, the remaining parameters are fixed to their reference values. The parameters' range has been decided based on the values documented in the literature and the histology measurements, which was discussed in more detail in Chapter 3 at each level of the multiscale

model development.

There are thirteen input parameters investigated for thyroid tissue (seven relating to morphological characteristics and six to electrical properties uncertainties), and eight for parathyroid (six geometrical, two electrical). In previous work by Walker [38] in electrical properties of cervical cells, the effects of the uncertainties in the material properties of the cell compartments have been investigated, hence, were excluded from this study and remained constant throughout all simulations along with the cell membrane thickness (8 nm). Tables 4.1 and 4.2 provide a full list of the parameters and their values considered in the local sensitivity study for both thyroid and parathyroid tissues with the reference values marked in bold.

4.2.2 Global sensitivity analysis

4.2.2.1 Study design

In the process of designing the global sensitivity study and choosing the appropriate methodology, it was important to consider a few factors: (i) the computational expense associated with a given method and (ii) the model nonlinearity. As highlighted in the Introduction (Section 4.1 Chapter 4), the variance-based sensitivity analysis, such as the Sobol method, is considered as a benchmark approach for complex nonlinear models. However, this method requires a high number of model evaluations, which is of the order of few thousands for a MC simulation and a few hundred to a few thousands for LHS. Since the proposed multiscale modelling pipeline for both glands is considered to be computationally demanding (depending on the model configurations, one full 14-frequency multiscale model simulation takes approximately 0:30-1:30h using the university High Performance Computing platform), the alternative global sensitivity method was selected in order to diminish the number of required model evaluations.

An initial exploration of the Sobol method has proven that <150 model evaluations are not sufficient for a correct calculation of the sensitivity indices. The obtained indices sum differed from 1, and a few of the calculated indices acquired negative values, which are indicators for an insufficient sample size. In contrast, a complete sensitivity analysis using the Sobol method would take longer than a month to complete for a single gland alone (with the assumption that 1000 simulation runs lasting one hour each), which is computationally intractable. For this reason, correlation-based approaches were considered to be more appropriate instead. In particular, the correlation-based Partial Rank Correlation Coefficient technique has been selected for this global sensitivity to address the model's nonlinearity and its methodology will be covered in more detail in the following sections.

To further decrease the computational expenses and the number of simulation runs, the Latin Hypercube Sampling method has been utilised, which will be described in detail in

the following section. Moreover, the decision to investigate two groups of input parameters (geometrical and electrical) separately resulted in a further decrease in the sample size for the global sensitivity analysis. The parameters division has also an additional advantage, as it can address two fundamentally different research question: first, highlighting the effects of the natural geometrical variability of the tissue structures on the observed electrical behaviour, and the other specifying the variability resulting from the lack of sufficient experimental data on the electrical properties of biological materials.

The model parameters selected for the global sensitivity study along with their range and distribution are summarised in Tables 4.3 to 4.6 and are divided by gland and the parameter group investigated. In a few instances, the range of the parameters shown below were also based on the local sensitivity outcomes, in particular, for the relative permittivity of fascia and follicular connective tissue. The initial local sensitivity analysis parameter screening also contributed to the reduction of the number of parameters for the global study, e.g. due to negligible variation of the obtained results. On this basis, it was decided to exclude the z_{cell} (cell size in the z direction) and $\varepsilon r_{colloid}$ (relative permittivity of colloid) parameters from the scope of the global sensitivity analysis.

Moreover, to further explore the effects of the superficial fascia layer on the results, the geometrical parameter sensitivity analysis has been performed twice for each gland: one including and one excluding this superficial compartment. In summary, the global sensitivity analysis comprises six separate substudies, where, for each gland, three sets of model evaluations have been performed and these are (i) geometrical parameters including fascia compartment, (ii) geometrical parameters excluding fascia compartment, (iii) electrical material properties (including the fascia compartment to study its electrical properties).

Finally, the organisation and hierarchy of the multiscale models (as shown in Fig. 4.1) permits the assessment of the impact of the input variations in an inter- and intracompartmental analysis, which will be the preferred approach for this global sensitivity analysis. Firstly, the intercompartmental analysis considers each parameter's influence on the calculated transfer impedivities at a given lower-scale level. Following this, it is possible to estimate how this effect is propagated in the multiscale model's hierarchy and how is affecting the results the macroscale, which is the main interest of this computational project. Utilising the inter- and intercompartmental approach will provide a more comprehensive understanding of the relevance of each level's properties on the bulk electrical behaviour of both tissues.

Description	Parameter [unit]	Values	Reference
Thyroid: geometrical parameters			
Microscale			
Cell length	x_{cell} [µm]	[6.5, **8.5**, 11.0]	[91; 92] + measurements*
Cell height	y_{cell} [µm]	[6.5, **8.5**, 11.0]	[91; 92] + measurements*
Cell width	z_{cell} [µm]	[6.5, **8.5**, 11.0]	[91; 92] + measurements*
Extracellular space thickness	d_{ECS} [µm]	[**0.3**, 0.5, 0.8]	Estimated from cervical epithelium measurements* [38; 95]
Mesoscale			
Follicle diameter	$d_{follicle}$ [µm]	[50, **100**, 150, 200]	[96] + measurements*
Connective tissue thickness	d_{ct} [µm]	[**1.0**, 2.5, 5.0]	Estimated
Macroscale			
Fascia thickness	d_{fascia} [mm]	[**0.00**, 0.10, 0.25, 0.50, 1.00]	Estimated
Thyroid: material properties			
Mesoscale			
Colloid conductivity	$\sigma_{colloid}$ [Sm^{-1}]	[0.25, **0.55**, 0.82, 1.48]	Table 3.5
Colloid relative permittivity	$\varepsilon r_{colloid}$ [-]	[50, 70, 87, **150**]	Table 3.5
Connective tissue conductivity	σ_{ct} [Sm^{-1}]	[0.03, **0.35**, 0.67]	Table 3.6
Connective tissue relative permittivity	εr_{ct} [-]	[1.5e4, **1e5**, 1e6, 1e7, 5e7]	Table 3.6
Macroscale			
Fascia conductivity	σ_{fascia} [Sm^{-1}]	[0.03, **0.35**, 0.67]	Table 3.6
Fascia relative permittivity	εr_{fascia} [-]	[1.5e4, **1e5**, 1e6, 1e7, 5e7]	Table 3.6

Table 4.1: *Parameters' values investigated in the one-at-a-time local sensitivity study for thyroid, * where noted the range of the parameters taken for the study was decided based on the literature values and own histological measurements discussed in section 2.1 in Chapter 3*

Description	Parameter [units]	Values	Reference
Parathyroid: geometrical parameters			
Microscale			
Cell length	x_{cell} [µm]	[6.0, **8.5**, 13.0]	[93] + measurements*
Cell hight	y_{cell} [µm]	[6.0, **8.5**, 13.0]	[93] + measurements*
Cell width	z_{cell} [µm]	[6.0, **8.5**, 13.0]	[93] + measurements*
Extracellular space thickness	d_{ECS} [µm]	[0.3, **0.5**, 0.8]	Estimated from cervical epithelium measurements* [38; 95]
Macroscale			
Fascia thickness	d_{fascia} [mm]	[**0.00**, 0.10, 0.25, 0.50]	Estimated
Parathyroid diameter	d_{para} [mm]	[3, **5**, 7]	[7]
Parathyroid: material properties			
Macroscale			
Fascia conductivity	σ_{fascia} [Sm^{-1}]	[0.03, **0.35**, 0.67]	Table 3.6
Fascia relative permittivity	εr_{fascia} [-]	[1.5e4, **1e5**, 1e6, 1e7]	Table 3.6

Table 4.2: *Parameters' values investigated in the one-at-a-time local sensitivity study for parathyroid, * where noted the range of the parameters taken for the study was decided based on the literature values and own histological measurements discussed in section 2.1 in Chapter 3*

Parameter [unit]	Distribution	Distribution indices	Value	Reference
		Microscale		
$cell_x$ [µm]	Normal	Mean	8.53 µm	Histology measurements
		Standard deviation	1.84 µm	(Chapter 3)
$cell_y$ [µm]	Normal	Mean	8.53 µm	Histology measurements
		Standard deviation	1.84 µm	(Chapter 3)
d_{ECS} [µm]	Uniform	Min	0.1 µm	Initial local sensitivity results and estimated from cervical epithelium measurements [38; 95]
		Max	0.5 µm	
		Mesoscale		
$d_{follicle}$ [µm]	Normal	Mean	113.77 µm	Histology measurements
		Standard deviation	63.13 µm	(Chapter 3)
d_{ct} [µm]	Uniform	Min	0.8 µm	Estimated
		Max	2.5 µm	
		Macroscale		
d_{fascia} [mm]	Uniform	Min	0.025 mm	Estimated
		Max	0.5 mm	

Table 4.3: *Thyroid tissue model input geometrical parameters and their probability distribution information*

Parameter	Distribution	Distribution indices	Value	Reference
		Mesoscale		
$\sigma_{colloid}$ [Sm^{-1}]	Uniform	Min	0.44 Sm^{-1}	Estimated based on
		Max	1.00 Sm^{-1}	previous simulation results
σ_{ct} [Sm^{-1}]	Uniform	Min	0.10 Sm^{-1}	Estimated based on
		Max	0.67 Sm^{-1}	previous simulation results
εr_{ct} [-]	Uniform	Min	1.5e4	Estimated based on
		Max	1e6	previous simulation results
		Macroscale		
σ_{fascia} [Sm^{-1}]	Uniform	Min	0.10 Sm^{-1}	Estimated based on
		Max	0.67 Sm^{-1}	previous simulation results
εr_{fascia} [-]	Uniform	Min	1.5e4	Estimated based on
		Max	1.0e6	previous simulation results

Table 4.4: *Thyroid tissue model input electrical parameters and their probability distribution information*

Parameter	Distribution	Distribution indices	Value	Reference
		Microscale		
$cell_x$ [µm]	Normal	Mean	7.59 µm	Histology measurements
		Standard deviation	1.45 µm	(Chapter 3)
$cell_y$ [µm]	Normal	Mean	7.59 µm	Histology measurements
		Standard deviation	1.45 µm	(Chapter 3)
d_{ECS} [µm]	Uniform	Min	0.4 µm	Estimated based on previous simulation results and on cervical epithelium measurements [38; 95]
		Max	0.9 µm	
		Macroscale		
d_{fascia} [mm]	Uniform	Min	0.025 mm	Estimated
		Max	0.500 mm	
d_{para} [mm]	Uniform	Min	3 mm	Estimated based on literature [7]
		Max	8 mm	

Table 4.5: *Parathyroid tissue model input geometrical parameters and their probability distribution information*

Macroscale				
σ_{fascia} [Sm^{-1}]	Uniform	Min	0.10 Sm^{-1}	Estimated based on
		Max	0.67 Sm^{-1}	previous simulation results
εr_{fascia} [-]	Uniform	Min	1.5e4	Estimated based on
		Max	1.0e6	previous simulation results

Table 4.6: *Parathyroid tissue model input electrical parameters and their probability distribution information*

4.2.2.2 Latin Hypercube Sampling

As mentioned previously, the Latin Hypercube Sampling method [119] generates the samples from the parameters range based on their probability density function by dividing it into N (number of samples) nonoverlapping and equiprobable intervals. The example of the division of normal and uniform distributions into the equiprobable intervals is visualised in Fig. 4.2. From each interval, a sample is selected randomly without replacement, and all samples are assigned with a sampling index i from 1 to N. The sampled parameters are afterward paired together randomly with the remaining sampled parameters to create a $K \cdot N$ LHS matrix, where K represents the total number of parameters. For each of N model evaluations, the model is assigned with the *ith* sample for all K parameters and the results for each simulation run are computed and assigned with the *ith* sampling index for organisation purposes.

The parameters' range sampling was performed using the pyDEO Design for Experiments for Python open-source python package. The list of parameters included in the study with their range and the distribution indices used for the LHS are summarised in Tables 4.3 to 4.6.

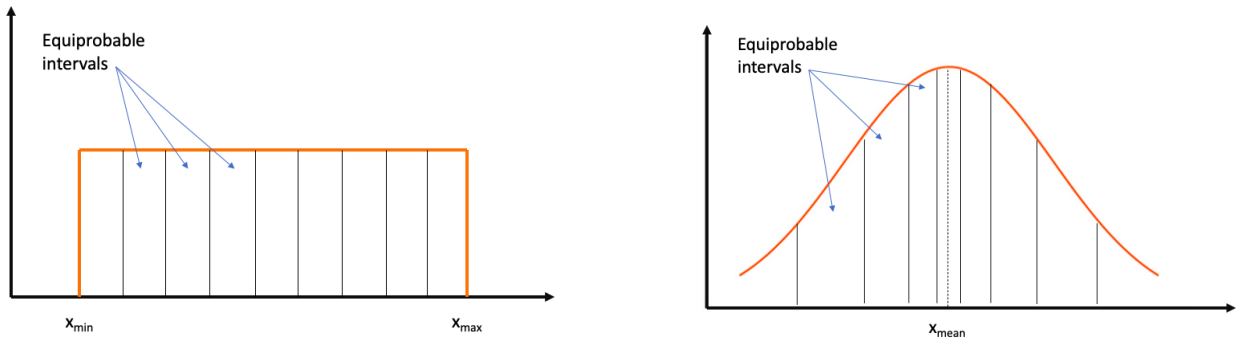

(a) **(b)**

Figure 4.2: *Equiprobable intervals for parameters with (a) uniform and (b) normal probability density functions for the Latin Hypercube Sampling*

4.2.2.3 Partial Rank Correlation Coefficient (PRCC)

The Partial Rank Correlation Coefficient method measures the strength of the linear association between a chosen input and output after the raw parameters' data is transformed into the ranking system. This approach permits the use of the correlation-based sensitivity method on the data exhibiting a nonlinear but monotonic relationship which is the case of this computational model presented in the study.

The standard correlation coefficient between kth input parameter x_k and output y is given by Eq. 4.1 [122]:

$$CC = \frac{Cov(x_k, y)}{\sqrt{Var(x_k)Var(y)}} = \frac{\sum_{i=1}^{N}(x_{ki} - \overline{x_k})(y_i - \overline{y})}{\sqrt{\sum_{i=1}^{N}(x_{ki} - \overline{x_k})^2 \sum_{i=1}^{N}(y_i - \overline{y})^2}} \tag{4.1}$$

where $Cov(x_k, y)$ – covariance between x and y, $Var(x_k)$,$Var(y)$ – variance of x_k and y respectively, N – number of samples, $\overline{x_k}$, $\overline{y}$ – mean values of x_k and y. The partial correlation coefficient (PCC) investigates the linear association between x_k and y after disregarding the linear effects of the other inputs on y. For PCC calculation, the Eq. 4.1 residuals $(x_{ki} - \overline{x_k})$ and $(y_i - \overline{y})$ are substituted with $(x_{ki} - \hat{x_k})$ and $(y_i - \hat{y})$, where $\hat{x_k}$ and $\hat{y}$ are linear regression models defined by Eq. 4.2 and 4.3:

$$\hat{x_k} = c_0 + \sum_{\substack{p=1 \\ p \neq k}}^{K} c_p x_p \tag{4.2}$$

$$\hat{y} = b_0 + \sum_{\substack{p=1 \\ p \neq k}}^{K} b_p x_p \tag{4.3}$$

where c_p and b_p – regression model coefficients, c_0 and b_0 are the constant term coefficients, K – number of input parameters.

In the PRCC correlation-based sensitivity the association between input and output parameter is calculated not on the raw data but based on their ranked-transformed equivalents. For each input and output parameter, the samples are organised from lowest to highest values and are assigned with integer ranks from 1 to N (number of samples).

The PRCC ranges from -1 to 1, with the extremities indicating the highest linear association between the investigated input-output pair, which is decreasing when the PRCC approaches zero (no linear association). Positive PRCC indicates that the output parameter increases with the increase of the input, while negative PRCC suggests the inverse input-output relationship. Based on the coefficient's range, the association strength between parameters was

divided into three groups: Low (<0.4), Medium (>0.4 and <0.7), and High (>0.7) association levels. One of these categories will be assigned to each input-output pair and PRCC will act as a sensitivity index in these global analyses.

The model evaluations are performed within two parameter groups for both tissue types and the PRCC sensitivity index is calculated for all input-output pairs at each level of thyroid and parathyroid multiscale model to explore and assess the inter- (parameters impact on the results belonging the same sublevel) and intracompartmental sensitivity (impact of the parameters belonging to different level compartments on the higher-scale results).

4.2.2.4 Sample size

In order to determine the optimal sample size, an initial convergence study has been performed on the geometrical parameters group for the thyroid tissue. The PRCC for each input-output pair was compared after performing repeated studies comprising various number of model evaluations: 30, 40, 60, 80, 100 and 150. As the results indicated, the PRCC for most of the input-output combinations did not converge, however, regardless of the sample size, the results exhibited the same level of association in each case (the PRCC were fluctuating around a value from the same range of Low, Medium or High association, as visualised in Appendix C). Therefore, it was decided to maintain the sample size at 100 samples per study.

4.2.3 Impedance spectra parameterisation – model output parameters

The resultant impedance spectra generated by simulations with each set of input parameters were evaluated qualitatively by plotting all impedance values against 14 frequencies relating to the *in vivo* measurements with the ZedScan^{TM} device. All plots presented in this chapter show the frequency-dependent real part of impedance values computed through each model evaluation.

However, for more detailed result analysis, the quantitative comparison was performed by selecting spectra indices characterising each region of the impedance curve. All simulated spectra have been parameterised by choosing three output indices: two impedance Z_1 and Z_{14} values at the first and last simulated frequency points (76 Hz and 625 kHz), relating to the impedance values before and after β dispersion, and the frequency f_{mid} at the middle of the dispersion (frequency for when impedance takes the middle value between Z_1 and Z_{14}). All three parameters have been displayed in Fig. 4.3 on an exemplary EIS curve. Both local and global sensitivity analyses have been evaluated based on the input parameters' effects on these three selected spectra indices.

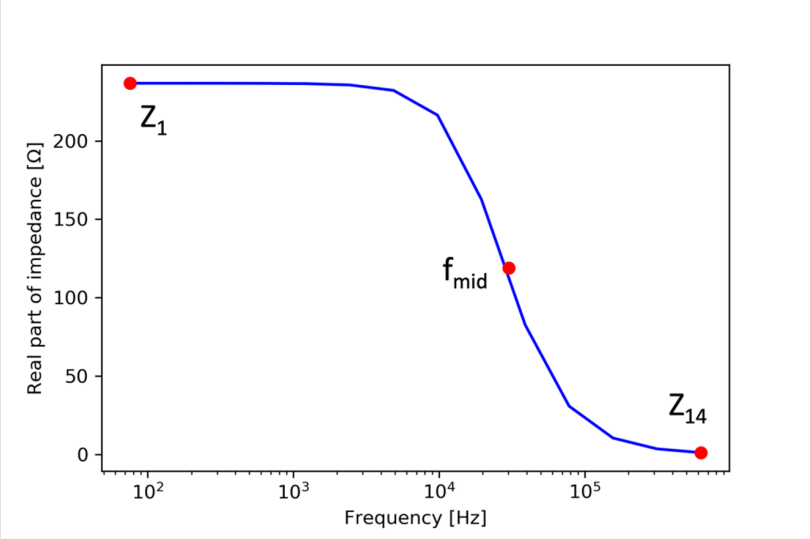

Figure 4.3: *Visualisation of three selected parameters of impedance curve, Z_1 – low frequency (76 Hz) impedance, Z_{14} – high frequency impedance (625 kHz) and f_{mid} – frequency in the middle of the β dispersion*

This spectra parameterisation was the preferred method for this study over the more established Cole parameters. Despite Cole-Cole model (Eq. 2.9 from Chapter 2) fitting being most commonly used for impedance spectra analysis, especially in the studies on biological tissues, the initial exploration of this method revealed limitations associated with the shape of the parathyroid spectra and the studied frequency range. In a few instances, the parathyroid spectra do not achieve the high-frequency plateau which resulted in underprediction of Z_∞ parameter with values generated being unrealistically close to zero. The attempt of the Cole-Cole model fitting parameterisation method and the Cole parameters comparison is further summarised in Appendix D.

4.3 Results

4.3.1 OAT local sensitivity study results

Following the implementation of the computational multiscale methodology outlined in Chapter 3, a full set of complex impedances were simulated at each frequency. However, in accordance with the commonly used data presentation for the experimental spectra, the computed results presented in this study are real impedance values at 14 frequency points in the range between 76 Hz - 625 kHz from the macroscale model simulations. For each computed spectrum, the Z_1, Z_{14}, and f_{mid} spectra indices have been specified in order to facilitate the quantitative comparison of the results. The lower-scale results for thyroid and parathyroid tissues are presented in Appendix E in a form of electrical material properties derived from

the micro- and mesoscale simulation results.

The local sensitivity study resulted in 36 and 19 computed EIS spectra where each of the input parameters was investigated in the OAT sensitivity study for thyroid and parathyroid respectively. Fig. 4.4 shows the range of the thyroid and parathyroid results with marked reference curves (Section 3.5 Chapter 3) for both glands. The results demonstrate a similar trend of higher impedance values for parathyroid tissue spectra compared to the thyroid seen in the reference curves. Nonetheless, the results ranges exhibit an overlap between the computed results that increases with the frequency.

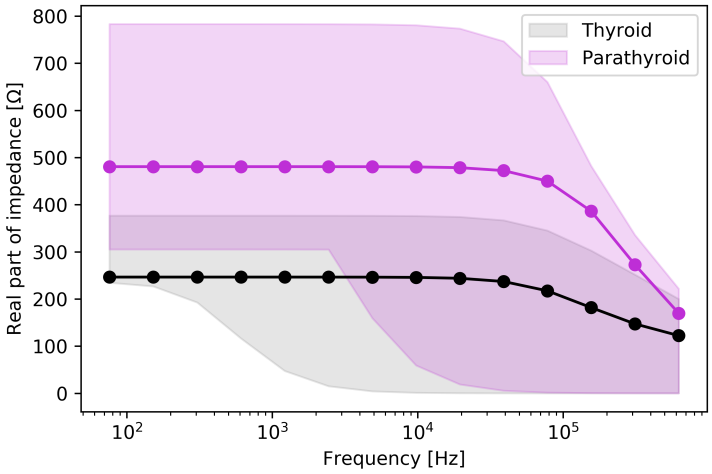

Figure 4.4: *Baseline computed impedance spectra obtained with the default input parameters for thyroid (black spectrum) and parathyroid (pink spectrum) tissues with marked range of all computed results obtained through the variation of geometrical and electrical properties summaries in Table 4.1 and 4.2*

The presentation of each simulated spectra rather than simply the baseline curves (as shown in Fig. 4.4) permits the inspection of the variation in the shape of individual spectra according to the investigated variation in the morphology and electrical properties, which is shown in Fig. 4.5a and 4.5b. A few outliers (marked with arrows) in both thyroid and parathyroid spectra represent the outcomes of the investigation of the parameter range extremities. In particular, the thyroid tissue outlier EIS curves characterised with decreased high-frequency impedance, result from high values of fascia or follicular connective tissue permittivities (εr_{fascia} and εr_{ct} >1e6). In contrast, low colloid conductivity ($\sigma_{colloid}$=0.25 Sm^{-1}) resulted in a thyroid spectrum of increased impedance in the whole frequency range. Similarly to the thyroid outcomes, high permittivity fascia values induced significant devia-

tions from the reference curve in parathyroid tissue spectra. Additionally, high values of cell dimension (x_{cell}= 13 µm) and thinnest layer of extracellular space (d_{ECS}=0.3 µm) resulted in spectra with unusually high impedance values across the frequency range. These particular outlier cases permitted the narrowing down of the parameter range in the subsequent global sensitivity.

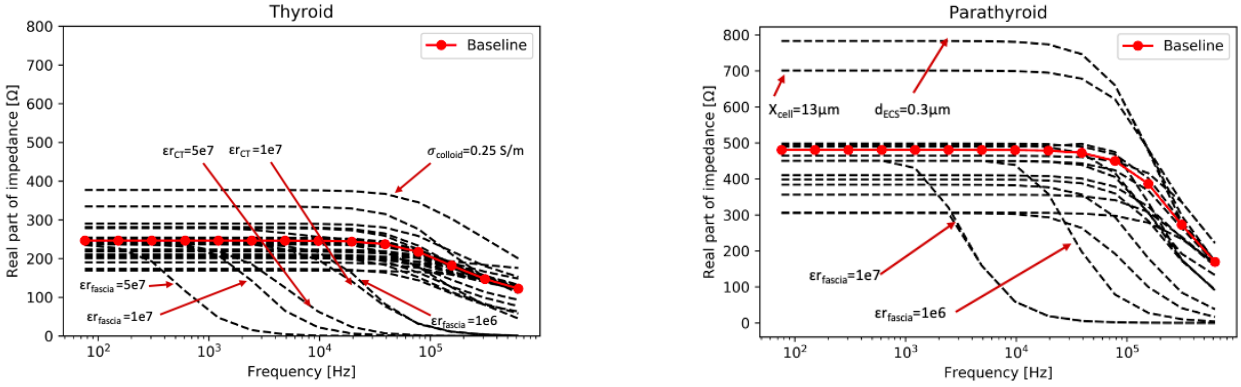

(a) **(b)**

Figure 4.5: *Qualitative comparison of impedance spectra computed for the OAT local sensitivity study with marked reference curves (red dotted curve) and outliers (red arrows) for (a) thyroid and (b) parathyroid, where: εr_{ct} – relative permittivity of follicular connective tissue, $\sigma_{colloid}$ - conductivity of colloid, εr_{fascia} – relative permittivity of fascia, x_{cell} – cell size in x direction, d_{ECS} – extracellular space thickness*

The isolated effect of each morphological and electrical input parameters on the selected EIS spectra indices (Z_1, Z_{14} and f_{mid}) is visualised in Fig. 4.6, where each bar shows the maximum and minimum percentage change from the mean result for each individual parameter.

4.3.1.1 Thyroid: geometrical parameters

As shown in Fig. 4.6a, thyroid impedance results were predominantly sensitive to changes in the size of the follicles ($d_{follicle}$) at the low frequencies (Z_1) and the thickness of the connective tissue (d_{ct}) at high frequencies (Z_{14}). The greatest differences in the middle frequency (f_{mid}) results were observed for the variations in the ECS thickness (d_{ECS}). All three spectra indices were insensitive to the changes in the cell width - dimension in the z direction (z_{cell}).

4.3.1.2 Thyroid: material properties

Fig. 4.6b shows the results for the local sensitivity analysis of the material properties of the thyroid model compartments. Among the parameters studied, the colloid conductivity

($\sigma_{colloid}$), connective tissue and fascia relative permittivities (εr_{ct} and εr_{fascia}) are these that have the most substantial impact on all three spectra indices, while the investigation of the remaining parameters resulted in less than ± 25% variation from the mean value of the spectra parameters.

4.3.1.3 Parathyroid

Fig. 4.6c shows that the ECS thickness (d_{ECS}) and cell length - size in the x direction (x_{cell}) - have the most significant influence on the low frequency impedance (Z_1). Similarly to the results from the thyroid model, the high frequency impedance (Z_{14}) is more sensitive to the changes in fascia thickness (d_{fascia}) and its permittivity (εr_{fascia}), with the middle frequency also exhibiting sensitivity to the latter (εr_{fascia}).

4.3.2 Global sensitivity study results

The global sensitivity study resulted in 600 multiscale model evaluations for both thyroid and parathyroid tissues: 100 from geometrical parameter variability investigation including a fascia compartment, 100 from geometrical parameters without the fascia compartment, and 100 from the material property uncertainties examination for each gland respectively. The parameter space sampling was performed using the LHS method taking into account the previously defined range and probability density functions for each parameter which are summarised in Tables 4.3 to 4.6. Each simulated impedance spectrum was parameterised with three indices the Z_1, Z_{14}, and f_{mid}, similar to the local sensitivity study outcomes. The input parameters and results matrices were subsequently transformed into their ranked equivalents in order to calculate the PRCC for each input and output parameters pair.

PRCCs were calculated for the results at each level of the multiscale model to assess the inter- and intracompartmental sensitivity. The visual comparison of the exemplary results showing High, Medium and Low association between a chosen input-output set is presented in Fig. 4.7 with the raw data and their rank-transformed form with the PRCC index.

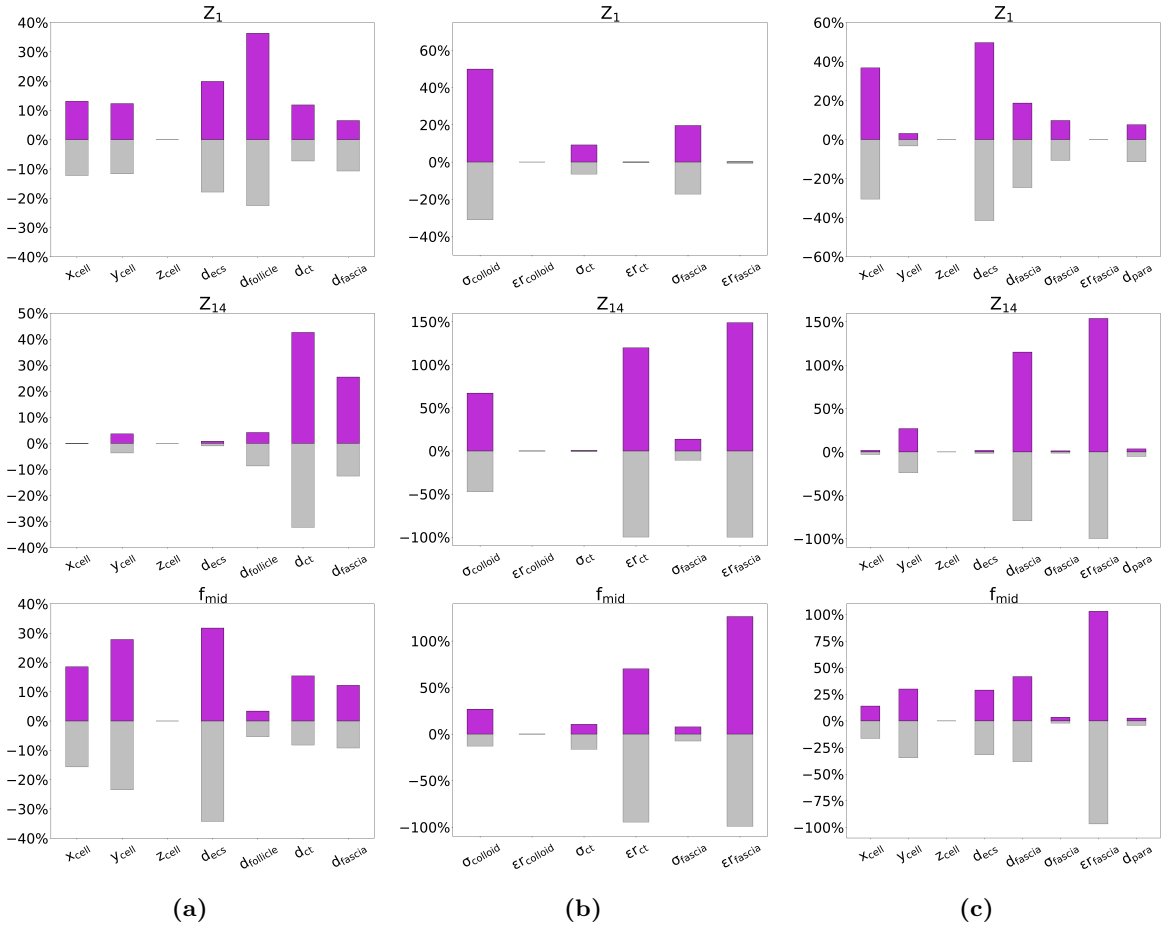

Figure 4.6: *Parameter sensitivity analysis results: (a) thyroid geometrical parameters, (b) thyroid material properties, (c) parathyroid parameters;* x_{cell}*,* y_{cell}*,* z_{cell} *- cell dimensions,* d_{ECS} *- ECS thickness,* $d_{follicle}$ *- dimensions of colloid compartment in the mesoscale model,* d_{ct} *- connective tissue thickness,* d_{fascia} *- fascia thickness,* d_{para} *- dimensions of parathyroid,* $\sigma_{colloid}$ *- conductivity of colloid,* $\varepsilon r_{colloid}$ *- relative permittivity of colloid,* σ_{ct} *- conductivity of connective tissue,* εr_{ct} *- relative permittivity of connective tissue,* σ_{fascia} *- conductivity of fascia,* εr_{fascia} *- relative permittivity of fascia*

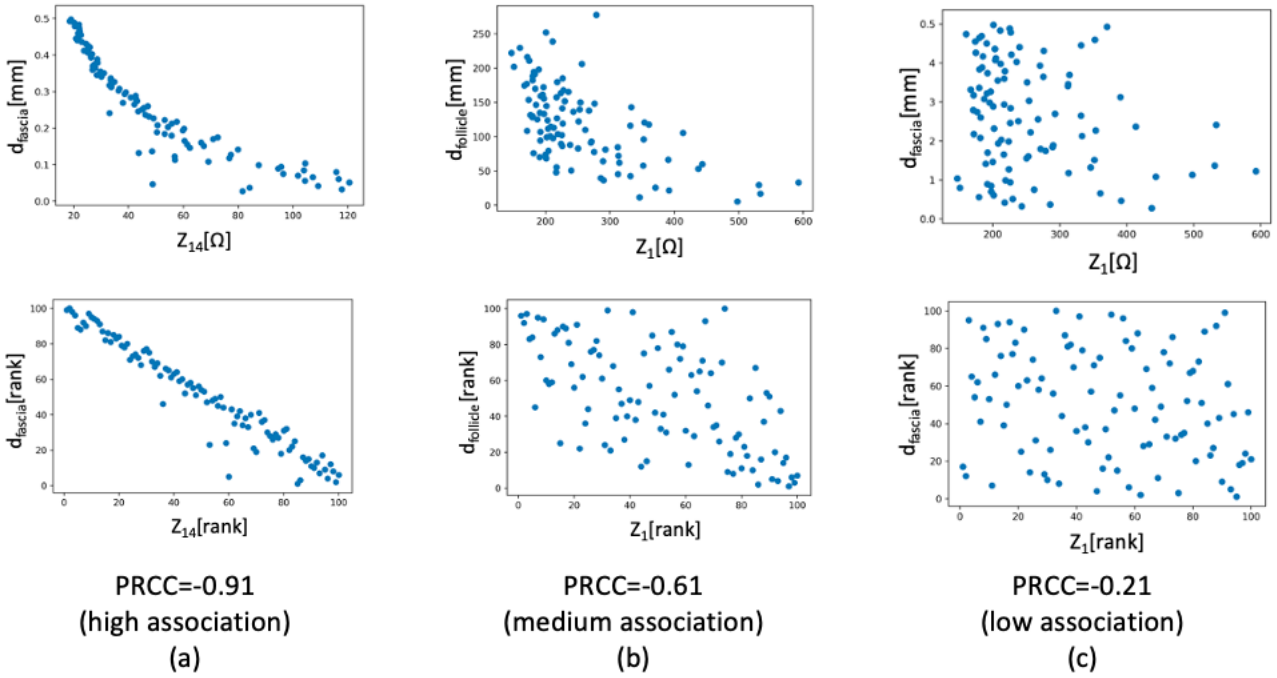

Figure 4.7: *Examples of the High, Medium and Low input-output linear association based on the PRCC of selected global sensitivity results for the thyroid tissue macroscale level showing the scatter plots of the raw (top row) and rank-transformed data (bottom row): (a) d_{fascia} and Z_{14}, (b) $d_{follicle}$ and Z_1 (c) d_{fascia} and Z_1*

Fig. 4.8 shows the impedance spectra obtained through the global sensitivity showing the spread of the results with regards to the reference curves obtained with the model default parameters (Section 3.5 Chapter 3). The qualitative comparison of the shape of the spectra reveals the wide range of the impedance results across all studied frequencies resulting from the variation of the geometrical parameters and material properties. Additionally, it is worth highlighting that the reference curves were obtained without the inclusion of any fascia compartment, which could explain the discrepancies seen Fig. 4.8 a, c, d, f between the default results and the EIS curves obtained in the global sensitivity analysis.

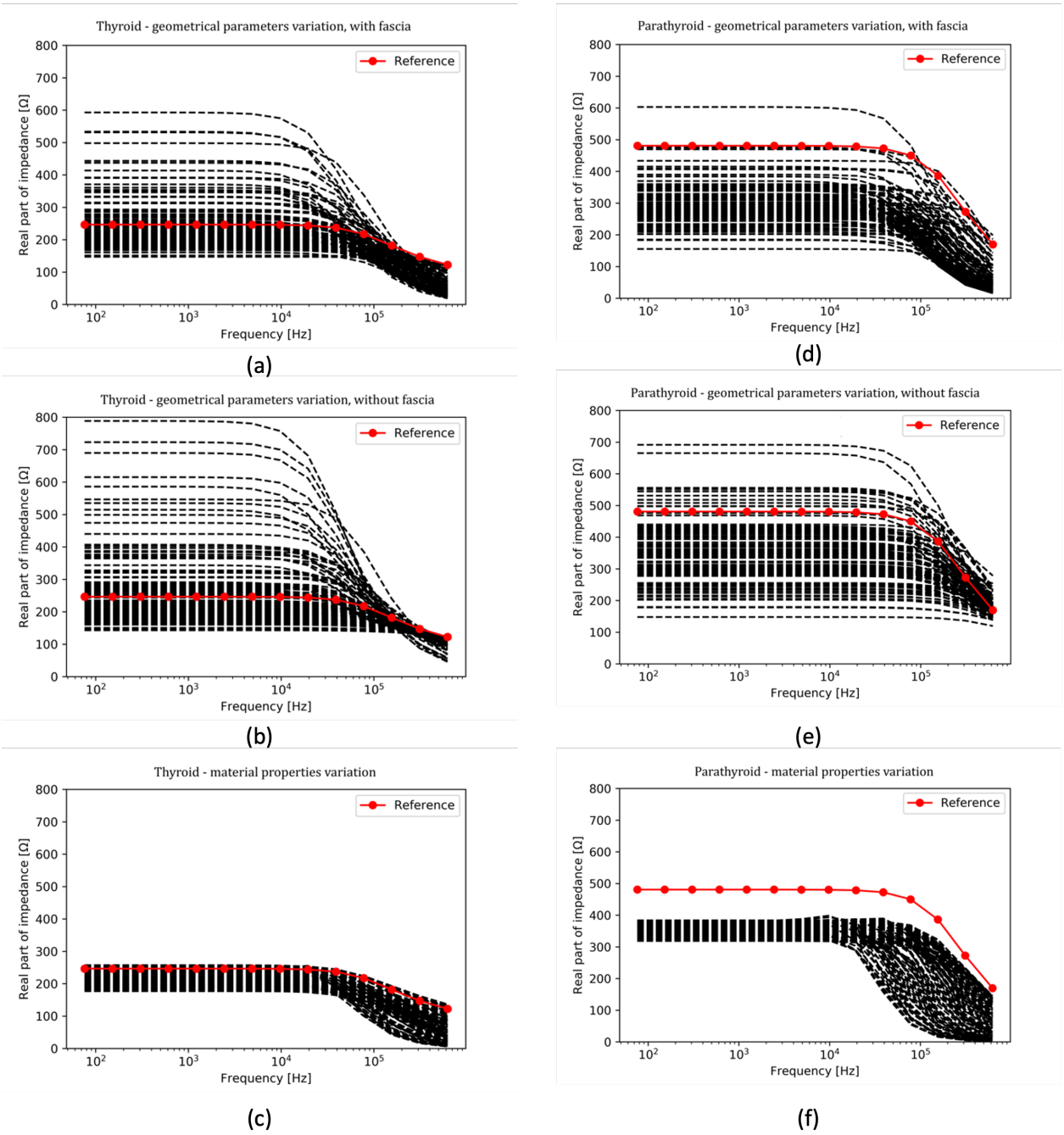

Figure 4.8: *Global sensitivity results in comparison to the reference results (red curves) for thyroid (a-c) and parathyroid (d-f) tissues: (a) and (d) show the investigation of geometrical parameters variations including fascia, (b) and (e) show the investigation of geometrical parameters variations including fascia*

The PRCC results of the global sensitivity study are presented in Tables 4.7 to 4.10 and are divided by glands and by the group of input parameters investigated. Each table comprises the inter- and intracompartmental sensitivity results, where the parameters from the intracompartmental study are marked with an asterisk. The Low, Medium, High association levels are additionally marked with green, yellow and red respectively. The PRCC indices included are characterised with the probability parameter $p<0.001$. The majority of the PRCC indices from the Low association level (PRCC <0.3) have not been included among the sensitivity study results. The negative PRCC values denote the opposite trend between input and output (increase in input parameter causes a decrease in the output values).

4.3.2.1 Thyroid: geometrical parameters

As Table 4.7 shows, cell thickness (y_{cell}) and the ECS thickness (d_{ECS}) are the most influential parameters on the microscale level results. Moreover, these parameters, especially d_{ECS}, continue to be impactful at the higher scales, e.g. showing a High association between d_{ECS} and Z_1, or a High association for d_{ECS} and Medium for y_{cell} with f_{mid} at the mesoscale. At the mesoscale, the Z_1 and Z_{14} results show Medium and High-level sensitivity to the size of the follicle ($d_{follicle}$), and also noteworthy is the Medium level association between Z_{14} and follicle connective tissue thickness (d_{ct}).

The macroscale results, mainly the high frequency impedance Z_{14} from the model evaluations including a fascia compartment, show the highest sensitivity to its thickness (d_{fascia}). Meanwhile, the low frequency impedance Z_1 is mostly correlated with the ECS thickness (d_{ECS}) and size of the follicle ($d_{follicle}$) which are parameters significantly associated with the lower scale results. Moreover, the dispersion frequency (f_{mid}) exhibits the highest association with d_{ECS}.

The results from the macroscale model simulations excluding the fascia compartment, as expected, show higher impact of the lower scale parameters compared to the results from the fascia comprising model equivalent. For the Z_{14} especially, a High association with the size of the follicle ($d_{follicle}$) can be observed, which was not considered as an influential parameter in the study including fascia. Moreover, High association can also be noted between Z_1 and input parameters such as d_{ECS} and $d_{follicle}$, and between f_{mid} and d_{ECS}.

Multiscale model level	Output parameter	Input parameter	PRCC	Association level
Microscale	Z_1	x_{cell}	0.58	Medium
		d_{ECS}	-0.86	High
	Z_{14}	y_{cell}	-0.95	High
	f_{mid}	y_{cell}	-0.58	Medium
		d_{ECS}	0.81	High
Mesoscale	Z_1	${x_{cell}}^*$	0.40	Low
		${d_{ECS}}^*$	-0.70	High
		$d_{follicle}$	-0.61	Medium
	Z_{14}	$d_{follicle}$	0.72	High
		d_{ct}	-0.60	Medium
	f_{mid}	${y_{cell}}^*$	-0.49	Medium
		${d_{ECS}}^*$	0.87	High
Macroscle (fascia)	Z_1	${d_{ECS}}^*$	-0.68	Medium
		${d_{follicle}}^*$	-0.61	Medium
		${x_{cell}}^*$	0.41	Medium
	Z_{14}	d_{fascia}	-0.97	High
	f_{mid}	${d_{ECS}}^*$	0.73	High
		${d_{follicle}}^*$	0.41	Medium
Macroscale (no fascia)	Z_1	${x_{cell}}^*$	0.39	Low
		${d_{ECS}}^*$	-0.87	High
		${d_{follicle}}^*$	-0.70	High
	Z_{14}	${d_{follicle}}^*$	0.85	High
	f_{mid}	${x_{cell}}^*$	-0.50	Medium
		${d_{ECS}}^*$	0.87	High

Table 4.7: *Global sensitivity analysis results for geometrical parameters investigation of the thyroid tissue model, * denotes the parameters from the lower-level models for the intracompartmental study investigation*

Multiscale model level	Output parameter	Input parameter	PRCC	Association level
Mesoscale	Z_1	$\sigma_{colloid}$	-0.98	High
	Z_{14}	$\sigma_{colloid}$	-0.75	High
		εr_{ct}	-0.61	Medium
	f_{mid}	$\sigma_{colloid}$	-0.58	Medium
		εr_{ct}	0.41	Low
		εr_{ct}	-0.64	Medium
Macroscale	Z_1	$\sigma_{colloid}$*	-0.97	High
	Z_{14}	εr_{fascia}	-0.85	High

Table 4.8: *Global sensitivity analysis results for electrical properties investigation of the thyroid tissue model, * denotes the parameters from the lower-level models for the intracompartmental study investigation*

4.3.2.2 Thyroid: electrical properties

The results presented in Table 4.8 provides the information on the thyroid model sensitivity to the uncertainties in electrical material properties on meso- and macroscale. On the mesoscale, the results Z_1 and Z_{14} show High, and f_{mid} - Medium association to colloid conductivity ($\sigma_{colloid}$). Both material properties characterising the follicular connective tissue (σ_{ct} and εr_{ct}) influence the Z_{14} and f_{mid} spectra parameters at Low or Medium levels. Meanwhile on the macroscale, Z_1 exhibits High level association with colloid conductivity ($\sigma_{colloid}$), and Z_{14} is the most sensitive to the changes in permittivity of fascia (εr_{fascia}) with a High level association. It is interesting to highlight, the f_{mid} spectrum parameter does not demonstrate any High nor Medium association with any of the investigated input parameters from the thyroid electrical properties group.

Multiscale model level	Output parameter	Input parameter	PRCC	Association level
Microscale	Z_1	x_{cell}	0.60	Medium
		d_{ECS}	-0.77	High
	Z_{14}	y_{cell}	-0.76	High
		d_{ECS}	-0.42	Low
		x_{cell}	0.37	Low
	f_{mid}	y_{cell}	-0.71	High
		d_{ECS}	0.54	Medium
		x_{cell}	-0.35	Low
Macroscale (fascia)	Z_1	${x_{cell}}^*$	0.49	Medium
		${d_{ECS}}^*$	-0.70	High
	Z_{14}	d_{fascia}	-0.88	High
	f_{mid}	${d_{ECS}}^*$	0.42	Medium
		${x_{cell}}^*$	-0.34	Low
		d_{fascia}	-0.77	High
Macroscale (no fascia)	Z_1	${x_{cell}}^*$	0.58	Medium
		${d_{ECS}}^*$	-0.78	High
	Z_{14}	${y_{cell}}^*$	-0.85	High
	f_{mid}	${y_{cell}}^*$	-0.65	Medium
		${d_{ECS}}^*$	0.44	Medium

Table 4.9: *Global sensitivity analysis results for geometrical parameters investigation of the parathyroid tissue model, * denotes the parameters from the lower-level models for the intracompartmental study investigation*

Multiscale model level	Output parameter	Input parameter	PRCC	Association level
Macroscale	Z_1	σ_{fascia}	-1.0	High
	Z_{14}	εr_{fascia}	-1.0	High
	f_{mid}	εr_{fascia}	-0.99	High

Table 4.10: *Global sensitivity analysis results for electrical properties investigation of the parathyroid tissue model, * denotes the parameters from the lower-level models for the intracompartmental study investigation*

4.3.2.3 Parathyroid: geometrical parameters

At the microscale of the parathyroid multiscale model, the impedance spectra indices are mostly sensitive to the y_{cell} and d_{ECS} in the geometrical parameters investigation (Table 4.9), which is comparable to the outcomes presented for the thyroid tissue model. This situation was anticipated by considering the similarities between the compartment structures of both microscale models.

In the parathyroid macroscale model including the superficial fascia layer, this compartment continues to be an influential parameter displaying a High association with the Z_{14} and f_{mid} spectra indices. Moreover, d_{ECS} remains an important parameter at the macroscale, showing a High and Medium association with Z_1 and f_{mid} spectra indices respectively. Additionally, it is worth mentioning that the cell length (x_{cell}) exhibits Medium association with both micro- and macroscale low frequency impedance Z_1.

The results computed using the macroscale model without the inclusion of fascia reveal that y_{cell} and d_{ECS} have stronger association to the Z_1 and Z_{14} parameters, compared to the parathyroid results from the simulation including the superficial layer. Moreover, the f_{mid} index is also impacted by these two parameters, where the PRCC suggests a Medium association.

4.3.2.4 Parathyroid: electrical properties

Only two input parameters have been investigated in the parathyroid electrical properties group (Table 4.10), and these two parameters exhibit a High association with all the impedance spectra indices: fascia conductivity (σ_{fascia}) with low frequency impedance (Z_1), and fascia permittivity (εr_{fascia}) with high frequency impedance (Z_{14}) and middle frequency (f_{mid}).

4.3.2.5 Comparison of the local and global sensitivity study results

Tables 4.11 and 4.12 summarise the key model parameters identified through the local and global sensitivity studies to have the highest impact on the selected spectra indices. Both study outcomes revealed a similar group of the parameters, which are: ECS thickness (d_{ECS}), cell size (x_{cell} and y_{cell}), and fascia thickness (d_{fascia}) with its electrical material properties (σ_{fascia} and εr_{fascia}) for both tissue types, and the size of the follcile ($d_{follicle}$) and the conductivity of colloid ($\sigma_{colloid}$) for thyroid tissue only. Nonetheless, the local sensitivity study appointed a few additional parameters that have not been among key parameters in the global sensitivity results. These are, for example, fascia conductivity (σ_{fascia}) and its thickness (d_{fascia}) with regards to the impact on low frequency impedance for thyroid and parathyroid respectively.

Output parameter	Significant input parameter
Thyroid	
Z_1	$\sigma_{colloid}$, $d_{follicle}$, d_{ECS}, σ_{fascia}
Z_{14}	εr_{fascia}, εr_{ct}, d_{ct}, $\sigma_{colloid}$, d_{fascia}
f_{mid}	εr_{fascia}, εr_{ct}, d_{ECS}, y_{cell}
Parathyroid	
Z_1	d_{ECS}, x_{cell}, d_{fascia}
Z_{14}	εr_{fascia}, d_{fascia}, y_{cell}
f_{mid}	εr_{fascia}, d_{fascia}, d_{ECS}, y_{cell}

Table 4.11: *Parameters significant for the changes in the output parameters for each gland as identified from the local sensitivity study in the order from showing the highest to lowest variation from the mean value*

Output parameter	Significant input parameter	
Thyroid: geometrical parameters		
	Fascia study	No-fascia study
Z_1	d_{ECS}, $d_{follicle}$, x_{cell}	d_{ECS}, $d_{follicle}$, x_{cell}
Z_{14}	d_{fascia}	$d_{follicle}$
f_{mid}	d_{ECS}, $d_{follicle}$	d_{ECS}, x_{cell}
Thyroid: material properties		
Z_1	$\sigma_{colloid}$	
Z_{14}	εr_{fascia}	
f_{mid}	-	
Parathyroid: geometrical parameters		
	Fascia study	No-fascia study
Z_1	d_{ECS}, x_{cell}	d_{ECS}, x_{cell}
Z_{14}	d_{fascia}	y_{cell}
f_{mid}	d_{fascia} , d_{ECS}, x_{cell}	y_{cell} , d_{ECS}
Parathyroid: material properties		
Z_1	σ_{fascia}	
Z_{14}	εr_{fascia}	
f_{mid}	εr_{fascia}	

Table 4.12: *Parameters significant for the changes in the output parameters for each gland as resulted from the global sensitivity study in the order from highest to lowest level of linear association*

4.4 Discussion

The presented sensitivity analysis aimed to investigate the impact of the characteristic features of thyroid and parathyroid tissue on the electrical behaviour of both tissue types across multiple spatial scales. The main objective was to explore the multiscale models' sensitivity to the variation of the geometrical properties of tissue structures related to the natural inter- and intrasubject variability, and the electrical material properties uncertainties associated with the lack of sufficient experimentally derived data. The model sensitivity has been evaluated using two separate methods by comparing the local and global approach.

4.4.1 Local sensitivity analysis – key findings

The range of all results computed for the OAT local sensitivity analysis is presented in Fig. 4.5 against the reference thyroid and parathyroid impedance spectra. Despite a distinct separation initially observed for the reference impedance curves (Section 3.5 Chapter 3), there is an overlap in the computed spectra across the whole studied frequency range resulting from the variations of numerous input parameters. Nonetheless, as seen in Fig. 4.5, most of the computed curves are in close proximity to the reference results for both glands. A few outliers mostly characterised with a low high-frequency impedance are the outcome of the examination of connective tissue and fascia permittivities, and do not represent the trend of the remaining results. The high values of permittivity (>1e6) assigned in those instances correspond to the values reported for tendon, which, despite its high collagen composition, is characterised with a much denser and highly organised structure of these fibres in comparison to fascia or thyroid connective tissue. Thus, these high permittivity values were subsequently excluded from the following global sensitivity analysis.

The OAT local sensitivity analysis approach is a blunt tool for assessing parameter sensitivity, with more sophisticated global parameter sensitivity analyses being the gold standard [117], especially for nonlinear models. However, given the long computational runtimes of the multiscale model (up to 5 min per frequency for the parathyroid macroscale model, giving >1h of computational time to obtain each 14-point impedance curve), the OAT method provides a convenient screening tool for the effect of individual parameters within a reasonable range and, despite covering only a fraction of the parameter space, has already highlighted significant and non-significant parameters for both tissues with less than 60 model evaluations for both glands combined. The parameters that have been considered significant are responsible for over 20% variation from the mean spectra parameters for each parameter.

To summarise, the most influential geometric parameters on the macroscale simulation results recognised by the local sensitivity study are size of the follicle ($d_{follicle}$), ECS thickness (d_{ECS}), follicular connective tissue (d_{ct}) and cell thickness (y_{cell}) for thyroid tissue, and ECS

thickness (d_{ECS}), cell dimensions (x_{cell}, y_{cell}) and fascia thickness (d_{fascia}) for parathyroid. Furthermore, the results demonstrated that all three spectra indices are insensitive to variations in the input parameters: cell size in the z direction (z_{cell}) and relative permittivity of colloid ($\varepsilon r_{colloid}$), hence, these parameters have been excluded from the subsequent global sensitivity analysis presented in this chapter. Nonetheless, the lack of documented electrical properties for colloid ($\sigma_{colloid}$), connective tissue (εr_{ct}) and fascia (εr_{fascia}) remains a significant challenge since, as visualised in Fig. 4.6b and 4.6c, uncertainties in these parameters are responsible for over >100% variation from the mean values of the investigated indices.

To summarise, with an feasible number of less than 60 model evaluations, the outcomes of this sensitivity study allowed a reduction in the number of the key model parameters, as well as their ranges (such as for the fascia permittivity) in the subsequent global sensitivity study. This demonstrates the utility and the benefits of the local OAT approach in the sensitivity investigation of a computational model.

4.4.2 Global sensitivity analysis – key findings

Global sensitivity methods were implemented into the study to provide a more comprehensive analysis with a much higher number of model evaluations to elucidate the parameters significance in determining the electrical impedance of both tissue types, where all the selected input parameters were varied simultaneously. Moreover, the model sensitivity was assessed at each level in the model hierarchy through the inter- and intracompartmental approach. Finally, this analysis permitted the verification of the outcomes of the much simpler local sensitivity analysis presented earlier in this Chapter.

The global sensitivity analysis results identified the important parameters that influence the impedance spectra indices at all levels of the multiscale model for both thyroid and parathyroid tissue when investigating the geometrical features. Out of the geometrical parameters investigated, the model results showed the highest sensitivity for microscale parameters such as the cell thickness (y_{cell}) and ECS thickness (d_{ECS}) for both glands. On the thyroid mesoscale, both the size of the follicle ($d_{follicle}$) and ECS thickness (d_{ECS}) were recognised as key parameters. For the same group of investigated parameters, two model variations have been explored, either including or excluding the superficial fascia compartment. From the models without the fascia compartment, the thyroid results continue to exhibit strong association with the lower scale parameters such as the size of follicle ($d_{follicle}$) and ECS thickness (d_{ECS}). Similar outcomes are observed for the parathyroid tissue results, for which cell size (y_{cell} and x_{cell}) and ECS thickness (d_{ECS}) are recognised as key parameters.

By comparison, after the fascia inclusion, all these parameters exhibit decreased level of association with the results, at the expense of the prominent role of fascia thickness (d_{fascia}).

In particular, after the inclusion of the fascia compartment, the association of low-frequency impedance (Z_1) with the ECS thickness (d_{ECS}) and size of the follicle ($d_{follcile}$) decreased from -0.87 to -0.68 and -0.70 to -0.61. Moreover, the fascia thickness predominantly affects the high-frequency impedance (Z_{14}) and the middle frequency (f_{mid}) parameters. These results provide evidence that the presence of the fascia layer not only influences the macroscale results but also dominates over the remaining lower-scale parameters, diminishing their impact on the impedance spectra indices as seen in the results summarised in the Tables 4.7 and 4.10. Therefore, it is recommended that all superficial fascia to be removed completely in future *in vivo* measurements in order to acquire accurate thyroid and parathyroid impedances during surgery.

Furthermore, the global sensitivity results revealed the dependence of results on the variation in the electrical properties of colloid and fascia by showing the High and Medium level association with the selected spectra indices of both tissue types. These results further highlight the consequence of the uncertainties in these structures properties affecting the prediction of the computed electrical behaviour of thyroid and parathyroid tissue.

Finally, the inter- and intracompatmental sensitivity analysis at each multiscale level allowed the examination of the impact of how each lower-scale parameter is propagated to the higher levels as additional influencing features are included in the higher levels. In most instances, the key parameters identified in the lower scale results gradually lost their significance when moving up in the model hierarchy which is a result of including more tissue features at higher scales. Despite having lower PRCC values, however, most of the lower-scale parameters continue to appear among the parameters impacting the macroscale results. Nonetheless, the parameters associated with the highest-level models (e.g. fascia properties) were often the most impactful on the macroscale scale spectra indices.

4.4.3 Local and global sensitivity analysis comparison

Despite using two different approaches (local and global), the results showed that both methods were successful in identifying a similar set of parameters significant for the results at the macroscale. ECS thickness (d_{ECS}), cell size (x_{cell} and y_{cell}), and fascia thickness (d_{fascia}) with its electrical material properties (σ_{fascia} and εr_{fascia}) are the key model features recognised through both sensitivity studies to have the most influence on the outcomes for both glands. Moreover, mesoscale parameters, such as the size of the follicle ($d_{follicle}$) and the conductivity of colloid ($\sigma_{colloid}$), were additionally identified as significant for the thyroid model outcomes.

As demonstrated by the results by both sensitivity analysis methods, the variation in the identified morphological parameters relating to tissue structure, as well as in the uncer-

tainty in the electrical properties of different tissue compartments, are considerable factors influencing the theoretical EIS curves. Therefore, the limitation in obtaining reliable model parameters can explain the wide variation of the results presented in Fig. 4.5 and 4.8. Model cell and follicle sizes have been determined based on the values reported in the literature and our own measurements. However, other morphological parameters were not investigated as thoroughly and their values were estimated for the purpose of this study (e.g. ECS thickness has been determined based on values used in previous cervical epithelium cells simulations [38] and electron emission microscopy images of dromedary camel parathyroid gland found in the literature [95]). The importance of appropriate ECS values is highlighted by the outcomes of these sensitivity studies, since this is one of the most important parameters that influences the low-frequency impedance for both tissue types. This is also in agreement with previous computational studies in EIS modelling of cervical epithelium [38].

A similar situation concerns the electrical properties of colloid, fascia and follicular connective tissue. The results demonstrate that the uncertainty in these parameters appear to have the most influence on the impedance spectra indices. Therefore, the uncertainty in the material properties remains a significant challenge that contributes to the uncertainties in computational model results. As mentioned in Chapter 3, since there is no reliable data provided in the literature on these properties which could be of use in the thyroid and parathyroid impedance investigation, these parameters had to be estimated based on other materials characterised by similar composition. However, constraining the properties of the colloid and fascia by additional computational or experimental investigation has the potential to reduce the variability of the outcomes of the proposed thyroid and parathyroid models.

Despite the similarity in the outcomes from both sensitivity analyses, it is important to note that the differences in the computational resources required for the chosen local and global methods are substantial. The OAT local sensitivity comprised less than 60 model evaluations, which is merely 10% of the simulations performed and required by the global sensitivity study. Given that the results from both approaches were comparable, the advantages in favour of the local method should be highlighted. The local sensitivity methods provided a successful parameter range screening that was achieved with relatively low computation resources.

Nonetheless, it is important to highlight that the OAT approach is not the most appropriate to identify the non-linear behaviour, since a limited number of points chosen from each parameters' range (3-5 points per parameter) cannot comprehensively represent the actual input-output relationship of the constructed thyroid and parathyroid models. This relationship, however, was possible to observe in the global sensitivity results, where 100 model evaluations have been performed for each parameter group, visualising the nonlinear relationship in the pre-processed data with the high PRCC (as demonstrated in Fig. 4.7a).

Additionally, it's important to remember that the chosen local and global approaches quantify the model sensitivity in two entirely distinct ways. The local OAT results present the model sensitivity as the relative change of maximum and minimum values from the mean result separately for each parameter. Meanwhile, the global correlation-based methods, such as the chosen calculation of PRCC, determine the strength of linear association between given input and output (in this case the calculation is performed on their rank-transformed values). This means that the rank-transformed parameter values with the highest PRCC are strongly associated with a given output parameter. These differences in appointing the key model parameters could have been a reason for observed discrepancies in the local and global results in a few instances (fascia conductivity and thickness recognised only in local sensitivity results). A notable impact of the isolated parameter variations does not necessarily suggest a strong linear relationship with an output parameter. The significance of each parameter can also be overshadowed during a global investigation where all the model parameters are varied simultaneously. Moreover, a notable disadvantage of the correlation-based method is that it is impossible to assess directly each parameter's absolute impact on the variance of the results. This means that, even for high PRCC values, the variation in the input parameters can cause relatively small changes in the output parameters. Additionally, the correlation-based method does not permit the investigation of the parameter interactions.

Therefore, future work based on the variance-based sensitivity method, such as the Sobol analysis, would permit to further elucidate the contribution of each geometrical and electrical property associated with the multiscale model compartments to the inter- and intracompartmental variability in the results. The apparent practical challenge in the Sobol method is the requirement of a high number of model evaluations (in order of a few thousands), which, as discussed previously, would require a very long computational time to provide sufficient dataset. To overcome this challenge, the future studies could also benefit from implementing surrogate modelling (such as Gaussian process emulators) which, trained on the existent dataset, could potentially deliver additional model evaluation results without the need of the computationally demanding multiscale simulations.

In summary, this Chapter fulfilled the RO4 that concerns the influence of the morphological and electrical properties of tissue features across multiple scales on the computed impedance spectra. In addition, the outcomes of the presented sensitivity analysis provided recommendations for future computational and experimental work. In particular, the analysis permitted the selection of the important tissue properties, such as properties of fascia, colloid, ECS thickness, cell and follicle sizes, which have the most significant impact on the computed EIS spectra. Therefore, the uncertainties in these parameters have a substantial impact on the computed spectra indices variation and should be considered in future modelling work. The outcomes of the sensitivity study also demonstrated that the natural variability of morpholog-

ical features can be responsible for a wide spread of the future measured impedance spectra across the studied frequency range, which can impact both tissues separability. In addition, the high correlation between the fascia compartment properties and the computed results emphasises the importance of this tissue's surgical removal prior to the thyroid and parathyroid tissue impedance acquisition in order to obtain reliable, 'uncontaminated' measurements.

Chapter 5

Computational and *in vivo* results comparison

In this chapter the results from previous local and global sensitivity analyses will be used to address the RO2, which aims to compare them against the *in vivo* measured electrical impedance spectra of thyroid and parathyroid previously acquired by Hillary et al. [3]. Through the comparison, the RO3 will be investigated where the respective thyroid and parathyroid separability will be evaluated based on both the computed and experimental measured *in vivo* results.

The comparison of the local sensitivity and *in vivo* measured results [3] presented in this chapter formed the basis of the peer reviewed paper published in IEEE Open Journal of Engineering in Medicine and Biology, and titled: 'Multiscale Model Development of Electrical Properties of Thyroid and Parathyroid Tissues' [116].

5.1 Introduction

The initial reference thyroid and parathyroid results (Fig. 3.18 Chapter 3) suggested a clear separation between both tissue types signifying the higher impedance values should be expected for the parathyroid tissue relative to the thyroid across the investigated frequency range. The results presented in Chapter 4 investigated the differences in the computationally derived impedance spectra and their characteristic features for the thyroid and parathyroid tissues based on the outcomes of the local and global sensitivity studies, where the effects of the morphological and electrical parameters of these tissues were explored.

In order to get a more comprehensive understanding of the reliability of the computed EIS spectra presented in Chapter 4, the theoretical results were verified against the *in vivo* measured human thyroid and parathyroid EIS spectra. The latter were acquired and previously

published by Hillary et al. [3] in the context of investigating the EIS applicability in differentiating healthy and pathological parathyroid glands from the adjacent soft tissues during surgery. Moreover, through the comparison, the feasibility of thyroid and parathyroid tissue differentiation based on their EIS spectra indices will be evaluated.

5.2 Methodology

5.2.1 *In vivo* dataset

The *in vivo* measured dataset provided by Hillary et al. [3] utilised the tetrapolar ZedScan^{TM} EIS device to acquire the electrical impedance spectra of thyroid and parathyroid tissue and was used in this study with the authors' permission. The *in vivo* measured dataset comprises mean impedance spectra (mean impedances calculated at each frequency from multiple measurements performed for each patient) of thyroid (n=53) and parathyroid (n=42) tissues. The *in vivo* measured spectra were obtained from the physiologically healthy sections of thyroid and parathyroid glands from the patients undergoing various types of thyroid or parathyroid surgeries. In the study, the impedance measurements have been additionally performed on the pathological parathyroid glands, as well as for the muscle and adipose tissues. Nonetheless, these measurements have not been included in the model verification, since the aim of the computational study is the investigation of healthy thyroid and parathyroid tissues.

The theoretical and *in vivo* measured results were compared both qualitatively, by plotting the theoretical spectra against the range of the experimental results range, and quantitatively, based on the impedance spectra parameterisation. The impedance spectra parameterisation method has been introduced in the previous Chapter 4 section 4.2.4 and was implemented to represent three most significant regions of an impedance spectrum for biological tissues: low-frequency impedance (Z_1), high-frequency impedance (Z_{14}) and the middle of the β dispersion (f_{mid}).

5.2.2 Thyroid and parathyroid tissue separability

In order to investigate the potential separation of thyroid and parathyroid based on the computed and *in vivo* measured data, the qualitative comparison of the results data has been performed through scatter plots visualising the relationship between each pair of the three spectra indices. Additionally, the Support Vector Classification (SVC) algorithm from scikit-learn, the open-source machine learning Python library, was used to separate the thyroid and parathyroid results using all three spectra indices. SVC is a type of supervised machine learning method used predominantly for classification tasks. The principle of the SVC is to find an optimal surface (or a hyperplane in a multidimensional dataset) separating the data by the most substantial margin, where the distance between the datapoints from different classes is maximised [134]. The datapoints closest to the hyperplane are known as the

support vectors, and their location determines the orientation and position of the hyperplane.

Receiver Operating Characteristic (ROC) curves have been subsequently plotted for the computed results (thyroid and parathyroid global sensitivity results from the geometrical parameters excluding fascia investigation) and *in vivo* experimental results separately. ROC curves visualise the relationship between the true positive rate and false positive rate at different thresholds for a binary classification. The ROC curve is constructed based on the given percentage of true positive cases and false positive cases that changes due to the increasing cut-off value (a parameter or parameters on which the classification is based on) [135]. Area under the ROC curve (AUC) is an indicator that determines the effectiveness of the classification model, with values close to 1 characterising a perfect classifier. AUC can be interpreted as the probability of correct positive case classification between a randomly selected pair of negative and positive cases [136]. AUC values of 0.5 or lower suggest that the model's performance is equal or worse than a random classification. This classification methodology has been implemented to differentiate Cervical Intraepithelial Neoplasia (CIN) from healthy cervical tissue using EIS [72] and combined EIS and colposcopy methods [137].

5.2.3 Comparison with the literature

Finally, the computed and *in vivo* measured results from Hillary et al. [3] for thyroid tissue will be compared against the impedivity results documented in the literature for this tissue type from modelled and experimental studies investigating both healthy and pathological tissues which have been summarised in Table 2.1 in Chapter 2.

5.3 Results

5.3.1 Reference curve comparison

A comparison of the reference thyroid and parathyroid curves, computed with the default set of model parameters, with the range of the *in vivo* experimental spectra is shown in Fig. 5.1. This visualisation implies that the reference computed spectra lie within the range of the experimental results. However, at frequencies below 100 kHz, the computed thyroid spectrum corresponds to the lower impedance values from the experimental data (Fig. 5.1a), with the opposite trend for the parathyroid (Fig. 5.1b).

5.3.2 Local sensitivity study results comparison with *in vivo* measured data

5.3.2.1 Qualitative comparison

Local sensitivity analysis was aimed to screen the parameter space in order to limit the range and number of key parameters prior to a more comprehensive global sensitivity investigation,

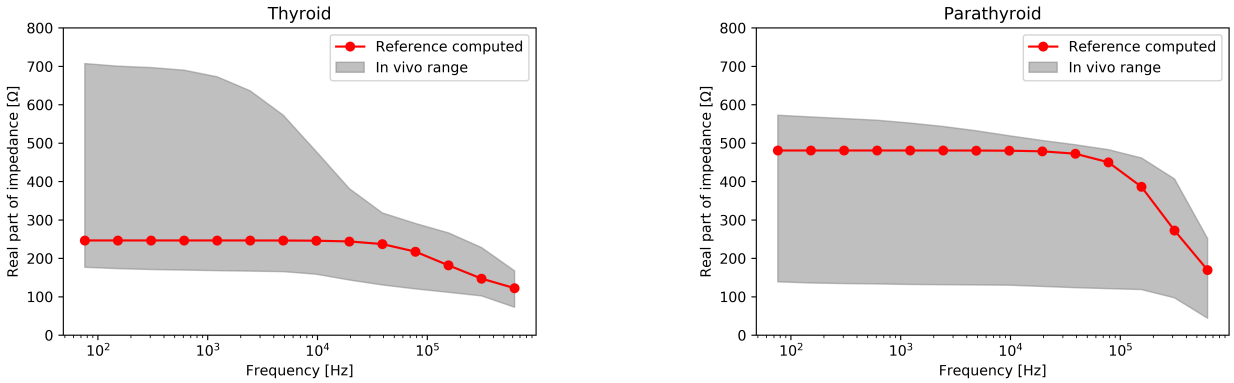

(a) **(b)**

Figure 5.1: *The computed reference curves (red spectra) comparison with the range of in vivo experimental results for (a) thyroid and (b) parathyroid tissue*

that is why the results from these two studies have been compared separately. The computed spectra obtained through the local sensitivity analysis (Chapter 4 Section 4.3.2) are plotted against the range of the experimental results in Fig. 5.2. The presentation of individual simulated spectra rather than simply the reference curves (as shown in Fig. 5.1) permits the inspection of the variation in the shape of individual spectra according to the investigated variation in the morphology and electrical properties in the local sensitivity analysis. It is apparent that there are similarities with *in vivo* measurements observed for both thyroid and parathyroid tissues with most of the computed EIS spectra falling within the range of the experimental results. As the majority of the computed curves are in a close proximity to the reference spectra, most of the thyroid and parathyroid results fit within the lower and higher impedance experimental ranges respectively.

5.3.2.2 Quantitative comparison

The quantitative comparison of the mean (± standard deviation) values of selected spectra parameters (Z_1, Z_{14} and f_{mid}) is presented in Table 5.1. A visual comparison of the experimental and computational spectra indices is presented in Fig. 5.3. Similar trends of higher mean Z_{14} and f_{mid} for parathyroid compared to thyroid tissue is apparent for both computed and experimental results, as seen in Table 5.1 and Fig. 5.3b and 5.3c. Conversely, the Z_1 computed results did not predict higher values for thyroid tissue over the parathyroid as observed in the experimental data. Nonetheless, the visual comparison of the spectra indices highlights that the majority of the computed results are in agreement and within the range of the experimental data. Moreover, most of the computed outliers (such as the curves obtained with very high fascia permittivities on macroscale and thin ECS layers on microscale) fall outside the *in vivo* measured range for both thyroid and parathyroid tissue. This provides further justification for the decision to narrow down these parameters in the following global

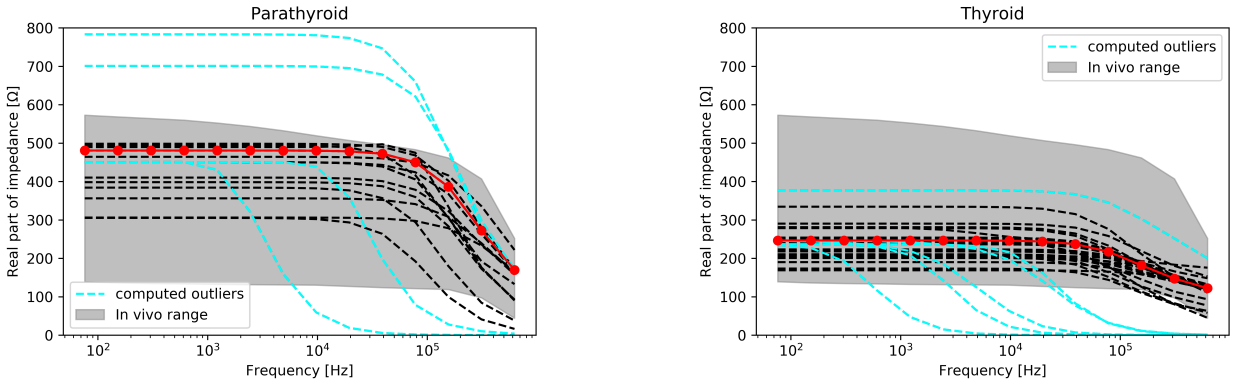

Figure 5.2: *Comparison of computed spectra from the local sensitivity analysis (black dashed lines, with blue spectra marking the outliers and the red dotted line marking the reference spectrum) against the range of experimental data (grey range) for: (a) thyroid, (b) parathyroid tissue*

sensitivity study.

	Computed	Experimental
	Thyroid	
Z_1 [Ω]	239.02 (±40.26)	325.42 (±117.00)
Z_{14} [Ω]	103.58 (±50.43)	112.50 (±15.67)
f_{mid} [kHz]	139.86 (±62.26)	62.23 (±48.52)
	Parathyroid	
Z_1 [Ω]	464.92 (±114.95)	280.58 (±97.37)
Z_{14} [Ω]	120.06 (±66.31)	132.70 (±35.50)
f_{mid} [kHz]	192.00 (±79.48)	157.26 (±69.67)

Table 5.1: *The mean (± standard deviation) values for the spectra parameters of the local sensitivity computed and in vivo measured results for both tissue types.*

5.3.3 Global sensitivity results comparison with *in vivo* measured data

5.3.3.1 Qualitative comparison

The computed impedance spectra obtained through the global sensitivity analysis and divided based on the investigated group of the input parameters for both glands are presented in Fig. 5.4 with the comparison to the range of experimental results. The computed results obtained through the variation of the geometrical parameters including the fascia compartment (Fig. 5.4 a and d) exhibit good fit and distribution of the impedance curves within the

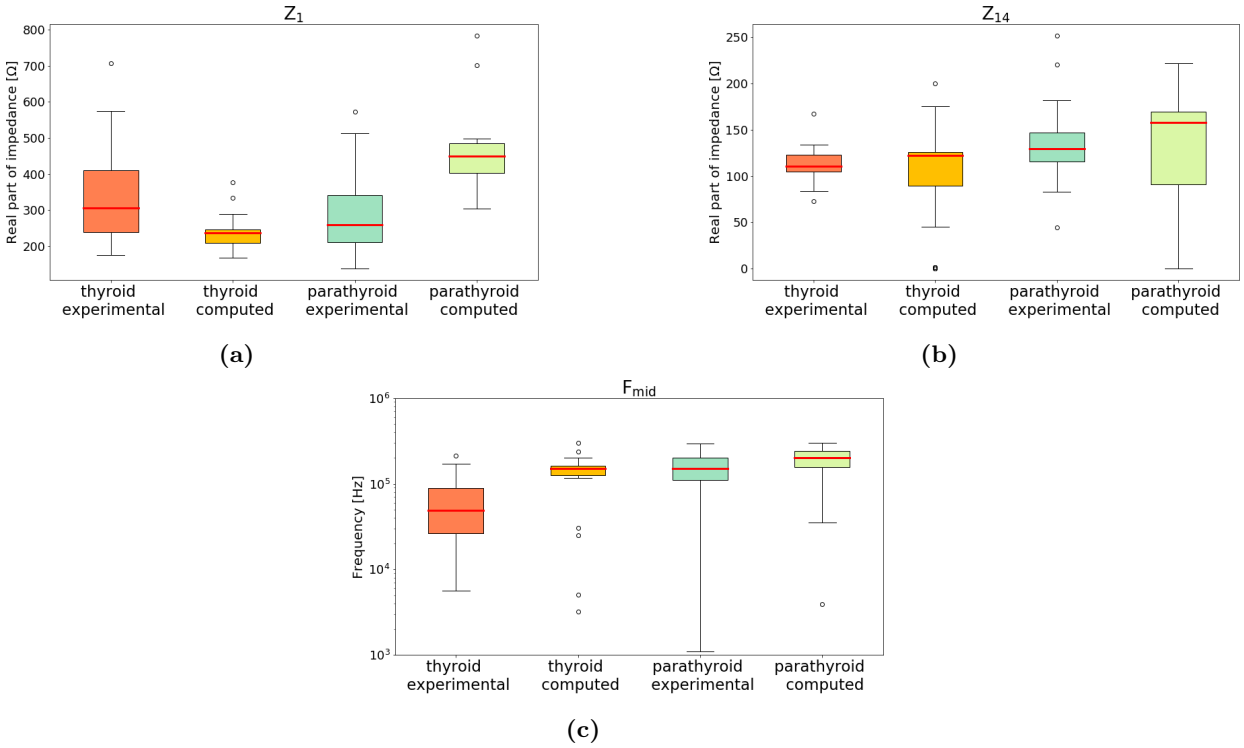

Figure 5.3: *Box and whisker plot of the spectra indices (Z_1- impedance at 76 Hz, Z_{14} - impedance at 625 kHz and f_{mid} - dispersion frequency) comparing both glands and the computed and experimental results*

range of the *in vivo* spectra for both glands. The best agreement between the computed and experimental data is especially noticeable in frequencies below 100 kHz, while above these frequencies the computed results underpredict the impedance when compared with the *in vivo* experimental results.

A better agreement in this high frequency region can, however, be observed in Fig. 5.4 b and e, where the impedance spectra have been acquired through the geometrical parameters variation excluding the superficial fascia compartment. However, in the frequency region below 100 kHz a few of the thyroid and parathyroid impedance spectra from this group of results fall above the upper limits of the *in vivo* measured results.

The computational investigation of the electrical property uncertainties (Fig. 5.4 c and f) shows that the default selected conductivity and relative permittivity values for the follicle, follicular connective tissue and fascia compartment (red reference curves) provide better agreement with the experimental results compared to the spread of the curves acquired through the variations in the properties of these compartments for both tissue types (marked with black dashed lines). The material property uncertainties mostly affect the impedance at

the frequencies above 10 kHz, where the most substantial differences between computed and *in vivo* measured spectra are observable. In this region, the computed prediction shows lower impedance compared to the *in vivo* measured results. Moreover, a substantial number of computed curves show impedance values tending to zero in the high-frequency region, which mostly results from the investigation of high values of fascia permittivity (as seen in Table 4.8 and 4.10 from Chapter 4 showing a high association between fascia properties and Z_{14}).

5.3.3.2 Quantitative comparison

The qualitative comparison of the same group of computed and experimental results in the form of mean (± standard deviation) values of the selected spectra indices is summarised in Table 5.2. Furthermore, the visual comparison in a form of box and whisker plots is presented in Fig. 5.5. The inspection of the Z_1 results in Table 5.2 reveals that the mean thyroid computed results from all three groups of global sensitivity investigation underpredicts the experimental mean results, with the opposite trend seen in the parathyroid results. However, considering the large standard deviation values for both computed and experimental data and the Z_1 spread visualised in Fig. 5.5, the similarities between the range and distribution of computed results from geometrical parameters investigations, and the experimental low-frequency impedance results are evident. These similarities were earlier confirmed by the assessment of the impedance curves from Fig. 5.4.

The high-frequency impedance (Z_{14}) comparison shows that the best agreement between the computed and experimental thyroid results is provided by the results from the geometrical properties investigation excluding the fascia compartment. In contrast, for parathyroid, based on the mean value and the distribution of the data, the results from this parameter group overpredict the Z_{14} parameter when compared to the *in vivo* results. The remaining computed result groups (geometrical parameters including fascia and material properties investigation results) show a high level of discrepancies when compared to the experimental data, exhibiting low Z_{14} impedance values for both tissue types.

The dispersion frequency (f_{mid}) in all computed result groups and for both glands is overpredicted in comparison to the experimental *in vivo* results as shown in both the mean value in Table 5.2 and the results visualisation in Fig. 5.5.

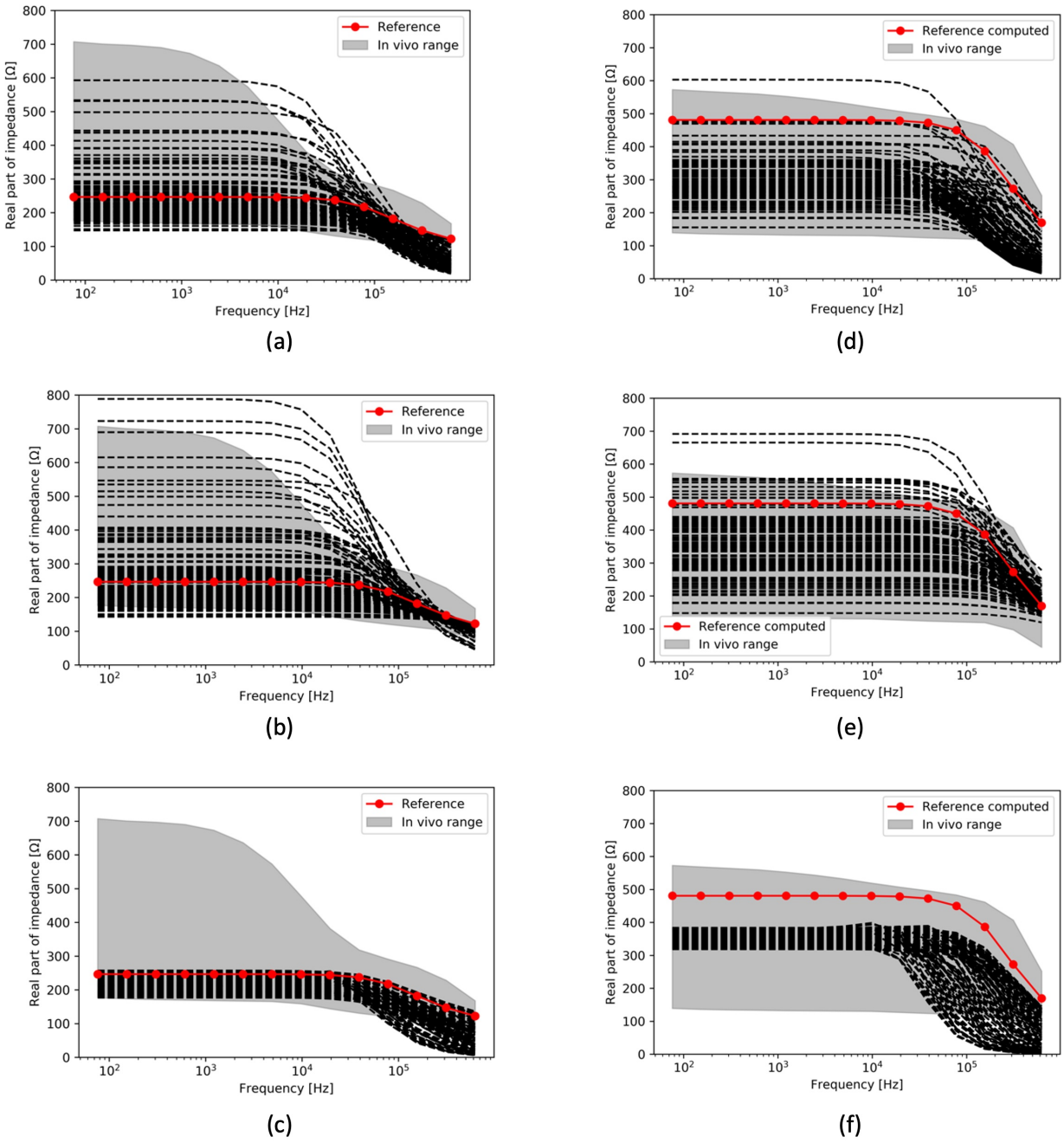

Figure 5.4: *Comparison of the computed spectra (black dashed lines, with the red dotted line marking the baseline spectrum) against the range of experimental data (grey range) for: (a-c) thyroid, (d-f) parathyroid tissue investigations, where (a) and (d) show the results from the investigation of geometrical properties including fascia, (b) and (e) the investigation of geometrical properties excluding fascia, (c) and (f) the investigation of material properties*

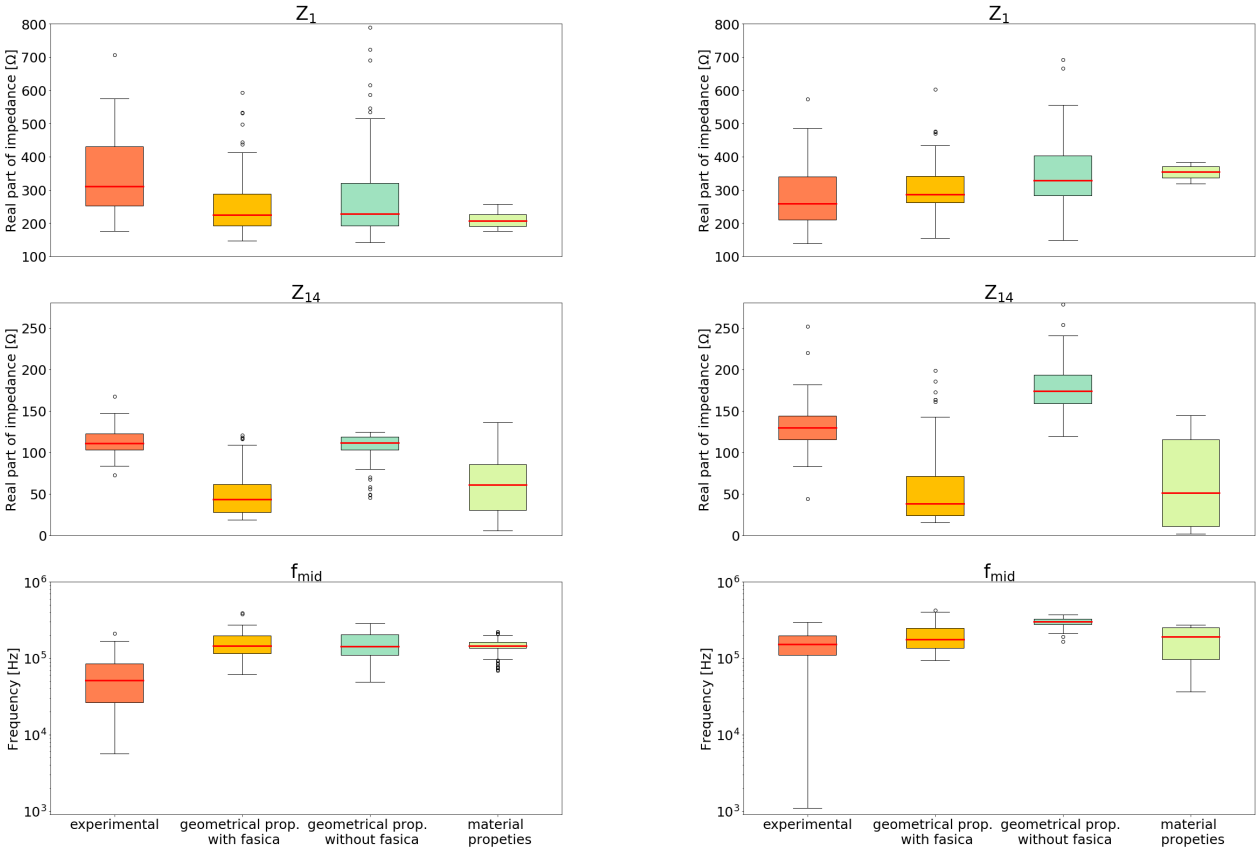

Figure 5.5: *Box and whisker plot of the spectra indices (Z_1- impedance at 76 Hz, Z_{14} - impedance at 625 kHz and f_{mid} - dispersion frequency) comparing the experimental results with each parameter group from the global sensitivity analysis for (a) thyroid and (b) parathyroid*

Parameter	Geometrical parameters including fascia	Geometrical parameters excluding fascia	Material properties	Experimental
		Thyroid		
Z_1 [Ω]	253.74 (± 88.93)	278.24 (± 131.05)	208.99 (± 60.83)	325.42 (± 117.00)
Z_{14} [Ω]	50.38 (± 27.87)	107.23 (± 17.43)	60.83 (± 35.73)	112.50 (± 15.67)
f_{mid} [kHz]	157.61 (± 63.40)	154.17 (± 61.43)	145.99 (± 30.90)	62.23 (± 48.52)
		Parathyroid		
Z_1 [Ω]	300.83 (± 68.64)	343.67 (± 107.55)	353.18 (± 19.78)	280.58 (± 97.37)
Z_{14} [Ω]	55.12 (± 43.35)	177.83 (± 34.12)	62.92 (± 51.86)	132.70 (± 35.50)
f_{mid} [kHz]	197.51 (± 77.10)	196.38 (± 52.40)	173.27 (± 81.70)	157.26 (± 69.67)

Table 5.2: *The mean (± standard deviation) values for the spectra parameters of the global sensitivity computed and experimental results for both tissue types in comparison to the in vivo measured dataset*

5.3.4 Classification of thyroid and parathyroid results

The separability of the thyroid and parathyroid spectra was assessed qualitatively using the scatter plots visualising the relationship between each pair of impedance spectra indices and is shown in Fig. 5.6 for both glands for both *in vivo* experimental and computed data. Due to the best agreement with the *in vivo* experimental results based on all three spectra indices, the computed dataset obtained through the geometrical properties investigation excluding the fascia compartment was chosen for this comparison.

Inspection of Fig. 5.6 reveals a good visual separation of the computed thyroid and parathyroid data (signified with the x markers) based on all pairs of spectra indices. Nonetheless, the experimental *in vivo* results (signified with o markers) suggest more difficulty in separating thyroid and parathyroid results due to the notable overlap between the data. The overlap is especially apparent in Fig. 5.6b, where the Z_1 and f_{mid} results are plotted against each other.

The Support Vector Classification algorithm was implemented to classify the thyroid and parathyroid data based on all three spectra indices from the computational global sensitivity analysis investigating the geometrical parameters excluding the fascia compartment and the *in vivo* experimental studies. The classification results are displayed in Fig. 5.7 in the form of the ROC curves, showing the Area Under the Curve (AUC) of 0.97 for the computed and 0.89 for the experimental results. These results indicate a good performance of the classification algorithm in differentiating between thyroid and parathyroid tissue spectra indices from both the computed and experimental dataset.

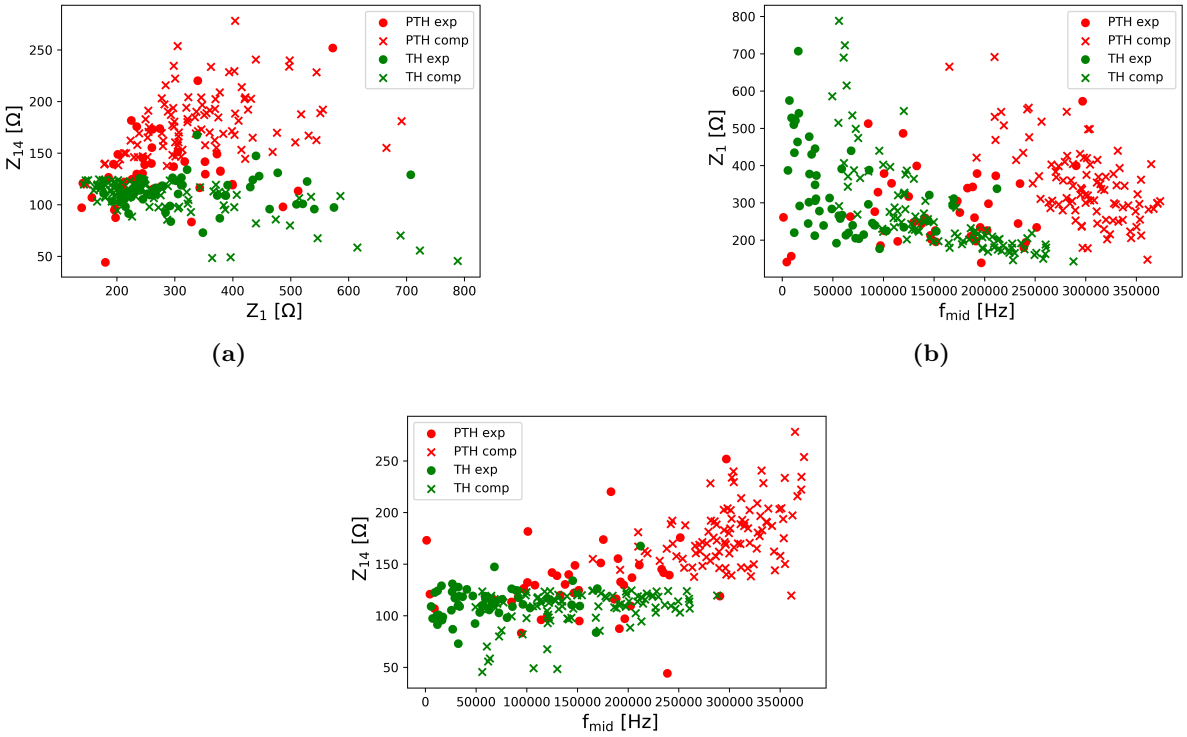

(a) **(b)** **(c)**

Figure 5.6: *Scatter plots of the selected spectra indices visualising the spread of the computed (x markers) and in vivo experimental (o markers) thyroid (TH) and parathyroid (PTH) results, (a) Z_{14} against Z_1 results, (b) Z_1 against f_{mid} results and (c) Z_1 against f_{mid} results*

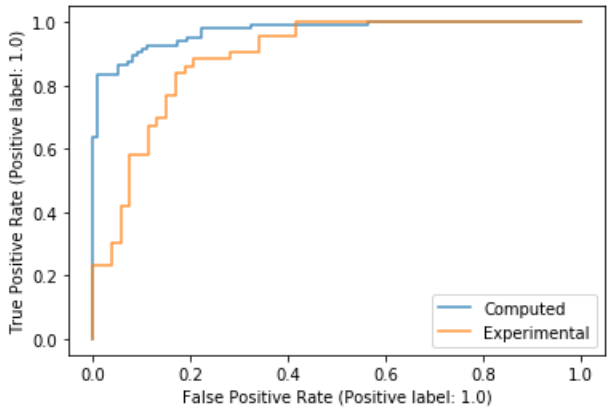

Figure 5.7: *The Receiver Operating Characteristic curves for the classification study performed with a Support Vector Classification algorithm on computed data from the global sensitivity analysis on results from the geometrical properties investigation excluding fascia (blue curve) and in vivo experimental data (orange curve)*

5.3.5 Comparison with the literature

Fig. 5.8 summarises the differences between the reference thyroid impedivity spectrum computed in this study and measured or modelled results reported in the literature. The impedivities of the *in vivo* measured data provided by Hillary et al. [3] and the computed results have been obtained by dividing the impedance results by ZedScan^{TM} calibration constant (68.41, which was derived thorough a macroscale model simulation with assigned uniform element material properties of 1 Sm^{-1}). This allows the direct comparison of these results with the thyroid impedivities documented in the literature.

As visualised in Fig. 5.8, the impedance values documented by Gabriel [26] are located outside the impedance or frequency range of the results measured by Hillary et al. [3]. The impedance modelled by Gabriel [26] at 100 Hz is about 100 Ω smaller than the reference thyroid impedance computed in this study. Comparing and interpreting the results presented by Cheng and Fu [61] is equally challenging since these specific impedivities have been measured in much higher frequencies (in the gigahertz region). There are, however, similarities between the outcomes of this computational work and the results collected by Yun et al. [22]. The reference computed curve lies within the measured range of healthy *ex vivo* measured range and additionally agrees with the range documented by Hillary et al. [3].

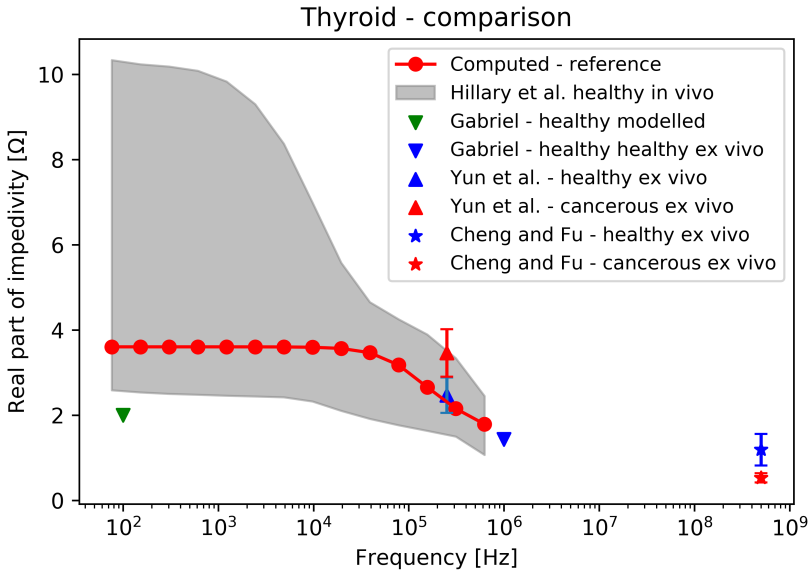

Figure 5.8: *Comparison of the thyroid impedivity results from additional modelling and experimental studies as reported in the literature*

5.4 Discussion

The purpose of this Chapter was the comparison between the thyroid and parathyroid computed impedance spectra with the *in vivo* experimental results performed in order to partly validate the developed multiscale models' outcomes. Additionally, the feasibility of differentiating and classifying the thyroid and parathyroid glands based on their computed and *in vivo* measured electrical behaviour has been evaluated.

The qualitative comparison between the simulated and *in vivo* results from Fig. 5.1, 5.2 and 5.4 show that the majority of the computed spectra predicted by the multiscale models falls within the range of the experimental EIS curves. Nonetheless, the most prominent discrepancies with the *in vivo* measured spectra are associated with the investigation of the electrical properties uncertainties (Fig. 5.4 c and f), which will be discussed separately from the remaining two groups of global sensitivity results.

A good agreement between the reference thyroid and parathyroid results and the *in vivo* experimentally acquired range of impedance presented in Fig. 5.1 highlights the reliability of the EIS theoretical prediction for both glands when both models are assigned with the default parameter values. It is important to note that the baseline results were generated without any attempt to adjust parameters to "fit" the measured data, which suggests the validity of a multiscale modelling approach and at least the approximate range of the morphological and electrical parameters selected in these instances.

For the local sensitivity analysis results, the best fit can be observed in the frequency region above 100 kHz for both tissue types. However, a closer inspection of the spectra indices presented in Fig. 5.2 and Table 5.1, reveals discrepancies between the computed and *in vivo* results in the Z_1 index representing the low-frequency impedance. In contrast to the differences between glands in computed results, the experimental data reports the opposite trend of higher low-frequency values for thyroid compared to parathyroid. Nonetheless, the global sensitivity results obtained through the investigation of the geometrical parameters show an improved agreement between computed and experimental Z_1 parameter for both tissue types, which can be observed in Fig. 5.4. This favourable agreement is further supported by the qualitative visualisation of the results (in Fig. 5.4 a, b, d, and e) where the computed impedance spectra are well distributed within the plotted experimental range. This observation also points to the possibility that the substantial variation in the *in vivo* experimental thyroid and parathyroid results, particularly at the frequencies below 100 kHz, may be explained by the inherent inter- and intrasubject variability of the morphological features of these tissues.

In contrast to the discrepancies in the low-frequency impedance of the local sensitivity re-

sults, both Z_{14} and f_{mid} indices show a similar trend for both computed and experimental results (Table 5.1) where both indices remain higher for the parathyroid than thyroid tissue in simulated and measured data. This situation is also demonstrated in the global sensitivity results summarised in Table 5.2. Moreover, the global sensitivity thyroid results from the geometrical parameters investigation show the best fit with the *in vivo* experimental results at high frequency impedance (Z_{14}) in the group of results excluding the fascia compartment (Fig. 5.5a). For the parathyroid (Fig. 5.5b), however, the fascia inclusion leads to underpredicted Z_{14} impedance when compared to experimental results, while its exclusion causes this parameter's overprediction. These results might indicate that some of the *in vivo* parathyroid glands, from which EIS data were collected, were covered with this thin superficial fascia layer, explaining the discrepancies between both computed datasets.

Finally, the local and global sensitivity results show that the computational model overpredicts the f_{mid} value for both tissue types. The reason for this could be the inappropriate selection of the poorly defined fascia and connective tissue relative permittivity, since these parameters mostly influence f_{mid} as much as the ECS thickness as revealed in Chapter 4. An additional explanation could be in the invalid assumption of the homogeneous structure for the models, which, as discussed by Markx et al. [69], can result in a sharp and narrow theoretical dispersion, compared to the results obtained experimentally. As explained further, the heterogeneity in the structures of the biological material is suspected to be responsible for wider β dispersion, possibly moving the f_{mid} towards lower frequencies. This could be verified through e.g., a larger multifollicular mesoscale model representing the thyroid follicles of different shapes and sizes. The heterogeneity of the thyroid follicular structure will be further addressed and investigated in Chapter 6.

The discussed discrepancies between the global sensitivity results concerning the electrical property uncertainties and the *in vivo* experimental data, especially in the high-frequency region above 10 kHz, are predominantly a consequence of the uncertainties of the fascia properties. As demonstrated in the previous Chapter 4, the model outcomes at high frequency (Z_{14}) are sensitive to this compartment's properties and thickness which was supported by the outcomes of local and global sensitivity analyses for both glands. The results visualised in Fig. 5.4 c and e suggest the validity of the initial parameter values selected for the reference thyroid and parathyroid results, implying that these values provide a better fit with the *in vivo* results in comparison to the computed spectra from the material properties uncertainty investigation obtained using non-default parameter values. Additionally, the small variation of the Z_1 and f_{mid} results for this group of computed results (Table 5.2) suggest that material property variations would not significantly affect the computational model prediction in the low-frequency impedance and the β dispersion regions. Moreover, this material property investigation, which was a part of the global sensitivity analysis, was not intended to provide reliable impedance spectra for the two tissue types; rather, its goal was to quantify the

model output uncertainties resulting from the poorly defined electrical properties of colloid, connective tissue, and fascia.

Alongside the discussed computational modelling limitations potentially affecting the predicted impedance spectra, the observed differences in the simulated and *in vivo* measured impedance could possibly also be explained by various measurement conditions associated with the experimental data collection. Firstly, the surgeon separates the superficial fascia from the glands before taking the EIS measurement, however, the removal might be incomplete, and it is not possible to quantify how much fascia is present on the tissue during the measurement. As demonstrated in the computational sensitivity study in Chapter 4, all three spectra indices are sensitive to the fascia thickness and its electrical properties. The impact of fascia inclusion is also visualised in Fig. 5.5 and Table 5.2, where the fascia presence in the computational model significantly lowers the Z_{14} and Z_1 parameters. Additionally, the presence of any fascia during the *in vivo* measurement could also explain the discrepancies in the high frequency impedance Z_{14} as observed in Fig. 5.5.

Moreover, as suggested by Hillary et al. [3], the substantial variation of *in vivo* results could be explained by the differences in the measurement conditions (temperature, humidity) and in the glands vascularity and viability (which is also difficult to assess during or after the surgery). Furthermore, Hillary et al. [3] discussed that the tip of the probe of the ZedScan$^{\text{TM}}$ device (5.5 mm) initially manufactured for the applications for cervical epithelium, is relatively large in comparison to parathyroid glands (typically 3-7 mm). Imprecise coverage of the parathyroid gland with the probe could lead to 'contamination' of measurements by adjacent tissues – thyroid, fascia, or adipose tissue – which is impossible to verify after the measurement has been acquired. Additional computational work on probe optimisation and various probe-tissue misplacement scenarios could help to better comprehend the importance of precision in *in vivo* EIS measurements which will be further discussed in Chapter 7.

Despite the similarities between the computed and *in vivo* measured EIS spectra for thyroid and parathyroid tissue it is not possible to validate the model due to the limited information that was provided along with the *in vivo* experimental dataset. In order to definitively assess the multiscale models' performance and the validity of the predicted results, and to evaluate the impact of the tissues' morphological features on their electrical behaviour, it would be crucial to provide histology images associated with each tissue EIS measurement. Having access to the real tissue morphology information, it would be possible to provide the model with the geometrical parameters specific to each tissue sample and evaluate the resultant computed impedance spectrum against the *in vivo* measurement.

The additional comparison of the results computed in this study and the results presented by Hillary et al. [3] against the thyroid impedivity results modelled or experimentally measured

and documented in the literature is presented in Fig. 5.8. The comparison reveals discrepancies between all these groups of results which could be explained by the differences in the measurement conditions, the instrumentation used and differences in the frequency range.

Finally, the possibility of distinguishing the thyroid and parathyroid tissues based on their electrical behaviour was investigated based on both computed and *in vivo* measured impedance results. As documented in Fig. 5.6, the presented computational results exhibit promising separability of thyroid and parathyroid based on all the variations of the selected spectra indices pairs. The visual separation, however, becomes challenging when accounting for the *in vivo* measured spectra indices, given the notable overlap of the *in vivo* measured thyroid and parathyroid results in all three cases in Fig. 5.7. Nonetheless, the promising outcomes of the classification study with a Support Vector Classification algorithm shows that both computed and experimental EIS spectra of thyroid and parathyroid tissue should be feasible to separate based on the indices characterising the impedance spectra of both tissues. Moreover, the performance of this thyroid and parathyroid classification model using the spectra indices for both computed (AUC of 0.97) and *in vivo* measured (AUC of 0.89) EIS data is comparable with the reported separability of normal and CIN cervical epithelium tissues using EIS methods (AUC of 0.95 and 0.88 for the separability based on two different Cole parameters) [72] and combined EIS and colposcopy in a follow up study comprising bigger patient group (AUC of 0.887) [137].

Nevertheless, it is important to highlight the limitations of the introduced classification method, which is the model performance dependence on the dataset size, and overfitting due to lack of division between training and testing datasets. It was assumed that splitting an already small *in vivo* measured dataset would lead to classification results not representing the whole dataset. Furthermore, the aim of this substudy was to demonstrate that there is a potential to distinguish thyroid and parathyroid tissues based on their EIS spectra indices. To further explore the classification algorithm's applicability in the tissue differentiation, it will be crucial to acquire a larger *in vivo* experimental dataset of thyroid and parathyroid tissues electrical impedance spectra for a more comprehensive classification study.

To summarise, this chapter fulfilled the RO2 and RO3 where the comparison of the computed and *in vivo* measured spectra was presented, and the tissue separability based on the spectra indices was assessed. Through the comparison with the *in vivo* measured spectra, the outcomes of this computational study were further verified. In particular, the results obtained through the variation of geometrical properties through the global sensitivity study showed a good agreement with the spread of the *in vivo* measurements, suggesting that the morphological features variation provide the variability in the results that is also observed and expected in the experimentally acquired spectra for thyroid and parathyroid tissues. Additionally, the positive qualitative and quantitative assessment of the thyroid and parathyroid

tissues differentiation suggest a good separability between these tissue types based on the computed spectra indices.

Chapter 6

Modelling tissue heterogeneity

In this chapter RO5 will be explored through the investigation and verification of previously implemented assumptions concerning tissue homogeneity at different scales. More complex meso- and macroscale geometries will be introduced and developed in order to assess the impact of follicular arrangement in the thyroid tissue and irregular boundaries between tissue structures on the electrical properties of thyroid.

6.1 Introduction

The implemented homogenisation approach in the presented computational models assumes that the properties of a single repeating structure is a representation of the electrical behaviour of the entire tissue itself. For that reason, the geometries up to this point represent simple cuboid shapes with a very regular arrangement on each level of multiscale modelling. Leading from that assumption, a single cell and follicular geometries have been selected at the lower scale levels to simulate the transfer impedivity to be transferred into the higher scale compartments. However, from the biological perspective observed in histology images (Fig. 1.2 from Chapter 1), the arrangement of structures in the thyroid and parathyroid tissue is much more heterogeneous and random compared to the regular tissue structure assumed so far in this computational study. Moreover, a comprehensive study investigating the follicle morphology changes reported that the follicle sizes can vary with age of the patient and location in the thyroid gland [6].

In other fields of bioengineering related computational modelling studies, with the example of mechanical properties of the bone tissue, there are well established methods of approaching the structural and compositional heterogeneity of the biological material. In particular, the tissue geometrical features can be obtained through high resolution imaging segmentation methods (e.g. Micro Computed Tomography imaging [138]) and the patient specific mechanical properties of bones derived from computed tomography images based on the relationship

between the images grayscale, the x-ray absorption of the bone and their mechanical properties [139]. To date, a similar established methodology to address heterogeneity has not been introduced to the studies investigating the electrical properties of biological tissues.

Nonetheless, previous clinical and computational research [38; 72] demonstrated the significance of the cellular structure in relationship to the electrical properties of epithelial tissue. In particular, in the computational study on the electrical behaviour of cervical epithelium by Walker [38], the arrangements of cells in a layered epithelium have been investigated and reported the impedivity differences of around 10 Ωm which are associated with the cell arrangement (bricked or stacked) and the number of cell layers included in the microscale geometry. The investigation of the number of cell layers in a microscale geometry has also been provided by Heath et al. [41] for oral tissues which reported the difference of 0.5 Ωm between impedivity of one and five cell layers. However, the influence of follicle arrangement and structure on electrical properties has not yet been investigated in the literature. As a result, it will be examined in this chapter by comparing the regular and irregular distribution of these structures in multifollicular mesoscale geometries with a single spherical follicle model under the homogeneity assumption.

In addition, in the previously developed macroscale models (Fig. 3.9 and 3.12 in Chapter 3) the transition between tissues assumes regular horizontal boundaries between different compartments, e.g. between fascia and thyroid or parathyroid tissue on the macroscale. Nevertheless, this simplification of recreating the complex tissue transitions could influence the macroscale level results, since, as seen in Fig. 6.1, the transition between tissues is often irregular and the fascia thickness can vary depending on the location on the gland. The thyroid macroscale model including the superficial fascia compartment will be modified in order to investigate the impact of the tissues boundary irregularities and compare to the results from the previous macroscale simulations assuming smooth and regular boundary between these compartments.

6.2 Methodology

6.2.1 Follicular arrangements

In order to investigate the effect of follicle organisation in a tissue, a single follicle and two multifollicular geometries representing a regular and random arrangement of follicles have been developed (Fig. 6.2) and the transfer impedance simulated for a thyroid mesoscale level investigation. Each model's geometry consists of two compartments – spherical follicles and exterior space representing the follicular cells separating each follicle. Each spherical follicle was assigned with the reference material properties of colloid material and the follicles' exterior – with cell properties obtained from the thyroid microscale simulation with the reference

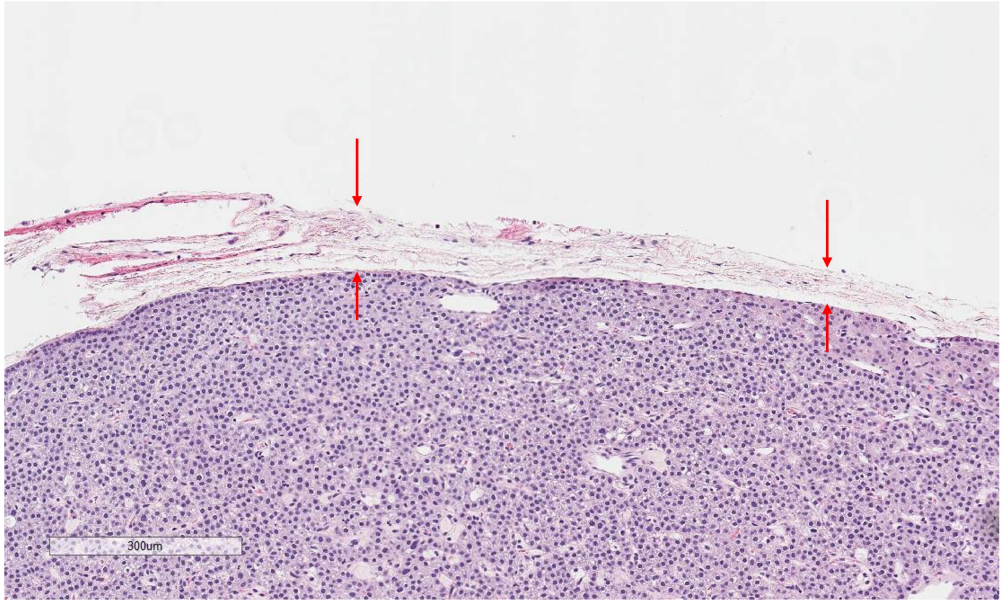

Figure 6.1: *Parathyroid histology image showing an irregular fascia layer, red arrows marking different thicknesses of superficial fascia covering the same gland, (K. Hunter – personal communication)*

geometrical parameters configuration. To aid the comparison, all three geometries (Fig. 6.2) have been generated to represent equal volumetric fraction of follicles (the percentage the follicles that occupy the whole volume). Three different values of follicles' densities in the tissue (10%, 15% and 20%) have been investigated using spherical geometries of equal size (100 µm of diameter). All three types of geometries have been utilised to derive the mesoscale transfer impedivity which was simulated in three directions (x, y, z) to further explore the effect of follicles arrangement with regards to the direction of the measurement. Due to the symmetry of the single follicle geometry (Fig. 6.2 a), in this case the transfer impedivity was simulated only in one of the model directions.

The regular follicular arrangement geometry (Fig. 6.2 b) was constructed using the Hexagonal Close Packing (HCP) of follicles to ensure equal distance between the spherical structures with the centres calculated based on Eq. 6.1-6.3:

$$2i + [(j + k)mod2] \cdot (r + s) \tag{6.1}$$

$$\sqrt{3}[j + 1/3(k \cdot mod2)] \cdot (r + s) \tag{6.2}$$

$$\frac{2\sqrt{6}}{3}k \tag{6.3}$$

where, *i, j, k* are the indices (starting with zero) representing the number of sphere for *x, y, z* coordinates, *r* – radius of spheres, *s* – separation. The follicle radius (r=50 µm) was constant for all three geometries and the separation *s* was adjusted in order to achieve a desired volumetric fraction of follicles in each geometry.

The irregular follicular arrangement (Fig. 6.2 c) was generated with a random spheres' distribution script implementing the restrictions of non-overlapping spheres separated at least by 5 µm distance from each other and the outer cuboid geometry boundary.

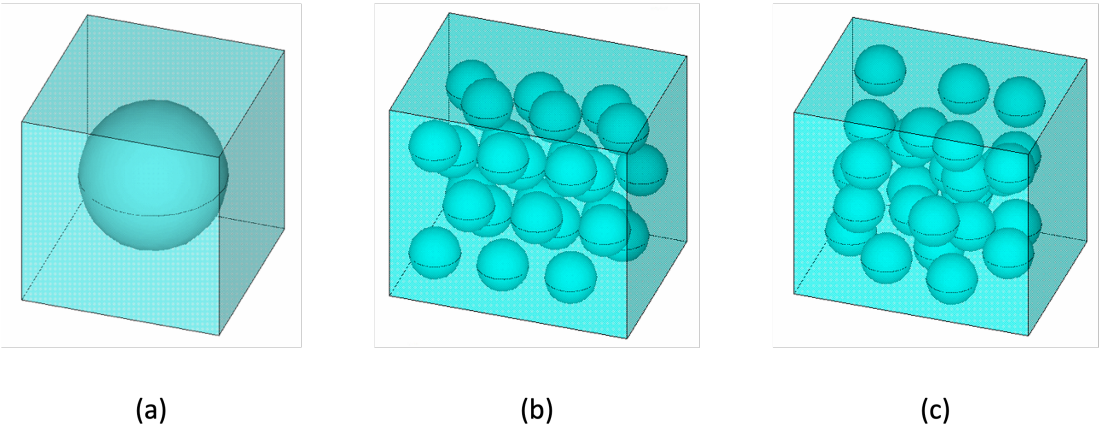

Figure 6.2: *Mesoscale model geometries for the follicular arrangement study: (a) single spherical follicle model, (b) regular arrangement of hexagonal close packed follicles, (c) random arrangement of follicles*

6.2.2 Irregular tissue boundaries

A thyroid tissue macroscale geometry including the superficial fascia compartment has been generated with a sinusoidal boundary between them (Fig. 6.3a in order to investigate the effect of the tissue boundary irregularities. Determined by the symmetry of the macroscale geometry, both compartments have been separated with a boundary defined by a cosine function (Eq. 6.4) where the function parameters, such as the amplitude A (range [0.10, 0.15, 0.20, 0.25] mm), number of periods n (range [2, 3, 4]) and the phase shift θ (range [0, π]) have been varied in order to explore their impact on the macroscale impedance:

$$y = A \cdot cos(n \cdot x + \theta) \tag{6.4}$$

The cosine function indices in relationship to the irregular boundary are visualised in Fig. 6.3b. The impedance results were compared against the previously computed outcomes from the macroscale model simulation with the uniform and regular transition between thyroid and fascia compartments. The depth of the thyroid-fascia boundary was set to 0.5 mm, the

investigation concerning different number of periods was performed with the amplitude A set to 0.25 mm, and in the study exploring the amplitude variation effect, the number of periods n included in the separating boundary was set to 3.

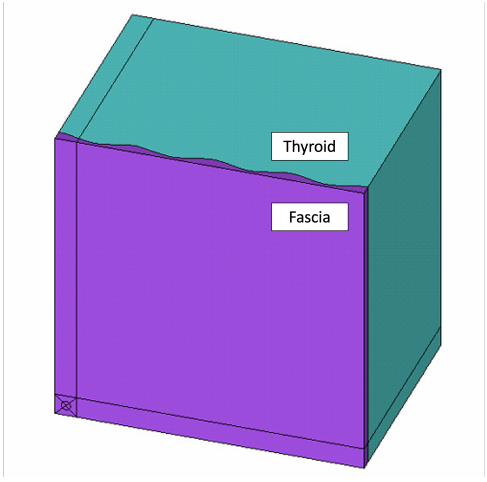

(a)

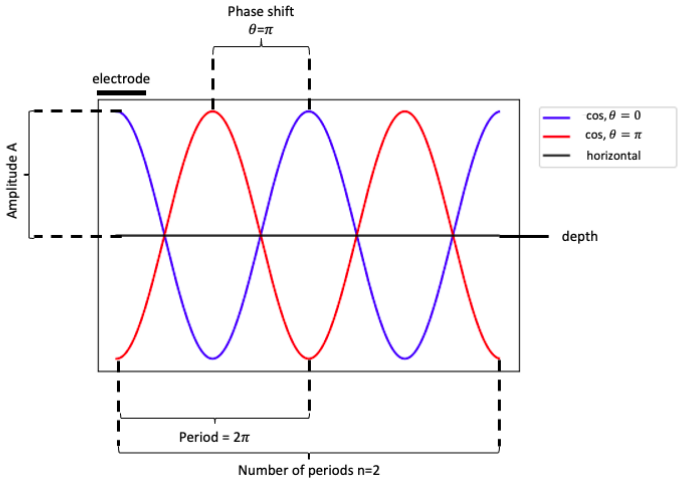

(b)

Figure 6.3: *Thyroid macroscale model geometry with the sinusoidal boundary between thyroid and fascia compartments: (a) one quarter of the macroscale thyroid model (blue) with superficial fascia (purple), (b) schematic highlighting the sinusoidal boundary indices and the differences to the reference horizontal boundary*

6.3 Results

6.3.1 Follicular arrangements study results

Nineteen additional mesoscale simulations have been performed to investigate the effect of the follicular arrangement and distribution in the thyroid tissue: for the multifollicular geometries (Fig. 6.2b and c) three transfer impedivity simulations have been performed per investigated density, and only one in the case of single follicle geometry (Fig. 6.2a) due to its symmetry. The comparison between the real part of the impedivity results is visualised in Fig. 6.4 which reveals that the results associated with all three geometries align across the simulated frequency range (results within 1% from the reference single sphere model), suggesting that the specific arrangement of follicles within the tissue is not significant, provided that the volumetric fraction of follicles is maintained. Moreover, a good agreement of the results is observed between the impedivity spectra associated with the same geometry (transfer impedivity simulation in three model directions) and between results computed from different follicle arrangement geometries.

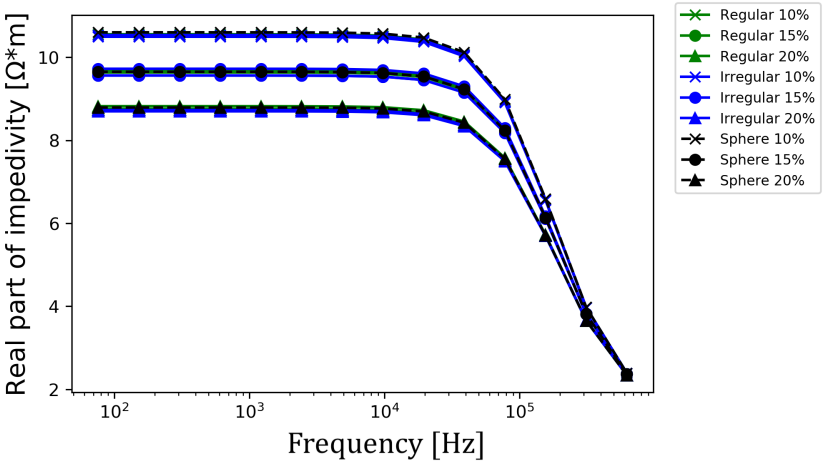

Figure 6.4: *Impedivity spectra obtained from three geometries of different follicle arrangement and complexity, green curves represent the results associated with the geometries with regular arrangement, blue – the irregular arrangement results and black – the single follicle model results*

6.3.2 Tissue boundary irregularity study

The tissue boundary irregularity investigation has been performed to explore the effect of the features of the cosine function separating the tissues on the differences in macroscale impedance when compared to the results assuming an even horizontal boundary between thyroid and parathyroid tissue. Fig. 6.3b shows a schematic visualising the differences in the boundary configurations resulting from the phase shift (blue spectra represent the phase

shift θ=0, red spectra: θ=π) in comparison to the horizontal boundary.

The effect of the number of periods n representing the frequency of the boundary irregularities is demonstrated in Fig. 6.5a, while Fig. 6.5b shows the results from the amplitude A investigation. All results from the irregular boundary investigation were compared against the results from the horizontal and regular thyroid-fascia boundary (black spectra in Fig. 6.5 a and b). The results in Fig. 6.5a report minimal differences between boundary irregularities characterised with different number of periods included along the thyroid and fascia edge.

The effect of the cosine function amplitude (Fig. 6.5b), that defines the maximal distance of the boundary irregularities from the centreline, is, however, more impactful than the number of periods as observed in Fig. 6.5a. The larger the amplitude magnitude, the higher the divergence in the low- and high frequency impedance results from the results with regular thyroid-fascia boundary. In particular, the impedance curves associated with the 0.1 mm amplitude slightly differ from the horizontal boundary results, showing the differences up to 2% and 3.5% in the low- and high-frequency impedance (Z_1 and Z_{14}). In contrast, the amplitude of 0.25 mm induces the differences in the parameters Z_1 and Z_{14} of up to 6% and 11%.

Additionally, the effect of the phase shift visualised in both Fig. 6.5 a and b shows the comparison between the blue and red spectra (θ=0 and θ=π respectively) which reveals the symmetrical placement of the curves with regards to the spectrum resulting from geometry with the horizontal boundaries (black curves).

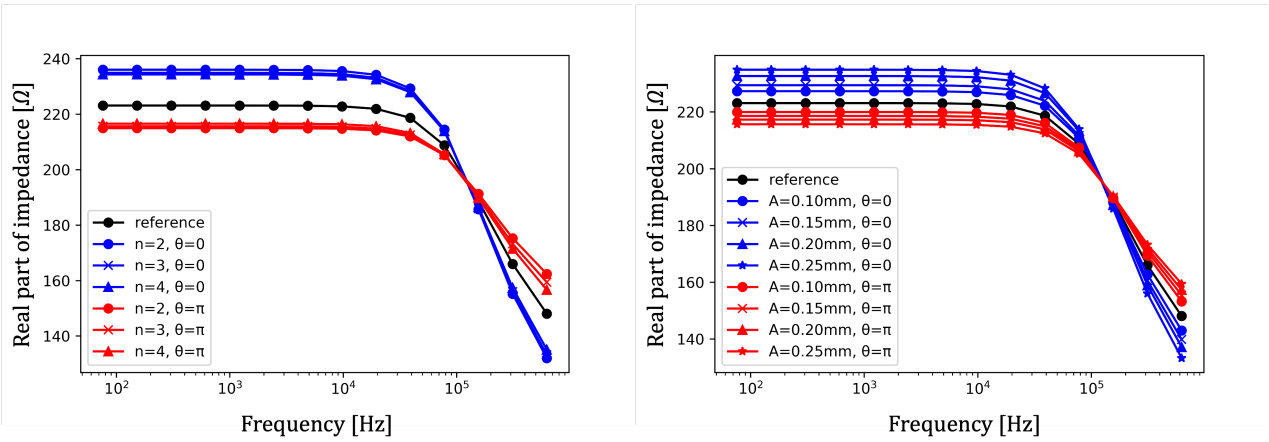

Figure 6.5: *Macroscale results from the simulation with the sinusoidal boundary between thyroid and fascia (a) investigation of the number of periods n, (b) investigation of the amplitude A*

6.4 Discussion

The additional studies presented in this chapter fulfilled the RO5 to verify two implementations of homogeneity assumptions in this multiscale model by investigating the effects of the follicles' arrangement on the mesoscale impedivity and the irregularities of the tissues' boundaries on the macroscale impedance.

The follicular arrangement investigation, seen in Fig. 6.4, provided the evidence that if the volumetric fraction of the follicles in the tissue is maintained, the variations in their arrangement (regular vs irregular arrangement) or the geometry simplicity (multifollicular vs single follicle geometry) play a minor role as the impedivity spectra obtained from each geometry align at all three examined densities within 1% from the reference curve obtained from a single follicle model. Moreover, the overlap of the results associated with the transfer impedivity simulations in three directions for each geometry specifically further implies that for the low volumetric fraction of the follicles in the tissue, the heterogenous arrangement of the structures will not impact the mesoscale results also with regards to the direction of the applied current. Therefore, the previously introduced homogeneity assumption utilising a simple single follicle geometry on the mesoscale level can be considered as justified, especially when compared against the differences arising from the previously introduced arrangements and complexity of the cellular structures on the microscale level simulations presented in the case of the cervical epithelium [38] and oral tissues [41].

Nonetheless, it is worth highlighting the limitations of the presented exploration of the mesoscale structure study. Firstly, the geometries representing different follicle distributions were characterised with a very low volumetric fraction of follicles in the tissue. The selected densities values were determined by the feasibility to create the irregular follicles arrangement geometries. Due to the random placement of the follicles it was challenging to increase the number of the spheres packed within the outer cuboid geometry without additional changes in the script determining the distance of each randomly generated sphere. However, modifying the script with the additional option to define a priori the position or region of each newly placed sphere has the potential to increase the follicular density in the random follicular arrangement [140]. Additionally, the volumetric fraction of the spherical structures in the Hexagonal Close Packing method has a limit of approximately 74%, which may still be too low to realistically replicate the exceptionally dense and tight arrangement of follicles in thyroid tissue. In order to broaden the understanding on the effect of the follicular arrangement it would be crucial to explore geometries characterised with higher volumetric ratio compared to the geometries investigated in this study. Considering the limitations arising from the spherical structures' generation, different geometry construction methods should be explored, such as different image segmentation techniques, preferably based on the 3D histology imaging.

Secondly, in this study the mesoscale model geometries consist of spherical follicles and the space separating them which was assigned with the cell electrical properties obtained from the microscale level simulation for the thyroid tissue. It is, however, a simplification and does not recreate the real thyroid tissue structure, where each follicle is encapsulated by a single layer of cuboidal epithelium with a thin sheet of loose connective tissue separating them. Nonetheless, such a structural assumption can be justified considering the purpose of this study, which was to investigate the effect of arrangement of the follicle structures and compare them to a simple spherical geometry. Additionally, by considering the limitations in achieving sufficient and realistic density of follicles, it may be challenging to obtain reliable mesoscale results with the presented follicular arrangement geometry variations, hence, improving the structural composition will play a minor role in increasing the accuracy of the results.

In the future work it would be beneficial to expand the presented mesoscale level study by investigating the effects of tissue heterogeneity manifesting in different sizes of the structures. As discussed previously in Chapter 2, the distribution of the cellular structures sizes in a tissue could influence the width of the impedance dispersion and the Cole model parameter - relaxation frequency f_c. The investigation of follicular arrangement comprising structures of various sizes could expand our understanding on how these spectra parameters could be influenced by the mesoscale heterogeneity.

Another area of future research could be focused on exploring the heterogeneity arising from variations in the follicle composition across the tissue. The possible deviations in colloid composition affecting the electrical properties of the tissue have been highlighted in Chapter 3 when discussing the mesoscale model development. It is documented that, depending on the activity of the gland, the colloid composition might differ between follicles in the same tissue and can change over time [101]. The outcomes of such an investigation could further reveal the limitations associated with the homogeneity assumptions concerning the structures and material properties on the mesoscale level of the computational model of thyroid tissue.

Finally, the effects of boundary irregularities between different tissue compartments on the macroscale have been verified against the results obtained with the geometries of a regular and horizontal boundary. In this study, the sinusoidal curve separating the thyroid and fascia compartments has been generated by varying the cosine function parameters: amplitude, number of the periods and phase shift that define the height, frequency and spatial orientation of the boundary irregularities. The results observed in Fig. 6.5 expose that the differences in the phase shift and the amplitude of the sinusoidal boundary have the most significant impact on the macroscale results and can raise up to 11% variation in the low-frequency impedance when compared to the results obtained with geometries with a regular

boundary between both tissues. The shape and irregularities of the tissue boundary directly determine the amount of the fascia material in the close proximity to the electrodes. The thicker fascia compartment underneath the electrodes, the more variation in the results is observed in comparison to the regular horizontal boundary results. This agrees with the outcomes previously discussed computational sensitivity study which highlights the significance of the fascia compartment thickness and its properties on the macroscale impedance.

This substudy revealed also that the irregularities in the tissue boundaries can raise differences in the macroscale results compared to the assumption of even and regular boundaries. However, the nature of the study was purely exploratory and theoretical, and the cosine function parameters were not derived from any histology images. Additionally, only two variations of the cosine function shift phases have been investigated which was determined by the symmetry of the macroscale model. Moreover, in the case of a gradual transition between two tissues that is seen in Fig. 6.1, it will be the fascia thickness directly underneath the probe that will predominantly affect the EIS measurement. Moreover, additional factors such as the differences in the material properties of the tissues investigated and the depth of the tissue edge can also influence the differences between the regular and irregular tissue boundaries with the hypothesis that edge irregularities may be more significant if they occur superficially.

Chapter 7

Probe misalignment and optimisation

This chapter addresses the RO6, where the effects of the tetrapolar ZedScan^{TM} probe misalignment on the parathyroid measurements and the exploration of different tetrapolar probe configurations in order to enhance the differences between measured thyroid and parathyroid spectra were investigated.

The work presented in this chapter formed the basis of the conference paper presented at MeMeA 2023 symposium titled: 'Computational Modelling of Probe Configurations for Electrical Impedance Spectroscopy-based Differentiation of Thyroid and Parathyroid Tissues' [141].

7.1 Introduction

As introduced in Chapter 1, the ZedScan^{TM} EIS probe is a commercial electrical impedance device which was primarily designed and manufactured for the diagnosis of Cervical Intraepithelial Neoplasia. The novel application of this probe in human thyroid and parathyroid tissue measurements presented by Hilary et al. [3] revealed several limitations of the ZedScan^{TM} device in the clinical environment concerning these tissue types. The encountered limitations, including the probe's long neck and the 5.5 mm tip size, demonstrated that the current ZedScan^{TM} device hardware might not be suitable to precisely cover structures as small as parathyroid glands (3-7 mm). The imprecisions in gland coverage arising from the size of the tetrapolar probe could potentially lead to data 'contamination' by tissues surrounding the glands and could prevent the explicit parathyroid glands identification.

In a potential future ZedScan^{TM} device designs dedicated specifically to the thyroid and parathyroid applications, it might be crucial to modify the current size and separation of

the electrodes in order to improve the ease of the parathyroid glands measurements and increase both tissues separability. To date, computational modelling techniques have been demonstrated to be a useful tool to explore novel EIS probe configurations, especially for the applications relating to cervical epithelium [77] and oesophagus [24].

In this Chapter, the previously developed computational models (Chapter 3) will be employed to explore and quantify the uncertainty associated with the imprecise parathyroid coverage with the ZedScan^{TM} EIS device. Moreover, the potential advantages arising from the probe size optimisation on the parathyroid tissue measurement, and the parathyroid and thyroid glands separability will be further evaluated.

7.2 Methodology

7.2.1 Probe misalignment study

In order to investigate the effects of the imprecise coverage of the parathyroid gland with the tetrapolar probe, models recreating two different scenarios were generated where either one (25% of the probe – Fig. 7.1a) or two (50% of the probe – Fig. 7.1b) of the electrodes are in contact with the parathyroid gland. To further inspect the possible influence associated with the type of contact electrodes (active or passive) on the measured impedance, all possible gland-electrode variations have been constructed. The parathyroids are considered to be surrounded by thyroid tissue for the probe misalignment simulation purposes. The obtained results were compared to the reference parathyroid and thyroid spectra generated and presented in Section 3.5 Chapter 3 in order to assess the relative effect on the tissues separation feasibility.

7.2.2 Electrode configuration optimisation study

In order to investigate whether the current size of the tip of the ZedScan^{TM} device may not be optimal for the parathyroid impedance measurement, a number of configurations considering the probe optimisation have been explored. The simulations have been performed to explore the effect of decreased electrode separation S and electrode radius R (marked in Fig. 7.2) on the measured electrical properties to suggest a configuration that could enhance thyroid and parathyroid separability. Nine different arrangements of electrode separations S=[1.4, 1.2, 1.0] mm and radii R=[0.3, 0.2, 0.1] mm have been investigated in both thyroid and parathyroid tissue models. The reference macroscale model recreates the electrode arrangements of the current tetrapolar ZedScan^{TM} probe with four electrodes (radii R=0.3 mm) arranged with the centres located on a circle of 2 mm diameter (separation S=1.4 mm). For comparison, the variation in electrode size and separation have been tested on models with and without the superficial 0.1 mm fascia compartment as seen in Fig. 3.12 in Chapter 3.

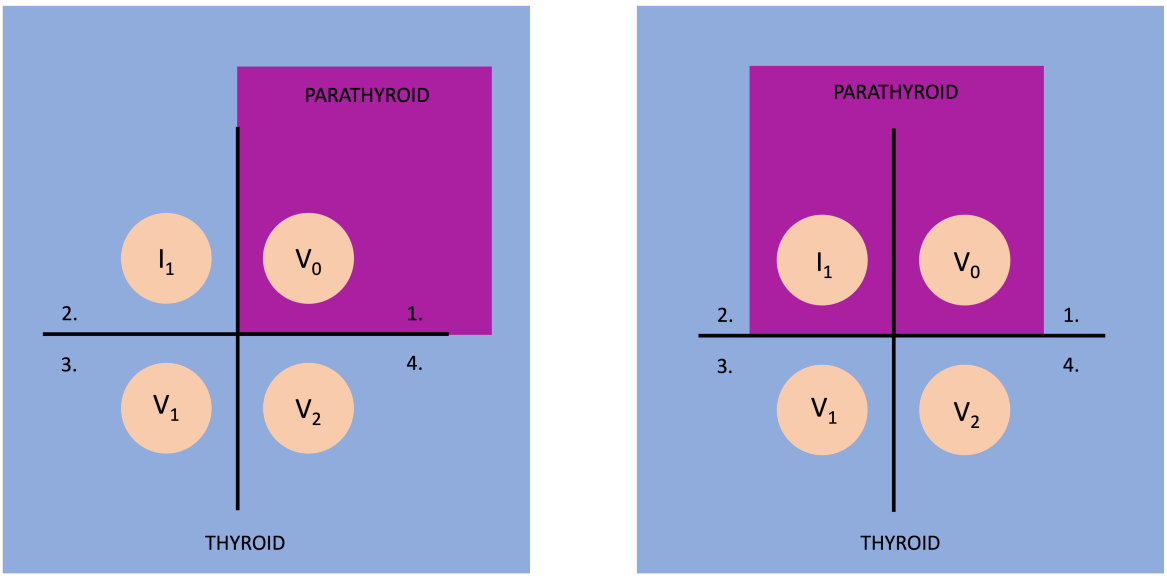

Figure 7.1: *Model schematics for the probe misalignment study illustrating two measurement scenarios when (a) one (25% of the probe) or (b) two (50% of the probe) electrodes are in contact with parathyroid gland, the simulation is repeated for the gland position in quarts 1-4; I_1, V_0, V_1, V_2 correspond to the tetrapolar electrode types*

Since impedance values recorded by the tetrapolar probe are sensitive to its geometrical features which are investigated in this part of the study, it is not sensible to compare the raw impedance data between the various cases. Therefore, the impedivity values were compared instead. These have been obtained through dividing the macroscale impedance results by geometric constants specific to each probe configuration. The latter were acquired through additional calibration simulations by assigning the model with each electrodes' setup with a material of 1 Sm^{-1} conductivity σ and without dielectric properties (0 relative permittivity εr).

7.2.3 Macroscale model characteristics

For the purposes of these probe misalignment and optimisation studies, the macroscale thyroid and parathyroid models have been utilised (Fig. 3.9 and 3.12 from Chapter 3) with assigned material properties obtained from the previous baseline micro- and mesoscale level simulations. For the models including the 0.1 mm superficial fascia layer, the baseline material properties of conductivity σ=0.35 Sm^{-1} and relative permittivity εr=1e5 have been selected.

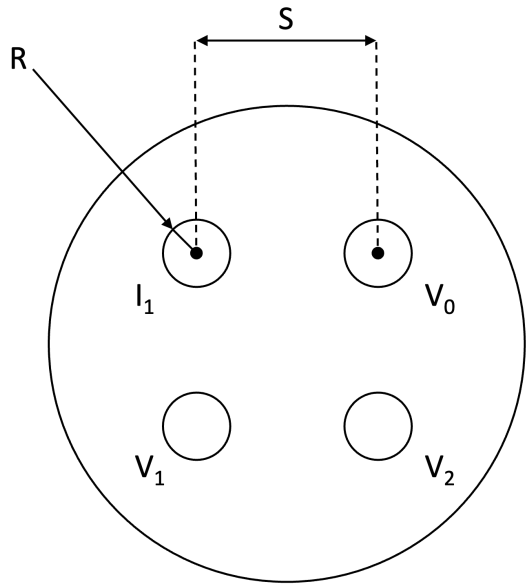

Figure 7.2: *Schematic of the tip of the ZedScan^{TM} probe marking the geometrical characteristics investigated in the probe optimisation study: R – electrode radius, S – electrodes separation; I_1, V_0, V_1, V_2 correspond to the tetrapolar electrode types*

7.3 Results

Eight and thirty-six macroscale simulations were performed for the probe misalignment and probe optimisation studies respectively. Each simulation provided a real part of impedance results at 14 frequencies from the range of 76 Hz – 625 kHz. The impedivity values have been calculated using the calibration constants for all the results from the probe optimisation study. Similarly to the parameterisation method introduced in Chapter 4, to aid the quantitative comparison of the results, each computed spectrum was parameterised with three indices: Z_1 – impedance at 76 Hz, Z_{14} – impedance at 625 kHz and f_{mid} – frequency in the middle of the dispersion (corresponding to the impedance value between Z_1 and Z_{14}).

7.3.1 Impact of the probe misalignment

Fig. 7.3 shows the results of the probe misalignment study with the spectra for different configurations of 50% (green spectra) and 25% (red spectra) probe-parathyroid coverage. Additionally, two reference spectra showing the thyroid (black solid line) and parathyroid (black dashed line) outcomes resulting from the accurate and symmetrical electrode placement were included for comparison. Table 7.1 summarises and compares the selected spectra indices obtained from the probe misalignment study and with the reference thyroid and parathyroid results.

As demonstrated in Fig. 7.3 and Table 7.1, the probe misalignment affects the parathy-

roid impedance values across the studied frequency range and all three spectra parameters Z_1, Z_{14} and f_{mid}. Furthermore, the computed impedance is reduced as the number of electrodes in contact with the parathyroid gland decreases, bringing the 'parathyroid' spectra closer to the reference thyroid result. It is also worth noting that the type of the contact electrode was an influential factor for the 50% probe coverage scenario – the impedance was higher for the mixed (one active and one passive) electrodes relative to the other combinations. Nonetheless, for the setup with a single contact electrode, there was no variation in the computed impedance values with respect to the electrode type. The data summarised in Table 7.1 shows that the imprecise parathyroid coverage reduces not only the real impedance values, but the dispersion frequency f_{mid} as well.

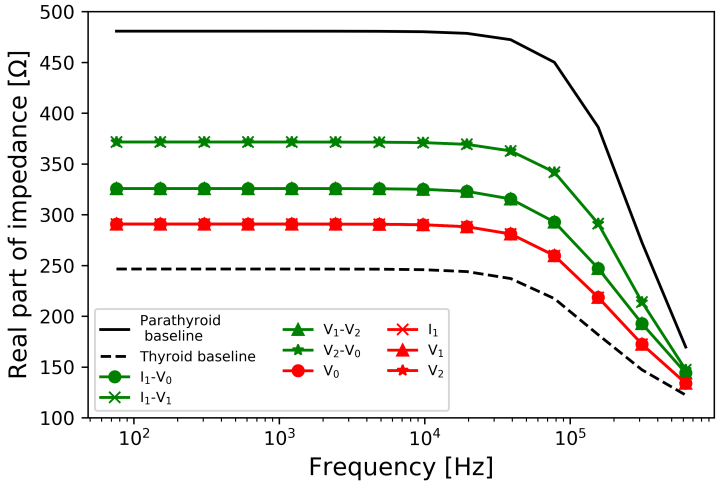

Figure 7.3: *Probe misalignment study results for 50% (green spectra) and 25% (red spectra) of probe-gland coverage, black spectra show the baseline parathyroid (solid line) and thyroid (dashed line) results from simulation with the probe placed symmetrically on the gland, I_1, V_0, V_1, V_2 labels correspond to the electrode types marked in Fig. 7.2*

Probe coverage	Z_1 [Ω]	Z_{14} [Ω]	f_{mid} [kHz]
Parathyroid baseline	480.69 (0%)	169.60 (0%)	240.25 (0%)
Thyroid baseline	246.47 (-49%)	122.31 (-28%)	150.46 (-37%)
50%: I_1-V_1, V_2-V_0	371.54 (-23%)	147.18 (-13%)	220.65 (-8%)
50%: I_1-V_0, V_1-V_2	325.71 (-32%)	144.04 (-15%)	191.37 (-20%)
25%: V_0, I_1, V_1, V_2	290.75 (-40%)	133.96 (-21%)	177.25 (-26%)

Table 7.1: *The quantitative data of the selected spectra indices (Z_1 – impedance at 76 Hz, Z_{14} – impedance at 625 kHz, f_{mid} – dispersion frequency) showing the results of the probe misalignment in comparison to parathyroid and thyroid results from precise (symmetrical) probe placement; I_1, V_0, V_1, V_2 correspond to the electrode types shown in Fig. 7.2, values in brackets show the relative difference to the parathyroid baseline results*

7.3.2 Probe optimisation study

In the probe optimisation study, each separation S and radii R configuration was investigated for both thyroid and parathyroid models, and the obtained impedivity spectra for simulations with and without fascia are shown in Fig. 7.4 and Fig. 7.5 respectively. This resulted in additional thirty-six simulations, nine for each gland and model configuration with and without the fascia inclusion.

Given that the probe optimisation had no impact on the thyroid impedivities in the models without fascia (Fig. 7.4), there is just the thyroid reference curve marked on the graph. Nonetheless, the different probe configurations were demonstrated to have an impact on the parathyroid results. In particular, there is a slight increase in the parathyroid impedivity at frequencies below 100 kHz with the decreased separation S between the electrodes. However, the results at 76 Hz show a difference of only 2.1% and 3.7% higher impedance for the cases characterised with optimised electrode separation S of 1.2 mm and 1.0 mm compared to the default ZedScan^{TM} electrode configuration (S=1.4 mm). In addition, the changes in the electrodes' radii did not affect the obtained impedivities for either tissue type.

Fig. 7.5 shows that including a 0.1 mm fascia layer influences the tissues' impedivity and slightly changes the impact of the electrodes' radius R and separation S on simulated electrical behaviour in comparison to the results obtained from models without this com-

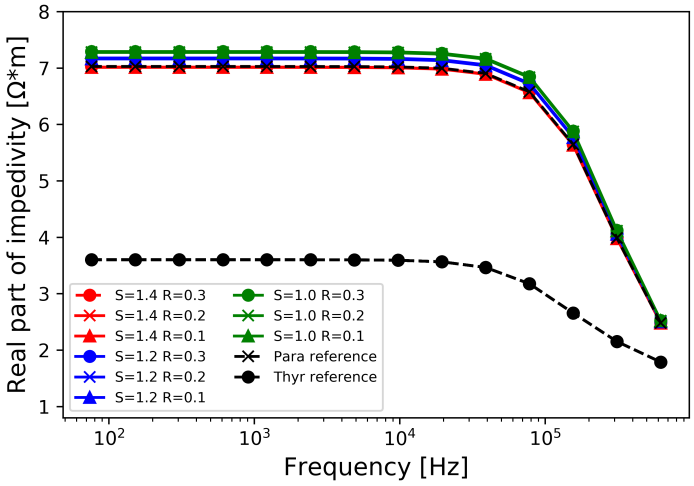

Figure 7.4: *Probe optimisation study results showing the effect of the electrodes separation S and radii R on the computed electrical properties of thyroid and parathyroid using models without fascia*

partment (Fig. 7.4). Firstly, the fascia compartment inclusion in the model reduces the separation between thyroid and parathyroid tissues by overall decreasing the recorded impedivity of parathyroid in the frequency range before the dispersion. It is also responsible for the overlap of the results in the region above 100 kHz between both tissue types. In particular, the difference between thyroid and parathyroid impedivity for the current ZedScan^{TM} configuration obtained through the simulation using models without and with fascia shows the decrease in those glands separation in Z_1: from 95% to 84% at 76 Hz, and Z_{14}: 39% to -24% at 625 kHz, where the percentage difference represents the relative difference of the parathyroid results with regards to the thyroid.

Fig. 7.5 a-d visualises the effects of electrodes radii R and separation S on the thyroid and parathyroid impedivity spectra separately. Fig. 7.5 a and b show the impact of the radius at different electrode separations. These results indicate that the smaller electrode distance increases the impedivity of parathyroid tissue across the investigated frequency range with the decreased electrode size. In addition, Fig. 7.5 c shows that the decreased electrode separation gradually decreases the parathyroid impedivity across all frequency points for the current ZedScan^{TM} electrode radius of 0.3 mm. For the smaller electrode size (R=0.1 mm), as visualised in Fig. 7.5 d, the decreased electrode separation reduces the parathyroid impedivity in the frequency range over 10 kHz. Moreover, the fascia properties result in variation in the simulated thyroid impedivity in the region above 100 kHz for both decreased electrode separation and radii.

A summary of the relative difference in the selected spectra indices between thyroid and parathyroid tissues including the fascia compartment, resulting from all possible variations of separation S and radius R, is presented in Fig. 7.6. As seen in the results, there are three probe configurations where the separability based on all three spectra is improved in comparison to the current ZedScan^{TM} device, and these are: S=1.2mm R=0.2 mm, S=1.2 mm R=0.1 mm and S=1.0 mm R=0.1 mm. Additionally, there is an overall trend in increasing thyroid-parathyroid difference based on f_{mid} parameter with the decreased separation S. The Z_1 and Z_{14} results do not follow any clear, similar pattern, most likely due to the extent of the differences (a few percentage) compared to the differences in f_{mid} (which reach over 200%) and the fact that the fascia layer has a different effect on the current flow through thyroid and parathyroid tissue respectively. It is worth noting, however, that considering the cases with the constant radii, the thyroid/parathyroid difference in low-frequency impedance index Z_1 decreases with reduced separation S.

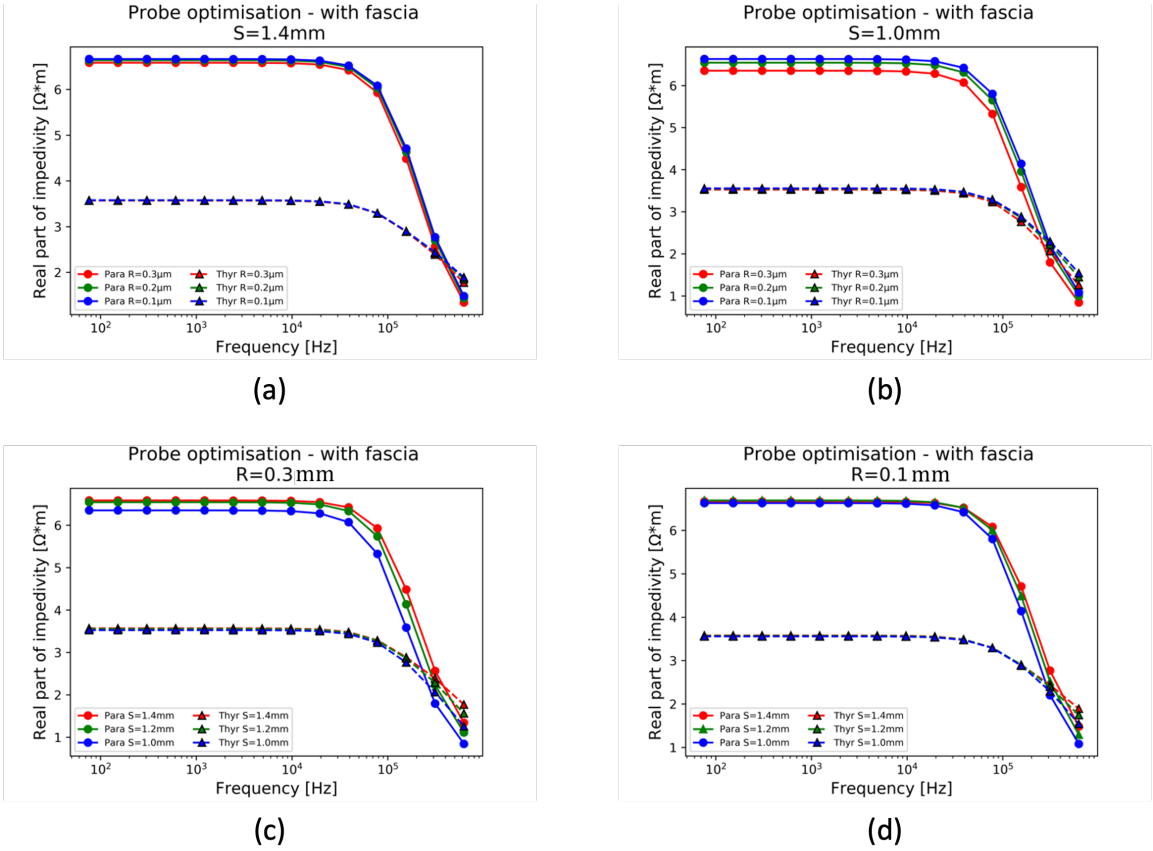

Figure 7.5: *Probe optimisation study results showing the effect of the electrodes separation S and radii R on the computed impedivity spectra of thyroid and parathyroid models including 0.1mm superficial fascia compartment; investigation of radius variations at separation (a) S=1.4mm and (b) S=1.0mm, and investigation of the separation variations for electrode radii (c) R=0.3mm and (d) R=0.1mm*

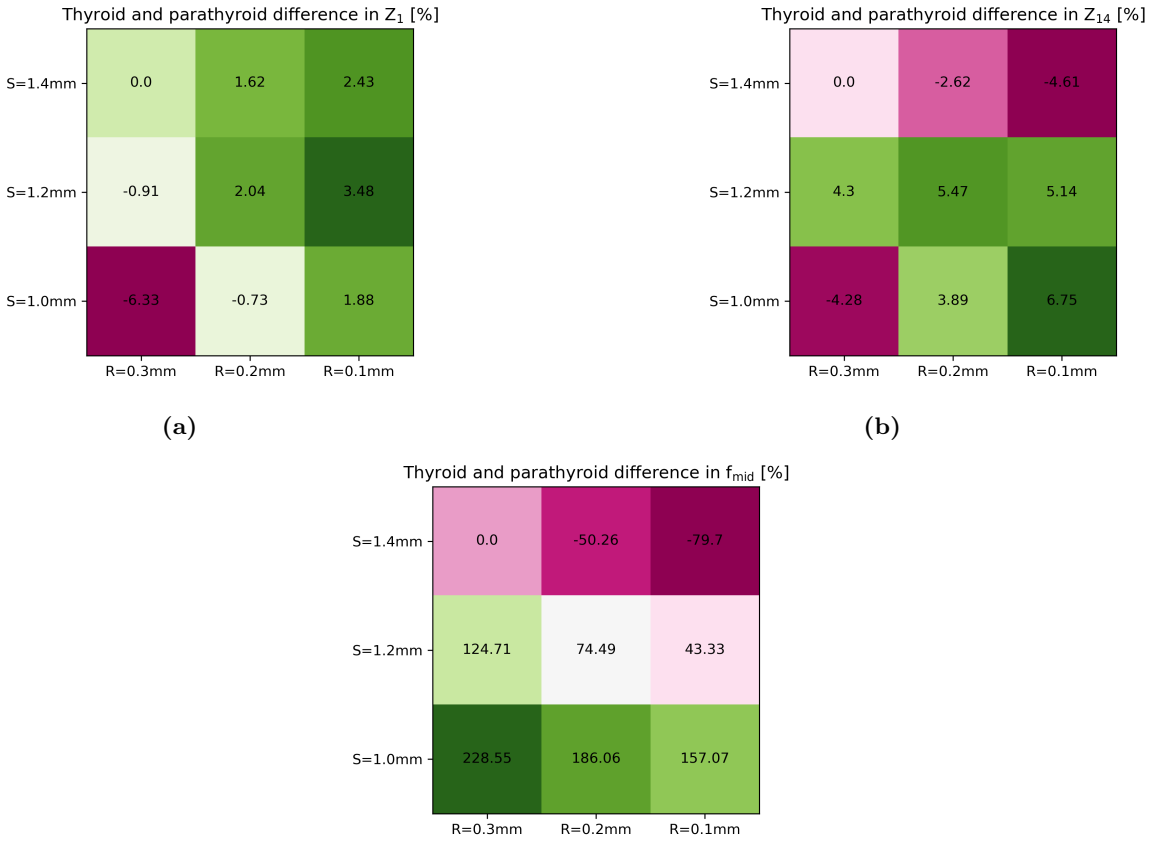

Figure 7.6: *Heatmaps visualising the effect of the electrode radius and separation on the differences in selected spectra indices Z_1, Z_{14} and f_{mid} relative to the default ZedScan^{TM} electrode configuration from the simulation including the fascia compartment into the models*

7.4 Discussion

The purpose of the study presented in this Chapter was the assessment of the parathyroid results variation arising from the inaccuracies in the EIS probe placement to fulfil RO6. Furthermore, the potential advantages on thyroid and parathyroid tissue separability resulting from the smaller size and separation of the ZedScan$^{\mathrm{TM}}$ tetrapolar electrodes were evaluated.

As demonstrated in the probe misalignment study, an inexact coverage of the parathyroid gland could result in lower impedance recordings across the whole studied frequency range compared to the expected (reference) value for parathyroid glands obtained from an accurate probe placement. Furthermore, it can be concluded that successful parathyroid tissue identification can be challenging in the cases of imprecise measurements. As visualised in

Fig. 7.3, the simulations from the misaligned probe cases lead to the 'contaminated' results which gradually get closer to the reference thyroid spectrum instead. By solely comparing the low-frequency index Z_1, the misalignment can reduce the difference in impedance between thyroid and parathyroid from 95% to nearly 18%. That also suggests that imprecise parathyroid coverage could partially explain the wide range of recorded *in vivo* parathyroid results (138.99-572.67 Ω in [3]) along with the effects of inter- and intrasubject variability in the morphology and composition of parathyroid and thyroid tissue investigated in Chapter 4 through local and global sensitivity study. In particular, by solely evaluating the parathyroid results, the probe misalignment can be responsible for a change up to 40% in low-frequency impedance Z_1 index compared to the baseline parathyroid spectrum. Such a difference is comparable to the effect of the parathyroid cell size (x_{cell}) and ECS thickness (d_{ECS}) variations and larger than the isolated effects of the remaining parameters investigated for parathyroid tissue.

Additionally, it is worth noting that the parathyroid spectra from the misalignment study are characterised by decreased impedance exclusively through the assumption that the parathyroid gland is surrounded by a material of lower conductivity such as thyroid tissue. The opposite trend of increased impedance would have been observed in an instance of the gland surrounded by the adipose tissue, known for its insulating properties (low frequency conductivity of 0.04 Sm^{-1} [26]).

It is moreover important to highlight that the ZedScan^{TM} device is equipped with a quality control setting which can detect if the tetrapolar probe was placed on a boundary between tissues with different properties (P. Heighfield, technical director of Zilico Ltd. – personal communication). The principle of the boundary detection is based on the methodology presented in 'Method and Probe for Measuring the Impedance of Human or Animal Body Tissue' patent by Brown and Tidy [142]. In this approach, the quality checks are performed prior to the impedance measurements, where the current is applied to the diagonal electrodes, and the remaining two electrodes measure the resultant potential. The new 'reference' electrodes are in the equal distance from the current path and should provide the same potential measurement in the case of the probe being placed on a tissue type with the same properties. Reference electrodes measurements showing different potential values (with the differences larger than a threshold value of over 10% or 20%) indicate that the probe was placed on the tissue boundary.

The boundary detection setting, however, was disabled in the initial set of the *in vivo* measurements collected by Hillary et al. [3]. Therefore, it is difficult to determine the extent of the impact of the probe misalignment that had on the spread on the parathyroid tissue results. However, due to the small size of the parathyroid glands, the boundary detection setting might prevent or obstruct the parathyroid tissue measurements in the follow-up studies,

therefore, alternative improvements to the EIS device hardware might need to be considered in the future.

An increase in parathyroid impedivities were seen in the probe optimisation investigation without including the fascia compartment (Fig. 7.4) in the cases of decreased electrode separation S. This indicates that measurements with a smaller electrode separation could more effectively distinguish between thyroid and parathyroid tissue for models without fascia. The increase in the impedivity could be explained, that, as a result of the smaller distance between the drive electrodes, I_1 and V_0, the injected current flows more superficially (which was demonstrated previously in the probe size investigations on the cervical epithelium [77]), gets constrained flowing solely through the parathyroid gland without capturing the properties of the adjacent thyroid tissue.

However, the documented extent of the separation improvement (up to 4% change in the low frequency impedance index Z1 compared to the parathyroid results for current ZedScan$^{\text{TM}}$ electrodes configuration) suggests, that the geometry of the tip of the probe is a far less significant factor compared to measurement precision responsible for up to 40% decrease in Z_1 index. Additionally, as demonstrated in Fig 7.4, decreasing the size of electrodes does not interfere with the recorded impedivity, hence, if there are no constraints on the technical and manufacturing side, smaller electrodes could successfully be incorporated into an optimised EIS probe to further improve the measurement accuracy. It is especially important to remember that smaller electrodes are more prone to surface polarisation, that is why a compromise in the size of the electrodes needs to be established in any potential future probe dedicated for parathyroid measurements.

Despite the observation that the optimised size of the tetrapolar probe has the potential to slightly improve the separation between the thyroid and parathyroid, it is important to highlight that this situation only applies when the EIS device is in direct contact with either of the glands. As seen in Fig. 7.5, the presence of just a thin superficial fascia layer (0.1 mm) brings the thyroid and parathyroid spectra closer in the low frequencies (the differences in Z_1 reduced from 95% to 84%). In the meantime, the impedance curves for both tissue types above 100 kHz tend to overlap which reduces the ability to distinguish between both tissue types. Such a situation can be explained by the more superficial current flow through the tissues in the cases of smaller electrode separation and the more conductive properties assigned to the fascia relative to parathyroid. However, further examination of the effect of the electrode arrangement in relation to the relative differences in thyroid and parathyroid selected spectra indices (Fig. 7.6) revealed three configurations that resulted in an increase in all studied spectra indices. These configurations are characterised with decreased radii R and separation S, which further suggests the reduced probe size would be more convenient and practical for the applications in thyroid and parathyroid tissue measurements, even in

the instances where the glands are covered with fascia.

Chapter 8

Discussion and Conclusions

The main hypothesis investigated in this dissertation was that computational modelling is a feasible tool to permit the elucidation of the differences between thyroid and parathyroid tissues based on their predicted electrical impedance. As demonstrated in the previous computational ([38; 74]) and *in vivo* ([72]) research on the electrical properties of tissues, structure and composition are the key factors influencing the frequency dependent impedance magnitude and the shape of the β dispersion for biological tissues. However, assessing the effects of each tissue characteristic on the electrical properties directly from EIS *in vivo* data is difficult since it only represents the bulk electrical properties of the entire examined tissue.

Computational modelling is an approach that allows the exploration of the connection of the tissue features with 'measured' EIS spectra and their indices. In particular, in the presented thesis this relationship is investigated by implementing a finite element multiscale modelling approach. The motivation for a multiscale model methodology application was related to the computational limitations arising from the requirement to include the cell membrane details in the model volume due to their characteristic dielectric properties. To date, the multiscale modelling has been implemented in the studies investigating the Cervical Intraepithelial Neoplasia [38], Oral Potentially Malignant Disorders [41] and skin properties [37; 75]. In this study the multiscale methodology was adapted by generating thyroid and parathyroid specific models from micro- to macroscale interconnected through the propagation of the lower-scale results in the model hierarchy. The multiscale approach was also broadened by including the follicular structures which are unique for the thyroid tissue, and, to date, have not been a subject of any computational multiscale investigation in the field of electrical properties of biological tissues.

The main area of interest of this thesis was the investigation of the tissue morphology and composition with their impact on the impedance spectra using comprehensive inter- and intracompartmental sensitivity analyses (Chapter 4). Moreover, the theoretical spectra were

compared against *in vivo* measured EIS spectra of healthy thyroid and parathyroid glands in order to verify the outcomes of the previously developed multiscale model of thyroid and parathyroid tissues (Chapter 5). The tissue separability based on computed and *in vivo* measured spectra indices was also presented and discussed in the same chapter. Following the outcomes of these investigations, additional simulations evaluating the homogeneity assumptions on the thyroid meso- and macroscale models were performed (Chapter 6). Furthermore, the assessment of the impact of the EIS measurement inaccuracies on the parathyroid results along with the examination of alternative electrodes configurations to suggest a potential enhancement in the thyroid and parathyroid tissues separability were presented in Chapter 7.

The main findings drawn from the study discussed in this thesis are outlined in this chapter, along with the discussion of the suggested future work directions.

8.1 Summary and main findings

8.1.1 RO1: Computational modelling of electrical impedance of thyroid and parathyroid tissue

As presented in Chapter 3 and 4, computational modelling is a feasible tool that can predict the electrical behaviour of biological tissues and can evaluate the relationship between these tissues characteristics and the resultant variations in the electrical impedance spectra on the example of healthy thyroid and parathyroid tissues. The electrical behaviour prediction permitted the assessment at each level in the tissue hierarchy by recreating the specific geometries of all substructures from the micro- to macroscale as presented in Chapter 3.

The electrical impedance results for the thyroid and parathyroid tissues obtained with the default setup of the model parameters showed that the parathyroid tissue impedance is anticipated to be higher than the thyroid tissue in the frequency range between 76 Hz and 625 kHz (frequencies corresponding to the ZedScan^{TM} device operating range).

8.1.2 RO2: Model results verification against *in vivo* measured data

The computed results verification performed against the *in vivo* measured healthy thyroid and parathyroid spectra (collected and published by Hillary et al. [3]) revealed a good agreement across all frequencies between the computed and *in vivo* measured EIS datasets, which confirms reliability of the proposed modelling methodology. A small number of outliers in the computed results (seen in Fig. 5.2 in Chapter 5) represent curves that were computed with either very high relative permittivities of fascia or connective tissue compartments or small extracellular space thickness values. The investigation of the wide ranges of these parameters which affects the EIS computed results was necessary due to the uncertainty in

these parameters reported in the literature. The remaining discrepancies observed between computed and *in vivo* measured results, especially in the high frequency impedance (Z_{14}) and the dispersion frequency (f_{mid}), similarly could be impacted by the insufficient experimental data on electrical properties of biological materials found in the literature. Nonetheless, it is possible that additional tissue, and surgery specific aspects (that were not considered in this computational study) could have contributed to the discrepancies. In particular, factors, such as presence of different tissues, structures or pathologies [3; 34; 143], the effects of temperature [144], glands' activity [101], viability [3; 2] and hydration [145] of the tissues were excluded from the scope of this thesis, however, have the potential to be responsible for the observed discrepancies with the *in vivo* measured results.

8.1.3 RO3: The Evaluation of thyroid and parathyroid tissue separability

The sensitivity study presented in Chapter 4 demonstrated that computational modelling can elucidate the distinguishing features between thyroid and parathyroid tissue EIS spectra that are driven on by their differences in morphology and composition. Taking into account the set of multiscale model evaluations for thyroid and parathyroid tissues computed through the variation of the geometrical parameters characterising features at multiple spatial scales demonstrated a promising qualitative (Fig. 5.6 Chapter 5) and quantitative (Fig. 5.7 Chapter 5) separation of these tissues based on three computed spectra indices: low and high frequency impedance (Z_1 and Z_{14}) and the dispersion frequency (f_{mid}). The computed data therefore, suggest that the thyroid and parathyroid tissue separability based on the EIS spectra indices should be achievable.

Despite a positive agreement between the *in vivo* experimental results and the computed impedance spectra, there is a clear overlap between the thyroid and parathyroid spectra indices derived from the *in vivo* measured EIS curves (Fig. 5.6 Chapter 5) which results in poorer tissue qualitative separability in comparison to the simulated results obtained in this study. Such a situation is a result of a dataset very limited in number of the *in vivo* measurements and suggests that EIS based differentiation between thyroid and parathyroid tissue in the clinical environment remains challenging. Additional *in vivo* data collection, will be, therefore, recommended for future thyroid and parathyroid EIS-based separability investigation. Nonetheless, the classification study revealed that the thyroid and parathyroid tissue separability (AUC of 0.97 and 0.89 for computed and *in vivo* measured results respectively) based on the impedance selected spectra indices is comparable to the ones reported for differentiation of Cervical Intraepithelial Neoplasia from healthy tissues using EIS measurements (AUC of 0.95 and 0.88 for the separation based on two different Cole parameters) [72] and combined EIS with colposcopy methods (AUC of 0.887) [137].

8.1.4 The investigation of factors influencing electrical properties of thyroid and parathyroid tissues

In this study, several groups of factors influencing the computed electrical behaviour of thyroid and parathyroid tissues have been selected and investigated. Table 8.1 and Fig. 8.1 show the summary of the results obtained in all previously discussed substudies (presented in Chapters 4-7) in a form of coefficient of variation (CoV). CoV is a relative measure of the data dispersion around the mean value and is derived as a ratio of standard deviation and mean values. This coefficient is an advantageous tool to compare the relative extent of the variation and spread of the results from different datasets, especially useful for the results comparison obtained in different sections of this computational study. Moreover, through this evaluation it is possible to assess the contribution of each parameter group to the overall computed results variability.

In the following sections, all examined groups of parameters, which are: morphological features, electrical properties, effects of tissue homogenisation assumptions, and effects of probe misalignment and optimisation, will be restated and evaluated in the context of the remaining findings of this thesis.

8.1.4.1 RO4: The effects of geometrical and electrical properties variations

Two separate sensitivity analyses methods (local and global) revealed the extent of the theoretical EIS results deviations due to the variations in the geometrical parameters (associated with natural variability in sizes of tissue structures across the multiscale) and the electrical material properties uncertainties (arising from poorly defined and measured electrical properties of colloid, connective tissue and fascia). The results indicate that of the geometrical parameters investigated, the extracellular space thickness, cell sizes and fascia thickness have the most significant impact on all three explored electrical impedance spectra indices for both tissue types. Both thyroid and parathyroid results also exhibit significant sensitivity to the uncertainties in the fascia electrical properties. Additionally, it was revealed that the size of the follicle and the colloid conductivity uncertainty are important factors when assessing the thyroid tissue impedance.

Furthermore, the evaluation of the coefficient of variation calculated for each results group (Table 8.1) shows that the geometrical parameters variations are most notably responsible for the variation in all three investigated spectra indices (Z_1, Z_{14} and f_{mid}) for thyroid tissue and the variation in low- (Z_1) and high frequency (Z_{14}) impedance for parathyroid tissue. It is worth highlighting that there are differences between the simulation results obtained through the variation of geometrical parameters including and excluding the fascia compartment. In particular, these outcomes further accentuate the importance of the fascia compartment excision during surgery due to its capability to 'contaminate' the true EIS measurement of both

Parameter group investigated	Z_1 [Ω]	Z_{14} [Ω]	f_{mid} [Hz]
Thyroid			
Geometrical parameters (fascia included)	0.35	0.55*	0.40*
Geometrical parameters (fascia excluded)	0.47*	0.16	0.40*
Electrical material properties	0.29	0.58*	0.21
Follicular arrangement	0.0041	0.0003	0.0075
Uneven boundaries	0.020	0.008	0.005
Parathyroid			
Geometrical parameters (fascia included)	0.23	0.79*	0.39
Geometrical parameters (fascia excluded)	0.31*	0.19	0.26
Electrical material properties	0.05	0.82*	0.47*
Probe misalignment	0.23	0.10	0.14
Probe optimisation'	0.04	0.08	0.04

Table 8.1: *Coefficient of variation comparison between the results from all computational substudies presented in this thesis defining the impact of each parameter group on the selected spectra indices (Z_1, Z_{14}, f_{mid}), * marks the highest coefficient of variation for each thyroid and parathyroid spectra index, ' the CoV was calculated for the results of simulations that excluded the superficial fascia layer*

glands. In contrast, the material property uncertainties most significantly influence the variation in the high frequency impedance (Z_{14}) for both tissue types and the spectra frequency (f_{mid}) for the parathyroid tissue.

The presented comparison of the local and global sensitivity analyses highlighted the value of a local approach in preceding and supporting a global analysis. In particular, the advantageous time efficient parameter screening method permits to limit the number and range of the key parameters that will be included in a more comprehensive analysis. In addition, the similarity of the outcomes from the local analysis matches with the global sensitivity results, suggesting that both approaches were appropriate for the purpose of assessing the model sensitivity to the geometrical parameters variability and electrical properties uncertainties. Nonetheless, expanding the presented sensitivity study using the variance decomposition methods (such as the Sobol analysis) and enhanced by the implementation of a surrogate modelling approach

could further verify and improve the sensitivity evaluation of the presented multiscale model of thyroid and parathyroid tissue.

Surrogate modelling using Gaussian process emulators has been successfully implemented to investigate the model sensitivity investigating the cardiac cell electrophysiology [132] or four chamber heart hemodynamics model [146]. Both studies performed a global sensitivity analysis using the variance-decomposition methods with relatively low number of model evaluations (220 and 180 for the cardiac cell model and the CFD heart model respectively). The benefits of decreasing the computational time to obtain the model results using the surrogate model are especially evident in the heart hemodynamics study, where each patient-specific CFD model required 10-20h to obtain the simulation outcomes of 4 heartbeats per case (which resulted in 7700h of computational time). By contrast, the Gaussian process emulator training and the global sensitivity study comprising a sample size of 10,000 required 5h to compute. The challenges with the surrogate model approach are finding the optimal number of model evaluations required for the emulator's training which might be time consuming, and the decreased efficiency in the case of a high number of input parameters considered.

8.1.4.2 RO5: The effects of tissue heterogeneity

The aim of the verification of the homogeneity assumptions on the meso- and macroscales was to investigate the effects of different spatial arrangement of follicles in the thyroid tissue and tissue boundary irregularities. The presented results revealed that, especially with the comparison to the remaining parameters inspected in this study (Table 8.1), both features resembling tissue heterogeneity have a marginal impact on the variation of the investigated spectra indices. The effects represented by the coefficient of variation of the follicular arrangement and irregular boundaries on the thyroid spectra indices was one and two orders of magnitude smaller when compared to the CoV obtained from the investigation of geometrical and electrical properties. Although it is important to further explore more complex geometries to better understand the impact of heterogeneity on the electrical simulation outcomes in the future studies, in particular due to the small number of heterogeneous models investigated in this study and the low follicular volumes considered in the mesoscales arrangements investigation. The tissue heterogeneity should be further explored especially by considering more sophisticated model generation based on morphology segmentations which will be discussed in the following sections.

Additionally, the proposed study concerning the tissue boundary irregularities despite having a marginal effect on the thyroid impedance, could be implemented in future in similar studies concerning different tissues. In particular, this methodology could be beneficial in the investigation of electrical properties of tissues that are characterised with 'grooves' in their morphology or in the transition between different tissue layers, broadening the studies on the

oesophageal glandular mucosa [24] or rete pegs in the oral tissue [41].

8.1.4.3 RO6: The effects of probe misalignment and optimisation

The exploratory simulations investigating the inaccuracies in parathyroid glands measurements with the tetrapolar ZedScan^{TM} device reported a significant variation of results arising from different extents of probe misalignment, especially in the frequencies below the β dispersion. As shown in Table 8.1, the extent of variation in the low frequency impedance (Z_1) associated with the misalignment is equivalent to the results variations associated with variability of geometrical parameters (CoV of 0.23). This suggests that measurement inaccuracies have a comparable effect on the spread of results as geometrical parameters, making them an important factor to consider, in particular, by highlighting the importance of the parathyroid measurement accuracy in the follow-up *in vivo* measurements.

The electrode size and separation optimisation study has been performed as a continuation of the misalignment investigation in order to explore the potential benefits coming from a decreased size and separation of the electrodes on the tip of the tetrapolar ZedScan^{TM} device. The results demonstrated that the EIS spectra are insensitive to electrode size differences in both tissues without the superficial fascia layer. In contrast, a decreased separation of the electrodes provides a slight improvement in the thyroid and parathyroid separation, however, the improvement of the results is minimal (CoV is an order of magnitude smaller) when comparing the coefficient of variation between the probe optimisation results with the geometrical parameters and electrical properties. Nonetheless, it is important to note that the smaller tip of the probe resulting from a reduced separation of electrodes could be advantageous during surgery in order to increase the ease of the electrical impedance acquisition from small structures, such as the parathyroid glands, and reduce the likelihood of misalignment. However, in the future manufacturing process concerning the EIS device it is important to bear in mind the challenges associated with the increased electrode-tissue surface impedance which is an issue concerning electrodes of a smaller size [26]. Additionally, a potential direction for future work is the exploration of non-tetrapolar electrode configurations which could provide more insight on the measurement technique that could enhance tissue differentiation during thyroid and parathyroid surgery.

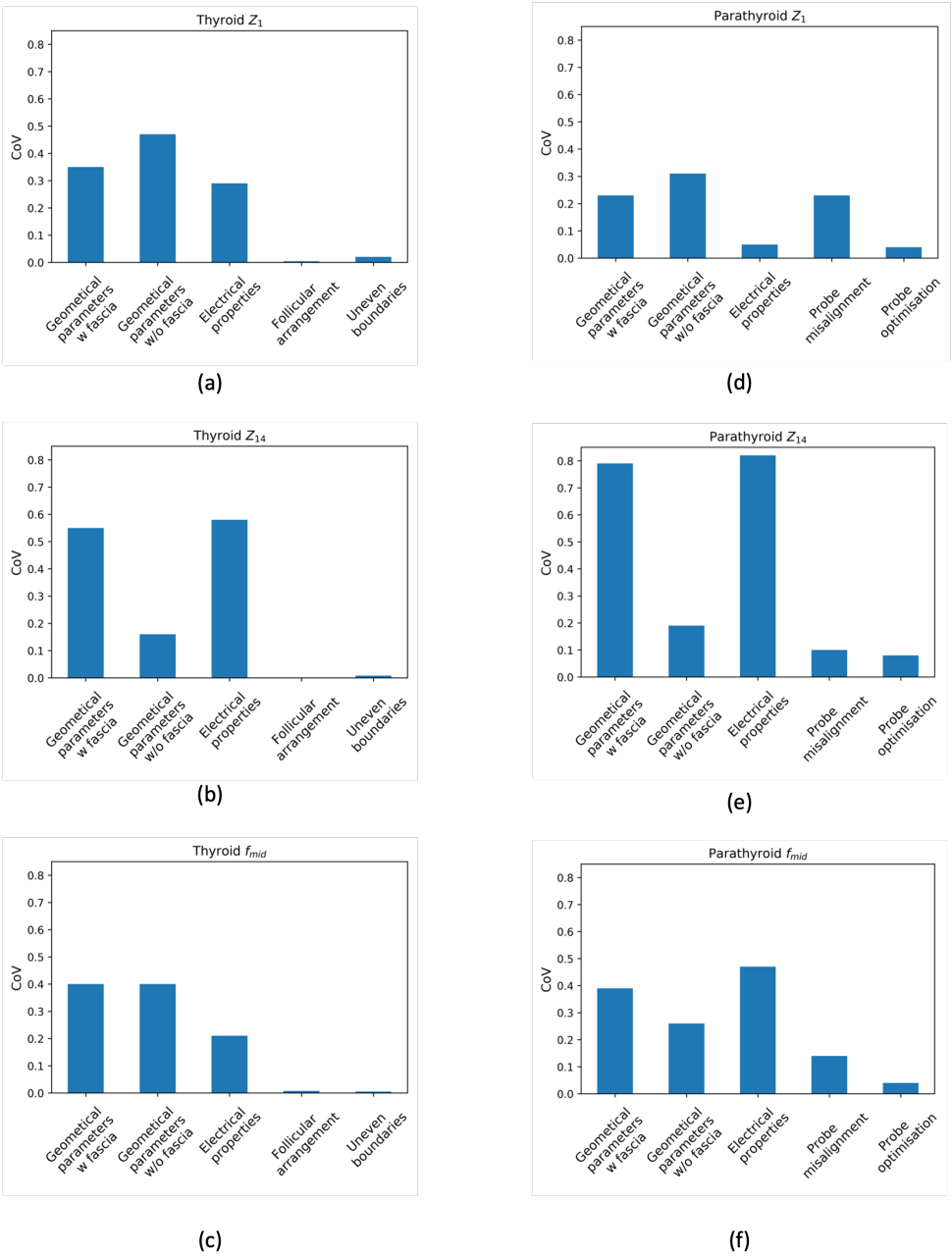

Figure 8.1: *Visual representation of the Coefficient of Variation for (a)-(c) thyroid and (d)-(f) parathyroid tissue impedance spectra indices (Z_1, Z_{14}, f_{mid})*

8.2 Limitations and future directions of the project

8.2.1 Model validation

Despite the promising agreement between the computed and *in vivo* measured EIS spectra (presented in Chapter 5), it was not possible to perform the comprehensive model validation. The ability to perform model validation was mostly restricted due to the limited number of the available *in vivo* measured thyroid and parathyroid impedance spectra and the lack of existing histology images of the tissue samples on which the EIS measurement was performed.

Moreover, it is further challenging to augment the available *in vivo* measured dataset with the measurements from other studies documenting thyroid and parathyroid electrical properties. It is difficult to compare the impedance measurements from different studies since each separate research study has been conducted with distinct methodologies, instrumentation and in different conditions while exploring different frequency ranges. In particular, due to the differences in the EIS instrumentation and the impact of the electrodes arrangement on the resultant impedance, it is not possible to compare the raw data without their conversion to the electrical conductivity/impedivity or relative permittivity values. The comparison of impedivity results shown in Fig. 5.8 in Chapter 5 revealed the discrepancies between this study results with the thyroid spectra provided by Hillary et al. [3] with the remaining limited data from modelling and experimental studies investigating electrical properties of thyroid.

In order to fully validate the proposed computational model, it will be necessary to gather a larger, coherent dataset of *in vivo* measured electrical impedance spectra of thyroid and parathyroid tissues in future studies. Furthermore, in order to associate each *in vivo* measured spectrum with a corresponding computed curve, it will be necessary to obtain case specific tissue features for each computational model evaluation. Knowing the significance of the tissue morphology on the electrical impedance of tissues provided by the results presented in this thesis sensitivity analysis, it would be desirable to derive the geometrical parameters for each individual case, e.g. from histology images obtained from each patient. Nonetheless, for the purposes of the model validation and with the ethical considerations to minimise the necessity of invasive biopsy on healthy human tissues, the additional EIS measurements and the histology samples collection possibly could be performed on an animal model. An additional comprehensive dataset, similar to the one for the rabbit tissues published by Antakia et al. [2], comprising EIS *in vivo* measurements with corresponding histology images would be adequate to perform the thyroid and parathyroid computational model validation. The challenge associated with the EIS measurements of the rabbit structures is the smaller size of thyroid and parathyroid glands in comparison to the human organs. In particular, the decreased thickness of thyroid gland (approximately 2-3 mm in rabbit against 2.5 cm in human thyroid) would require the inclusion of the structures underneath the thyroid gland

in the macroscale model, such as cartilaginous trachea. Additionally, the presence of a thyroid capsule comprising layers of adipose and fibrous tissue [147] might also be required for consideration in the computational model of rabbit thyroid tissue.

Another alternative to invasive biopsies from healthy tissues for model validation is the implementation of tissue engineering, which is predominantly used and explored in regenerative medicine and aims to restore and improve the functionality of a given organ after an in vitro derived graft implantation. There are examples in the literature demonstrating a successful reconstruction of a functional thyroid follicular structures [148] and parathyroid tissue patches [149] using bioprinting methods. Tissue engineered samples of thyroid and parathyroid tissue could be used for both *in vitro* EIS measurements and subsequent histology images analysis for the computational model validation without the requirement of human or animal tissue biopsies.

8.2.2 Model geometries

The presented geometries incorporated in the multiscale modelling framework for both thyroid and parathyroid tissue represent very simplified shapes of cells and follicles under the homogeneity assumption. Despite demonstrating the low impact of the follicular arrangements on the thyroid mesoscale impedivity, it would be desirable to study more realistic geometrical representation of the tissue morphology and the 3D organisation of the tissue structures. Especially since the follicular arrangement study explored a narrow range of follicular volume ratios of the thyroid tissue due to the challenges in achieving higher densities.

A feasible starting point would be to adapt the segmentation methods that are already established and utilised in other fields of computational modelling and bioengineering. Unfortunately, just as vital as CT and MRI imaging are in mechanical engineering in musculoskeletal applications, their resolution is insufficient for the reconstruction of the microstructure of thyroid and parathyroid tissues. Furthermore, due to the dielectric properties of cellular membranes, it is necessary to include cellular features in modelling work when investigating the electrical properties of biological tissues. Therefore, it is crucial to identify an imaging technique with high accuracy (of a few hundred nanometres) that permits cellular and follicular level segmentation. There are two technologies worth considering in the morphological segmentation in the future work, and these are standard 2D or 3D histology images or optical coherence tomography imaging.

As mentioned before, a constraint associated with obtaining patient-specific histology samples is the invasive nature of biopsy itself. Nonetheless, due to the accessibility of previously collected histology data (K. Hunter – personal communication) and wide collection of histology data published in the literature (including virtual pathology databases such as [150]),

follicular segmentation from generic images could be a good starting point for the investigation of more realistic and heterogeneous follicular structure. Fig. 8.2 presents an attempt to recognise the contours of follicles from a histology image with an open-source image processing software Fiji (ImageJ) [151] with its Morphological Segmentation setting aimed for biological images segmentation, labelling and analysis. The limitation of follicular structure segmentation presented in Fig. 8.2 is the lack of cell layer and connective tissue compartments. Nonetheless, with further modifications to the segmentation methodology and the incorporation of 3D images, histological image analysis could be a viable approach for realistic thyroid tissue mesoscale geometries that could be incorporated into the multiscale modelling framework.

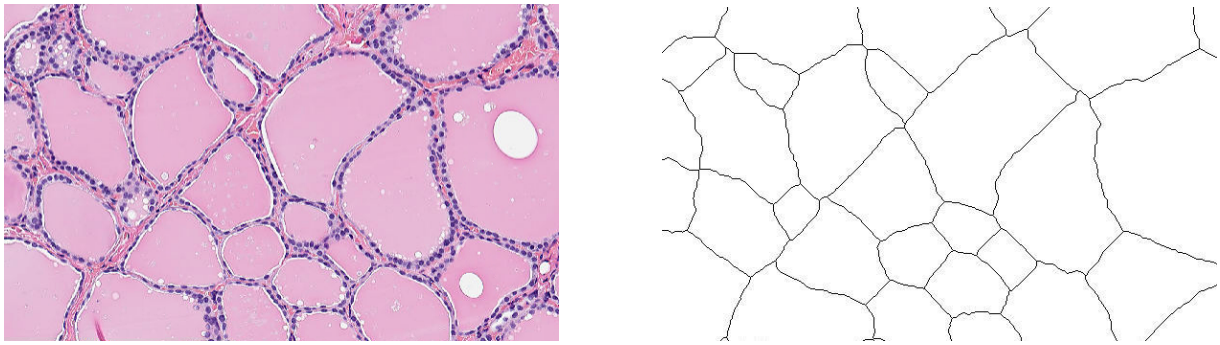

(a) **(b)**

Figure 8.2: *Follicular structure segmentation example, (a) thyroid histology image, stained with eosin and haematoxylin (K. Hunter – personal communication), (b) follicular structure contours recognised with Morphological Segmentation operation in Fiji*

The feasibility of a segmentation approach based on histology has already been demonstrated in the studies of tissue reconstruction utilising this imaging technique to recreate the heterogenous structure of tissues. In particular, Lv et al. [79] introduced the heterogeneous follicular structure segmentation from 2D histology images in the first computational model proposed in the literature, created to explore electrical and heat transmission properties of thyroid tissue during electroporation. It was, however, not possible to compare the results of this study with the thyroid simulation outcomes provided in this thesis due to the modelling limitations presented in Lv et al. [79], which included disregarding the cellular features in the model and using a direct current simulation.

Additionally, worth mentioning are studies using deep learning methods in blood vessels segmentation from 3D histology [152] or segmentation of hepatic steatosis [153] from 2D images. The latter, due to their spherical shapes, show some structural similarities to thyroid follicles. Both papers highlight the benefits of the unsupervised machine learning methods in

image analysis and morphological segmentation, which could be considered in future studies when addressing the thyroid tissue heterogeneity.

An important consideration of the histology imaging for the morphology is the shrinkage and distortion of the tissue structures associated with the preparation of the histology samples [154]. These types of alterations in the tissue structures impose restrictions on the reliability of the microstructural information that can be obtained from the histology images and are necessary to be accounted for and minimised in the future morphology segmentation.

In contrast to histology imaging, optical coherence tomography (OCT) is a non-invasive imaging method with the typical transverse resolution of a few to dozen micrometres and the depth penetration of a few millimetres (1-3 mm) [155]. OCT was previously documented as a successful 3D imaging technique of thyroid tissue, visualising the follicular structure in case of healthy and pathological thyroid tissue [156; 157]. Considering the non-invasive nature of the OCT imaging, which utilises the broadband near-infrared light to create microstructure images, this technique could be safely incorporated to assist the EIS measurements during thyroidectomy. This imaging approach could also be a feasible alternative to the histology samples acquisition via invasive biopsy procedure. From the computational perspective, however, the depth penetration provided by OCT imaging could be a limitation in the thyroid image segmentation, especially since the presented macroscale model geometry represents a tissue volume of 15 mm. However, even a few millimetres of model volume segmented from the OCT imaging could be sufficient for the mesoscale structure investigation. Knowing the constraints of low follicular densities in the developed model geometries, it would be especially useful to utilise OCT-based model segmentation for the follicular arrangements in order to verify the previously obtained results and methodologies.

8.2.3 Geometrical and electrical model properties

As revealed in the sensitivity analysis and by the comparison with the outcomes of the remaining substudies in this thesis, the variations in morphology and the uncertainties in the electrical material properties are the most prominent groups of tissue features that influence the macroscale electrical impedance. As highlighted in Chapter 3, it is often challenging to obtain reliable model parameters of thyroid and parathyroid tissue, especially in the cases of the extracellular space thickness or for the electrical properties of colloid and fascia, which had to be estimated and their 'real' values remain unknown. Given the outcomes of the sensitivity analyses, both thyroid and parathyroid macroscale impedance spectra are sensitive to these three key parameters. Therefore, the lack of sufficient material property measurements and the high-resolution microscopy images of thyroid and parathyroid tissue structures continue to be a significant challenge which impacts the accuracy of the model predictions. Additional experimental work concerning the elucidation of the properties of colloid and fascia, and in-

vestigation of the ECS thickness of thyrocytes and chief cells is, therefore, advised and will be crucial in the future for the reliable quantification of thyroid and parathyroid impedance. Moreover, the overall lack of the electrical properties measurements of the biological material, the wide variation of these parameters where they are reported and the insufficient information considering the measurement conditions remains a significant challenge in computational modelling of electrical properties of tissues.

8.2.4 Data presentation

In electrical impedance investigation studies concerning biological materials, it is often a common practice to assess the tissues impedance by visualising the real part of impedance changes against the frequency, also known as the real impedance Bode plot. This data presentation was also a preferred approach in this thesis due to the convenience for the *in vivo* measured data comparison. Nonetheless, in the fields of material science and electrochemical engineering, where electrical impedance spectroscopy methods are commonly used, different data presentation methods are utilised for different applications. In example, the relationship between frequency-dependent real and imaginary part of impedance (Z' and Z") is often analysed in a form of a Nyquist plot or the complex impedance is transformed into and presented in three different formalisms: admittance Y^*, electric modulus M^* and complex capacitance C^*. A comprehensive summary of various equivalent circuits and schematics visualising behaviour of different materials using different complex impedance formalisms is presented in a thesis by Heath [42].

In future work, it would be valuable to explore different complex impedance formalisms and data presentation methods in order to extract additional parameters that could characterise and potentially differentiate thyroid and parathyroid tissues based on the *in vivo* measured impedance. The Nyquist plot, for example, takes a semi-circular form for an equivalent circuit consisting of a resistor and a capacitor connected in parallel, which is an equivalent model that frequently represents the behaviour of biological structures. The Nyquist plot is especially convenient to define the relaxation frequency (where $f = RC\omega$), which is represented by the highest point of the semicircle.

Fig. 8.3 shows the Nyquist plots of *in vivo* measured data collected by Hillary et al. [3] and the data computed in this thesis through the variation in geometrical parameters. The semi-circular shape of the curves can be recognised in the computed data and in a few curves from the *in vivo* experimental examples. There are a few instances in the *in vivo* measured spectra (especially visible in the thyroid tissue group – Fig. 8.3 a) where Nyquist plot's shape reveals the appearance of a beginning of a second semi-circle. Such a situation suggests a more complex equivalent circuit behaviour of two parallel resistors and capacitors connected in series. This equivalent circuit is characterised with two distinct relaxation frequencies

that suggest multiple current paths through the tissues and layered structure of tissues with different properties.

Nonetheless, the Nyquist plots presented in Fig. 8.3 show the limitation of this data presentation for the currently available set of *in vivo* measured and computed results, mainly that the frequency range investigated in this study (up to 625 kHz) is not sufficiently broad to observe the full characteristic semi-circular shape. This is most prominently visualised in Fig. 8.3 c, where most of the *in vivo* measured parathyroid curves do not represent the characteristic shape. This suggests that collecting *in vivo* measured impedance in a higher frequency range for the Nyquist plot analysis would potentially provide additional information to discriminate thyroid and parathyroid tissue. The benefits of exploring a higher frequency range in future *in vivo* measurements could also permit the Cole-Cole model (Eq. 2.9 Chapter 2) fitting to extract the Cole parameters which is the golden standard in impedance spectra parameterisation.

To summarise, exploring different complex impedance data presentation methods and complex impedance formalisms could potentially increase understanding of the differences in the electrical properties of thyroid and parathyroid tissue. This will permit identifying additional impedance spectroscopy-based parameters which could provide a more favourable separation of these two tissue types compared to the spectra parameters evaluated in this study.

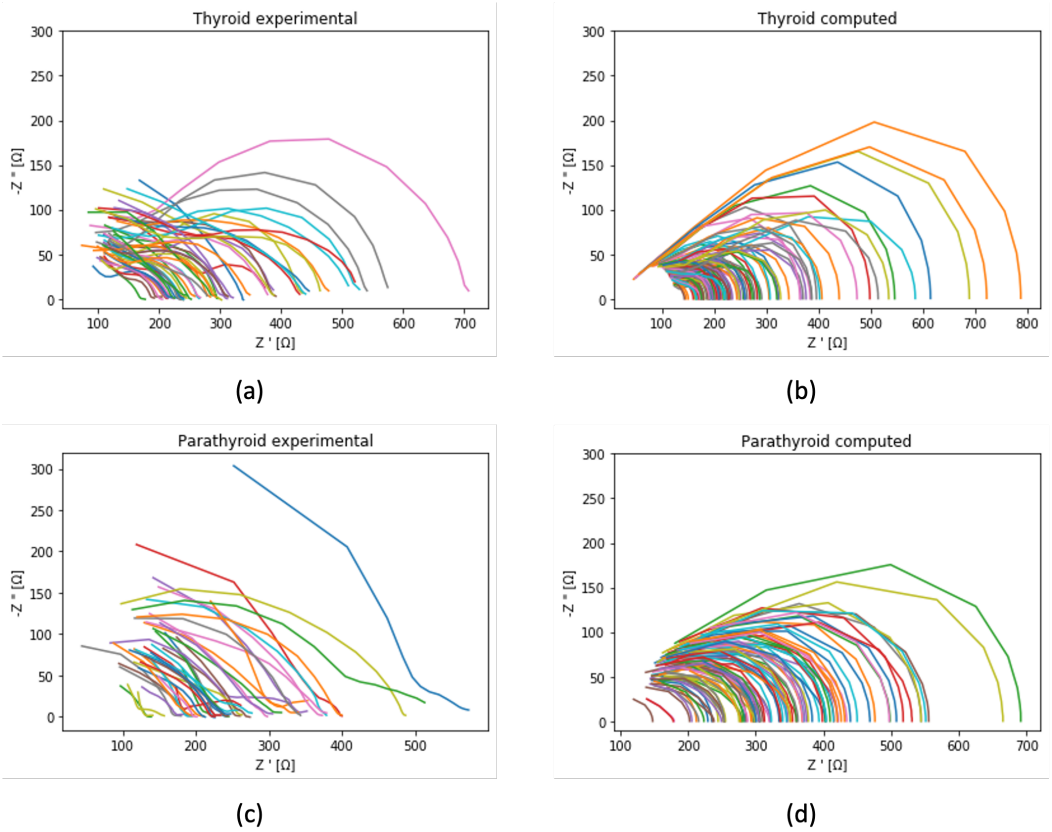

Figure 8.3: *The comparison of Nyquist plots for: (a) in vivo measured thyroid results, (b) computed thyroid results, (c) in vivo measured thyroid results, (d) computed thyroid results*

8.2.5 Discrimination of other tissue types

The main aim of the presented thesis was the comparison of the computed electrical properties of healthy thyroid and parathyroid tissues. However, as Hillary et al. [3] mentioned, the parathyroid glands can be mistaken for soft tissue structures other than benign thyroid tissue nodules, such as adipose or lymphatic tissue. The consideration of additional tissue types in the future experimental and modelling work would provide a more comprehensive group of properties. This would further aid the definition of the benefits and limitations associated with EIS-based parathyroid detection during thyroidectomy.

Nonetheless, some of the limitations associated with the *in vivo* measurements and the modelling work on adipose and lymphatic tissue can already be recognised. Firstly, adipose tissue is characterised by a very low conductivity which is approximately one order of magnitude lower than the other soft tissue types found in the neck, according to the results presented by Gabriel [26] (low-frequency thyroid conductivity: 0.50 Sm^{-1} against adipose tissue con-

ductivity: 0.04 Sm^{-1}). The substantial differences in tissue conductivities could in theory be advantageous to distinguish the adipose tissue. However, high tissue resistivity can cause difficulties in data acquisition using the EIS ZedScan^{TM} probe, which was discussed by Hillary et al. [3]. Increasing the complex impedance acquisition range could permit impedance measurement for tissues with very widespread conductivities, nonetheless, it would require additional improvements in the ZedScan^{TM} instrumentation.

Secondly, other structures worth considering in future investigations are lymph nodes which are typically slightly larger than parathyroid glands (about 1 cm in diameter). Lymphatic tissue is highly heterogeneous, consisting of various types of cells with different arrangements, functions and sizes. Additionally, different morphological structures are located in the convex and concave halves of the nodes, which would be challenging to reconstruct in the future computational work.

Finally, the presented multiscale modelling framework for thyroid and parathyroid tissues could also be adjusted and utilised to investigate the impedance changes induced by different pathologies of these two glands. In example, Yun et al. [22] and Cheng and Fu [61] have already experimentally investigated the EIS based detection of cancerous changes in the thyroid tissue. It could be an interesting direction and an application of the generated models to explore how the cancer-induced changes in follicular sizes and arrangements could impact the thyroid tissue impedance and how this information could improve the cancer EIS-based detection during surgery.

8.3 Conclusions

In this thesis the multiscale modelling framework has been implemented for novel applications in simulating the thyroid and parathyroid electrical impedance relating to the electrical impedance spectroscopy measurements during surgery. In particular, this study comprises the first ever computational model to explore parathyroid tissue electrical properties. The formulated research hypothesis has been supported through the proposed methodology and results obtained by successfully fulfilling the research objectives. These demonstrated the feasibility of the computational methods to explore the differences between thyroid and parathyroid tissue electrical impedance driven on by the variations in their morphology and composition. The proposed comprehensive inter- and intracompartmental sensitivity analysis presented in this study elucidated the model's sensitivity to the variations of different tissue features and revealed the geometrical and electrical parameters crucial for both tissues macroscopic electrical behaviour, which has been performed for the first time for healthy thyroid and parathyroid tissues. Moreover, the results presented in this thesis suggest a good differentiation of computed healthy thyroid and parathyroid tissue based on the selected impedance spectra indices and demonstrate positive tissue separability comparable to the ones reported

for healthy and dysplastic cervical epithelium using EIS measurements.

Additionally, the work presented in this thesis is an example of how computational modelling can broaden the understanding of the relationship between the features of biological tissues and their morphology with its application aimed to enhance and improve existing medical procedures. In particular, the outcomes of this project suggested that it should be possible to recognise the differences between theoretical impedance spectra of thyroid and parathyroid tissues and presented specific recommendations, both for the surgical procedure and for future hardware developments, in order to improve the electrical impedance-based differentiation of these tissues during surgery. In particular, the study revealed the importance of additional experimental elucidation of electrical properties of tissue structures, the significance of the fascia compartment removal a priori to the thyroid and parathyroid EIS measurements and the benefits resulting from potential optimisation of the EIS probe electrode size and separation on the parathyroid measurement accuracy. Moreover, this study further emphasises the utility of computational modelling as a complementary tool to *in vivo* experimental work highlighting how the cooperation between engineering, science and medicine can provide better interdisciplinary research and improve healthcare.

Bibliography

[1] O. Edafe and S. P. Balasubramanian, "Incidence, Prevalence and Risk Factors for Post-surgical Hypocalcaemia and Hypoparathyroidism," *Gland surgery*, vol. 6, pp. S59–S68, dec 2017.

[2] R. Antakia, B. Brown, P. Highfield, T. Stephenson, N. Brown, and S. Balasubramanian, "Electrical Impedance Spectroscopy to Aid Parathyroid Identification and Preservation in Central Compartment Neck Surgery: A Proof of Concept in a Rabbit Model," *Surgical innovation*, vol. 23, oct 2015.

[3] S. L. Hillary, B. H. Brown, N. J. Brown, and S. P. Balasubramanian, "Use of Electrical Impedance Spectroscopy for Intraoperative Tissue Differentiation During Thyroid and Parathyroid Surgery," *World Journal of Surgery*, 2019.

[4] F. A. Khan YS, "Histology, Thyroid Gland.," in *StatPearls [Internet]*, Treasure Island (FL): StatPearls Publishing, 2021.

[5] R. Arrangoiz, F. Cordera, D. Caba, M. Muñoz, E. Moreno, and E. Luque-de León, "Comprehensive Review of Thyroid Embryology, Anatomy, Histology, and Physiology for Surgeons," *International Journal of Otolaryngology and Head & Neck Surgery*, vol. 07, pp. 160–188, jul 2018.

[6] J. Lee, S. Yi, Y. E. Kang, H.-W. Kim, K. H. Joung, H. J. Sul, K. S. Kim, and M. Shong, "Morphological and Functional Changes in the Thyroid Follicles of the Aged Murine and Humans," *Journal of pathology and translational medicine*, vol. 50, pp. 426–435, nov 2016.

[7] A. Ramas, A. Jakubovic-Cičkisic, S. Umihanic, M. Sulejmanovic, and F. Brkic, "Correlation Between the Parathyroid Glands Size and Parathormones Value in Patients with Hyperparathyroidism," *Medical archives (Sarajevo, Bosnia and Herzegovina)*, vol. 73, pp. 249–252, aug 2019.

[8] J. S. Lowe and P. G. Anderson, "Chapter 14 - Endocrine System," in *Stevens & Lowe's Human Histology (Fourth Edition) (Fourth Edition)* (J. S. Lowe and P. G. Anderson, eds.), pp. 263–285, Philadelphia: Mosby, 2015.

[9] D. R. Chadwick, "Hypocalcaemia and Permanent Hypoparathyroidism After Total/Bilateral Thyroidectomy in the BAETS Registry," *Gland surgery*, vol. 6, pp. S69–S74, dec 2017.

[10] O. M. Walter, "Hypoparathyroidism as a Complication of Thyroid Surgery," *Radiology*, vol. 14, pp. 504–507, may 1930.

[11] O. Edafe and S. P. Balasubramanian, "Incidence, Prevalence and Risk Factors for Post-surgical Hypocalcaemia and Hypoparathyroidism," *Gland Surgery*, vol. 6, pp. S59–S68, dec 2017.

[12] C. Paras, M. Keller, A. Mahadevan-Jansen, L. White, and J. Phay, "Near-infrared Autofluorescence for the Detection of Parathyroid Glands," *Journal of Biomedical Optics*, vol. 16, p. 067012, jun 2011.

[13] J. L. Doppman, "Reoperative Parathyroid Surgery; Localization Procedures," in *Progress in Surgery*, pp. 117–132, 1986.

[14] S. M. Cohen, J. E. Noel, C. L. Puccinelli, and L. A. Orloff, "Ultrasound Identification of Normal Parathyroid Glands," *OTO Open*, vol. 5, p. 2473974X211052857, oct 2021.

[15] A. M. Agarwal, J. S. Bentz, R. Hungerford, and D. Abraham, "Parathyroid Fine-needle Aspiration Cytology in the Evaluation of Parathyroid Adenoma: Cytologic Findings from 53 Patients," *Diagnostic Cytopathology*, vol. 37, pp. 407–410, jun 2009.

[16] S. W. Kim, H. S. Lee, and K. D. Lee, "Intraoperative Real-time Localization of Parathyroid Gland with Near Infrared Fluorescence Imaging," *Gland surgery*, vol. 6, pp. 516–524, oct 2017.

[17] Y. Shinden, A. Nakajo, H. Arima, K. Tanoue, M. Hirata, Y. Kijima, K. Maemura, and S. Natsugoe, "Intraoperative Identification of the Parathyroid Gland with a Fluorescence Detection System," *World Journal of Surgery*, vol. 41, pp. 1506–1512, jun 2017.

[18] E. M. Brown and R. J. MacLeod, "Extracellular Calcium Sensing and Extracellular Calcium Signaling," *Physiological Reviews*, vol. 81, pp. 239–297, jan 2001.

[19] Hartl D, Obongo R, Guerlain J, Breuskin I, Abbaci M, "Intraoperative Parathyroid Gland Identification Using Autofluorescence: Pearls and Pitfalls," *World J Surg Surgical Res*, vol. 2, 2019.

[20] A. Siperstein, E. Berber, R. Mackey, M. Alghoul, K. Wagner, and M. Milas, "Prospective Evaluation of Sestamibi Scan, Ultrasonography, and Rapid PTH to Predict the Success of Limited Exploration for Sporadic Primary Hyperparathyroidism," *Surgery*, vol. 136, no. 4, pp. 872–880, 2004.

[21] P. Bertemes-Filho, "Electrical Impedance Spectroscopy," in *Bioimpedance in Biomedical Applications and Research*, pp. 5–27, mar 2018.

[22] J. Yun, Y.-T. Hong, K.-H. Hong, and J.-H. Lee, "Ex Vivo Identification of Thyroid Cancer Tissue Using Electrical Impedance Spectroscopy on a Needle," *Sensors and Actuators B: Chemical*, vol. 261, pp. 537–544, 2018.

[23] Zilico Limited, "ZedScan™ a new standard in colposcopy - technical brochure," 2013.

[24] D. M. Jones, *Measurement and Modelling of the Electrical Properties of Normal and Pre-cancerous Oesophageal Tissue*. PhD thesis, The University of Sheffield, 2003.

[25] J. J. P. Alix, H. E. McDonough, B. Sonbas, S. J. French, D. G. Rao, V. Kadirkamanathan, C. J. McDermott, T. J. Healey, and P. J. Shaw, "Multi-dimensional Electrical Impedance Myography of the Tongue as a Potential Biomarker for Amyotrophic Lateral Sclerosis," *Clinical Neurophysiology*, vol. 131, no. 4, pp. 799–808, 2020.

[26] C. Gabriel, *Compilation of the Dielectric Properties of Body Tissues at RF and Microwave Frequencies*. King's College London, 1996.

[27] R. Höber, "Eine Methode, die Elektrische Leitfhigkeit im Innern von Zellen zu Messen," *Pflüger's Archiv für die gesamte Physiologie des Menschen und der Tiere*, vol. 133, no. 4, pp. 237–253, 1910.

[28] H. Fricke and S. Morse, "The Electic Resistance and Capacity of Blood for Frequencies Between 800 and 4(1/2) Milion Cycles," *The Journal of general physiology*, vol. 9, pp. 153–167, nov 1925.

[29] K. S. Cole and R. H. Cole, "Dispersion and Absorption in Dielectrics I. Alternating Current Characteristics," *The Journal of Chemical Physics*, vol. 9, pp. 341–351, apr 1941.

[30] H. P. Schwan, "Electrical Properties of Tissue and Cell Suspensions," in *Advances in Biological and Medical Physics* (J. H. Lawrence and C. A. Tobias, eds.), vol. 5, pp. 147–209, Elsevier, 1957.

[31] H. P. Schwan, "Electrical Properties of Tissues and Cell Suspensions: Mechanisms and Models," in *Proceedings of 16th Annual International Conference of the IEEE Engineering in Medicine and Biology Society*, vol. 1, pp. A70–A71 vol.1, 1994.

[32] R Pethig and D B Kell, "The Passive Electrical Properties of Biological Systems: Their Significance in Physiology, Biophysics and Biotechnology," *Physics in Medicine & Biology*, vol. 32, no. 8, p. 933, 1987.

[33] U. Birgersson, E. Birgersson, and S. Ollmar, "Estimating Electrical Properties and the Thickness of Skin with Electrical Impedance Spectroscopy: Mathematical Analysis and Measurements," *Journal of Electrical Bioimpedance*, vol. 3, jul 2012.

[34] B. Wang, Y. Liu, J. Wu, Y. Liu, P. Wang, H. Liu, H. Wang, T. Wang, J. Wang, Y. Tang, and J. Zhang, "Bioelectrical Impedance Spectroscopy Can Assist to Identify the Parathyroid Gland During Thyroid Surgery," *Frontiers in Endocrinology*, vol. 13, p. 963520, 2022.

[35] S. Mazumder, "Chapter 1 - Introduction to Numerical Methods for Solving Differential Equations," pp. 1–49, Academic Press, 2016.

[36] A. Polycarpou, "Introduction to the Finite Element Method in Electromagnetics," *Synthesis Lectures on Computational Electromagnetics*, vol. 1, pp. 1–126, jan 2006.

[37] A. Hartinger, R. Guardo, V. Kokta, and H. Gagnon, "A 3-D Hybrid Finite Element Model to Characterize the Electrical Behavior of Cutaneous Tissues," *IEEE Transactions on Biomedical Engineering*, vol. 57, pp. 780–789, apr 2010.

[38] D. C. Walker, *Modeling the Electrical Properties of Cervical Epithelium*. PhD thesis, University of Sheffield, 2001.

[39] D. C. Walker, R. H. Smallwood, A. Keshtar, B. A. Wilkinson, F. C. Hamdy, and J. A. Lee, "Modelling the Electrical Properties of Bladder Tissue Quantifying Impedance Changes Due to Inflammation and Oedema," *Physiological Measurement*, vol. 26, no. 3, pp. 251–268, 2005.

[40] A. Keshtkar and S. Madaen, "The Comparison of Measured Impedance of the Bladder Tissue with the Computational Modeling Results," *Journal of Analytical Research in Clinical Medicine*, vol. 3, pp. 225–230, nov 2015.

[41] J. P. Heath, K. D. Hunter, C. Murdoch, and D. C. Walker, "Computational Modelling for Electrical Impedance Spectroscopy-Based Diagnosis of Oral Potential Malignant Disorders (OPMD)," 2022.

[42] J. P. Heath, *Simulation of Impedance Spectroscopy in Electroceramics Using a Finite Element Method*. PhD thesis, University of Sheffield, 2017.

[43] S. Pandey, D. Kumar, O. Parkash, and L. Pandey, "Impedance Spectroscopy: A Powerful Technique for Study of Electronic Ceramics," p. Ch. 5, Rijeka: IntechOpen, 2019.

[44] X. Zhao, H. Zhuang, S.-C. Yoon, Y. Dong, W. Wang, and W. Zhao, "Electrical Impedance Spectroscopy for Quality Assessment of Meat and Fish: A Review on Basic Principles, Measurement Methods, and Recent Advances," *Journal of Food Quality*, vol. 2017, p. 6370739, 2017.

[45] M. E. Astashev, E. M. Konchekov, L. V. Kolik, and S. V. Gudkov, "Electric Impedance Spectroscopy in Trees Condition Analysis: Theory and Experiment," 2022.

[46] Y. Liu, D. Li, J. Qian, B. Di, G. Zhang, and Z. Ren, "Electrical Impedance Spectroscopy (EIS) in Plant Roots Research: A Review," *Plant Methods*, vol. 17, no. 1, p. 118, 2021.

[47] M. I. N. Zhang, T. Repo, J. H. M. Willison, and S. Sutinen, "Electrical Impedance Analysis in Plant Tissues: on the Biological Meaning of Cole-Cole α in Scots Pine Needles," *European Biophysics Journal*, vol. 24, no. 2, pp. 99–106, 1995.

[48] D. Dean, R. Thillaiyan, D. Machado, and R. Sundararajan, "Electrical Impedance Spectroscopy Study of Biological Tissues," *Journal of electrostatics*, vol. 66, pp. 165–177, apr 2008.

[49] B. Sanchez, J. Schoukens, R. Bragos, and G. Vandersteen, "Novel Estimation of the Electrical Bioimpedance Using the Local Polynomial Method. Application to In Vivo Real-Time Myocardium Tissue Impedance Characterization During the Cardiac Cycle," *IEEE Transactions on Biomedical Engineering*, vol. 58, no. 12, pp. 3376–3385, 2011.

[50] B. Sanchez, G. Vandersteen, I. Martin, D. Castillo, A. Torrego, P. J. Riu, J. Schoukens, and R. Bragos, "In Vivo Electrical Bioimpedance Characterization of Human Lung Tissue During the Bronchoscopy Procedure. A Feasibility Study," *Medical Engineering & Physics*, vol. 35, no. 7, pp. 949–957, 2013.

[51] P. Mohr, U. Birgersson, C. Berking, C. Henderson, U. Trefzer, L. Kemeny, C. Sunderkötter, T. Dirschka, R. Motley, M. Frohm-Nilsson, U. Reinhold, C. Loquai, R. Braun, F. Nyberg, and J. Paoli, "Electrical Impedance Spectroscopy as a Potential Adjunct Diagnostic Tool for Cutaneous Melanoma," *Skin Research and Technology*, vol. 19, pp. 75–83, may 2013.

[52] L. Das, S. Das, and J. Chatterjee, "Electrical Bioimpedance Analysis: A New Method in Cervical Cancer Screening," *Journal of Medical Engineering*, vol. 2015, pp. 1–5, feb 2015.

[53] C. Murdoch, B. H. Brown, V. Hearnden, P. M. Speight, K. D'Apice, A. M. Hegarty, J. A. Tidy, T. J. Healey, P. E. Highfield, and M. H. Thornhill, "Use of Electrical Impedance Spectroscopy to Detect Malignant and Potentially Malignant Oral Lesions," *International journal of nanomedicine*, vol. 9, pp. 4521–4532, sep 2014.

[54] A. Stojadinovic, A. Nissan, Z. Gallimidi, S. Lenington, W. Logan, M. Zuley, A. Yeshaya, M. Shimonov, M. Melloul, S. Fields, T. Allweis, R. Ginor, D. Gur, and C. Shriver, "Electrical Impedance Scanning for the Early Detection of Breast Cancer in Young Women: Preliminary Results of a Multicenter Prospective Clinical Trial," *Journal of*

clinical oncology : official journal of the American Society of Clinical Oncology, vol. 23, pp. 2703–2715, apr 2005.

[55] V. Mishra, H. Bouayad, A. Schned, J. Heaney, and R. J. Halter, "Electrical Impedance Spectroscopy for Prostate Cancer Diagnosis," in *2012 Annual International Conference of the IEEE Engineering in Medicine and Biology Society*, pp. 3258–3261, 2012.

[56] A. Stojadinovic, S. I. Fields, C. D. Shriver, S. Lenington, R. Ginor, G. E. Peoples, H. B. Burch, T. Peretz, H. R. Freund, and A. Nissan, "Electrical Impedance Scanning of Thyroid Nodules Before Thyroid Surgery: A Prospective Study," *Annals of Surgical Oncology*, vol. 12, no. 2, pp. 152–160, 2005.

[57] B. Zheng, M. E. Tublin, A. H. Klym, and D. Gur, "Classification of Thyroid Nodules Using a Resonance-frequency-based Electrical Impedance Spectroscopy: a Preliminary Assessment," *Thyroid : official journal of the American Thyroid Association*, vol. 23, pp. 854–862, jul 2013.

[58] Barber D C and Brown B H, "Applied Potential Tomography," *Journal of Physics E: Scientific Instruments*, vol. 17, no. 9, p. 723, 1984.

[59] V. A. Cherepenin, A. Y. Karpov, A. V. Korjenevsky, V. N. Kornienko, Y. S. Kultiasov, M. B. Ochapkin, O. V. Trochanova, and J. D. Meister, "Three-dimensional EIT Imaging of Breast Tissues: System Design and Clinical Testing," *IEEE Transactions on Medical Imaging*, vol. 21, no. 6, pp. 662–667, 2002.

[60] T. Tidswell, A. Gibson, R. H. Bayford, and D. S. Holder, "Three-Dimensional Electrical Impedance Tomography of Human Brain Activity," *NeuroImage*, vol. 13, no. 2, pp. 283–294, 2001.

[61] Y. Cheng and M. Fu, "Dielectric Properties for Differentiating Normal and Malignant Thyroid Tissues," *Medical science monitor : international medical journal of experimental and clinical research*, vol. 24, pp. 1276–1281, mar 2018.

[62] Y. Zou and Z. Guo, "A Review of Electrical Impedance Techniques for Breast Cancer Detection," *Medical Engineering & Physics*, vol. 25, no. 2, pp. 79–90, 2003.

[63] M. Ahmed, "An Electrical Impedance Tomography System for Thyroid Gland with a Tiny Electrode Array," *International Journal of Biomedical Engineering and Science (IJBES)*, vol. 3, pp. 41–49, jul 2016.

[64] J. C. M. Garnett, "Colours in Metal Glasses and in Metallic Films," *Philosophical Transactions of the Royal Society of London. Series A, Containing Papers of a Mathematical or Physical Character*, vol. 203, pp. 385–420, jul 1904.

[65] V. Markel, "Introduction to the Maxwell Garnett Approximation: Tutorial," *Journal of the Optical Society of America A*, vol. 33, p. 1244, jul 2016.

[66] N. Nasir and M. Al Ahmad, "Cells Electrical Characterization: Dielectric Properties, Mixture, and Modeling Theories," *Journal of Engineering*, vol. 2020, p. 9475490, 2020.

[67] M. V. Haeverbeke, M. Stock, and B. D. Baets, "Equivalent Electrical Circuits and Their Use Across Electrochemical Impedance Spectroscopy Application Domains," *IEEE Access*, vol. 10, pp. 51363–51379, 2022.

[68] D. Miklavčič, N. Pavšelj, and F. X. Hart, "Electric Properties of Tissues," in *Wiley Encyclopedia of Biomedical Engineering*, vol. 6, Hoboken, NJ, USA: John Wiley & Sons, Inc., apr 2006.

[69] G. H. Markx, C. L. Davey, and D. B. Kell, "To What Extent is the Magnitude of the Cole-Cole α of the β-dielectric Dispersion of Cell Suspensions Explicable in Terms of the Cell Size Distribution?," *Bioelectrochemistry and Bioenergetics*, vol. 25, no. 2, pp. 195–211, 1991.

[70] S. Etoz and C. Brace, "Development of Water Content Dependent Tissue Dielectric Property Models," *IEEE Journal of Electromagnetics, RF and Microwaves in Medicine and Biology*, vol. PP, p. 1, nov 2018.

[71] D. J. Bora and R. Dasgupta, "Estimation of Skin Impedance Models with Experimental Data and a Proposed Model for Human Skin Impedance," *IET Systems Biology*, vol. 14, pp. 230–240, oct 2020.

[72] B. H. Brown, J. A. Tidy, K. Boston, A. D. Blackett, R. H. Smallwood, and F. Sharp, "Relation Between Tissue Structure and Imposed Electrical Current Flow in Cervical Neoplasia," *The Lancet*, vol. 355, no. 9207, pp. 892–895, 2000.

[73] C. E. Miller and C. S. Henriquez, "Three-dimensional Finite Element Solution for Biopotentials: Erythrocyte in an Applied Field," *IEEE Transactions on Biomedical Engineering*, vol. 35, no. 9, pp. 712–718, 1988.

[74] S. Huclova, D. Erni, and J. Fröhlich, "Modelling Effective Dielectric Properties of Materials Containing Diverse Types of Biological Cells," *Journal of Physics D: Applied Physics*, vol. 43, no. 36, p. 365405, 2010.

[75] S. Huclova, D. Erni, and J. Fröhlich, "Modelling and Validation of Dielectric Properties of Human Skin in the MHz Region Focusing on Skin Layer Morphology and Material Composition," *Journal of Physics D: Applied Physics*, vol. 45, p. 025301, jan 2012.

[76] D. M. Jones, R. H. Smallwood, D. R. Hose, B. H. Brown, and D. C. Walker, "Modelling of Epithelial Tissue Impedance Measured Using Three Different Designs of Probe," *Physiological Measurement*, vol. 24, pp. 605–623, may 2003.

[77] S. V. Gandhi, D. C. Walker, B. H. Brown, and D. O. C. Anumba, "Comparison of Human Uterine Cervical Electrical Impedance Measurements Derived Using Two Tetrapolar Probes of Different Sizes," *BioMedical Engineering OnLine*, vol. 5, no. 1, p. 62, 2006.

[78] C. N. Schooling, T. Jamie Healey, H. E. McDonough, S. J. French, C. J. McDermott, P. J. Shaw, V. Kadirkamanathan, and J. J. P. Alix, "Modelling and Analysis of Electrical Impedance Myography of the Lateral Tongue," *Physiological Measurement*, vol. 41, p. 125008, dec 2020.

[79] Y. Lv, Y. Zhang, J. Huang, Y. Wang, and B. Rubinsky, "A Study on Nonthermal Irreversible Electroporation of the Thyroid," *Technology in Cancer Research & Treatment*, vol. 18, p. 1533033819876307, jan 2019.

[80] P. C. Calvo, O. Campo, C. Guerra, S. Castaño, and F. Fonthal, "Design of Using Chamber System Based on Electrical Impedance Spectroscopy (EIS) to Measure Epithelial Tissue," *Sensing and Bio-Sensing Research*, vol. 29, p. 100357, 2020.

[81] P. Marszalek, J. J. Zielinsky, M. Fikus, and T. Y. Tsong, "Determination of Electric Parameters of Cell Membranes by a Dielectrophoresis Method," *Biophysical journal*, vol. 59, pp. 982–987, may 1991.

[82] J. Gimsa, T. Müller, T. Schnelle, and G. Fuhr, "Dielectric Spectroscopy of Single Human Erythrocytes at Physiological Ionic Strength: Dispersion of the Cytoplasm," *Biophysical Journal*, vol. 71, no. 1, pp. 495–506, 1996.

[83] W. H. Coulter, "High-speed Automatic Blood Cell Counter and Size Analyzer," *Preliminary draft of a talk presented before the National Electronics Conference, Chicago*, 1956.

[84] ANSYS, "Theory Reference for the Mechanical APDL and Mechanical Aplications," 2009.

[85] T. Kotnik and D. Miklavcic, "Second-order Model of Membrane Electric Field Induced by Alternating External Electric Fields," *IEEE Transactions on Biomedical Engineering*, vol. 47, no. 8, pp. 1074–1081, 2000.

[86] J. Yang, Y. Huang, X. Wang, X.-B. Wang, F. F. Becker, and P. R. C. Gascoyne, "Dielectric Properties of Human Leukocyte Subpopulations Determined by Electrorotation as a Cell Separation Criterion," *Biophysical Journal*, vol. 76, no. 6, pp. 3307–3314, 1999.

[87] H. Morgan, T. Sun, D. Holmes, S. Gawad, and N. G. Green, "Single Cell Dielectric Spectroscopy," *Journal of Physics D: Applied Physics*, vol. 40, no. 1, pp. 61–70, 2006.

[88] L. A. Geddes and L. E. Baker, "The Specific Resistance of Biological Material — A Compendium of Data for the Biomedical Engineer and Physiologist," *Medical and biological engineering*, vol. 5, no. 3, pp. 271–293, 1967.

[89] F. A. Duck, "Chapter 6 - Electrical Properties of Tissue," in *Physical Properties of Tissues* (F. A. Duck, ed.), pp. 167–223, London: Academic Press, 1990.

[90] F. Bordi, C. Cametti, A. Rosi, and A. Calcabrini, "Frequency Domain Electrical Conductivity Measurements of the Passive Electrical Properties of Human Lymphocytes," *BBA - Biomembranes*, vol. 1153, no. 1, pp. 77–88, 1993.

[91] Z. Kmieć, G. Kotlarz, B. Śmiechowska, and A. Myśliwski, "The Effect of Fasting and Refeeding on Thyroid Follicule Structure and Thyroid Hormone Levels in YOung and Old Rats," *Archives of Gerontology and Geriatrics*, vol. 26, no. 2, pp. 161–175, 1998.

[92] N. M. Ali Rajab, M. Ukropina, and M. Cakic-Milosevic, "Histological and ultrastructural alterations of rat thyroid gland after short-term treatment with high doses of thyroid hormones," *Saudi Journal of Biological Sciences*, vol. 24, no. 6, pp. 1117–1125, 2017.

[93] C. S. Ritter, B. H. Haughey, B. Miller, and A. J. Brown, "Differential Gene Expression by Oxyphil and Chief Cells of Human Parathyroid Glands," *The Journal of clinical endocrinology and metabolism*, vol. 97, pp. E1499–E1505, aug 2012.

[94] A. Uzman, "Molecular Biology of the Cell (4th ed.): Alberts, B., Johnson, A., Lewis, J., Raff, M., Roberts, K., and Walter, P.," *Biochemistry and Molecular Biology Education*, vol. 31, pp. 212–214, jul 2003.

[95] M. Al-Zghoul, "Macro- and Micro-Morphological Studies on the Parathyroid Glands of Dromedary Camel," *Pakistan Veterinary Journal*, vol. 37, pp. 59–64, jan 2017.

[96] A. Faggiano, J. Coulot, N. Bellon, M. Talbot, B. Caillou, M. Ricard, J.-M. Bidart, and M. Schlumberger, "Age-dependent Variation of Follicular Size and Expression of Iodine Transporters in Human Thyroid Tissue," *Journal of nuclear medicine : official publication, Society of Nuclear Medicine*, vol. 45, pp. 232–237, feb 2004.

[97] W. F. Boron and E. L. Boulpaep, *Medical Physiology : a Cellular and Molecular Approach*. Philadelphia, PA: Saunders Elsevier, 2012.

[98] S. Smeds, "A Microgel Electrophoretic Analysis of the Colloid Proteins in Single Rat Thyroid Follicles. II. The Protein Concentration of the Colloid in Single Rat Thyroid Follicles," *Endocrinology*, vol. 91, pp. 1300–1306, nov 1972.

[99] B. Anderberg, S. Eneström, J. Gillquist, B. Kägedal, J. C. Månsson, and S. Smeds, "Protein Composition in Single Follicles, Homogenates and Fine-needle Aspiration Biopsies from Normal and Diseased Human Thyroid," *European Journal of Endocrinology*, vol. 96, no. 3, pp. 328–334, 1981.

[100] A. Gorbman and K. Ueda, "Electrical Properties of Thyroid Follicles in Normal and Thyrotropin-injected Frogs and in Premetamorphic and Metamorphic Tadpoles," *General and Comparative Endocrinology*, 1963.

[101] H. L. Krüskemper and P. Reichertz, "Der Einfluss von Thyrotropem Hormon auf das Elektrogramm der Schilddruese," *Acta Endocrinologica*, vol. XXXIV, no. III, pp. 390–398, 1960.

[102] J. A. Williams, "Effects of TSH on Thyroid Membrane Properties," *Endocrinology*, vol. 86, pp. 1154–1158, may 1970.

[103] K. Verma, S. Prasad, A. Kumaresan, T. Mohanty, S. S. Layek, T. Patbandha, and S. Chand, "Characterization of Physico-chemical Properties of Cervical Mucus in Relation to Parity and Conception Rate in Murrah Buffaloes," *Veterinary World*, vol. 7, pp. 467–471, jul 2014.

[104] D. M. Hidalgo, G. Cassar, R. Manjarin, J. C. Dominguez, R. M. Friendship, and R. N. Kirkwood, "Relationship Between Vaginal Mucus Conductivity and Time of Ovulation in Weaned Sows," *Canadian journal of veterinary research = Revue canadienne de recherche veterinaire*, vol. 79, pp. 151–154, apr 2015.

[105] H. Darvishi, M.-H. Khoshtaghaza, M. Zarein, and M. Azadbakht, "Ohmic Processing of Liquid Whole Egg, White Egg and Yolk," *Agric Eng Int: CIGR Journal*, vol. 14, pp. 224–230, dec 2012.

[106] M. Amiali, M. O. Ngadi, V. G. S. Raghavan, and D. H. Nguyen, "Electrical Conductivities of Liquid Egg Products and Fruit Juices Exposed to High Pulsed Electric Fields," *International Journal of Food Properties*, vol. 9, pp. 533–540, sep 2006.

[107] J. Wang, J. Tang, Y. Wang, and B. Swanson, "Dielectric Properties of Egg Whites and Whole Eggs as Influenced by Thermal Treatments," *LWT - Food Science and Technology*, vol. 42, no. 7, pp. 1204–1212, 2009.

[108] C. Bircan and S. A. Barringer, "Use of Dielectric Properties to Detect Egg Protein Denaturation," *Journal of Microwave Power and Electromagnetic Energy*, vol. 37, pp. 89–96, jan 2002.

[109] T. Dinh, M. Wang, S. Serfaty, and P. Joubert, "Contactless Radio Frequency Monitoring of Dielectric Properties of Egg White During Gelation," *IEEE Transactions on Magnetics*, vol. 53, no. 4, pp. 1–7, 2017.

[110] M. A. Kandadai, J. L. Raymond, and G. J. Shaw, "Comparison of Electrical Conductivities of Various Brain Phantom Gels: Developing a 'Brain Gel Model'," *Materials Science and Engineering: C*, vol. 32, no. 8, pp. 2664–2667, 2012.

[111] M. Gulino, P. Bellia, F. Falciglia, F. Musumeci, A. Pappalardo, A. Scordino, and A. Triglia, "Role of Water Content In Dielectric Properties and Delayed Luminescence of Bovine Achilles' Tendon," *FEBS Letters*, vol. 579, no. 27, pp. 6101–6104, 2005.

[112] S. J. Nagel, C. G. Reddy, L. A. Frizon, M. K. Chardon, M. Holland, A. G. Machado, G. T. Gillies, M. A. Howard 3rd, and S. Wilson, "Spinal Dura Mater: Biophysical Characteristics Relevant to Medical Device Development," *Journal of medical engineering & technology*, vol. 42, pp. 128–139, feb 2018.

[113] J. J. Struijk, J. Holsheimer, G. Barolat, J. He, and H. B. K. Boom, "Paresthesia Thresholds in Spinal Cord Stimulation: a Comparison of Theoretical Results with Clinical Data," *IEEE Transactions on Rehabilitation Engineering*, vol. 1, no. 2, pp. 101–108, 1993.

[114] D. Lee, B. Hershey, K. Bradley, and T. Yearwood, "Predicted Effects of Pulse Width Programming in Spinal Cord Stimulation: a Mathematical Modeling Study," *Medical and Biological Engineering and Computing*, vol. 49, pp. 765–774, jul 2011.

[115] K. Nowak, E. Mix, J. Gimsa, U. Strauss, K. Sriperumbudur, R. Benecke, and U. Gimsa, "Optimizing a Rodent Model of Parkinson's Disease for Exploring the Effects and Mechanisms of Deep Brain Stimulation," *Parkinson's disease*, vol. 2011, p. 414682, apr 2011.

[116] M. Matella, K. Hunter, S. Balasubramanian, and D. C. Walker, "Multiscale Model Development for Electrical Properties of Thyroid and Parathyroid Tissues," *IEEE Open Journal of Engineering in Medicine and Biology*, pp. 1–9, 2023.

[117] A. Saltelli, K. Aleksankina, W. Becker, P. Fennell, F. Ferretti, N. Holst, S. Li, and Q. Wu, "Why So Many Published Sensitivity Analyses are False: A Systematic Review of Sensitivity Analysis Practices," *Environmental Modelling & Software*, vol. 114, pp. 29–39, 2019.

[118] D. P. Kroese and R. Y. Rubinstein, "Monte Carlo Methods," *WIREs Computational Statistics*, vol. 4, pp. 48–58, jan 2012.

[119] M. D. McKay, R. J. Beckman, and W. J. Conover, "A Comparison of Three Methods for Selecting Values of Input Variables in the Analysis of Output from a Computer Code," *Technometrics*, vol. 21, pp. 239–245, may 1979.

[120] A. Khan, L. Lye, and T. Husain, "Latin Hypercube Sampling for Uncertainty Analysis in Multiphase Modelling," *Journal of Environmental Engineering and Science*, vol. 7, pp. 617–626, nov 2008.

[121] A. Tervonen, T. O. Ihalainen, S. Nymark, and J. Hyttinen, "Structural Dynamics of Tight Junctions Modulate the Properties of the Epithelial Barrier," *PLOS ONE*, vol. 14, p. e0214876, apr 2019.

[122] S. Marino, I. B. Hogue, C. J. Ray, and D. E. Kirschner, "A Methodology for Performing Global Uncertainty and Sensitivity Analysis in Systems Biology," *Journal of Theoretical Biology*, vol. 254, no. 1, pp. 178–196, 2008.

[123] I. M. Sobol, "Global Sensitivity Indices for Nonlinear Mathematical Models and Their Monte Carlo Estimates," *Mathematics and Computers in Simulation*, vol. 55, no. 1, pp. 271–280, 2001.

[124] W. Donders, W. Huberts, F. van de Vosse, and T. Delhaas, "Personalization of Models with Many Model Parameters: an Efficient Sensitivity Analysis Approach: Efficient Sensitivity Analysis for Large Model Personalization," *International Journal for Numerical Methods in Biomedical Engineering*, vol. 31, may 2015.

[125] N. Saint-Geours, J.-S. Bailly, C. Lavergne, and F. Grelot, "Latin Hypercube Sampling of Gaussian Random Field for Sobol' Global Sensitivity Analysis of Models with Spatial Inputs and Scalar Output," jul 2010.

[126] X. Zhang, M. Trame, L. Lesko, and S. Schmidt, "Sobol Sensitivity Analysis: A Tool to Guide the Development and Evaluation of Systems Pharmacology Models," *CPT: Pharmacometrics & Systems Pharmacology*, vol. 4, feb 2015.

[127] D. C. Collins and R. Avissar, "An Evaluation with the Fourier Amplitude Sensitivity Test (FAST) of which Land-surface Parameters are of Greatest Importance in Atmospheric Modeling," *Journal of Climate*, vol. 7, pp. 681–703, jun 1994.

[128] A. Saltelli and R. Bolado, "An Alternative Way to Compute Fourier Amplitude Sensitivity Test (FAST)," *Computational Statistics & Data Analysis*, vol. 26, no. 4, pp. 445–460, 1998.

[129] M. Renardy, C. Hult, S. Evans, J. J. Linderman, and D. E. Kirschner, "Global Sensitivity Analysis of Biological Multiscale Models," *Current Opinion in Biomedical Engineering*, vol. 11, pp. 109–116, 2019.

[130] L. Possenti, S. Gregorio, G. Casagrande, M. Costantino, T. Rancati, and P. Zunino, "A Global Sensitivity Analysis Approach Applied to a Multiscale Model of Microvascular Flow," *Computer Methods in Biomechanics and Biomedical Engineering*, vol. 23, pp. 1–10, jul 2020.

[131] Y. Liu, X. Yin, P. Arendt, W. Chen, and H.-Z. Huang, "A Hierarchical Statistical Sensitivity Analysis Method for Multilevel Systems With Shared Variables," *Journal of Mechanical Design*, vol. 132, mar 2010.

[132] E. T. Chang, M. Strong, and R. H. Clayton, "Bayesian Sensitivity Analysis of a cCrdiac Cell Model using a Gaussian Process Emulator," *PLoS ONE*, vol. 10, jun 2015.

[133] C. Angione, E. Silverman, and E. Yaneske, "Using Machine Learning as a Surrogate Model for Agent-based Simulations," *PLOS ONE*, vol. 17, p. e0263150, feb 2022.

[134] Y. Zhang, "Support Vector Machine Classification Algorithm and Its Application BT - Information Computing and Applications," (Berlin, Heidelberg), pp. 179–186, Springer Berlin Heidelberg, 2012.

[135] V. Bewick, L. Cheek, and J. Ball, "Statistics Review 13: Receiver Operating Characteristic Curves," *Critical Care*, vol. 8, no. 6, p. 508, 2004.

[136] J. Eng, "Receiver Operating Characteristic Analysis: A Primer," *Academic Radiology*, vol. 12, pp. 909–916, jul 2005.

[137] J. A. Tidy, B. H. Brown, T. J. Healey, S. Daayana, M. Martin, W. Prendiville, and H. C. Kitchener, "Accuracy of Detection of High-grade Cervical Intraepithelial Neoplasia using Electrical Impedance Spectroscopy with Colposcopy," *BJOG: An International Journal of Obstetrics & Gynaecology*, vol. 120, pp. 400–411, mar 2013.

[138] M. C. Costa, G. Tozzi, L. Cristofolini, V. Danesi, M. Viceconti, and E. Dall'Ara, "Micro Finite Element Models of the Vertebral Body: Validation of Local Displacement Predictions," *PLOS ONE*, vol. 12, p. e0180151, jul 2017.

[139] C. Winsor, X. Li, M. Qasim, C. R. Henak, P. J. Pickhardt, H. Ploeg, and M. Viceconti, "Evaluation of Patient Tissue Selection Methods for Deriving Equivalent Density Calibration for Femoral Bone Quantitative CT Analyses," *Bone*, vol. 143, p. 115759, 2021.

[140] E. Lozano, D. Roehl, W. Celes, and M. Gattass, "An Efficient Algorithm to Generate Random Sphere Packs in Arbitrary Domains," *Computers & Mathematics with Applications*, vol. 71, no. 8, pp. 1586–1601, 2016.

[141] M. Matella, D. C. Walker, and K. Hunter, "Computational Modelling of Probe Configurations for Electrical Impedance Spectroscopy-based Differentiation of Thyroid and Parathyroid Tissues," in *2023 IEEE International Symposium on Medical Measurements and Applications (MeMeA)*, pp. 1–6, 2023.

[142] B. Borwn and J. Tidy, "Method and Probe for Measuring the Impedance of Human or Animal Body Tissue," 2011.

[143] S. Huang, W. Cai, S. Han, Y. Lin, Y. Wang, F. Chen, G. Shao, Y. Liu, X. Yu, Z. Cai, Z. Zou, S. Yao, Q. Wang, and Z. Li, "Differences in the Dielectric Properties of Various Benign and Malignant Thyroid Nodules," *Medical Physics*, vol. 48, pp. 760–769, feb 2021.

[144] C. Rossmann and D. Haemmerich, "Review of Temperature Dependence of Thermal Properties, Dielectric Properties, and Perfusion of Biological Tissues at Hyperthermic and Ablation Temperatures," *Critical Reviews in Biomedical Engineering*, vol. 42, may 2015.

[145] M. Morin, T. Ruzgas, P. Svedenhag, C. D. Anderson, S. Ollmar, J. Engblom, and S. Björklund, "Skin Hydration Dynamics Investigated by Electrical Impedance Techniques In Vivo and In Vitro," *Scientific Reports*, vol. 10, no. 1, p. 17218, 2020.

[146] E. Karabelas, S. Longobardi, J. Fuchsberger, O. Razeghi, C. Rodero, M. Strocchi, R. Rajani, G. Haase, G. Plank, and S. Niederer, "Global Sensitivity Analysis of Four Chamber Heart Hemodynamics Using Surrogate Models," *IEEE Transactions on Biomedical Engineering*, vol. 69, no. 10, pp. 3216–3223, 2022.

[147] M. Zakrevska and A. Tybinka, "Histogical Structure of the Thyroid Gland in Rabbits with Different Types of Autonomous Tonus," *Scientific Messenger of LNU of Veterinary Medicine and Biotechnologies*, vol. 22, pp. 119–127, aug 2020.

[148] E. A. Bulanova, E. V. Koudan, J. Degosserie, C. Heymans, F. D. Pereira, V. A. Parfenov, Y. Sun, Q. Wang, S. A. Akhmedova, I. K. Sviridova, N. S. Sergeeva, G. A. Frank, Y. D. Khesuani, C. E. Pierreux, and V. A. Mironov, "Bioprinting of a Functional Vascularized Mouse Thyroid Gland Construct," *Biofabrication*, vol. 9, p. 034105, aug 2017.

[149] H. W. Yu, B. S. Kim, J. Y. Lee, K. Lee, M. Ahn, J. Jang, D.-W. Cho, and J. Y. Choi, "Tissue printing for engineering transplantable human parathyroid patch to improve parathyroid engraftment, integration, and hormone decretion in vivo," *Biofabrication*, vol. 13, p. 035033, jul 2021.

[150] U. o. L. Division of Pathology Data Analytics, Leeds Institute of Medical Research, "Virtual Pathology at the University of Leeds." https://www.virtualpathology.leeds.ac.uk [Accessed: 2023/07/30].

[151] J. Schindelin, I. Arganda-Carreras, E. Frise, V. Kaynig, M. Longair, T. Pietzsch, S. Preibisch, C. Rueden, S. Saalfeld, B. Schmid, J.-Y. Tinevez, D. J. White, V. Hartenstein, K. Eliceiri, P. Tomancak, and A. Cardona, "Fiji: an Open-source Platform for Biological-image Analysis," *Nature Methods*, vol. 9, no. 7, pp. 676–682, 2012.

[152] M. Lapierre-Landry, Y. Liu, M. Bayat, D. L. Wilson, and M. W. Jenkins, "Digital Labeling for 3D Histology: Segmenting Blood Vessels without a Vascular Contrast Agent Using Deep Learning," *Biomedical Optics Express*, vol. 14, no. 6, pp. 2416–2431, 2023.

[153] M. Roy, F. Wang, H. Vo, D. Teng, G. Teodoro, A. B. Farris, E. Castillo-Leon, M. B. Vos, and J. Kong, "Deep-learning-based Accurate Hepatic Steatosis Quantification for Histological Assessment of Liver Biopsies," *Laboratory Investigation*, vol. 100, no. 10, pp. 1367–1383, 2020.

[154] M. J. West, "Tissue Shrinkage and Stereological Studies," *Cold Spring Harbor Protocols*, vol. 2013, p. pdb.top071860, mar 2013.

[155] U. Sharma, E. Chang, and S. Yun, "Long-wavelength Optical Coherence Tomography at 1.7 μm for Enhanced Imaging Depth," *Optics express*, vol. 16, pp. 19712–19723, dec 2008.

[156] C. Zhou, Y. Wang, A. D. Aguirre, T.-H. Tsai, D. W. Cohen, J. L. Connolly, and J. G. Fujimoto, "Ex Vivo Imaging of Human Thyroid Pathology Using Integrated Optical Coherence Tomography and Optical Coherence Microscopy," *Journal of biomedical optics*, vol. 15, no. 1, p. 16001, 2010.

[157] S. J. Erickson-Bhatt, K. J. Mesa, M. Marjanovic, E. J. Chaney, A. Ahmad, P.-C. Huang, Z. G. Liu, K. Cunningham, and S. A. Boppart, "Intraoperative Optical Coherence Tomography of the Human Thyroid: Feasibility for Surgical Assessment," *Translational Research*, vol. 195, pp. 13 – 24, 2018.

Appendices

Appendix A

Histology measurements

The measurement of the cell and follicle sizes for thyroid (thyrocyte and follicle) and parathyroid (chief cell) tissues were performed through manual measurement using image analysis software ImageJ and ImageScope. The sample size for the measurement was determined based on the mean value convergence – change of <0.5% compared to the mean value from a smaller sample size, which is shown in Fig. A.1 for all measured structures. The measurements have been performed in up to four different locations in one histology image to investigate intrasubject variability of the structures.

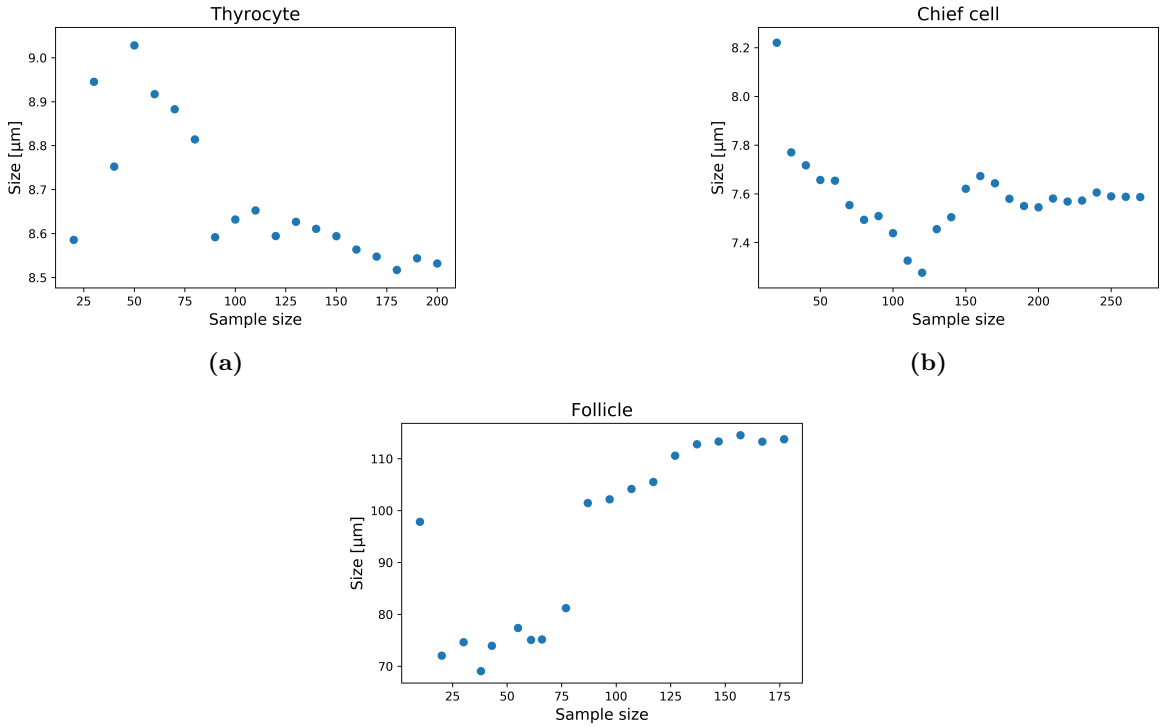

Figure A.1: *Plots visualising the size of the measured structures based on the sample size for (a) thyrocyte, (b) chief cell, (c) thyroid follicle*

Appendix B

Mesh convergence study

Fig. B.1, B.2, and B.4 show the results for mesh convergence study for the models at each level of multiscale. In the mesh density study, the variations in impedivity (for micro- and mesoscale) or impedance (macroscale) were investigated when increasing the number of elements or aspect ratio along the edges of each model. Fig. B.3 clarifies the edges A, B, C that were considered in the mesh density study on the macroscale level.

Microscale model

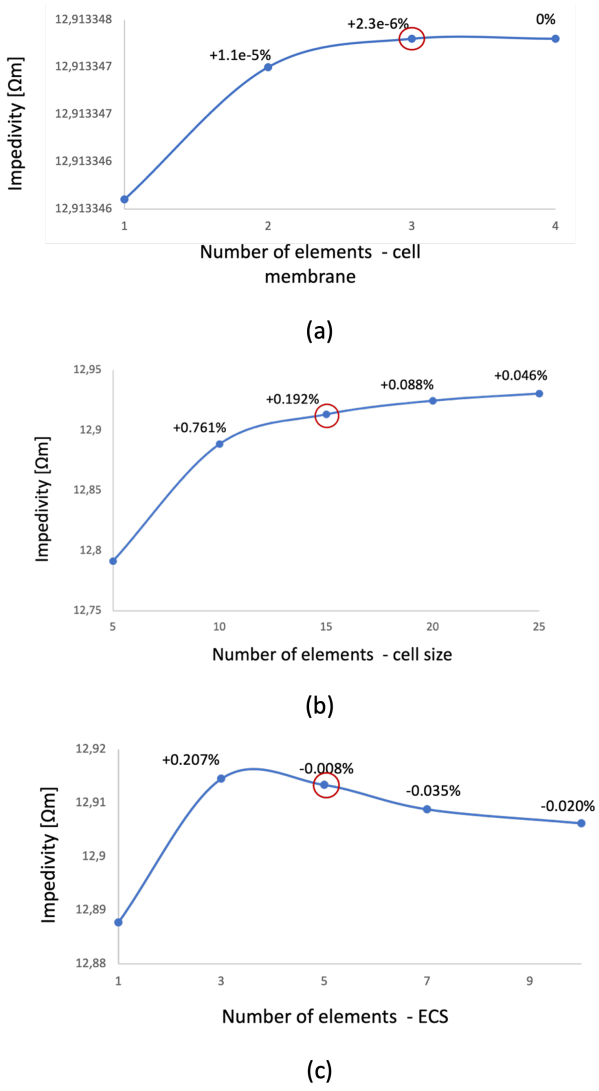

Figure B.1: *The relative effect of the element number on the impedivity when investigating (a) number of elements along cell member compartment, (b) number of elements along cell edge, (c) number of elements along ECS compartment*

Mesoscale model

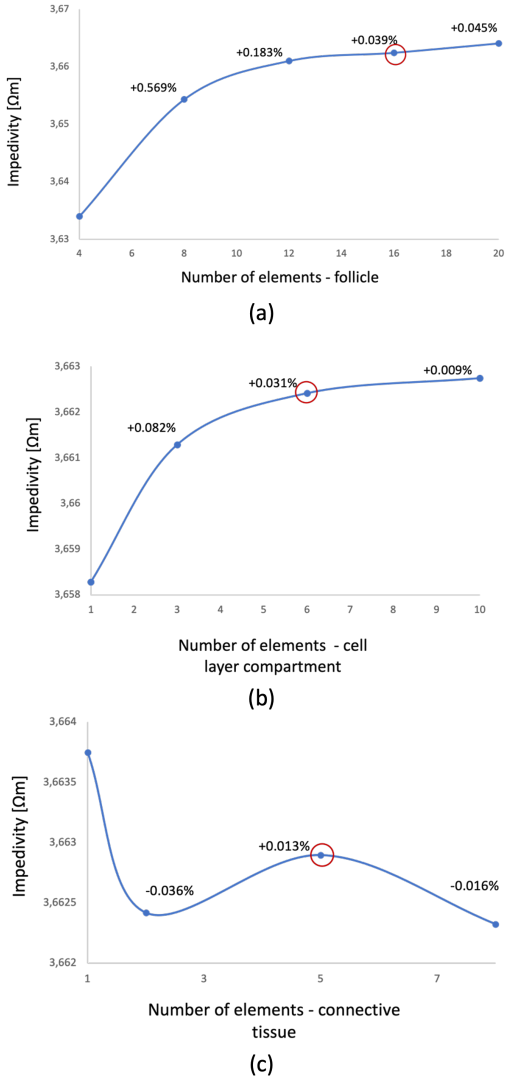

Figure B.2: *The relative effect of the element number on the impedivity when investigating (a) number of elements along follicle edge, (b) number of elements along cell layer compartment, (c) number of elements along connective tissue compartment*

Macroscale model

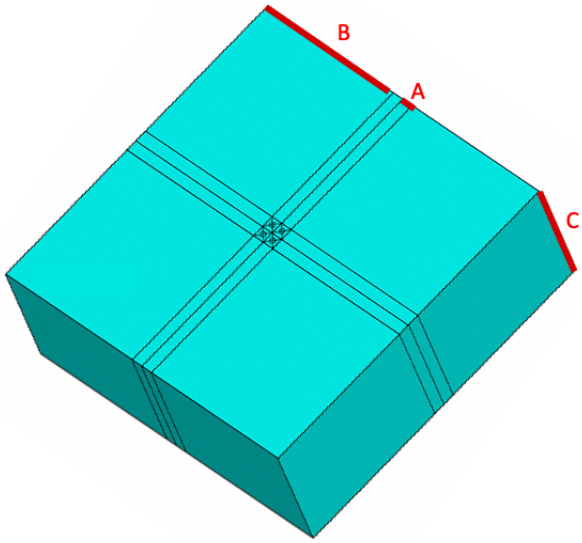

Figure B.3: *Macroscale model with marked edges A-C which were considered in the mesh density study*

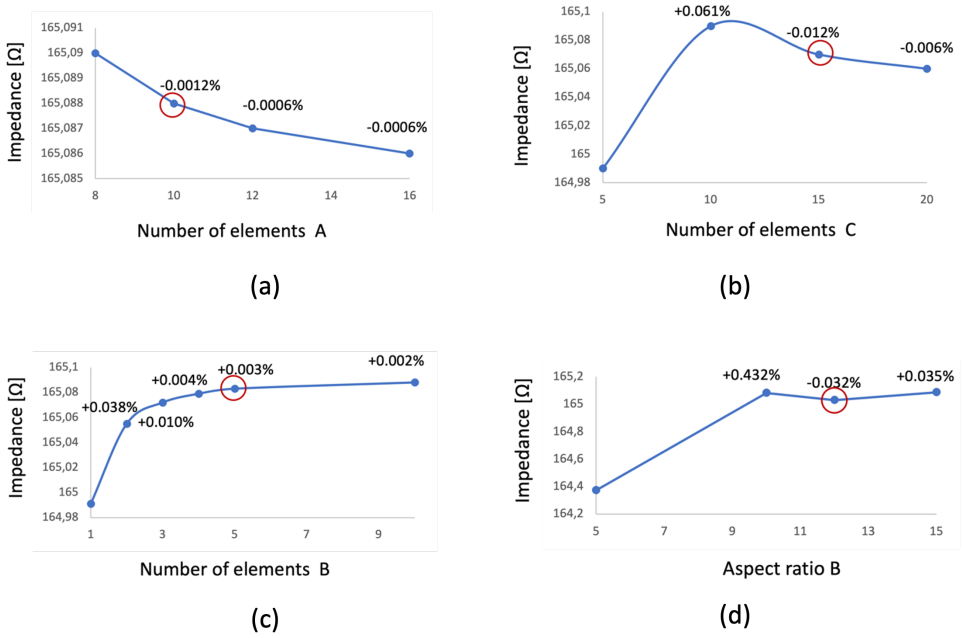

Figure B.4: *The relative effect of the element number or aspect ratio on the impedance when investigating (a) number of elements along edge A, (b) number of elements along edge C, (c) number of elements along edge B (d) aspect ratio of the elements along edge B*

Appendix C

Sample size for global sensitivity study

The sample size study was performed to determine the variations of the PRCC results based on the number of model evaluations considered in the analysis. Fig. C.1 presents a few examples of the PRCC values for sample size 30, 40, 80, 100, 150 based on the microscale level thyroid results. Despite the increased model evaluation numbers, all results fell within the same association category: Low (red), Medium (yellow) or High (green).

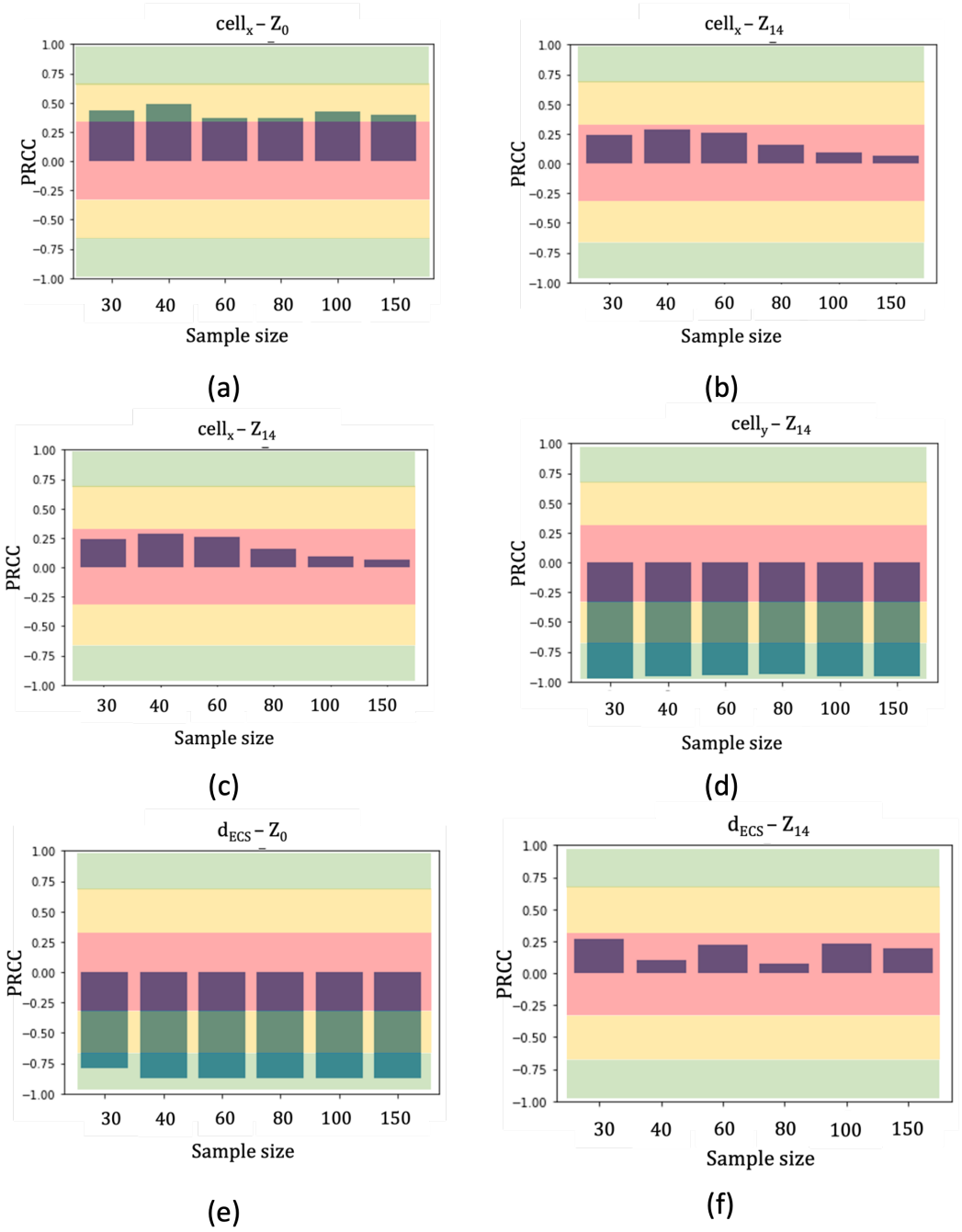

Figure C.1: *The results of the sample size study showing the variation in the PRCC value for the microscale results: (a) and (b) x_{cell} association with the Z_1 (medium) and Z_{14} (low) spectra indices, (c) and (d) y_{cell} association with the Z_1 (low) and Z_{14} (high) spectra indices, (e) and (f) d_{ECS} association with the Z_1 (high) and Z_{14} (low) spectra indices*

Appendix D

Cole-Cole model fitting

The Cole-Cole model fitting has been performed using the scipy.optimize python library using the curve_fit function that use of the nonlinear least squares method to fit the defined function (in this case the Cole-Cole equation Eq. 2.9 from Chapter 2) to the data in order to extract the Cole parameters.

In the case of the computed results, the initial model fitting resulted with satisfactory results, when the threshold of the parameters were partly reinforced manually before the model fitting: the Z_0 parameter was required to within $\pm 20\ \Omega$ from the impedance value at the frequency point of 76 Hz, Z_∞ lower than 180 Ω, f_c from the range between 10^3-10^7 Hz, and α between [0,1]. Similar bounds were introduced to the model fitting to the experimental results.

Unfortunately, due to the shape of the experimental curves for some of the thyroid and most of the parathyroid spectra, the Z_∞ parameter was incorrectly assessed to the values close to zero, which is highly unlikely representing the real high-frequency impedance value, bearing in mind the current still flows through the intracellular space which is characterised with its own resistivity. Fig. D.1 shows the box and whisker plot for all four fitted Cole parameters between computed and *in vivo* results for both tissue types.

As shown in Fig. D.1, the difference between the computed and experimental Z_∞ are substantial. Especially for parathyroid tissue, the majority of experimental results fall close to zero, while the computed result are within a wide range between 0-125 Ω, similarly to Z_∞ for *in vivo* thyroid. This suggests that Cole-Cole model fitting is not an appropriate method of impedance spectra parameterisation in the case of the available data set, and the results from Fig. D.1 discarded.

Interestingly, the fitted α parameter is characterised with considerable discrepancy between

the computed and *in vivo* results for both glands. This is in agreement with previous computational research documented in the literature [69], that also noticed that the theoretical computational models underestimates the dispersion width, mainly due to the homogenisation assumption. It can be implied that the wider experimental spectrum is a result of the distribution of many relaxation times associated with different structures and their shape and sizes building the tissue [32]. On the other hand, it is also hypothesised that the movement of the free and bound charges in the biological tissues is a cooperative process which increases the width of the dispersion [68].

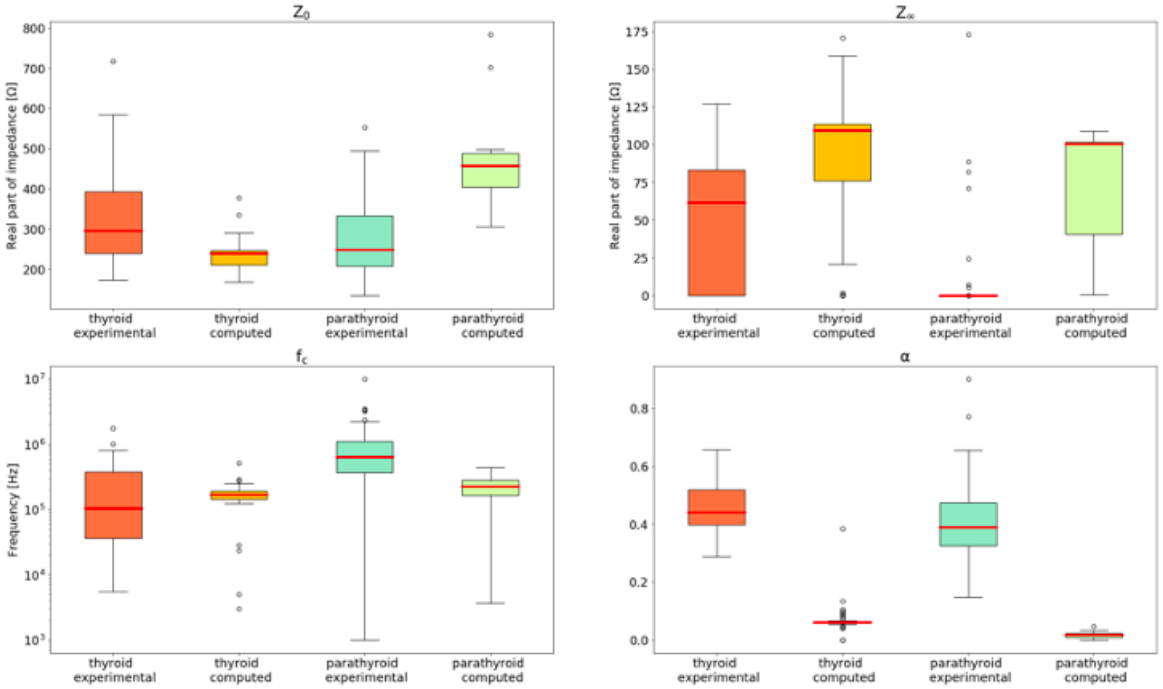

Figure D.1: *Fitted Cole parameters comparison between experimental and computed results for thyroid and parathyroid tissue*

Appendix E

Lower scale level results from local sensitivity analysis

This Appendix comprises the effective conductivity and relative permittivity results obtained during the micro- and mesoscale simulations for thyroid and parathyroid tissues during the local sensitivity analysis presented in Chapter 4.

Conductivity [Sm^{-1}]	frequency [Hz]	baseline	x_{cell} 6.5µm	x_{cell} 11µm	y_{cell} 6.5µm	y_{cell} 11µm	z_{cell} 6.5µm	z_{cell} 11µm	d_{ECS} 0.3µm	d_{ECS} 0.5µm	d_{ECS} 0.8µm
	76	0.07960	0.10291	0.06205	0.08094	0.07865	0.07960	0.07959	0.07961	0.13430	0.21918
	152	0.07960	0.10291	0.06205	0.08094	0.07865	0.07960	0.07959	0.07961	0.13430	0.21918
	305	0.07960	0.10291	0.06205	0.08094	0.07865	0.07960	0.07959	0.07961	0.13430	0.21918
	610	0.07960	0.10291	0.06205	0.08094	0.07865	0.07960	0.07959	0.07961	0.13430	0.21918
	1220	0.07960	0.10292	0.06205	0.08094	0.07865	0.07960	0.07960	0.07961	0.13430	0.21918
	2441	0.07961	0.10292	0.06206	0.08094	0.07866	0.07961	0.07960	0.07961	0.13430	0.21919
	4882	0.07963	0.10294	0.06209	0.08096	0.07871	0.07963	0.07963	0.07964	0.13432	0.21919
	9765	0.07973	0.10303	0.06221	0.08101	0.07891	0.07974	0.07973	0.07974	0.13438	0.21923
	19531	0.08014	0.10339	0.06268	0.08121	0.07971	0.08014	0.08014	0.08015	0.13461	0.21935
	39062	0.08175	0.10482	0.06455	0.08204	0.08286	0.08176	0.08175	0.08176	0.13552	0.21987
	78125	0.08810	0.11044	0.07189	0.08533	0.09502	0.08811	0.08810	0.08811	0.13915	0.22190
	156250	0.11176	0.13148	0.09904	0.09801	0.13722	0.11177	0.11176	0.11178	0.15306	0.22984
	312500	0.18517	0.19768	0.18141	0.14245	0.24365	0.18518	0.18517	0.18521	0.20078	0.25878
	625000	0.32633	0.32894	0.33234	0.25738	0.38416	0.32634	0.32632	0.32644	0.31718	0.34244

Table E.1 Electrical conductivity derived from the thyroid tissue microscale model simulations performed for local sensitivity analysis

Relative permittivity [-]	frequency [Hz]	baseline	x_{cell} 6.5µm	x_{cell} 11µm	y_{cell} 6.5µm	y_{cell} 11µm	z_{cell} 6.5µm	z_{cell} 11µm	d_{ECS} 0.3µm	d_{ECS} 0.5µm	d_{ECS} 0.8µm
	76	5579.26410	5809.54491	5405.99359	4031.31970	7748.21987	5579.40363	5579.15322	5580.12193	5185.93666	4596.91600
	152	5579.26405	5809.54485	5405.99355	4031.31968	7748.21972	5579.40359	5579.15317	5580.12188	5185.93662	4596.91597
	305	5579.26385	5809.54460	5405.99338	4031.31961	7748.21912	5579.40338	5579.15297	5580.12168	5185.93647	4596.91585
	610	5579.26305	5809.54360	5405.99270	4031.31934	7748.21671	5579.40258	5579.15216	5580.12088	5185.93583	4596.91538
	1220	5579.25984	5809.53962	5405.99001	4031.31826	7748.20708	5579.39938	5579.14896	5580.11767	5185.93330	4596.91349
	2441	5579.24700	5809.52367	5405.97921	4031.31392	7748.16853	5579.38653	5579.13611	5580.10484	5185.92316	4596.90592
	4882	5579.19565	5809.45987	5405.93602	4031.29656	7748.01436	5579.33519	5579.08476	5580.05353	5185.88262	4596.87566
	9765	5578.99021	5809.20463	5405.76325	4031.22713	7747.39757	5579.12975	5578.87932	5579.84825	5185.72043	4596.75457
	19531	5578.16856	5808.18384	5405.07224	4030.94938	7744.93144	5578.30812	5578.05765	5579.02726	5185.07172	4596.27025
	39062	5574.88494	5804.10497	5402.31044	4029.83888	7735.08613	5575.02461	5574.77396	5575.74625	5182.47880	4594.33416
	78125	5561.79585	5787.85493	5391.29732	4025.40399	7696.00304	5561.93589	5561.68456	5562.66752	5172.13592	4586.60752
	156250	5510.16182	5723.89310	5347.78886	4007.77968	7544.31056	5510.30328	5510.04935	5511.07380	5131.22563	4555.98629
	312500	5314.51878	5483.57439	5182.00168	3939.07332	7003.10261	5314.66483	5314.40251	5315.57560	4974.62089	4437.88886
	625000	4672.46420	4717.00454	4627.18194	3689.99513	5526.82980	4672.61668	4672.34232	4673.90862	4442.70579	4026.14717

Table E.2 Relative permittivity derived from the thyroid tissue microscale model simulations performed for local sensitivity analysis

Conductivity [Sm^{-1}]	frequency [Hz]	baseline	x_{cell} 6.5µm	x_{cell} 11µm	y_{cell} 6.5µm	y_{cell} 11µm	z_{cell} 6.5µm	z_{cell} 11µm	d_{ECS} 0.3µm	d_{ECS} 0.5µm	d_{ECS} 0.8µm
	76	0.27767	0.31387	0.24352	0.31236	0.24567	0.27768	0.27767	0.26954	0.33945	0.40526
	152	0.27767	0.31387	0.24352	0.31236	0.24567	0.27768	0.27767	0.26954	0.33945	0.40526
	305	0.27767	0.31387	0.24352	0.31236	0.24567	0.27768	0.27767	0.26954	0.33945	0.40526
	610	0.27767	0.31387	0.24352	0.31236	0.24567	0.27768	0.27767	0.26954	0.33945	0.40526
	1220	0.27768	0.31388	0.24353	0.31237	0.24569	0.27769	0.27768	0.26955	0.33946	0.40526
	2441	0.27771	0.31390	0.24357	0.31238	0.24573	0.27771	0.27770	0.26958	0.33947	0.40527
	4882	0.27781	0.31398	0.24371	0.31245	0.24592	0.27782	0.27781	0.26968	0.33952	0.40531
	9765	0.27824	0.31429	0.24429	0.31271	0.24665	0.27824	0.27823	0.27010	0.33972	0.40545
	19531	0.27990	0.31554	0.24656	0.31374	0.24955	0.27991	0.27990	0.27176	0.34051	0.40601
	39062	0.28617	0.32020	0.25509	0.31753	0.26030	0.28617	0.28616	0.27800	0.34337	0.40786
	78125	0.30711	0.33573	0.28294	0.33012	0.29416	0.30711	0.30710	0.29897	0.35259	0.41267
	156250	0.36005	0.37732	0.34790	0.36515	0.36711	0.36005	0.36004	0.35251	0.37925	0.42469
	312500	0.44353	0.45014	0.44065	0.43211	0.46278	0.44353	0.44352	0.43815	0.43827	0.45686
	625000	0.52998	0.53105	0.53090	0.51324	0.54713	0.52998	0.52997	0.52797	0.52157	0.52173

Table E.3 Electrical conductivity derived from the thyroid tissue mesoscale model simulations performed for local sensitivity analysis, part 1

Conductivity [Sm^{-1}]	frequency [Hz]	$d_{follicle}$ 50μm	$d_{follicle}$ 100μm	$d_{follicle}$ 150μm	$d_{follicle}$ 200μm	d_{ct} 1μm	d_{ct} 2.5μm	d_{ct} 5μm	$\sigma_{colloid}$ 0.25 [Sm^{-1}]	$\sigma_{colloid}$ 0.55 [Sm^{-1}]	$\sigma_{colloid}$ 0.82 [Sm^{-1}]	$\sigma_{colloid}$ 1.48 [Sm^{-1}]
	76	0.20470	0.27767	0.32535	0.36016	0.27767	0.32548	0.33503	0.18162	0.27767	0.32806	0.39486
	152	0.20470	0.27767	0.32535	0.36016	0.27767	0.32548	0.33503	0.18162	0.27767	0.32806	0.39486
	305	0.20470	0.27767	0.32535	0.36016	0.27767	0.32548	0.33503	0.18163	0.27767	0.32806	0.39486
	610	0.20470	0.27767	0.32535	0.36016	0.27767	0.32548	0.33504	0.18163	0.27767	0.32807	0.39487
	1220	0.20471	0.27768	0.32536	0.36017	0.27768	0.32550	0.33506	0.18163	0.27768	0.32808	0.39488
	2441	0.20474	0.27771	0.32538	0.36019	0.27771	0.32557	0.33514	0.18164	0.27771	0.32811	0.39493
	4882	0.20485	0.27781	0.32548	0.36028	0.27781	0.32585	0.33549	0.18169	0.27781	0.32826	0.39514
	9765	0.20529	0.27824	0.32588	0.36065	0.27824	0.32696	0.33685	0.18188	0.27824	0.32884	0.39598
	19531	0.20702	0.27990	0.32743	0.36207	0.27990	0.33129	0.34216	0.18264	0.27990	0.33114	0.39930
	39062	0.21357	0.28617	0.33325	0.36740	0.28617	0.34722	0.36148	0.18550	0.28617	0.33984	0.41190
	78125	0.23595	0.30711	0.35239	0.38474	0.30711	0.39625	0.41972	0.19492	0.30711	0.36928	0.45549
	156250	0.29657	0.36005	0.39886	0.42568	0.36005	0.49996	0.54219	0.21836	0.36005	0.44632	0.57639
	312500	0.40705	0.44353	0.46670	0.48258	0.44353	0.63955	0.71991	0.25797	0.44353	0.57251	0.79472
	625000	0.54800	0.52998	0.52998	0.53242	0.52998	0.79047	0.97730	0.31302	0.52998	0.69826	1.02451

Table E.4 Electrical conductivity derived from the thyroid tissue mesoscale model simulations performed for local sensitivity analysis, part 2

Conductivity [Sm^{-1}]	frequency [Hz]	$\varepsilon r_{colloid}$ 50	$\varepsilon r_{colloid}$ 70	$\varepsilon r_{colloid}$ 87	$\varepsilon r_{colloid}$ 150	σ_{ct} 0.03[Sm^{-1}]	σ_{ct} 0.35[Sm^{-1}]	σ_{ct} 0.67[Sm^{-1}]	εr_{ct} 1.5e4	εr_{ct} 1e5	εr_{ct} 1e6	εr_{ct} 1e7	εr_{ct} 5e7
	76	0.27767	0.27767	0.27767	0.27767	0.24447	0.27437	0.28560	0.27767	0.27767	0.27767	0.27772	0.27869
	152	0.27767	0.27767	0.27767	0.27767	0.24448	0.27437	0.28560	0.27767	0.27767	0.27767	0.27787	0.28032
	305	0.27767	0.27767	0.27767	0.27767	0.24454	0.27437	0.28560	0.27767	0.27767	0.27768	0.27838	0.28325
	610	0.27767	0.27767	0.27767	0.27767	0.24478	0.27438	0.28560	0.27767	0.27767	0.27771	0.27971	0.28898
	1220	0.27768	0.27768	0.27768	0.27768	0.24571	0.27438	0.28561	0.27768	0.27768	0.27782	0.28218	0.30094
	2441	0.27771	0.27771	0.27771	0.27771	0.24887	0.27442	0.28563	0.27770	0.27771	0.27821	0.28691	0.33295
	4882	0.27781	0.27781	0.27781	0.27781	0.25655	0.27455	0.28572	0.27781	0.27781	0.27939	0.29680	0.44686
	9765	0.27824	0.27824	0.27824	0.27824	0.26614	0.27505	0.28609	0.27811	0.27824	0.28209	0.32129	0.89226
	19531	0.27990	0.27990	0.27990	0.27990	0.27288	0.27701	0.28755	0.27941	0.27990	0.28821	0.40381	2.66156
	39062	0.28617	0.28617	0.28617	0.28617	0.28093	0.28391	0.29319	0.28444	0.28617	0.30414	0.71666	9.61593
	78125	0.30710	0.30710	0.30710	0.30711	0.30259	0.30548	0.31287	0.30212	0.30711	0.34818	1.87697	35.78611
	156250	0.36001	0.36002	0.36002	0.36005	0.35588	0.35869	0.36469	0.34941	0.36005	0.46108	5.71043	124.73384
	312500	0.44335	0.44339	0.44342	0.44353	0.43913	0.44214	0.44803	0.42727	0.44353	0.69267	17.31592	404.90626
	625000	0.52922	0.52937	0.52950	0.52998	0.52542	0.52855	0.53455	0.50514	0.52998	1.22285	56.03356	1358.1019

Table E.5 Electrical conductivity derived from the thyroid tissue mesoscale model simulations performed for local sensitivity analysis, part 3

Relative permittivity [-]	frequency [Hz]	baseline	x_{cell} 6.5µm	x_{cell} 11µm	y_{cell} 6.5µm	y_{cell} 11µm	z_{cell} 6.5µm	z_{cell} 11µm	d_{ECS} 0.3µm	d_{ECS} 0.5µm	d_{ECS} 0.8µm
	76	12768.4126	11126.7925	14592.7993	10098.6382	16328.7759	12768.2701	12768.5232	12700.5092	8772.7395	6600.5642
	152	12768.4061	11126.7869	14592.7919	10098.6331	16328.7675	12768.2646	12768.5166	12700.5030	8772.7346	6600.5577
	305	12768.3817	11126.7639	14592.7637	10098.6121	16328.7285	12768.2403	12768.4923	12700.4800	8772.7139	6600.5308
	610	12768.2855	11126.6728	14592.6480	10098.5279	16328.5751	12768.1430	12768.3950	12700.3890	8772.6321	6600.4239
	1220	12767.8977	11126.3084	14592.1854	10098.1905	16327.9615	12767.7552	12768.0082	12700.0222	8772.3044	6599.9963
	2441	12766.3474	11124.8499	14590.3349	10096.8403	16325.5071	12766.2049	12766.4569	12698.5549	8770.9940	6598.2861
	4882	12760.1602	11119.0349	14582.9447	10091.4632	16315.7053	12760.0177	12760.2707	12692.7036	8765.7775	6591.4832
	9765	12735.6307	11096.0681	14553.5532	10070.2644	16276.6949	12735.4882	12735.7411	12669.4949	8745.2754	6564.8283
	19531	12640.8312	11008.5973	14438.6637	9990.1042	16123.8448	12640.6902	12640.9415	12579.7303	8668.6788	6466.4674
	39062	12302.5417	10711.2969	14014.0676	9724.5223	15556.2942	12302.4027	12302.6506	12258.4838	8425.9645	6169.8812
	78125	11277.2647	9899.7995	12649.2828	9044.5215	13755.5999	11277.1442	11277.3587	11277.3665	7880.7545	5620.2169
	156250	8864.8906	8108.9967	9446.6126	7605.3010	9919.8946	8864.8270	8864.9403	8935.6962	6910.6561	5041.0889
	312500	5603.4372	5479.9771	5595.1207	5262.3411	6008.1535	5603.4260	5603.4461	5701.5439	5287.7502	4368.7416
	625000	3600.5324	3603.8440	3560.2824	3374.0705	3927.2501	3600.5363	3600.5293	3666.6580	3667.3810	3457.4817

Table E.6 Relative permittivity derived from the thyroid tissue mesoscale model simulations performed for local sensitivity analysis, part 1

Relative permittivity [-]	frequency [Hz]	$d_{follicle}$ 50μm	$d_{follicle}$ 100μm	$d_{follicle}$ 150μm	$d_{follicle}$ 200μm	d_{ct} 1μm	d_{ct} 2.5μm	d_{ct} 5μm
	76	13188.6656	12768.4126	11892.9527	10922.9281	12768.4126	24989.1839	30862.3862
	152	13188.6609	12768.4061	11892.9452	10922.9203	12768.4061	24989.1701	30862.3685
	305	13188.6430	12768.3817	11892.9177	10922.8917	12768.3817	24989.1088	30862.2931
	610	13188.5723	12768.2855	11892.8090	10922.7788	12768.2855	24988.8667	30861.9940
	1220	13188.2880	12767.8977	11892.3705	10922.3235	12767.8977	24987.8983	30860.7976
	2441	13187.1512	12766.3474	11890.6176	10920.5032	12766.3474	24984.0246	30856.0114
	4882	13182.6164	12760.1602	11883.6215	10913.2379	12760.1602	24968.5643	30836.9202
	9765	13164.6671	12735.6307	11855.8784	10884.4269	12735.6307	24907.1875	30761.2974
	19531	13095.7294	12640.8312	11748.5653	10772.9759	12640.8312	24668.9375	30470.2101
	39062	12854.6771	12302.5417	11364.7990	10374.5711	12302.5417	23810.0643	29449.9849
	78125	12151.4090	11277.2647	10204.9386	9178.5204	11277.2647	21241.3799	26584.4338
	156250	10469.3495	8864.8906	7584.7964	6566.8998	8864.8906	16054.7234	21145.7661
	312500	7799.5019	5603.4372	4387.1196	3597.3348	5603.4372	10855.5564	15763.9450
	625000	5674.4351	3600.5324	2661.5771	2119.0624	3600.5324	8046.1666	12755.2159

Table E.7 Relative permittivity derived from the thyroid tissue mesoscale model simulations performed for local sensitivity analysis, part 2

Relative permittivity [-]	frequency [Hz]	$\sigma_{colloid}$ 0.25 [Sm^{-1}]	$\sigma_{colloid}$ 0.55 [Sm^{-1}]	$\sigma_{colloid}$ 0.82 [Sm^{-1}]	$\sigma_{colloid}$ 1.48 [Sm^{-1}]	$\varepsilon r_{colloid}$ 50	$\varepsilon r_{colloid}$ 70	$\varepsilon r_{colloid}$ 87	$\varepsilon r_{colloid}$ 150
	76	6670.4956	12768.4126	17099.3248	24059.0561	12745.1562	12749.8075	12753.7611	12768.4126
	152	6670.4921	12768.4061	17099.3170	24059.0475	12745.1496	12749.8009	12753.7545	12768.4061
	305	6670.4791	12768.3817	17099.2880	24059.0152	12745.1253	12749.7765	12753.7301	12768.3817
	610	6670.4277	12768.2855	17099.1735	24058.8873	12745.0289	12749.6802	12753.6339	12768.2855
	1220	6670.2207	12767.8977	17098.7119	24058.3724	12744.6404	12749.2919	12753.2456	12767.8977
	2441	6669.3929	12766.3474	17096.8664	24056.3138	12743.0875	12747.7395	12751.6936	12766.3474
	4882	6666.0893	12760.1602	17089.5022	24048.1019	12736.8897	12741.5438	12745.4998	12760.1602
	9765	6652.9903	12735.6307	17060.3187	24015.5972	12712.3183	12716.9807	12720.9438	12735.6307
	19531	6602.3508	12640.8312	16947.7035	23890.7226	12617.3527	12622.0484	12626.0397	12640.8312
	39062	6421.8181	12302.5417	16547.4680	23453.0588	12278.4205	12283.2447	12287.3453	12302.5417
	78125	5885.6358	11277.2647	15333.8115	22152.9944	11250.7770	11256.0744	11260.5772	11277.2647
	156250	4744.2294	8864.8906	12338.6424	18803.7987	8830.7589	8837.5850	8843.3872	8864.8906
	312500	3462.0320	5603.4372	7758.8994	12658.0170	5553.4580	5563.4544	5571.9512	5603.4372
	625000	2745.1496	3600.5324	4564.1532	7182.8885	3535.2060	3548.2736	3559.3802	3600.5324

Table E.8 Relative permittivity derived from the thyroid tissue mesoscale model simulations performed for local sensitivity analysis, part 3

Relative permittivity [-]	frequency [Hz]	σ_{ct} 0.03[Sm^{-1}]	σ_{ct} 0.35[Sm^{-1}]	σ_{ct} 0.67[Sm^{-1}]	εr_{ct} 1.5e4	εr_{ct} 1e5	εr_{ct} 1e6	εr_{ct} 1e7	εr_{ct} 5e7
	76	94816.3320	13539.8755	12052.7823	10259.7295	12768.4126	39326.7900	303785.7883	1377166.8935
	152	94777.2431	13539.8613	12052.7781	10259.7256	12768.4061	39323.3855	300542.2520	1233484.9322
	305	94619.8745	13539.8062	12052.7635	10259.7121	12768.3817	39309.6771	289633.5308	1083841.5342
	610	93997.7652	13539.5872	12052.7061	10259.6591	12768.2855	39255.4054	264619.5324	961061.3733
	1220	91601.6031	13538.7085	12052.4731	10259.4440	12767.8977	39045.1406	233575.9311	861936.9728
	2441	83279.0302	13535.1985	12051.5424	10258.5846	12766.3474	38298.8623	207533.1099	804967.1185
	4882	62385.5310	13521.2672	12047.8200	10255.1477	12760.1602	36291.9555	185762.6199	781070.3848
	9765	35544.8487	13467.1647	12032.9572	10241.4239	12735.6307	33198.5730	171607.6020	772915.3269
	19531	19957.1147	13273.0226	11973.9579	10186.9352	12640.8312	30316.8643	165203.4882	770549.6380
	39062	14348.5559	12708.4798	11745.0460	9975.3715	12302.5417	27740.7548	162719.4315	769726.6551
	78125	11859.7967	11444.0717	10929.3605	9219.8235	11277.2647	25351.9587	161261.8749	768781.0724
	156250	9027.5616	8915.0676	8724.2779	7167.2209	8864.8906	22536.7963	158970.5652	766626.2031
	312500	5639.3071	5614.6704	5568.2864	4197.3070	5603.4372	19339.2070	155926.2347	763616.3869
	625000	3609.5434	3603.3309	3591.7126	2274.8299	3600.5324	17352.9816	153976.2067	761681.6108

Table E.9 Relative permittivity derived from the thyroid tissue mesoscale model simulations performed for local sensitivity analysis, part 4

Conductivity [Sm^{-1}]	frequency [Hz]	baseline	x_{cell} 6.5µm	x_{cell} 11µm	y_{cell} 6.5µm	y_{cell} 11µm	z_{cell} 6.5µm	z_{cell} 11µm	d_{ECS} 0.3µm	d_{ECS} 0.5µm
	76	0.27767	0.18585	0.08958	0.13946	0.13016	0.13430	0.07961	0.13430	0.21918
	152	0.27767	0.18585	0.08958	0.13946	0.13016	0.13430	0.07961	0.13430	0.21918
	305	0.27767	0.18585	0.08958	0.13946	0.13016	0.13430	0.07961	0.13430	0.21918
	610	0.27767	0.18585	0.08958	0.13946	0.13016	0.13430	0.07961	0.13430	0.21918
	1220	0.27768	0.18586	0.08959	0.13946	0.13017	0.13430	0.07961	0.13430	0.21918
	2441	0.27771	0.18586	0.08959	0.13946	0.13018	0.13431	0.07961	0.13430	0.21919
	4882	0.27781	0.18587	0.08961	0.13947	0.13022	0.13432	0.07964	0.13432	0.21919
	9765	0.27824	0.18592	0.08969	0.13949	0.13040	0.13438	0.07974	0.13438	0.21923
	19531	0.27990	0.18611	0.08999	0.13958	0.13113	0.13461	0.08015	0.13461	0.21935
	39062	0.28617	0.18689	0.09119	0.13996	0.13398	0.13552	0.08176	0.13552	0.21987
	78125	0.30711	0.18996	0.09594	0.14148	0.14502	0.13915	0.08811	0.13915	0.22190
	156250	0.36005	0.20176	0.11406	0.14745	0.18364	0.15306	0.11178	0.15306	0.22984
	312500	0.44353	0.24256	0.17458	0.16988	0.28303	0.20078	0.18521	0.20078	0.25878
	625000	0.52998	0.34409	0.31266	0.24148	0.41786	0.31718	0.32644	0.31718	0.34244

Table E.10 Electrical conductivity derived from the parathyroid tissue microscale model simulations performed for local sensitivity analysis

Relative permittivity [-]	frequency [Hz]	baseline	x_{cell} 6.5µm	x_{cell} 11µm	y_{cell} 6.5µm	y_{cell} 11µm	z_{cell} 6.5µm	z_{cell} 11µm	d_{ECS} 0.3µm	d_{ECS} 0.5µm	x_{cell} 6.5µm
	76	12768.4126	5295.7742	5090.5724	3420.0388	9000.3681	5186.0079	5185.6656	5580.1219	5185.9367	4596.9160
	152	12768.4061	5295.7741	5090.5724	3420.0387	9000.3679	5186.0078	5185.6655	5580.1219	5185.9366	4596.9160
	305	12768.3817	5295.7739	5090.5723	3420.0387	9000.3669	5186.0077	5185.6654	5580.1217	5185.9365	4596.9159
	610	12768.2855	5295.7731	5090.5718	3420.0386	9000.3630	5186.0070	5185.6648	5580.1209	5185.9358	4596.9154
	1220	12767.8977	5295.7698	5090.5698	3420.0379	9000.3472	5186.0045	5185.6622	5580.1177	5185.9333	4596.9135
	2441	12766.3474	5295.7566	5090.5617	3420.0354	9000.2842	5185.9944	5185.6521	5580.1048	5185.9232	4596.9059
	4882	12760.1602	5295.7039	5090.5295	3420.0255	9000.0320	5185.9538	5185.6115	5580.0535	5185.8826	4596.8757
	9765	12735.6307	5295.4930	5090.4008	3419.9856	8999.0232	5185.7917	5185.4493	5579.8483	5185.7204	4596.7546
	19531	12640.8312	5294.6496	5089.8861	3419.8262	8994.9904	5185.1430	5184.8006	5579.0273	5185.0717	4596.2702
	39062	12302.5417	5291.2790	5087.8282	3419.1886	8978.9001	5182.5501	5182.2076	5575.7463	5182.4788	4594.3342
	78125	11277.2647	5277.8434	5079.6159	3416.6409	8915.1779	5172.2074	5171.8644	5562.6675	5172.1359	4586.6075
	156250	8864.8906	5224.8424	5047.0746	3406.4936	8670.1269	5131.2979	5130.9529	5511.0738	5131.2256	4555.9863
	312500	5603.4372	5024.0377	4921.6344	3366.5870	7824.3794	4974.6960	4974.3444	5315.5756	4974.6209	4437.8889
	625000	3600.5324	4365.8239	4484.8412	3217.1320	5725.1795	4442.7876	4442.4247	4673.9086	4442.7058	4026.1472

Table E.11 Relative permittivity derived from the parathyroid tissue microscale model simulations performed for local sensitivity analysis

Appendix F

Publications

I. M. Matella, K. Hunter, S. Balasubramanian, and D. C. Walker, "Multiscale Model Development for Electrical Properties of Thyroid and Parathyroid Tissues," IEEE Open J. Eng. Med. Biol., pp. 1–9, 2023.

II. M. Matella, D. C. Walker, and K. Hunter, "Computational Modelling of Probe Configurations for Electrical Impedance Spectroscopy-based Differentiation of Thyroid and Parathyroid Tissues," in 2023 IEEE International Symposium on Medical Measurements and Applications (MeMeA), 2023, pp. 1–6.

IEEE Open Journal of Engineering in Medicine and Biology

Technology

Multiscale Model Development for Electrical Properties of Thyroid and Parathyroid Tissues

M. Matella, K. Hunter, S. Balasubramanian, *D. C. Walker

***Abstract*—*Goal:* Electrical impedance spectroscopy (EIS) has been suggested as a possible technique to differentiate between thyroid and parathyroid tissue during surgery. This study aims to explore this potential using computational models to simulate the impedance spectra of these tissues, and examine how they are influenced by specific differences in tissue composition and morphology. *Materials and methods:* Finite element models of thyroid and parathyroid tissues at multiple scales were created, and simulated spectra were compared to existing data collected using ZedScan^{TM} probe during surgery. Geometrical and material properties were varied in a local sensitivity study to assess their relative influence. *Results:* Both simulated and measured EIS parathyroid spectra show a higher β dispersion frequency relative to thyroid. However, impedances exhibit overlap at frequencies below 100 kHz. A computational sensitivity study identified uncertainties in extracellular space dimensions, and properties of colloid and fascia compartments as having a significant effect on simulated impedance spectra characteristics. *Conclusions:* We have demonstrated the utility of our multiscale model in simulating impedance spectra and providing insight into their sensitivity to variations in tissue features. Our results suggest that distinguishing between the thyroid and parathyroid spectra is challenging, but could be improved by constraining the properties of colloid and fascia through further computational or experimental research.**

***Index Terms*—Electrical Impedance Spectroscopy, Finite Element Modelling, Thyroid and Parathyroid Tissue Discrimination, Thyroidectomy**

***Impact Statement*- The presented computational study investigated the electrical impedance spectroscopy as a potential method to discriminate thyroid and parathyroid tissue during thyroidectomy.**

I. INTRODUCTION

THYROIDECTOMY is a well-established surgical procedure that encompasses various types of thyroid surgeries. The most prevalent complications associated with the procedure are hypoparathyroidism and hypocalcaemia that are both a result of inadvertent damage or excision of the adjacent parathyroid glands. According to the UK Registry of Endocrine and Thyroid Surgeons which is the most coherent documentation of thyroidectomies performed between 2010-2014 in the UK, 23.6 and 6.5% of patients having whole gland thyroidectomy, respectively, experienced temporary or late hypocalcaemia [1].

The major concern during the surgery are the parathyroid glands themselves, which, due to their small size and location, could be mistaken for other structures (adipose tissues, lymph nodes or benign thyroid nodules) [2]. In general, surgeons rely on their own experience and judgement during the surgery to locate and preserve normal parathyroid glands. However, introducing an additional measurement tool that would guide the surgeon during the procedure, would be beneficial to decrease the risks of hypoparathyroidism and hypocalcaemia. To date, fluorescence imaging has been considered a potentially useful aid to the surgeon to differentiate parathyroid glands from adjacent tissues [3], [4].

A. Electrical Impedance Spectroscopy

Electrical Impedance Spectroscopy (EIS) is a measurement technique that could be incorporated to the thyroidectomy procedure. In its principle, a small alternating current is passed through soft tissues, and the resultant impedance is measured across a range of frequencies, allowing the construction of a characteristic impedance curve, or "spectrum" for that tissue. The diagnostic value of EIS has been documented and implemented to detect lesions in skin [5], cervix [6], oral tissue [7], bladder [8], prostate [9], breast tissue [10] and oesophagus [11]. After being exposed to electrical field, the electrical conduction by the biological structures is possible due to the ions concentrated in different structures. Moreover, tissues are capable not only of conducting, but also of retaining electrical charge, which is attributed mainly to the properties of the cell membranes. In the case of biological tissues, EIS spectra are characterised by the β dispersion – a substantial fall in the real part of impedance values in the kHz-MHz region, which is a result of the capacitive nature of the cell membrane.

The principle of measurement of a typical tetrapolar EIS device is shown in Fig. 1 with the example of a commercial probe ZedScan^{TM}, Zilico Limited, currently licensed for use to detect changes in cervical epithelium accompanying colposcopy. A known magnitude of the alternating current I flows through the two active electrodes, meanwhile, passive electrodes capture the potential difference required to the impedance calculation at each frequency.

Furthermore, the electrical behaviour of biological tissues has been a subject of various computational studies documented in the literature. Multiscale Finite Element (FE) models

This paper got submitted for review on June 26th, 2023.

M. Matella and *D. C. Walker are with the Computer Science Department, University of Sheffield, Sheffield S1 4DP, UK and Insigneo, Institute for in silico Medicine, Sheffield S1 3JD, UK (correspondence e-mail: d.c.walker@sheffield.ac.uk).

K. Hunter is with the Liverpool Head and Neck Centre, Molecular and Clinical Cancer Medicine, University of Liverpool, Liverpool L69 7TX, UK

S. Balasubramanian is with Department of Oncology and Metabolism, Royal Hallamshire Hospital School of Medicine and Biomedical Sciences, University of Sheffield, Sheffield S10 2RX, UK

(a) (b)

Fig. 1. Electrical Impedance Spectroscopy device: (a) ZedScan™ [12], (b) tip of the tetrapolar probe showing the principle of the measurement, a known current I flows between the active electrodes (I_1 and V_0) while the passive electrodes (V_1 and V_2) capture the potential difference at each frequency

relating to the EIS tetrapolar probe measurements of cervical epithelium [13], bladder [14] and oral tissues [15] have been developed to determine the changes in tissues electrical properties due to cancerous lesions. Some studies have focused on skin, such as a FE model simulating the electrical properties of skin pathologies [16], or assessing the thickness of stratum corneum with an analytical model [17]. Another research group proposed a parameterisation method to investigate the impact of the cell shapes on their electrical properties [18] and expanded the research to skin properties investigation using analytical and numerical methods [19]. There is only one study [20] constructing a FE model to explore the electrical and heat transfer properties of thyroid tissue, with the emphasis on the follicular structure and colloid's conductivity. Nonetheless, the cellular details have not been included in this model nor studied separately in this case.

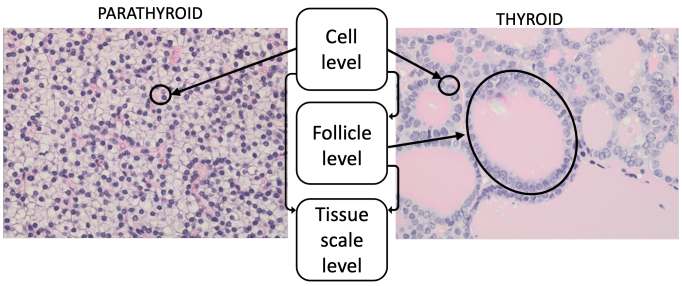

Fig. 2. Thyroid and parathyroid histology images with labelled levels of complexity corresponding to the levels of the computational model

B. Aim of the study

The differences in the thyroid and parathyroid impedance recorded with an EIS probe have already been evaluated empirically in [2] suggesting the regions in both tissues' spectra that could allow their discrimination. However, the EIS measurements solely inform of the bulk electrical properties without the ability to make the connection between the recorded impedance spectra and the tissue characteristics responsible for the observed behaviour. That connection, however, can be explored by implementing computational modelling to accompany the EIS experimental results and complement them in order to provide more insight into the mechanisms that influence tissue impedance.

Moreover, as previous research has demonstrated [6], [13], the frequency-dependent impedance, and hence the shape of the dispersion, depend on the geometrical characteristics and organisation of the structures within the tissue, along with the tissues' material composition and their electrical properties. Therefore, tissue types' structural differences at the cellular or supra-cellular level might be expected to give rise to different impedance curves. Those differences in the case of thyroid and parathyroid tissue (Fig.2) are substantial with thyroid being composed of an arrangement of cell-lined colloid-filled follicles, which are entirely absent in parathyroid, the latter being composed of closely packed chief cells.

The aim of this project is to develop a mechanistic model recreating thyroid and parathyroid tissues' structure and composition, to simulate their theoretical electrical behaviour and to compare against the in vivo measurements presented in [2]. Furthermore, the influence of specific features of thyroid and parathyroid tissue structure on different characteristics of the impedance spectra will be investigated through a local sensitivity study.

II. MATERIALS AND METHODS

A. Finite element modelling of electrical tissue properties

As highlighted in the Introduction, computational models can be a useful tool to simulate and evaluate the effect of various tissue characteristics on the impedance spectra. For the purposes of this study, numerical modelling (of which the FE approach is an example) is more suitable than the analytical methods, such as Maxwell Mixture Theory [21], that requires numerous assumptions in the structure of the model and its homogeneity which are not adequate in the context of thyroid and parathyroid. FE analysis is a well-established numerical method for solving electric field problems, including in biological systems. Through the process of discretisation, boundary conditions and assignment of element material properties, FE modelling can approximate the potential distribution within the domain. The latter is divided into a substantial number of small elements connected at nodes where the electric scalar potential is being approximated based on the assigned boundary conditions and material properties, such as electric conductivity and relative permittivity in the case of an electrical simulation. For this study, the quasistatic time-harmonic simulation approach has been applied using the FE commercial software Ansys Mechanical APDL. Further details concerning the electrical scalar potential approximation are summarised in the Supplementary Materials Section I.

B. Multiscale model development

As previously mentioned, the unique frequency-dependent properties of tissues are a result of the capacitive nature of cell membranes, which makes them a crucial component for inclusion in the model. However, due to their small size (~8 nm), it is not computationally feasible to include them in a tissue model recreating the impedance measurement with EIS

probe, which requires a simulation volume of the order of centimetres. Such a model would comprise over trillion nodes for thyroid tissue only, which is computationally intractable.

To overcome this limitation, a multiscale modelling approach was implemented, where the tissue's structure is considered as a set of hierarchical substructures, representing different levels of complexity from cellular level (microscale) to tissue level (macroscale). For the thyroid tissue, an additional scale (mesoscale) has been included to reconstruct this tissue's basic structural unit – the follicle. The models of different scale are visualised in Fig. 3.

Transfer impedivities are calculated, starting with the lowest model hierarchy (microscale) and passed to the higher level models in the form of element material properties. For lower scale models (cell and follicle), the effective impedivity is simulated at 14 frequency points f from the range of 76Hz – 625kHz which correspond to the measurement points and range of the Zedscan^{TM} device. Subsequently, the results are processed to calculate electric conductivity (σ) and relative permittivity (ε_r) from (1) and (2), to assign as material properties in the appropriate higher-level model compartments:

$$\sigma(f) = d/(A \cdot Z'(f)) \tag{1}$$

$$\varepsilon_r(f) = (Y''(f)/2\pi f \cdot \varepsilon_0) \cdot (d/A) \tag{2}$$

where:

$$Y''(f) = -Z''(f)/((Z'(f))^2 + (Z''(f))^2) \tag{3}$$

where:

where: d and A – thickness and cross-sectional area of the model, ε_0 – permittivity of free space (8.854 x 10^{-12} Fm^{-1}), Z' and Z'' – real and imaginary part of effective impedance obtained from lower level simulation, Y'' – imaginary part of admittance. The derived electrical material properties are then transferred to the appropriate elements of the adjacent higher scale model, according to the tissues' hierarchical structure, i.e. thyroid microscale level results are assigned to the cell layer compartment elements of the mesoscale model, and then the follicle mesoscale results are passed on to the thyroid compartment at macroscale. Similarly, the parathyroid microscale results are assigned to elements of this gland's compartment at the macroscale level (as there is no mesoscale model for parathyroid tissue).

Thyroid model:

The microscale model (Fig. 3a) consists of three compartments: cytoplasm, cell membrane and extracellular space (ECS) layer. All simulated cells are anuclear due to the outcomes of previous research [13] which concluded that due to the more conductive properties of the nuclear membrane in comparison to the cell membrane, the nucleus and its membrane have a negligible effect on the effective electrical properties of cells. The mesoscale model (Fig. 3b) comprises colloid (a protein-rich material), homogenised cells (material properties obtained from the microscale level simulation) and connective tissue layer compartments. All models assume simplified cuboidal structures after initial exploration demonstrated that shape and arrangement have a negligible effect on impedance properties compared to other characteristics of interest (data not shown).

The macroscale model recreates the electrode arrangements of a tetrapolar EIS ZedScan^{TM} probe with the 0.6 µm electrodes arranged with the centers located on a circle of 2 mm diameter (Fig. 3e). The impedance is obtained by dividing the injected current of 6 µA assigned to the driving electrode (I_1) by the potential difference recorded by the passive electrodes (V_1 and V_2). The dimensions of the macroscale models were identical for both tissue types: 40x40x15 mm (the cross-section through the cuboid thyroid model is shown in Fig. 3c). A superficial fascia layer was included in this model, representing loose connective tissue which encapsulates the glands. The surgeon is able to distinguish and peel off the superficial fascia before placing the probe for the EIS measurement, however, the extent of tissue removal cannot be guaranteed. Hence the effects of fascia layer, its thickness and material properties are also explored in this study.

Parathyroid model:

Reflecting on the parathyroid's tight cellular morphology, only two sublevels in multiscale modelling have been recognised. The microscale parathyroid model was constructed in the same manner as the three-compartmental thyroid cell model (Fig. 3a). Moreover, the parathyroid macroscale model shows similarities to the thyroid model in terms of dimensions and the boundary conditions set up. The model adjusted to the parathyroid recreates the tissue layout when the EIS measurement is performed when parathyroid is surrounded by thyroid tissue - on the posterior surface of the thyroid - and the electrodes are positioned symmetrically in the centre of the gland (Fig. 3d).

C. *Parameter sensitivity study*

To investigate the impact of various geometrical and electrical properties of the compartments in all submodels on the macroscale impedance, a local intercompartmental sensitivity analysis was performed in an one-at-a-time (OAT) manner to determine the isolated effects of the parameters on the simulation results. In the intercompartmental analysis, the studied input parameters belong to structures across different scales and their effects are propagated and evaluated at the highest scale, in this case by comparing the macroscale computed EIS spectra. For each parameter, its baseline (usually mean of values reported in the literature), minimum and maximum values have been chosen for analysis (in a few cases, more than three points have been selected to better cover the whole parameter range), with remaining parameters fixed to their baseline value. The parameters' range has been decided based on the values documented in the literature and our own histology measurements.

There have been thirteen input parameters investigated for thyroid tissue (seven relating to morphological characteristics and six to electrical properties uncertainties), and eight for parathyroid (six geometrical, two electrical). In previous work [13] in electrical properties of cells, the effects of the uncertainties in the material properties of the cell compartments have been investigated, hence, were excluded from this study and kept constant throughout all simulations along with the cell membrane thickness (8 nm).

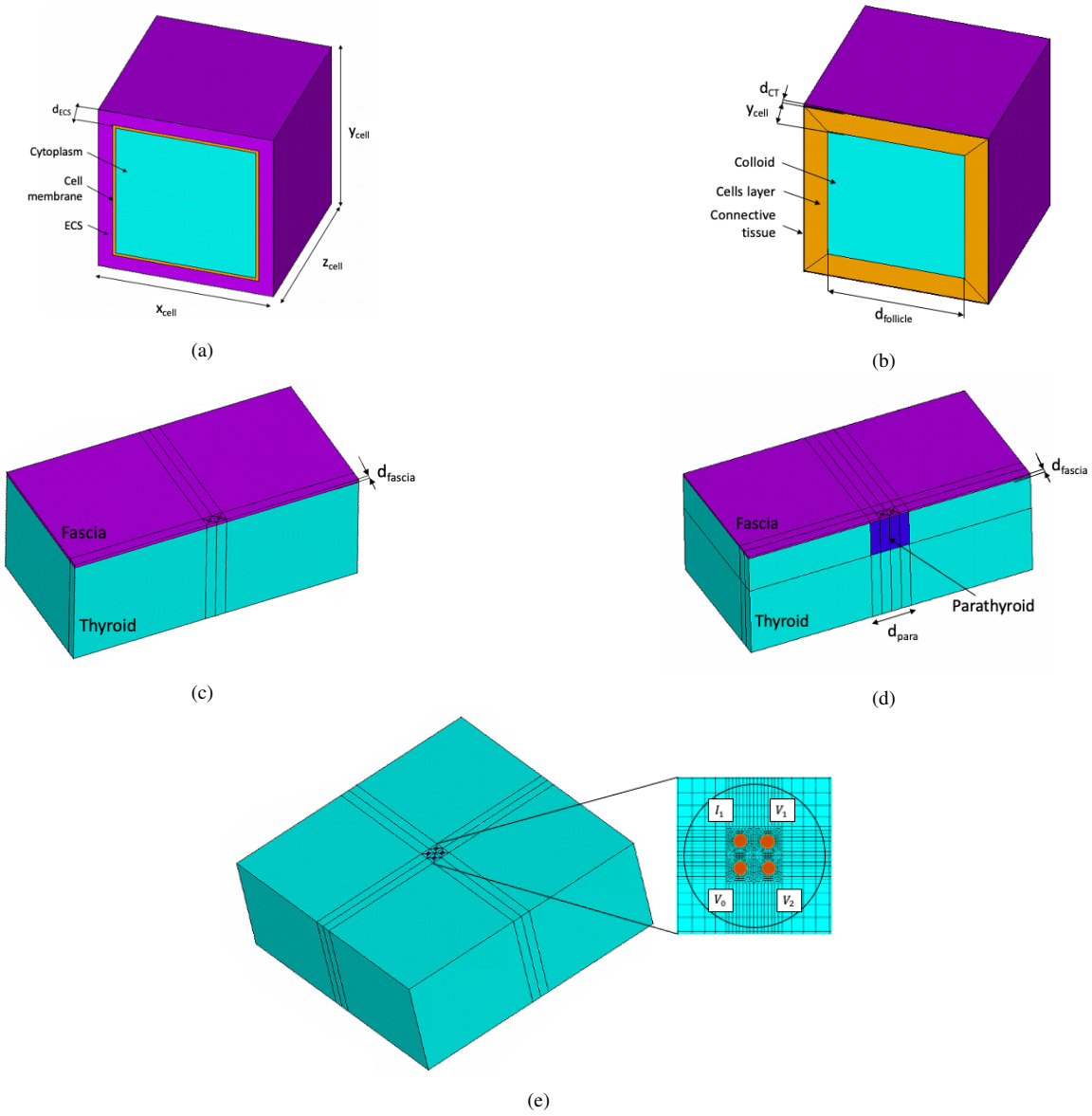

Fig. 3. Multiscale model developments with labeled compartments: (a) microscale model, (b) mesoscale model, (c) thyroid macroscale model, (d) parathyroid macroscale model, (e) macroscale model with the electrode pattern, where: x_{cell}, y_{cell}, z_{cell} - cell dimensions, d_{ECS} - ECS thickness, $d_{follicle}$ - dimensions of colloid compartment in the mesoscale model , d_{CT} - connective tissue thickness, d_{fascia} - fascia thickness, d_{para} - dimensions of parathyroid gland, (I_1 and V_0) - active electrodes, (V_1 and V_2) - passive electrodes

Full list of the values of the investigated and fixed parameters is summarised in detail in Section II of Supplementary Materials (Tables II and III) with further discussion.

D. Parametrisation of simulated spectra

In order to make a quantitative comparison between the results, each simulated spectrum has been parameterised by selecting three indices: two impedance values Z_1 and Z_{14} at the lowest and highest frequency points (76 Hz and 625 kHz), and the dispersion frequency f_{mid} at the centre of the dispersion (frequency for when impedance takes the mid-point value between Z_1 and Z_{14}).

E. Comparison with in vivo measurements

The in vivo measurements were previously published [2] and the experimental data from the thyroid and parathyroid tissue was used in the study with the authors' permission. The mean EIS measurements of thyroid (n=53) and parathyroid (n=42) have been taken for the analysis and, similarly to the simulated spectra, three indices, Z_1, Z_{14} and f_{mid} extracted for each experimental spectrum for the quantitative comparison.

III. RESULTS

All computed results presented are real impedance values at 14 frequencies in the range between 76Hz-625kHz from the macroscale model simulations (the lower-scale results in a form of electrical material properties are summarised in

the Supplementary Dataset). The study resulted in 36 and 19 computed EIS spectra, where each of the input parameters was investigated in the OAT sensitivity study for thyroid and parathyroid respectively. To aid the quantitative comparison, the Z_1, Z_{14} and f_{mid} spectra indices have been derived for each computed and measured in vivo spectrum.

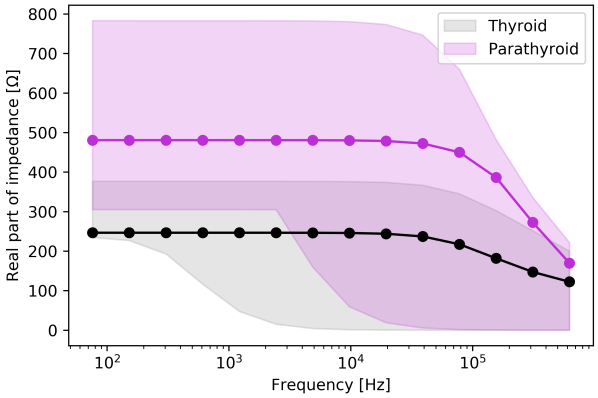

Fig. 4. Baseline computed impedance spectra obtained with the default input parameters for thyroid (black spectrum) and parathyroid (pink spectrum) tissues with marked range of all computed results obtained through the variation of geometrical and electrical properties summaries in Table II and III from Supplementary Materials

A. Computed impedance spectra

The frequency-dependent baseline impedance spectra obtained for thyroid and parathyroid tissues with the range of the curves generated by varying geometrical and electrical properties (summarised in Table II and III from Supplementary Materials) are displayed in Fig. 4. These results imply that it is expected to observe higher impedance across all frequencies for the parathyroid compared to thyroid when both models are at their default configuration of morphological and electrical properties. However, the inspection of the results' range reveals an overlap between the computed results that increases with the frequency.

B. Computed and measured in vivo impedance comparison

Computed spectra are plotted against the range of the experimental results in Fig. 5. The presentation of individual simulated spectra rather than simply the baseline curve (as shown in Fig. 4) permits the inspection of the variation in the shape of individual spectra according to the investigated variation in the morphology and electrical properties. It is apparent that there are similarities with in vivo measurements observed for both thyroid and parathyroid tissues. However, at frequencies below 100kHz, the computed thyroid spectra correspond to the lower impedance values from the experimental data, with the opposite trend for the parathyroid case.

The quantitative comparison of the mean (±standard deviation) values of extracted spectra parameters (Z_1, Z_{14} and f_{mid}) is presented in Table I. A visual comparison of the experimental and computational chosen spectra parameters is pictured in Fig. 6. Similar trends of higher mean Z_{14} and f_{mid} for parathyroid tissue is documented for both computed and experimental results as seen in Table I and Fig. 6b and 6c. Conversely, the Z_1 computed results did not predict higher values for thyroid tissue over the parathyroid as observed in the experimental data. Nonetheless, the visual comparison of the spectra indices highlights that the majority of the computed results is in agreement and within the range of the experimental data.

SELECTED SPECTRA INDICES

	Thyroid	Parathyroid
Computed:		
$Z_1[\Omega]$	239.02 (±40.26)	464.92 (±114.95)
$Z_{14}[\Omega]$	103.58 (±50.43)	120.06 (±66.31)
$f_{mid}[kHz]$	139.86 (±62.26)	192.00 (±79.48)
Experimental:		
$Z_1[\Omega]$	325.42 (±117.00)	280.58 (±97.37)
$Z_{14}[\Omega]$	112.50 (±15.67)	132.70 (±35.50)
$f_{mid}[kHz]$	62.23 (±48.52)	157.26 (±69.67)

TABLE I. The mean (±standard deviation) values for the extracted spectra indices for the computed and experimental results for both tissue types.

C. Parameter sensitivity study

Finally, an itercompartmental local sensitivity study has been performed to investigate the isolated effect of each morphological and electrical input parameter on the selected macroscale spectra indices: Z_1, Z_{14} and f_{mid}. The parameters were varied accordingly to the values presented in Section II of Supplementary Materials (Tables II and III) in the OAT manner. Each bar shows the maximum and minimum percentage change from the mean result calculated for each parameter.

Thyroid: geometrical parameters

As shown in Fig. 7a, thyroid impedance results were predominantly sensitive to changes in the size of the follicles ($d_{follicle}$) at the low frequencies (Z_1) and the thickness of the connective tissue (d_{ct}) at high frequencies (Z_{14}). The greatest differences in the middle frequency (f_{mid}) results were observed for the variations in the ECS thickness (d_{ECS}). All three extracted indices were insensitive to the changes in the cell width - dimension in the z direction (z_{cell}).

Thyroid: material properties

Fig. 7b shows the results for the sensitivity analysis of the material properties of the thyroid model compartments. Among the parameters studied, the colloid conductivity ($\sigma_{colloid}$), connective tissue and fascia relative permittivity (εr_{CT} and εr_{fascia}) are those that have the most substantial impact on all three indices, while variation in the other parameters resulted in less than ±25% variation from the mean value of the spectra parameters.

Parathyroid parameter study

Fig. 7c shows that the ECS thickness (d_{ECS}) and cell length - size in the x direction (x_{cell}) - have the most significant influence on the Z_1. Similarly to the results from the thyroid model, the high frequency impedance is more sensitive to the changes in fascia thickness (d_{fascia}) and its permittivity

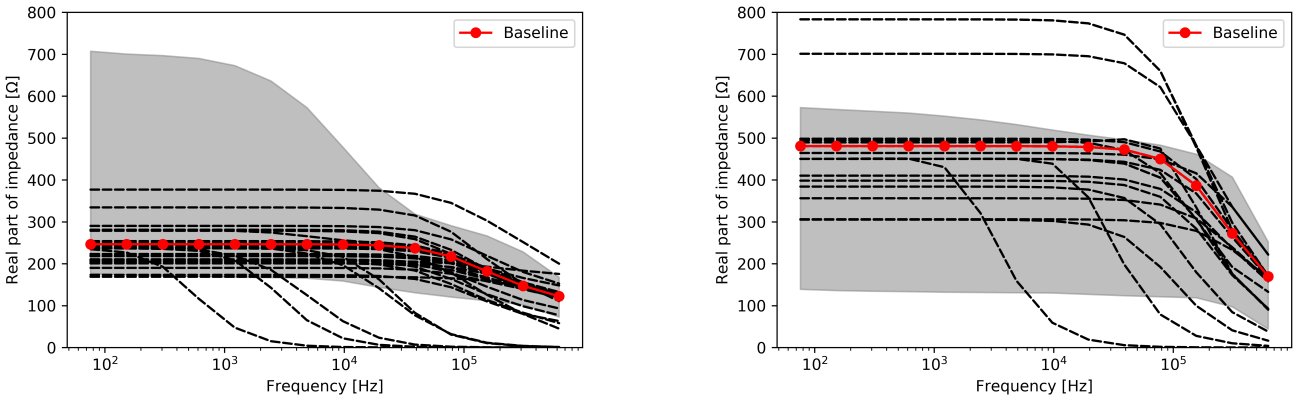

(a) (b)

Fig. 5. Comparison of the computed spectra (black dashed lines, with the red dotted line marking the baseline spectrum) against the range of experimental data (grey range) for: (a) thyroid, (b) parathyroid tissue

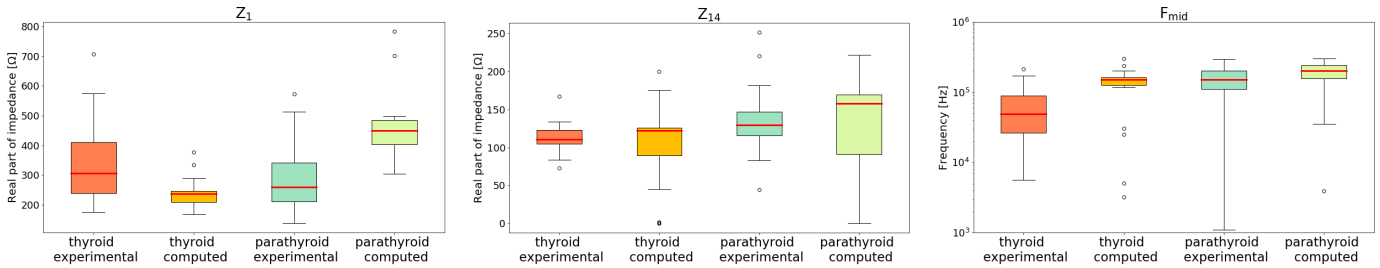

(a) (b) (c)

Fig. 6. Box and whisker plot of the extracted spectra indices (Z_1 - impedance at 76 Hz, Z_{14} - impedance at 625kHz and f_{mid} - dispersion frequency) comparing both glands and the computed and experimental results

(εr_{fascia}), with the middle frequency also exhibiting sensitivity to the latter (εr_{fascia}).

IV. DISCUSSION

The purpose of this study was to develop and apply a computational model to investigate the potential of electrical impedance spectroscopy to differentiate tissues during thyroidectomy. The presented multiscale finite-element modelling pipeline was designed to simulate the theoretical EIS spectra for thyroid and parathyroid tissues in order to analyse and compare them to curves obtained during in vivo measurements. Moreover, the effects of the variability in geometrical parameters and uncertainty in material properties of these tissues at micro-, meso- and macroscales on the ”measured” impedance have been evaluated.

A qualitative comparison of simulated results, as shown in Fig. 4, indicates a distinct difference between the baseline thyroid and parathyroid spectra. The baseline results suggest the parathyroid impedance is expected to be higher than thyroid impedance, with the parathyroid impedance value being about 95% and 37% higher than for the thyroid at 76Hz and 625kHz respectively. However, it is worth noting that there is an overlap in the whole range of computed spectra resulting from various input parameters investigation. Nonetheless, as seen in Fig. 5 most of the theoretical curves are in close proximity to the baseline result of both glands. A few outliers characterised with low-frequency β dispersion that are affecting the low range of results are the outcome of the examination of varying connective tissue and fascia permittivities, and do not represent the trend of the remaining computed results. The high values of permittivity (over 1e6) assigned in those instances correspond to the values reported for the tendon, which, despite its high collagen composition, is characterised with a different structure compared to fascia or thyroid connective tissue and thus such values can be excluded from future simulations.

The comparison between the simulated and in vivo results from Fig. 5 shows that the majority of the theoretical spectra predicted by our model lies within the range of the experimental EIS curves. The best fit can be observed in the frequency region above 100kHz for both tissue types. However, a closer inspection of the spectra indices presented in Fig. 6a and Table I, reveals discrepancies between the computed and in vivo results in the Z_1 index representing the low-frequency impedance. In contrast to the differences in computed results seen in in Fig. 4, the experimental data reports the opposite tendency, with higher low-frequency values for thyroid compared to parathyroid. Fig. 5 and 6 show wide variation in both modelled and measured data, which will contribute to this discrepancy.

It is important to note that the baseline results (red curves

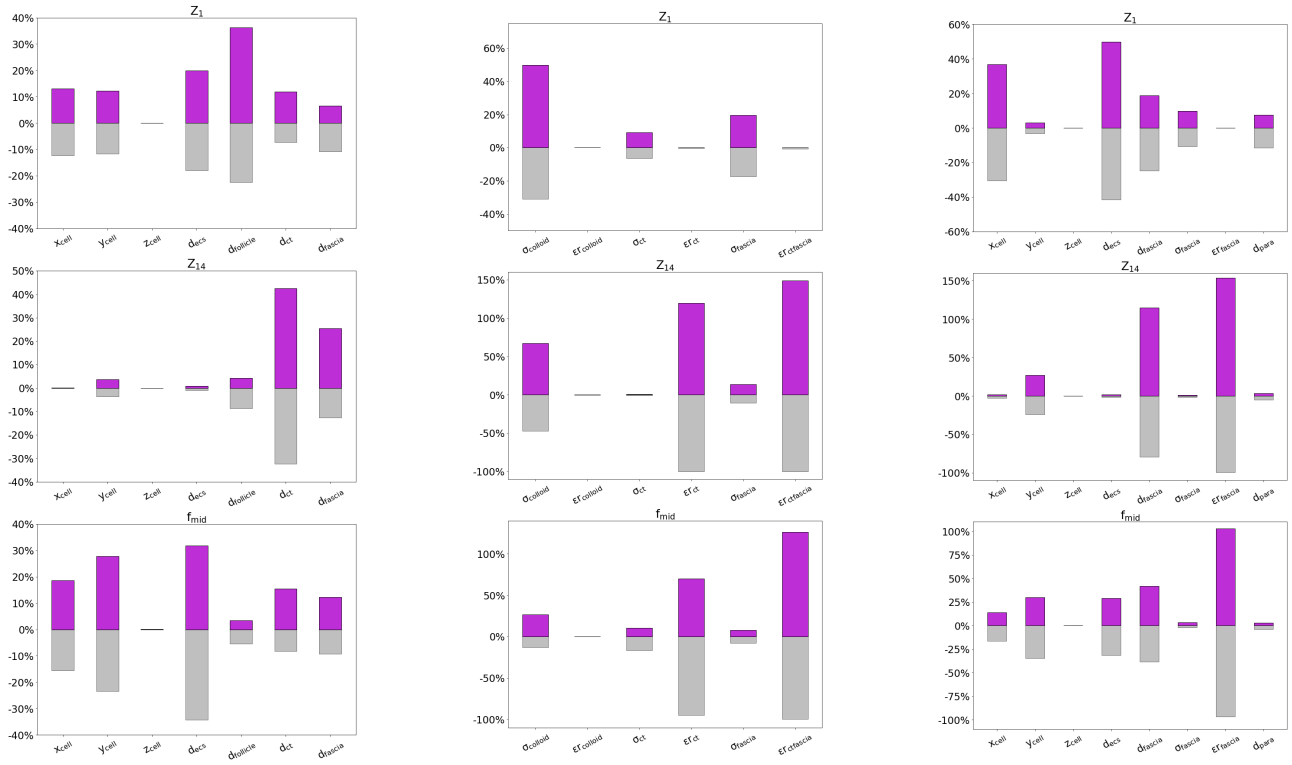

(a) (b) (c)

Fig. 7. Parameter sensitivity analysis results: (a) thyroid geometrical parameters, (b) thyroid material properties, (c) parathyroid parameters; x_{cell}, y_{cell}, z_{cell} - cell dimensions, d_{ECS} - ECS thickness, $d_{follicle}$ - dimensions of colloid compartment in the mesoscale model, d_{CT} - connective tissue thickness, d_{fascia} - fascia thickness, d_{para} - dimensions of parathyroid, $\sigma_{colloid}$ - conductivity of colloid, $\varepsilon r_{colloid}$ - relative permittivity of colloid, σ_{ct} - conductivity of connective tissue, εr_{ct} - relative permittivity of connective tissue, σ_{fascia} - conductivity of fascia, εr_{fascia} - relative permittivity of fascia

in 5) were generated without any attempt to adjust parameters to "fit" the measured data, which suggests the validity of a multiscale modelling approach and at least the approximate range of the morphological and electrical parameters selected. A useful feature of this computational model is the ability to explore how variations or uncertainties in either morphological features included in the model, or estimated electrical properties associated with features on different scales can impact the simulated results. In particular, our multiscale approach allows us to calculate the intercompartmental sensitivity of selected model outputs (in this case the extracted spectra indices) at the macroscale to changes in the inputs at lower scales.

As demonstrated by this sensitivity analysis, the variation in morphological parameters relating to tissue structure, as well as in the uncertainty in the electrical properties of different tissue compartments, are significant factors influencing the theoretical EIS curves. Therefore, the limitation in obtaining reliable model parameters for the model could partially explain the observed discrepancies in low-frequencies. Model cell and follicle sizes have been determined based on the values reported in the literature and our own measurements, however, other morphological parameters were not investigated as thoroughly and their magnitudes were estimated for this study purposes (e.g. ECS thickness has been determined based on previous cervical epithelium cells simulations [13] and electron emission microscopy images of dromedary camel parathyroid gland found in the literature [22]). As shown in Fig. 7a and 7c, the ECS thickness is one of the most important parameters that influences the low-frequency impedance for both tissue types, which is in agreement with previous computational studies in EIS modelling of cervical epithelium [13]. Additionally, the parameter study presented here mostly explored the effect of the extremities of the values reported in the literature which very coarsely covers the parameters' range.

The discrepancies in the simulated and in vivo measured low-frequency impedance could possibly also be explained by the measurement uncertainties associated with the experimental data collection. The surgeon separates the superficial fascia from the glands before taking the EIS measurement, however, sometimes the removal may be incomplete and it is not possible to quantify how much fascia is present on the tissue during the measurement. As demonstrated by our computational sensitivity study, all three spectra indices are sensitive to the fascia thickness and its electrical properties, with variation in fascia parameters associated with up to 150% change in impedance and dispersion frequency, notably decreasing the feasibility of tissue differentiation.

As noted in [2], the substantial variation of in vivo results could be explained by the differences in the measurements' conditions (temperature, humidity) and in the glands vascularity and viability (which is also difficult to assess during or after the surgery). Furthermore, in [2] it is discussed that the

tip of the probe of the ZedScan^{TM} device (5.5 mm) initially manufactured for the applications for cervical epithelium, is relatively large in comparison to parathyroid glands (typically 3-7 mm). Imprecise coverage of the parathyroid gland with the probe could lead to "contamination" of measurements by adjacent tissues – thyroid, fascia or adipose tissue – which is impossible to verify after the measurement. Additional computational work on probe optimisation and various probe-tissue misplacement scenarios could help to better grasp the importance of precision in EIS in vivo measurements.

In contrast to the discrepancies in the low-frequency impedance, both Z_{14} and f_{mid} indices show a similar trend for both computed and experimental results (Table 1): i.e. both indices are higher for the parathyroid than thyroid tissue in simulated and measured data. Nonetheless, when the magnitude of the differences (less than 10%) and the standard deviation are taken into consideration, there is a large overlap in the range of both parameters, preventing a clear separation of thyroid and parathyroid.

Lastly, the computational model over-predicts the f_{mid} parameter for both tissue types. The reason for this could be inappropriate selection of the poorly defined fascia and connective tissue relative permittivity, since those parameters mostly influence f_{mid}, as much as the ECS thickness (Fig. 7b and 7c). An additional explanation could be in the invalid assumption of the homogeneous structure for the models, which, as discussed in [23], can result in a sharp and narrow theoretical dispersion, compared to the results obtained experimentally. As explained further, the heterogeneity in the structures of the biological material is suspected to be responsible for wider β dispersion, possibly moving the f_{mid} towards lower frequencies. This could be verified through e.g. a larger multifollicular mesoscale model representing the thyroid follicles of different shapes and sizes.

The OAT local sensitivity analysis approach is a blunt tool for assessing parameter sensitivity, with more sophisticated global parameter sensitivity analyses being the gold standard [24], especially for non-linear models. However, given the long computational runtimes of our model (up to 5 min per frequency for the parathyroid macroscale model, giving $>$ 1h of computational time to obtain each impedance curve), the OAT method provides a convenient screening tool of the effect of individual parameters within a reasonable range and, despite covering only a fraction of the parameter space, has already highlighted significant and non-significant parameters for both tissues. In particular, all three spectra indices are insensitive to variations in the input parameters: cell size in the z direction (z_{cell}) and relative permittivity of colloid ($\varepsilon r_{colloid}$), hence, those parameters can be excluded from future parameter sensitivity investigation. On the other hand, the lack of documented electrical properties of colloid, connective tissue and fascia remains a significant challenge since, as visualised in the Fig. 7b and 7c, uncertainties in those parameters are responsible for over ±100% variation from the mean values in the investigated spectra indices. Nonetheless, the outcomes of this sensitivity study will allow to narrow down the range of the parameters, such as the fascia permittivity, in the future work. In addition, a future global sensitivity analysis, where multiple input parameter values are varied simultaneously, with suitable sampling of the entire parameter space will provide a more accurate assessment of the effect of model parameter uncertainty, estimate the sensitivity of the model to the input parameters and verify the outcomes of this local sensitivity study.

Further sensitivity analysis will also provide a larger sample size of theoretical impedance spectra which could provide additional input in elucidating the features differentiating the thyroid and parathyroid, which was not possible to determine based on the results of the local sensitivity study presented in this paper. Establishing clear differences in the electrical behaviour of the two tissue types would provide the justification for incorporating the EIS measurements as a tool for tissue differentiation during thyroidectomy.

V. CONCLUSION

In this study, multiscale finite element models of thyroid and parathyroid tissues have been developed to investigate their electrical properties and simulate their theoretical impedance curves corresponding to the EIS measurement. The presented macroscale impedance results are within the range of the in vivo measured spectra. However, observed discrepancies between computed and in vivo results and similarities in studied spectra indices for both tissues suggest that differentiation of the two tissues based on their measured electrical impedance in the range studied is not straightforward. Our computational parameter sensitivity study elucidated the isolated effect of chosen input parameters on features of the impedance spectra, highlighting in particular, the significance of the variations in the geometrical parameters (ECS thickness, follicle size, connective tissue thickness) resulting from the natural inter- and intrasubject morphological variability and uncertainties in material properties (colloid conductivity, relative permittivity of connective tissue and fascia) that come from insufficient experimental data on electrical properties of biological materials.

Our study emphasises the utility of computational models as a complement to in vivo EIS data measurement, particularly as a tool to study the influence of multiscale tissue features on macroscopic electrical properties. Further work will include a global sensitivity study, as well as an investigation into the impact of probe-misalignment and potential benefits of a smaller probe tip, to further broaden the understanding of the electrical properties of thyroid and parathyroid tissue and how impedance measurement may enhance tissue differentiation in thyroid surgery. Given the non-invasive nature of EIS measurement, this would be advantageous for both the surgeon and the patient, in terms of the potential benefits of the EIS-guided parathyroid detection in reducing the risks of hypoparathyroidism and hypocalcaemia.

SUPPLEMENTARY MATERIALS

Supplementary Materials document provides additional information for the Materials and Methods section, including additional description of the Finite Element modelling

approach (Section I) and a detailed summary on the model parameters (Section II). Additionally, the conductivities and permittivities derived from the lower-scale model simulations are summarised in the Supplementary Dataset.

ACKNOWLEDGMENT

The authors would like to acknowledge Zilico Ltd. (https://zilico.co.uk) for obtaining the funding for the project, Prof. Brian Brown for the expertise in the computational modelling relating to Electrical Impedance Spectroscopy, and the IT Services at The University of Sheffield for the provision of services for High Performance Computing.

REFERENCES

[1] D. R. Chadwick, "Hypocalcaemia and permanent hypoparathyroidism after total/bilateral thyroidectomy in the BAETS Registry," *Gland surgery*, vol. 6, no. Suppl 1, pp. S69–S74, dec 2017. [Online]. Available: https://pubmed.ncbi.nlm.nih.gov/29322024https://www.ncbi.nlm.nih.gov/pmc/articles/PMC5756750/

[2] S. L. Hillary, B. H. Brown, N. J. Brown, and S. P. Balasubramanian, "Use of Electrical Impedance Spectroscopy for Intraoperative Tissue Differentiation During Thyroid and Parathyroid Surgery," *World Journal of Surgery*, 2019. [Online]. Available: https://doi.org/10.1007/s00268-019-05169-7

[3] S. W. Kim, H. S. Lee, and K. D. Lee, "Intraoperative real-time localization of parathyroid gland with near infrared fluorescence imaging," *Gland surgery*, vol. 6, no. 5, pp. 516–524, oct 2017.

[4] Y. Shinden, A. Nakajo, H. Arima, K. Tanoue, M. Hirata, Y. Kijima, K. Maemura, and S. Natsugoe, "Intraoperative Identification of the Parathyroid Gland with a Fluorescence Detection System," *World Journal of Surgery*, vol. 41, no. 6, pp. 1506–1512, jun 2017. [Online]. Available: http://link.springer.com/10.1007/s00268-017-3903-0

[5] P. Mohr, U. Birgersson, C. Berking, C. Henderson, U. Trefzer, L. Kemeny, C. Sunderkötter, T. Dirschka, R. Motley, M. Frohm-Nilsson, U. Reinhold, C. Loquai, R. Braun, F. Nyberg, and J. Paoli, "Electrical impedance spectroscopy as a potential adjunct diagnostic tool for cutaneous melanoma," *Skin Research and Technology*, vol. 19, no. 2, pp. 75–83, may 2013. [Online]. Available: https://doi.org/10.1111/srt.12008

[6] B. H. Brown, J. A. Tidy, K. Boston, A. D. Blackett, R. H. Smallwood, and F. Sharp, "Relation between tissue structure and imposed electrical current flow in cervical neoplasia," *The Lancet*, vol. 355, no. 9207, pp. 892–895, 2000. [Online]. Available: https://www.sciencedirect.com/science/article/pii/S0140673699090959

[7] C. Murdoch, B. H. Brown, V. Hearnden, P. M. Speight, K. D'Apice, A. M. Hegarty, J. A. Tidy, T. J. Healey, P. E. Highfield, and M. H. Thornhill, "Use of electrical impedance spectroscopy to detect malignant and potentially malignant oral lesions," *International journal of nanomedicine*, vol. 9, pp. 4521–4532, sep 2014. [Online]. Available: https://pubmed.ncbi.nlm.nih.gov/25285005https://www.ncbi.nlm.nih.gov/pmc/articles/PMC4181751/

[8] B. A. Wilkinson, R. H. Smallwood, A. Keshtar, J. A. Lee, and F. C. Hamdy, "Electrical Impedance Spectroscopy and the Diagnosis of Bladder Pathology: A Pilot Study," *The Journal of Urology*, vol. 168, no. 4, Part 1, pp. 1563–1567, 2002. [Online]. Available: https://www.sciencedirect.com/science/article/pii/S0022534705645211

[9] V. Mishra, H. Bouayad, A. Schned, J. Heaney, and R. J. Halter, "Electrical impedance spectroscopy for prostate cancer diagnosis," in *2012 Annual International Conference of the IEEE Engineering in Medicine and Biology Society*, 2012, pp. 3258–3261.

[10] A. Stojadinovic, A. Nissan, Z. Gallimidi, S. Lenington, W. Logan, M. Zuley, A. Yeshaya, M. Shimonov, M. Melloul, S. Fields, T. Allweis, R. Ginor, D. Gur, and C. Shriver, "Electrical Impedance Scanning for the Early Detection of Breast Cancer in Young Women: Preliminary Results of a Multicenter Prospective Clinical Trial," *Journal of clinical oncology : official journal of the American Society of Clinical Oncology*, vol. 23, pp. 2703–2715, apr 2005.

[11] C. A. González-Correa, B. H. Brown, R. H. Smallwood, N. Kalia, C. J. Stoddard, T. J. Stephenson, S. J. Haggie, D. N. Slatter, and K. D. Bardhan, "Virtual Biopsies in Barrett's Esophagus Using an Impedance Probe," *Annals of the New York Academy of Sciences*, vol. 873, no. 1, pp. 313–321, apr 1999. [Online]. Available: https://doi.org/10.1111/j.1749-6632.1999.tb09479.x

[12] Zilico Limited, "ZedScan™ a new standard in colposcopy - technical brochure." [Online]. Available: www.zilico,co.uk

[13] D. C. Walker, "Modeling the Electrical Properties of Cervical Epithelium," Ph.D. dissertation, University of Sheffield, 2001.

[14] D. C. Walker, R. H. Smallwood, A. Keshtar, B. A. Wilkinson, F. C. Hamdy, and J. A. Lee, "Modelling the electrical properties of bladder tissuequantifying impedance changes due to inflammation and oedema," *Physiological Measurement*, vol. 26, no. 3, pp. 251–268, 2005.

[15] J. P. Heath, K. D. Hunter, C. Murdoch, and D. C. Walker, "Computational Modelling for Electrical Impedance Spectroscopy-Based Diagnosis of Oral Potential Malignant Disorders (OPMD)," 2022.

[16] A. Hartinger, R. Guardo, V. Kokta, and H. Gagnon, "A 3-D Hybrid Finite Element Model to Characterize the Electrical Behavior of Cutaneous Tissues," *Biomedical Engineering, IEEE Transactions on*, vol. 57, pp. 780–789, may 2010.

[17] U. Birgersson, E. Birgersson, and S. Ollmar, "Estimating electrical properties and the thickness of skin with electrical impedance spectroscopy: Mathematical analysis and measurements," *Journal of Electrical Bioimpedance*, vol. 3, jul 2012.

[18] S. Huclova, D. Erni, and J. Fröhlich, "Modelling effective dielectric properties of materials containing diverse types of biological cells," *Journal of Physics D: Applied Physics*, vol. 43, no. 36, p. 365405, 2010. [Online]. Available: http://dx.doi.org/10.1088/0022-3727/43/36/365405

[19] ——, "Modelling and validation of dielectric properties of human skin in the MHz region focusing on skin layer morphology and material composition," *Journal of Physics D: Applied Physics*, vol. 45, no. 2, p. 025301, jan 2012. [Online]. Available: http://stacks.iop.org/0022-3727/45/i=2/a=025301?key=crossref.48544880ea59acc1fd00f0b22bef3b80

[20] Y. Lv, Y. Zhang, J. Huang, Y. Wang, and B. Rubinsky, "A Study on Nonthermal Irreversible Electroporation of the Thyroid," *Technology in Cancer Research Treatment*, vol. 18, p. 1533033819876307, jan 2019. [Online]. Available: https://doi.org/10.1177/1533033819876307

[21] N. Nasir and M. Al Ahmad, "Cells Electrical Characterization: Dielectric Properties, Mixture, and Modeling Theories," *Journal of Engineering*, vol. 2020, p. 9475490, 2020. [Online]. Available: https://doi.org/10.1155/2020/9475490

[22] M. Al-Zghoul, "Macro- and Micro-Morphological Studies on the Parathyroid Glands of Dromedary Camel," *Pakistan Veterinary Journal*, vol. 37, pp. 59–64, jan 2017.

[23] G. H. Markx, C. L. Davey, and D. B. Kell, "To what extent is the magnitude of the Cole-Cole α of the β-dielectric dispersion of cell suspensions explicable in terms of the cell size distribution?" *Bioelectrochemistry and Bioenergetics*, vol. 25, no. 2, pp. 195–211, 1991. [Online]. Available: https://www.sciencedirect.com/science/article/pii/030245989187003Y

[24] A. Saltelli, K. Aleksankina, W. Becker, P. Fennell, F. Ferretti, N. Holst, S. Li, and Q. Wu, "Why so many published sensitivity analyses are false: A systematic review of sensitivity analysis practices," *Environmental Modelling Software*, vol. 114, pp. 29–39, 2019. [Online]. Available: https://www.sciencedirect.com/science/article/pii/S1364815218302822

Computational Modelling of Probe Configurations for Electrical Impedance Spectroscopy-based Differentiation of Thyroid and Parathyroid Tissues

Malwina Matella
Department of Computer Science
The University of Sheffield
Sheffield, UK
mmatella1@sheffield.ac.uk
ORCID: 0000-0003-2109-335X

Dawn C. Walker
Department of Computer Science
The University of Sheffield
Sheffield, UK
dcwalker@sheffield.ac.uk
ORCID: 0000-0001-8801-8093

Keith Hunter
Liverpool Head and Neck Centre
The University of Liverpool
Liverpool, UK
keith.hunter@liverpool.ac.uk

Abstract*—Background: The ZedScan™ probe is an electrical impedance spectroscopy (EIS) device originally developed as a tool to diagnose Cervical Intraepithelial Neoplasia (CIN), recently explored as a potential tool to distinguish parathyroid glands from the surrounding tissues during surgery [1]. As reported, the relatively large size of the tip of the probe (5.5 mm) can be problematic to accurately cover and measure the impedance of small structures, such as parathyroid glands (3-7 mm). In this study, we will utilise a computational model to quantify the uncertainty associated with the probe misalignment and evaluate the benefits of reducing the size of the probe on thyroid and parathyroid differentiation. Materials and Methods: Multiscale finite element models of thyroid and parathyroid were developed to investigate the impact of the EIS measurement accuracy of various probe-parathyroid misalignment scenarios. Subsequently, the macroscale impedivity of thyroid and parathyroid tissues was simulated with smaller probe configurations to explore the benefits of probe optimisation. Results: The probe misalignment study reported up to 40%, 21% and 26% decrease in low- and high-frequency impedance and impedance frequency, respectively, compared to results with a desirable parathyroid-probe coverage. The decrease in parathyroid impedance brings the results closer to thyroid baseline EIS spectrum, reducing the feasibility of tissues separation. The probe optimisation study reported about 4% increase in parathyroid's low-frequency impedance, showing a slight improvement in the thyroid and parathyroid differentiation. Conclusions: This study revealed the importance of the accuracy of the EIS measurement with the ZedScan™ device by demonstrating that imprecise parathyroid coverage could result in 'contaminated' measurements constraining their differentiation. Moreover, a smaller probe-tip design has the potential to further increase the ease of acquiring accurate parathyroid results, slightly improving the separation between the tissues on the basis of EIS measurements.

***Index Terms*—Electrical Impedance Spectroscopy, Finite Element Modelling, Thyroid and Parathyroid Tissue Discrimination, Probe Misalignment, Probe Optimisation**

I. Introduction

ZedScan™, Zilico Limited (Fig. 1a) [2], is a commercial electrical impedance spectroscopy (EIS) probe primarily designed and manufactured for applications in cervical epithelium. Specifically, it has been demonstrated to provide enhanced effectiveness in the detection of cervical intraepithelial neoplasia compared to the standard colposcopy procedure [3]. This EIS device, however, was also explored as a tool in applications for other tissues, such as diagnosis of oral potential malignant disorder [4], [5], and lately, also during thyroid and parathyroid surgeries ([1], [6]) to distinguish parathyroid glands from the surrounding tissues. Due to their small size and location on the posterior wall of the thyroid tissue, healthy parathyroids may get damaged or accidentally removed, which could lead to hypoparathryodism and hypocalceama which are the most frequent complications associated with this type of surgery [7]. The EIS device has the potential for a non-invasive parathyroids identification, and therefore, could enhance their location and preservation.

In their in vivo experimental study, Hillary et al. [1] discussed several limitations of the ZedScan™ device in the thyroid and parathyroid surgery setting, including its long neck and the 5.5 mm tip size (Fig. 1b), which, anticipated for the use during colposcopy, might not be adequate to precisely cover structures as small as parathyroids (3-7 mm). Imprecise coverage of the parathyroid glands with the probe could potentially lead to the data 'contamination' by tissues surrounding the glands and could prevent clear parathyroid glands identification.

In a previous study (under review [8]), we developed multiscale finite element (FE) models that recreate the cellular and supracellular structure of thyroid and parathyroid tissues in order to investigate the relationship between the macroscale impedance relating to the EIS measurement with the ZedScan™ probe, and the variation of tissue morphological features and material properties uncertainties at different scales. In this paper we will employ the previously generated computational models to explore and quantify the uncertainty associated with the imprecise parathyroid coverage with the ZedScan™ EIS device. Additionally, the potential advantages associated with the size optimisation of the tip of the probe on the parathyroid tissue measurement, and the parathyroid and

The study was funded by Zilico Ltd. (https: //zilico.co.uk) and EPSRC Case Studentship

thyroid glands separation will be further evaluated, which, to date has been explored computationally for the applications relating to cervical epithelium [9] and oesophagus [10].

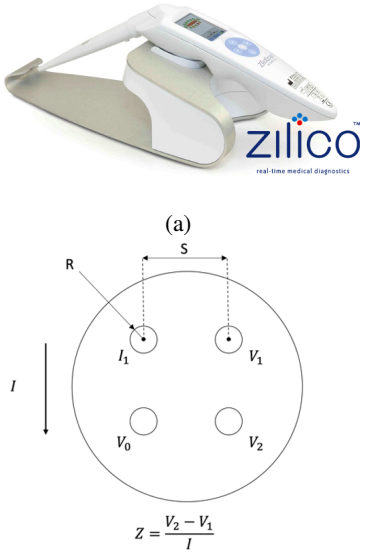

Fig. 1: Electrical impedance spectroscopy device: (a) ZedScanTM, Zilico Limited probe image [2]; (b) schematic of the tip of the ZedScan™ probe marking the principle of measurement: a known current I flows between the active electrodes (I_1 and V_0) while the passive electrodes (V_1 and V_2) capture the potential difference at each frequency, R – electrode radius, S – electrodes separation

II. Materials and Methods

A. Finite element tissue models

The multiscale FE modelling framework was developed in order to decrease the computational expenses associated with cell membrane details inclusion, which are a crucial structure responsible for the unique frequency-dependent behaviour of biological tissue, mainly for the considerable fall in the real part of impedance around the kHz-MHz region known as β dispersion. The inclusion of such small cellular substructures (8 nm) into a model volume of several centimeters required for EIS related electrical simulation would result in over trillion nodes, which is computationally intractable. This constraint is overcome by multiscale modelling, which divides the tissue's structure into hierarchical substructures that represent various levels of tissue's complexity, from cellular (microscale), through follicular (mesoscale) appearing solely in thyroid, to tissue scale level (macroscale). Submodels' transfer impedivities are simulated and calculated, starting with the lowest model hierarchy (microscale) and passed to the higher-level models in the form of element material properties (electrical conductivity σ and relative permittivity ε_r). To simulate the electrical impedance of both tissues, the commercial software ANSYS Mechanical APDL with its quasistatic time-harmonic simulation [11] was utilised.

For the purposes of this study, the macroscale thyroid and parathyroid models have been implemented (Fig. 2) with assigned material properties obtained from previous micro- and mesoscale level simulations (under review [8]). The default macroscale model recreates the electrode arrangements of the tetrapolar ZedScan™ probe with four electrodes (radius R=0.3 mm) arranged with the centres located on a circle of 2 mm diameter (separation S=1.4 mm).

B. Probe misalignment study

In order to investigate the effects of the imprecise coverage of the parathyroid gland with the tetrapolar probe, models recreating two different scenarios were generated where either one (25% of the probe – Fig 3a) or two (50% of the probe - Fig. 3b) of the electrodes are in contact with the parathyroid gland. To further inspect the possible influence associated with the type of contact electrodes (active or passive) on the measured impedance, all possible gland-electrode variations have been constructed. The parathyroids are considered to be surrounded by thyroid tissue for the purposes of this study (Fig. 2). The obtained results were compared to the baseline parathyroid and thyroid spectra generated in the previous study (unpublishd [8]) to assess the relative effect on the tissues separation feasibility.

C. Probe optimisation study

In order to investigate whether the current size of the tip of the ZedScan™ device may not be optimal for the parathyroid impedance measurement, a few model setups looking into the probe optimisation have been investigated. The simulations have been performed to explore the effect of decreased electrodes' separation S and electrodes' radii R (marked in Fig. 1b) on the measured electrical properties to suggest a configuration that could enhance thyroid and parathyroid differentiation. Nine different arrangements of electrode separations S=[1.4, 1.2, 1.0] mm and radii R=[0.3, 0.2, 0.1] mm have been investigated in both thyroid and parathyroid tissue models.

Since impedance values recorded by the tetrapolar probe are sensitive to its geometrical features investigated in this part of the study, it is not sensible to compare the raw impedance data between the various cases. Therefore, the impedivity values were compared instead that have been obtained through dividing the macroscale impedance results by geometric constants specific to each probe configuration. The latter were acquired through additional calibration simulations by assigning model with each electrodes' setup with material of 1 Sm^{-1} conductivity σ and without dielectric properties (0 relative permittivity ε_r).

III. Results

The study resulted in eight and eighteen macroscale simulations for the probe misalignment and probe optimisation studies respectively. Each simulation provided real part of impedance values at 14 frequencies from the 76Hz-625kHz range corresponding to the ZedScan™ operating frequency

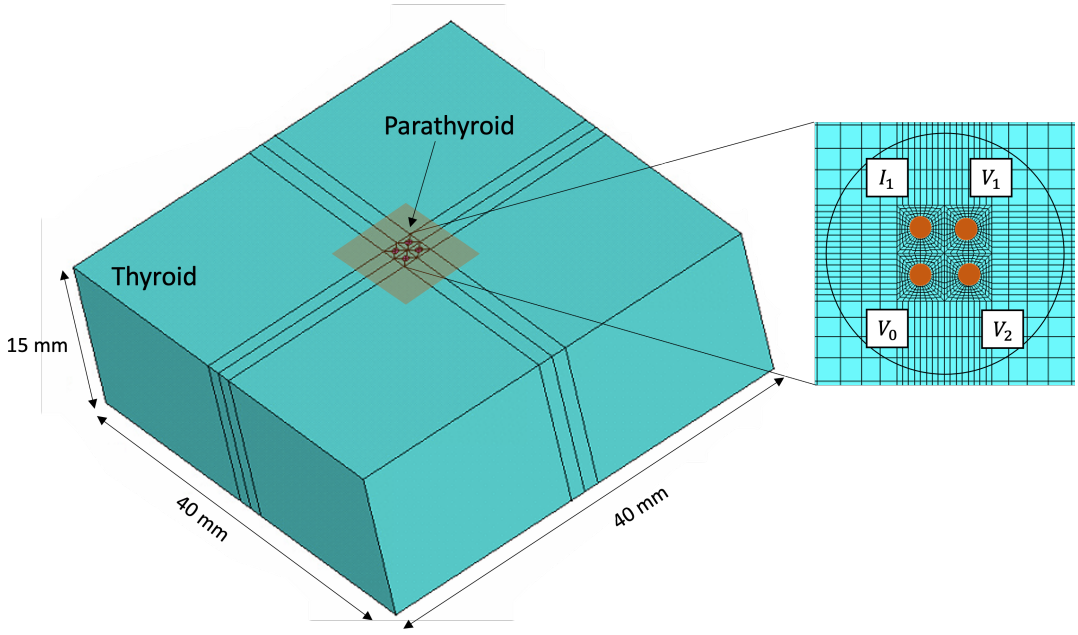

Fig. 2: Macroscale model for thyroid or parathyroid tissue (shaded orange region highlights the location of parathyroid) with marked electrodes configuration from the current ZedScan^{TM} device, where I_1 – driving electrode, V_0 – ground electrode, V_1 and V_2 – passive electrodes

range. To aid the quantitative comparison of the results, each computed spectrum was parameterised with three indices: Z_1 – impedance at 76Hz, Z_{14} – impedance at 625kHz and f_{mid} – frequency in the middle of the dispersion (relating to the impedance value between Z_1 and Z_{14}).

A. *Probe misalignment study*

Fig. 4 shows the results for the probe misalignment study with the spectra for different configuration of 50% and 25% probe-parathyroid coverage and two baseline spectra showing the thyroid and parathyroid outcomes resulting from the accurate and symmetrical electrodes' placement. The probe misalignment affects the impedance values across the studied frequency range and all three spectra parameters Z_1, Z_{14} and f_{mid}, as presented in Table I. Furthermore, the computed impedance is reduced as the number of electrodes in contact with the parathyroid gland decreases. It is also worth noting that the type of the contact electrode was an influential factor for the 50% probe coverage scenario – the impedance was higher for the mixed (one active and one passive) electrodes relative to the other combinations. Nonetheless, for the setup with a single contact electrode, there was no variation in the computed impedance values with respect to the electrode type. The data summarised in Table I shows that the imprecise parathyroid coverage lowers not only the real impedance values, but the dispersion frequency f_{mid} as well.

Probe coverage	**Z_1 [Ω]**	**Z_{14} [Ω]**	**f_{mid} [kHz]**
50%: I_1-V_1, V_2-V_0	371.54	147.18	220.65
50%: I_1-V_0, V_1-V_2	325.71	144.04	191.37
25%: V_0, I_1, V_1, V_2	290.75	133.96	177.25
Parathyroid baseline	480.69	169.60	240.25
Thyroid baseline	246.47	122.31	150.46

TABLE I: The quantitative data of the selected spectra indices (Z_1 – impedance at 76Hz, Z_{14} – impedance at 625kHz, f_{mid} – dispersion frequency) showing the results of the probe misalignment in comparison to parathyroid and thyroid results from precise (symmetrical) probe placement. I_1, V_0, V_1 and V_2 labels correspond to the electrode types from the Fig. 1b and Fig. 3

B. *Probe optimisation study*

In the probe optimisation study, each separation S and radii R configuration was investigated for both thyroid and parathyroid models, and the obtained impedivity spectra are shown in Fig. 5. Given that the probe optimisation had no impact on the thyroid impedivities, there is just one thyroid curve marked on the graph (black spectrum). Nonetheless, there is a slight increase in the parathyroid impedivity at frequencies below 100kHz with the decreased separation S between the electrodes. However, the results at 76Hz show a difference of only 2.1% and 3.7% higher impedance for the cases characterised with optimised electrode separation S

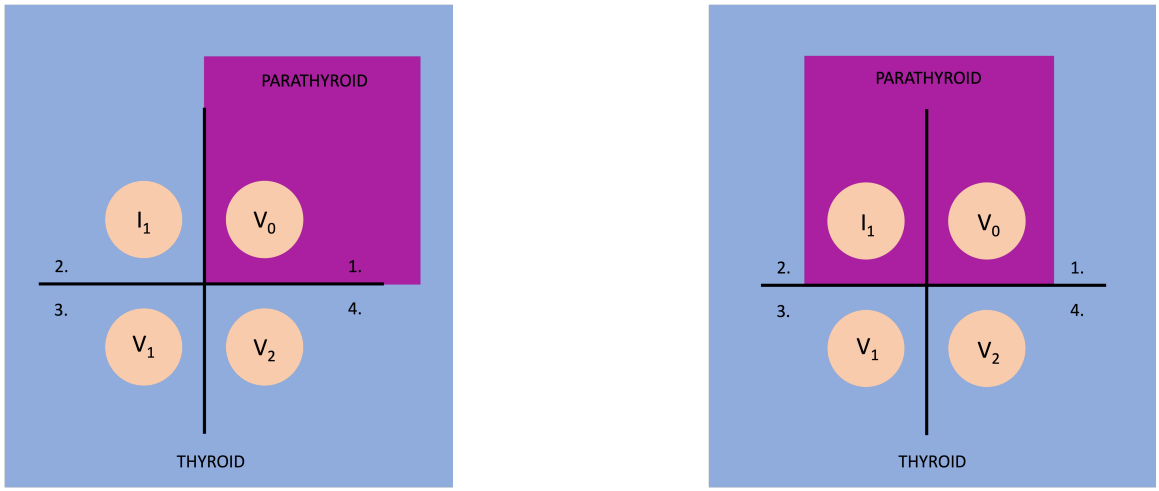

(a) (b)

Fig. 3: Model schematics for the probe misalignment study illustrating two measurement scenarios when (a) one (25% of the probe) or (b) two (50% of the probe) electrodes are in contact with parathyroid gland, the simulation is repeated for the gland position in quarts 1-4

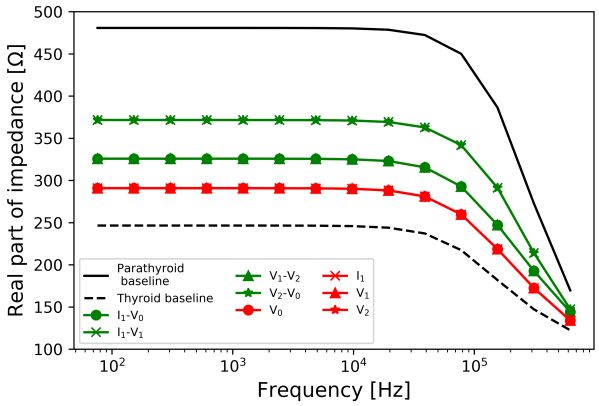

Fig. 4: Probe misalignment study results for 50% (green spectra) and 25% (red spectra) of probe-gland coverage, black spectra show the baseline parathyroid (solid line) and thyroid (dashed line) results from simulation with the probe placed symmetrically on the gland, I_1, V_0, V_1 and V_2 labels correspond to the electrode types from the Fig. 1b and Fig. 3

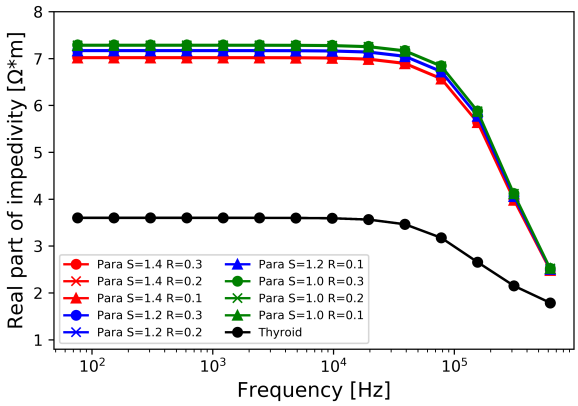

Fig. 5: Probe optimisation study results showing the effect of the electrodes separation S and radii R on the simulated electrical properties of thyroid and parathyroid, Para – parathyroid

of 1.2 mm and 1.0 mm compared to the default ZedScan™ electrode configuration (S=1.4 mm). Additionally, the changes in the electrodes' radii did not affect the obtained impedivities for both tissue types.

IV. Discussion

The objective of the presented study was to utilise computational modelling to investigate, quantify, and reveal the significance of potential imprecision in the parathyroid tissue EIS measurements on the parathyroid and thyroid tissues differentiation during surgery. Moreover, the study was aimed to suggest changes in the ZedScan™ tetapolar probe's tip geometry to improve these tissue's separation based on their electrical properties.

As highlighted in the probe misalignment study results, an inexact coverage of the parathyroid gland could result in lower impedance recordings across the whole studied frequency range compared to the expected (baseline) value for parathyroid glands obtained from an accurate probe placement configuration. Furthermore, it can be concluded that the successful parathyroid tissue identification can be challenging in the case of imprecise measurements, since, as visualised in Fig. 4, the simulations from the misaligned probe cases (Fig. 3) lead to the 'contaminated' results which get closer to the baseline thyroid spectrum instead. By solely comparing the low-frequency index Z_1, the misalignment can reduce

the difference in impedance between thyroid and parathyroid from 95% to nearly 18%. That also suggests that inaccurate parathyroid coverage could partially explain the wide range of recorded in vivo parathyroid results (138.99-572.67 Ω in [1]) along with the effects of inter- and intrasubject variability in the morphology and composition of parathyroid and thyroid tissue verified in the previous computational study (under review [8]).

Additionally, it is worth noting that the parathyroid spectra from the misalignment study are characterised with decreased impedance exclusively through the assumption that parathyroid gland is surrounded by a material of lower conductivity such as thyroid tissue. The opposite trend of increased impedance would have been observed e.g. in an instance of the gland surrounded by the adipose tissue, known for its insulating properties (low frequency conductivity of 0.04 Sm^{-1} [12]).

An increase in parathyroid impedivities were seen in the probe optimisation investigation (Fig. 5) in the case of decreased electrode separation S, which shows that measurements with a smaller probe could more effectively distinguish between thyroid and parathyroid tissue. That increase in the impedivity could be explained, that, as a result of the smaller distance between the drive electrodes, I_1 and V_0, the injected current flows more superficially (which was demonstrated previously in the probe size investigations on the cervical epithelium [9]), gets constrained flowing solely through the parathyroid gland without capturing the properties of the adjacent thyroid tissue. However, the documented extent of the separation improvement (up to 4% change in the low frequency impedance index Z_1 compared to the parathyroid results for current ZedScan™ electrodes configuration) suggests, that the tip of the probe's geometry is a far less significant factor compared to measurement precision responsible for up to 40% decrease in Z_1 index. Additionally, as it was demonstrated in Fig. 5, decreasing the size of electrodes does not interfere with the recorded impedivity, hence, if there are no contraindications from the technical and manufacturing point of view, smaller electrodes can successfully be incorporated into an optimised EIS probe to further improve the measurement accuracy.

Finally, in this study we demonstrated the benefits of computational modelling techniques which may be useful to optimise the hardware of medical devices. In particular, the FE simulations presented in this study offer fast, safe and low-cost predictions of the impact of the size and arrangement of the ZedScan™ EIS probe electrodes, in comparison to the process of manufacturing different sets of the probe-electrodes configurations and the collection of numerous in vivo measurements, similar to the experimental study presented by Hillary et al. [1]. A potential direction for future work is the exploration of non-tetrapolar electrode configurations which could provide more insight on the measurement technique that could enhance tissue differentiation during thyroid and parathyroid surgery.

V. Conclusions

This study explored the significance of measurement accuracy using the ZedScan™ device by illustrating how inaccurate parathyroid coverage could lead to 'contaminated' EIS readings which constrain the ability of EIS to aid in the differentiation of the parathyroid and thyroid tissues' during surgery. Furthermore, the probe misalignment was suggested as a possible explanation for the wide range of the in vivo parathyroid impedance measurements documented in the literature. Finally, results of the probe optimisation study suggested that a smaller tip design has the potential to further increase the ease of acquiring reliable parathyroid results by improving the separation between the parathyroid and thyroid tissues on the basis of their EIS spectra.

Acknowledgment

The authors would like to acknowledge Zilico Ltd. (https://zilico.co.uk) for obtaining the funding for the project, Prof. Brian Brown for the expertise in the computational modelling relating to Electrical Impedance Spectroscopy, Prof. Saba Balasubramanian for the expertise in endocrine surgeries, and the IT Services at The University of Sheffield for the provision of services for High Performance Computing.

References

[1] S. L. Hillary, B. H. Brown, N. J. Brown, and S. P. Balasubramanian, "Use of Electrical Impedance Spectroscopy for Intraoperative Tissue Differentiation During Thyroid and Parathyroid Surgery," *World Journal of Surgery*, 2019. [Online]. Available: https://doi.org/10.1007/s00268-019-05169-7

[2] Zilico Limited, "ZedScan™ a new standard in colposcopy - technical brochure." [Online]. Available: www.zilico,co.uk

[3] J. A. Tidy, B. H. Brown, T. J. Healey, S. Daayana, M. Martin, W. Prendiville, and H. C. Kitchener, "Accuracy of detection of high-grade cervical intraepithelial neoplasia using electrical impedance spectroscopy with colposcopy," *BJOG: An International Journal of Obstetrics Gynaecology*, vol. 120, pp. 400–411, 3 2013, https://doi.org/10.1111/1471-0528.12096. [Online]. Available: https://doi.org/10.1111/1471-0528.12096

[4] J. P. Heath, K. D. Hunter, C. Murdoch, and D. C. Walker, "Computational Modelling for Electrical Impedance Spectroscopy-Based Diagnosis of Oral Potential Malignant Disorders (OPMD)," 2022.

[5] C. Murdoch, B. H. Brown, V. Hearnden, P. M. Speight, K. D'Apice, A. M. Hegarty, J. A. Tidy, T. J. Healey, P. E. Highfield, and M. H. Thornhill, "Use of electrical impedance spectroscopy to detect malignant and potentially malignant oral lesions," *International journal of nanomedicine*, vol. 9, pp. 4521–4532, sep 2014. [Online]. Available: https://pubmed.ncbi.nlm.nih.gov/25285005https://www.ncbi.nlm.nih.gov/pmc/articles/PMC4181751/

[6] R. Antakia, B. Brown, P. Highfield, T. Stephenson, N. Brown, and S. Balasubramanian, "Electrical Impedance Spectroscopy to Aid Parathyroid Identification and Preservation in Central Compartment Neck Surgery: A Proof of Concept in a Rabbit Model," *Surgical innovation*, vol. 23, oct 2015.

[7] D. R. Chadwick, "Hypocalcaemia and permanent hypoparathyroidism after total/bilateral thyroidectomy in the BAETS Registry," *Gland surgery*, vol. 6, no. Suppl 1, pp. 69–74, dec 2017. [Online]. Available: https://pubmed.ncbi.nlm.nih.gov/29322024https://www.ncbi.nlm.nih.gov/pmc/articles/PMC5756750/

[8] M. Matella, K. Hunter, S. P. Balasubramanian, and D. C. Walker, " Multiscale Model Development for Electrical Properties of Thyroid and Parathyroid Tissues (under review)."

[9] S. V. Gandhi, D. C. Walker, B. H. Brown, and D. O. C. Anumba, "Comparison of human uterine cervical electrical impedance measurements derived using two tetrapolar probes of different sizes," *BioMedical Engineering OnLine*, vol. 5, no. 1, p. 62, 2006. [Online]. Available: https://doi.org/10.1186/1475-925X-5-62

[10] D. M. Jones, R. H. Smallwood, D. R. Hose, B. H. Brown, and D. C. Walker, "Modelling of epithelial tissue impedance measured using three different designs of probe," *Physiological Measurement*, vol. 24, no. 2, pp. 605–623, may 2003. [Online]. Available: https://iopscience.iop.org/article/10.1088/0967-3334/24/2/369

[11] ANSYS, "Theory Reference for the Mechanical APDL and Mechanical Aplications," 2009.

[12] C. Gabriel, *Compilation of the dielectric properties of body tissues at RF and microwave frequencies*. King's College London, 1996. [Online]. Available: https://books.google.pl/books?id=4MvhMgEACAAJ